Crystallography Reports, Vol. 45, No. 1, 2000, pp. 1–5. Translated from Kristallografiya, Vol. 45, No. 1, 2000, pp. 7–11.

CRYSTAL SYMMETRY

Three-dimensional Point Groups of Hypercrystallographic Second-order *P*-symmetries and Their Multidimensional Applications

A. F. Palistrant and A. M. Zamorzaev†

Moldova State University, Chisinau, 277009 Moldova

Received January 26, 1998

Abstract—All the three-dimensional point groups G_{30}^{P} of 624 hypercrystallographic second-order *P*-symmetries have been derived at $P \simeq G_{5430}$. On this basis, it was established that the category G_{87630} of eight-dimensional point groups with the invariant hyperplane and the 6- and 3-dimensional planes enclosed into this category has 814871 groups. A universal formula is derived for calculation of the number of new groups generated by an arbitrary category of the symmetry groups generalized with due regard for the above 624 *P*-symmetries. © *2000 MAIK "Nauka/Interperiodica".*

1. Recently, Zamorzaev and Palistrant, using the notions of strong group isomorphism and isomorphism of *P*-symmetries [2], have derived the three-dimensional point groups G_{30}^{P} of the complete *P*-symmetry for 122 hypercrystallographic first-order *P*-symmetries (at $P \simeq G_{430}$) [1]. This provided for the establishment of 64678 seven-dimensional point groups with the invariant hyperplane with the enclosed three-dimensional plane, i.e., the groups of the category G_{7630}. The present paper is a logical continuation of the study performed in [1] and deals with (1) the calculation of all the three-dimensional point groups G_{30}^{P} of the complete *P*-symmetry for 624 hypercrystallographic second-order *P*-symmetries (at $P \simeq G_{5430}$) [3, 4] and their description with the eight-dimensional groups of the category G_{87630}; (2) the derivation of a universal formula for determination of the number of new groups generated by any category of the symmetry groups and their generalization with due regard for 624 hypercrystallographic second-order *P*-symmetries.

2. Using the analogy with the hypercrystallographic first-order *P*-symmetries ($P \simeq G_{5430} \simeq G_{30}^{2}$), we define the hypercrystallographic second-order *P*-symmetries ($P \simeq G_{430} \simeq G_{30}^{1}$) as complete or incomplete (P_0, 2, 2, 2)-symmetries (in distinction from the hypercrystallographic first-order *P*-symmetries which are complete or incomplete (P_0, 2, 2)-symmetries [1]). In this case, attributing the subscripts 1, 2, …, *p* and the signs "+" and "–" in the above three meanings, we arrive at:

(i) $P = P_2$ (the P_2-symmetry or the first-order hypercrystallographic symmetry, i.e., the complete or incomplete (P_0, 2, 2)-symmetry). Thus, we obtain 122 *P*-symmetries indicated in [3, 4, 1];

(ii) $P = P_2 \times \{(+, -)\}$ (the P_2-symmetry is first-order hypercrystallographic symmetry and the signs "+" or "–" are used in their third meaning). This leads to 122 additional *P*-symmetries (for example, *1-, (2*1)-, ($\underline{4}$3*1)-, (1'*1)-, (21'*1)-, (2'*1)-, (2'*1)-, (2'$\underline{1}$*1)-, and ($\underline{2}$2'*1)-symmetry);

(iii) $P \simeq P_2$, $P \subset P_2 \times \{(+, -)\}$, $P \not\supseteq \{(+, -)\}$ (P_2 and the signs "+" and "–" are the same), and we obtain 380 additional different *P*-symmetries (for example, *$\underline{1}$-, *1'-, (2*$\underline{1}$)-, (2$\underline{1}$'*1)-, *2-, *4'-, *$\underline{2}$'-, (*2$\underline{1}$1')-, and ($\underline{2}$*$\overline{2}$)-symmetry) [3, 4]. The bar under the symbols of these 624 *P*-symmetries, the prime on the upper right, and the asterisk on the upper left have the same meaning as in the symbols of three-fold antisymmetry [5].

To facilitate and abridge the complete derivation of the G_{30}^{P} groups for 624 second-order *P*-symmetries, we invoke the concepts of strong isomorphism of the groups and isomorphism of *P*-symmetries [2].

Let G_1 and G_2 be the groups with the set equivalence of the elements, which possesses the property of equivalence. Then the isomorphism of G_1 on G_2 is called strong if it provides the property of all the equivalent elements and the elements equally included into G_1 to have the corresponding equivalent elements in G_2, and of nonequivalent elements equally included into G_1 to have the corresponding nonequivalent elements equally included into G_2 (cf. with [1]). Zamorzaev [2] has proved that the number of different *Q*-intermediate groups of the *P*-symmetry with the given generatrix is equal to the number of various junior groups of P_0-sym-

† Deceased.

metry having the same generatrix, provided that the factor-group P/Q is strongly isomorphic to P_0 ($P/Q \cong P_0$).

The P- and the P'-symmetries are called isomorphic if $P \cong P'$. In this case, in the families of groups of the P- and the P'-symmetries, both the numbers of different junior groups and the numbers of various intermediate groups are the same. Therefore, preliminarily dividing 624 hypercrystallographic second-order P-symmetries into isomorphism classes, one can study in detail only 44 nonisomorphic classes of the total 624 ones. Therefore, the junior and the intermediate rosette and border groups G_{20}^P and G_{21}^P of 624 hypercrystallographic second-order P-symmetries have been derived [3, 4]. The detailed analysis was performed for 44 nonisomorphic classes. The same method is used below to generalize 32 crystallographic classes G_{30} with the above 624 hypercrystallographic P-symmetries.

3. Proceed to the analysis of the point groups G_{30}^P at $P \simeq G_{5430}$. In accordance with the general theory of P-symmetry and the methods of their derivation from the classical groups [6–8], these groups are divided into generating, senior, junior, and intermediate ones. Using the same reasons as in Sect. 3 of [1], we obtain 32 generating and $32 \times 623 = 19936$ senior groups. Now, we have to derive junior and intermediate groups of 623 P-symmetries. Similar to [3, 4], to reduce the list of the P-symmetries and the types of intermediate Q groups, we use the methods A, B, and C. These methods reduce to writing one representative of 3, 7, and 21 symbols of various P (or Q) groups of the same form. For example, the notation ($\underline{1} - A$) is interpreted as $\langle\langle \underline{1}\text{-}, 1'\text{-}, \text{and } \underline{1}'\text{-}\rangle\rangle$; the notation ($\underline{2} - B$) is interpreted as $\langle\langle \underline{2}\text{-}, 2'\text{-}, *2\text{-}, \underline{2}'\text{-}, *\underline{2}\text{-}, *2'\text{-}, *\underline{2}'\text{-}\rangle\rangle$; the notation ($2'\underline{1} - C$), as $\langle\langle 2'\underline{1}\rangle\text{-}, (*2\underline{1})\text{-}, (*2'\underline{1})\text{-}, (\underline{2}1')\text{-}, (*21')\text{-}, (*\underline{2}1')\text{-}, (\underline{2}*1)\text{-}, (2'*1)\text{-}, (\underline{2}'*1)\text{-}, (\underline{2}\ \underline{1}')\text{-}, (*2\underline{1}')\text{-}, (*\underline{2}\ \underline{1}')\text{-}, (\underline{2}*\underline{1})\text{-}, (2'*\underline{1})\text{-}, (\underline{2}'*\underline{1})\text{-}, (2'*1')\text{-}, (\underline{2}*1')\text{-}, (\underline{2}'*1')\text{-}, (2*\underline{1}')\text{-}, (\underline{2}'*\underline{1}')\text{-}, (*2*\underline{1}')\text{-}\rangle\rangle$ (cf. with [3, 4]).

At the 2-, ($\underline{1} - B$)-, and ($\underline{2} - B$)-symmetries, the category G_{30} generates 58 junior groups (altogether $58 \times 15 = 870$ groups), and, at the 3-symmetry, 7 junior groups. At the 4- and ($\underline{4} - B$)-symmetries, G_{30} generates 4 junior and 58 2-intermediate groups (altogether $4 \times 8 + 58 \times 8 = 496$ groups). At the 6-, ($3\underline{1} - B$)-, and ($\underline{6} - B$)-symmetries, the category G_{30} generates 7 junior and 65 intermediate groups, for example, at the 6-symmetry, we have 7 junior, 7 2-intermediate, and 58 3-intermediate groups (altogether $7 \times 15 + 65 \times 15 = 1080$ groups). At the ($2\underline{1} - B$)-, ($\underline{1}1' - B$)-, ($2'\underline{1} - C$)-, and ($\underline{2}2' - B$)-symmetries, the category G_{30} generates 26 junior + 58 2-intermediate = 84 groups; at (22)-symmetry, 116 junior and 174 intermediate groups [for example, at the ($2\underline{1}$)-symmetry, we obtain 116 junior, 58 $\underline{1}$-, 2-, $\underline{2}$-intermediate groups (altogether $116 \times 42 + 174 \times 42 = 12180$ groups)]. At the ($2\underline{2} - B$)-symmetry, the category G_{30} generates 64 junior and 116 intermediate groups [for example, at the $2\underline{2}$-symmetry, we obtain 64 junior, 58 2-, and $\underline{2}$-intermediate groups (altogether $64 \times 7 + 116 \times 7 = 1260$ groups)]. At the (32)- and ($3\underline{2} - B$)-symmetries, the category G_{30} generates 10 junior and 58 3-intermediate groups (altogether $10 \times 8 + 58 \times 8 = 544$ groups), and, at the (42)- and ($4\underline{2} - B$)-symmetries, it generates 5 junior and 180 intermediate groups (for example, at the (42)-symmetry, we obtain 5 junior, 64 2-intermediate, 58 4-, and (22)-intermediate groups (altogether $5 \times 8 + 180 \times 8 = 1480$ groups). At the ($\underline{4}2 - B$)- and ($\underline{4}2' - C$)-symmetries, the category G_{30} generates 6 junior and 290 intermediate groups [for example, at the ($\underline{4}2$)-symmetry, we obtain 6 junior, 116 2-intermediate, 58 $\underline{4}$-, (22)-, and ($2\underline{2}$)-intermediate groups (altogether $6 \times 28 + 290 \times 28 = 8288$ groups)]. At the (62)- and ($6\underline{2} - B$)-symmetries, G_{30} generates 8 junior and 190 intermediate groups; in particular, at the (62)-symmetry, we obtain 8 junior, 10 2-intermediate, 64 3-intermediate, 58 6-, and (32)-intermediate groups (altogether $8 \times 8 + 190 \times 8 = 1584$ groups). At the ($\underline{6}2 - B$)-, ($32\underline{1} - B$)-, ($\underline{6}2' - C$)-, and ($32'\underline{1} - C$)-symmetries, the category G_{30} generates 12 junior and 300 intermediate groups; for example, at the ($\underline{6}2$)-symmetry, we obtain 12 junior, 10 $\underline{2}$-intermediate, 116 3-intermediate, 58 $\underline{6}$-, (32)-, and ($3\underline{2}$)-intermediate groups (altogether $12 \times 56 + 300 \times 56 = 17472$ groups). At the ($4\underline{1} - B$)- and ($4'\underline{1} - C$)-symmetries, G_{30} generates 4 junior and 298 intermediate groups; for example, at the ($4\underline{1}$)-symmetry, we obtain 4 junior, 4 $\underline{1}$-, 4 $\underline{2}$-intermediate, 116 2-intermediate, 58 4-, 58 $\underline{4}$-, and 58 ($2\underline{1}$)-intermediate groups (altogether 4×28 junior + 298×28 intermediate = 8456 groups). At the ($6\underline{1} - B$)-, ($3\underline{1}1' - B$)-, and ($6'\underline{1} - C$)-symmetries, G_{30} generates 6 junior and 318 intermediate groups; for example, at the ($6\underline{1}$)-symmetry, we obtain 6 junior, 7 $\underline{1}$-, 7 2-, and 7 $\underline{2}$-intermediate, 116 3-intermediate, 7 ($2\underline{1}$)-intermediate, 58 6-, 58 $\underline{6}$-, and 58 ($3\underline{1}$)-intermediate groups (altogether $6 \times 35 + 318 \times 35 = 11340$ groups). At the ($22\underline{1} - B$)-symmetry, the category G_{30} generates 39 junior and 380 intermediate groups; for example, at the ($22\underline{1}$)-symmetry, we obtain 39 junior, 26 $\underline{1}$-intermediate, 116 2-intermediate, 64 $\underline{2}$-intermediate, 58 (22)-, 58 ($2\underline{1}$)-, and 58 ($2\underline{2}$)-intermediate groups (altogether $39 \times 7 + 380 \times 7 = 2933$). At the ($42\underline{1} - B$)- and ($42'\underline{1} - C$)-symmetries, G_{30} generates 6 junior and 880 intermediate groups; for example, at the ($42\underline{1}$)-symmetry, we obtain 6 junior, 104 2-intermediate, 5 $\underline{1}$-intermediate, 5 $\underline{2}$-intermediate, 116 4-, 116 (22)-, and 116 ($2\underline{2}$)-intermediate, 64 $\underline{4}$-, 64 ($2\underline{1}$)-intermediate, 58 ($4\underline{1}$)-, 58 ($22\underline{1}$)-, 58 (42)-, 58 ($4\underline{2}$)-, and 58 ($\underline{4}2$)-intermediate groups (altogether $6 \times 28 + 880 \times 28 = 24808$ groups). At the ($62\underline{1} - B$)- and ($62'\underline{1} - C$)-symmetries, the category G_{30} generates 8 junior and 908 intermediate groups; for example, at the ($62\underline{1}$)-symmetry, we obtain 8 junior, 8 $\underline{1}$-, 8 $\underline{2}$-intermediate, 12 2-intermediate, 104 3-intermediate, and 10 ($2\underline{1}$)-intermediate, 116 6-, 116 (32)-, and 116 ($3\underline{2}$)-intermediate, 64 $\underline{6}$- and 64 ($3\underline{1}$)-intermediate, 58 ($6\underline{1}$)-, 58 ($32\underline{1}$)-, 58 ($6\underline{2}$)-, 58 ($6\underline{2}$)-, and 58 ($\underline{6}2$)-

intermediate groups (altogether $8 \times 28 + 908 \times 28 = 25648$ groups). At the (23)-symmetry, the category G_{30} generates 2 junior and 7 (22)-intermediate groups (altogether 9 groups), and, at the (43)- and ($\underline{4}3 - B$)-symmetries it generates 3 junior and 68 intermediate groups. For example, at the (43)-symmetry, we obtain 3 junior, 10 (22)-intermediate, and 58 (23)-intermediate groups (altogether $3 \times 8 + 68 \times 8 = 568$ groups). At the ($23\underline{1} - B$)-symmetry, G_{30} generates 1 junior and 74 intermediate groups; for example, at the ($23\underline{1}$)-symmetry, we obtain 1 junior, 7 (22)-intermediate, 7 ($22\underline{1}$)-intermediate, 2 $\underline{1}$-intermediate, and 58 (23-intermediate groups (altogether $1 \times 7 + 74 \times 7 = 525$ groups). At the ($43\underline{1} - B$)- and ($4'3\underline{1} - C$)-symmetries, G_{30} generates 2 junior and 315 intermediate groups; for example, at the ($43\underline{1}$)-symmetry, we obtain 2 junior, 3 $\underline{1}$-intermediate, 12 (22)-intermediate, 116 (23)-intermediate, 10 ($22\underline{1}$)-intermediate, 58 ($23\underline{1}$)-, 58 (43)-, and 58 ($\underline{4}3$)-intermediate groups (altogether $2 \times 28 + 315 \times 28 = 8876$ groups). At the ($2\underline{1}1' - B$)-, ($\underline{1}1'*1$)-, ($*2\underline{1}1' - B$)-, and ($2'*2\underline{1} - B$)-symmetries, G_{30} generates 196 junior and 1218 intermediate groups; for example, at the ($2\underline{1}1'$)-symmetry, we obtain 196 junior, 116 2-, 116 ($\underline{1} - A$)-, 116 ($\underline{2} - A$)-intermediate, 58 ($2\underline{1} - A$)-, 58 ($\underline{1}1'$)-, 58 ($2'\underline{1} - A$)-intermediate (altogether $196 \times 22 + 1218 \times 22 = 31108$ groups). At the ($22'\underline{1} - C$)-symmetry, we obtain 104 junior and 766 intermediate; at the ($22'\underline{1}$)-symmetry, we obtain 104 junior and 64 $\underline{1}$- and $\underline{2}$-intermediate, 116 2-, 2'-and $\underline{2}'$-intermediate, trans. 58 (22'), ($2\underline{2}'$)-, ($\underline{2}2'$)-, ($2\underline{1}$)-, and ($2'\underline{1}$)-intermediate (altogether $104 \times 21 + 766 \times 21 = 18270$ groups). At the ($4'2\underline{1} - C$)- and ($4'*2\underline{1} - C$)-symmetries, 8 junior and 1426 intermediate; thus, for ($4'2\underline{1}$)-symmetry we obtain 8 junior, 6 $\underline{1}$- and $\underline{2}$-intermediate, 196 2-intermediate, 116 4'-, $\underline{4}'$-, ($2\underline{1}$)-, (22)-, and ($2\underline{2} - A$)-intermediate and 58 ($4'\underline{1}$)-, 58 ($4'\underline{2}$)-, 58 ($\underline{4}'2$)-, 58 ($4'\underline{2}$)-, 58 ($\underline{4}'2$)-, 58 ($22\underline{1}$)-, and 58 ($22'\underline{1}$)-intermediate groups (altogether $8 \times 42 + 1426 \times 42 = 60228$ groups). At the ($6'2\underline{1} - C$)-, ($32\underline{1}1' - B$)-, ($3*2\underline{1}1' - B$)-, and ($6'*2\underline{1} - C$)-symmetries, G_{30} generates 12 junior and 1460 intermediate groups; for example, at the ($32\underline{1}1'$)-symmetry, we obtain 12 junior, 12 ($\underline{1} - A$)-intermediate, 196 3-intermediate, 10 ($\underline{1}1'$)-intermediate, 116 ($3\underline{1} - A$)-, 116 (32)-, and 116 ($3\underline{2} - A$)-intermediate, and 58 ($3\underline{1}1'$)-, 58 ($32\underline{1} - A$)-, and 58 ($32'\underline{1} - A$)-intermediate groups (altogether $12 \times 56 + 1460 \times 56 = 82432$ groups). The remaining P-symmetries yield no junior G_{30}^P groups.

At the ($4\underline{1}1' - B$)- and ($*4\underline{1}1' - B$)-symmetries, G_{30} generates 1454 intermediate groups[1]; for example, at the ($4\underline{1}1'$)-symmetry, we obtain 196 2-intermediate, 4 ($\underline{1} - A$)-, 4 ($\underline{2} - A$)-intermediate, 4 ($\underline{1}1'$)-, and 4 ($2'\underline{1} - A$)-intermediate, 116 4-, 116 ($\underline{4} - A$)-, and 116 ($2\underline{1} - A$)-intermediate, 58 ($4\underline{1} - A$)-, 58 ($4'\underline{1} - A$)-, and 116 ($2\underline{1}1'$)-intermediate groups (altogether $1454 \times 14 = 20356$ groups). At the ($6\underline{1}1' - B$)-, ($3\underline{1}1'*1$)-, and ($*6\underline{1}1' - B$)-symmetries, the category G_{30} generates 1512 groups; for example, at the ($6\underline{1}1'$)-symmetry, we obtain 6 ($\underline{1} - A$)-, 6 2-, and 6 ($\underline{2} - A$)-intermediate, 196 3-intermediate, 7 ($2\underline{1} - A$)-, 7 ($\underline{1}1'$)-, and 7 ($2'\underline{1} - A$)-intermediate, 116 6-, 116 ($3\underline{1} - A$)-, and 116 ($\underline{6} - A$)-intermediate, 7 ($2\underline{1}1'$)-intermediate, 58 ($6\underline{1} - A$)-, 58 ($3\underline{1}1'$)-, and 58 ($6'\underline{1} - A$)-intermediate groups (altogether $1512 \times 15 = 22680$ groups). At the ($22\underline{1}1' - B$)-symmetry, the category G_{30} generates 2177 groups; for example, at the ($22\underline{1}1'$)-symmetry, we obtain 196 2-intermediate, 39 ($\underline{1} - A$)-intermediate, 104 ($\underline{2} - A$)-intermediate, 26 ($\underline{1}1'$)-intermediate, 64 ($2'\underline{1} - A$)-intermediate, 116 (22)-, 116 ($2\underline{1} - A$)-, 116 ($2\underline{2} - A$)-, and 116 ($\underline{2}2'$)-intermediate, 58 ($22\underline{1} - A$)-, 58 ($2\underline{1}1'$)-, and 58 ($22'\underline{1} - A$)-intermediate groups (altogether $2177 \times 7 = 15239$ groups). At the ($42\underline{1}1' - B$)- and ($4*2\underline{1}1' - B$)-symmetries, G_{30} generates 4758 groups; for example, at the ($42\underline{1}1'$)-symmetry, we obtain 6 ($\underline{1} - A$)- and 6 ($\underline{2} - A$)-intermediate, 5 ($\underline{1}1'$)- and 5 ($2'\underline{1} - A$)-intermediate, 104 ($\underline{4} - A$)- and 104 ($2\underline{1} - A$)-intermediate, 196 4-, 196 (22)-, and 196 ($2\underline{2}' - A$)-intermediate, 116 (42)-, 116 ($4\underline{1} - A$)-, 116 ($4\underline{2} - A$)-, 116 ($\underline{4}2 - A$)-, 116 ($\underline{4}2' - A$)-, 116 ($22\underline{1} - A$)-, and 116 ($22'\underline{1} - A$)-intermediate, 64 ($2\underline{1}1'$)- and 64 ($4'\underline{1} - A$)-intermediate, and 58 ($42\underline{1} - A$)-, 58 ($42'\underline{1} - A$)-, 58 ($4'2\underline{1} - A$)-, 58 ($4\underline{1}1'$)-, and 58 ($22\underline{1}1'$)-intermediate groups (altogether $4758 \times 14 = 66612$ groups). At the ($62\underline{1}1' - B$)- and ($6*2\underline{1}1' - B$)-symmetries, the category G_{30} generates 4840 groups; for example, at the ($62\underline{1}1'$)-symmetry, we obtain 8 ($\underline{1} - A$)- and 8 ($\underline{2} - A$)-intermediate, 12 2-intermediate, 8 ($\underline{1}1'$)- and 8 ($2'\underline{1} - A$)-intermediate, 12 ($2\underline{1} - A$)-intermediate, 196 6-, 196 (32)-, and 196 ($3\underline{2} - A$)-intermediate, 104 ($\underline{6} - A$)- and 104 ($3\underline{1} - A$)-intermediate, 10 ($2\underline{1}1'$)-intermediate, 116 ($6\underline{1} - A$)-, 116 (62)-, 116 ($6\underline{2} - A$)-, 116 ($\underline{6}2 - A$)-, 116 ($32\underline{1} - A$)-, 116 ($32'\underline{1} - A$)-, and 116 ($\underline{6}2' - A$)-intermediate, 64 ($3\underline{1}1'$)- and 64 ($6'\underline{1} - A$)-intermediate, and 58 ($62\underline{1} - A$)-, 58 ($62'\underline{1} - A$)-, 58 ($6'2\underline{1}$)-, 58 ($6\underline{1}1'$)-, and 58 ($32\underline{1}1'$)-intermediate groups (altogether $4840 \times 14 = 67760$ groups). At the ($23\underline{1}1' - B$)-symmetry, G_{30} generates 329 groups; for example, at the ($23\underline{1}1'$)-symmetry we obtain 1 ($\underline{1} - A$)-intermediate, 2 ($\underline{1}1'$)-intermediate, 6 (22)-intermediate, 7 ($22\underline{1} - A$)-intermediate, 116 (23)-intermediate, 7 ($22\underline{1}1'$)-intermediate, and 58 ($23\underline{1} - A$)-intermediate groups (altogether $329 \times 7 = 2303$ groups). At the ($43\underline{1}1' - B$)- and ($*43\underline{1}1' - B$)-symmetries, the category G_{30} generates 1481 groups; for example, at the ($43\underline{1}1'$)-symmetry, we obtain 2 ($\underline{1} - A$)-intermediate, 3 ($\underline{1}1'$)-intermediate, 12 (22)-intermediate, 12 ($22\underline{1} - A$)-intermediate, 196 (23)-intermediate, 116 (43)-, 116 ($\underline{4}3 - A$)-, and 116 ($23\underline{1} - A$)-intermediate, 10 ($22\underline{1}1'$)-intermediate, 58 ($43\underline{1} - A$)-, and 58 ($4'3\underline{1} - A$)-, and 58 ($23\underline{1}1'$)-intermediate groups (altogether $1481 \times 14 = 20734$ groups).

4. The above-listed 33 isomorphism classes of the second-order hypercrystallographic P-symmetries include first-order hypercrystallographic P-symmetries (cf. with Sec. 3 in [1]). The remaining 11 classes are essentially new, since they do not include first-order hypercrystallographic P-symmetries [2–4]. For these

[1] The word "intermediate" is thereafter dropped.

P-symmetries, it is necessary to calculate only *Q*-intermediate groups. As has been pointed out, at such *P*-symmetries, the crystallographic classes G_{30} cannot generate junior groups.

At the ($2\underline{1}1'^*1$)-symmetry, from 32 G_{30} we derive 196 ($\underline{1}-B$)-, 196 2-, and 196 ($\underline{2}-B$)-intermediate, 116 ($\underline{1}1'-B$)-, 116 ($2\underline{1}-B$)-, and 116 ($2'\underline{1}-C$)-intermediate, and 58 ($2\underline{1}1'-B$)-, 58 ($\underline{1}1'^*1$)-, and 58 ($^*2\underline{1}1'-B$)-intermediate groups (altogether $196\times 15 + 116\times 35 + 58\times 15 = 7870$ groups). At the ($2^*2\underline{1}1'-B$)-symmetry, G_{30} generates 4702 groups; for example, at the ($2^*2\underline{1}1'$)-symmetry, we obtain 104 ($\underline{1}-A$)- and 104 ($\underline{2}-A$)-intermediate, 196 2-, 196 *2-, and 196 ($^*\underline{2}-A$)-intermediate, 64 ($\underline{1}1'$)- and 64 ($2'\underline{1}-A$)-intermediate, 116 ($2\underline{1}-A$)-, 116 (2*2)-, 116 ($2^*\underline{2}-A$)-, 116 ($^*2\underline{1}-A$)-, 116 ($^*2'\underline{1}-A$)-, 116 ($\underline{2}^*2-A$)-, and 116 ($\underline{2}^*2'-A$)-intermediate, and 58 ($2\underline{1}1'$)-, 58 ($^*2\underline{1}1'$)-, 58 ($2^*2\underline{1}-A$)-, 58 ($2^*2'\underline{1}-A$)-, and 58 ($2'^*2\underline{1}-A$)-intermediate groups (altogether $4702\times 7 = 32914$ groups).

At the ($^*42\underline{1}1'-B$)-symmetry, the category G_{30} generates 7942 groups; for example, at the ($^*42\underline{1}1'$)-symmetry, we obtain 8 ($\underline{1}-A$) and 8 ($\underline{2}-A$)-intermediate, 196 ($2\underline{1}-A$)-, 196 ($\underline{2}2$)-, 196 ($2\underline{2}-B$)-, 196 *4-, and 196 ($^*\underline{4}-A$)-intermediate, 6 ($\underline{1}1'$)-, and 6 ($2'\underline{1}-A$)-intermediate, 116 ($2\underline{1}1'$)-, 116 ($22\underline{1}-A$)-, 116 ($22'\underline{1}-A$)-, 116 ($2^*2\underline{1}-A$)-, 116 ($2^*2'\underline{1}-A$)-, 116 ($^*4\underline{1}-A$)-, 116 ($^*4'\underline{1}-A$)-, 116 (*42)-, 116 ($^*\underline{4}2-A$)-, 116 ($^*4\underline{2}-A$)-, 116 ($^*\underline{4}\,\underline{2}-A$)-, 116 ($^*\underline{4}2'-A$)-, and 116 ($^*4\underline{2}'-A$)-, and 58 ($22\underline{1}1'$)-, 58 ($2^*2\underline{1}1'$)-, 58 ($^*4\underline{1}1'$)-, 58 ($^*42\underline{1}-A$)-, 58 ($^*4'\overline{2}\underline{1}-A$)-, 58 ($^*42'\underline{1}-A$)-, and 58 ($^*4'2'\underline{1}-A$)-intermediate groups (altogether $7942\times 7 = 55594$ groups). At the ($^*62\underline{1}1'-B$)- and ($32\underline{1}1'^*1$)-symmetries, we obtain 8048 groups; for example, at the ($32\underline{1}1'^*1$)-symmetry, we obtain 12 ($\underline{1}-B$)-intermediate, 12 ($\underline{1}1'-B$)-intermediate, 196 ($3\underline{1}-B$)-, 196 (32)-, and 196 ($3\underline{2}-B$)-intermediate, 10 ($\underline{1}1'^*1$)-intermediate, 116 ($3\underline{1}1'-B$)-, 116 ($32\underline{1}-B$)-, and 116 ($32'\underline{1}-C$)-intermediate, and 58 ($3\underline{1}1'^*1$)-, 58 ($32\underline{1}1'-B$)-, and ($3^*2\underline{1}1'-B$)-intermediate groups (altogether $8048\times 8 = 64384$ groups).

At the ($4\underline{1}1'^*1$)-symmetry, the category G_{30} generates 4 ($\underline{1}1'-B$)- and 4 ($2'\underline{1}-C$)-intermediate, 196 ($2\underline{1}-B$)-, 196 4-, and 196 ($\underline{4}-B$)-intermediate, 4 ($\underline{1}1'^*1$)-, and 4 ($^*2\underline{1}1'-B$)-intermediate, 116 ($2\underline{1}1'-B$)-, 116 ($4\underline{1}-B$)-, and 116 ($4'\underline{1}-C$)-intermediate, and 58 ($2\underline{1}1'^*1$)-, 58 ($4\underline{1}1'-B$)-, and 58 ($^*4\underline{1}1'-B$)-intermediate groups (altogether $4\times 28 + 196\times 15 + 4\times 8 + 116\times 35 + 58\times 15 = 8014$ groups). At the ($6\underline{1}1'^*1$)-symmetry, G_{30} generates 6 ($\underline{1}1'-B$)-, 6 ($2\underline{1}-B$)-, and 6 ($2'\underline{1}-C$)-intermediate, 196 ($3\underline{1}-B$)-, 196 6-, and 196 ($\underline{6}-B$)-intermediate, 7 ($\underline{1}1'^*1$)-, 7 ($2\underline{1}1'-B$)-, and 7 ($^*2\underline{1}1'-B$)-intermediate, 116 ($3\underline{1}1'-B$)-, 116 ($6\underline{1}-B$)-, and 116 ($6'\underline{1}-C$)-intermediate, 7 ($2\underline{1}1'^*1$)-intermediate, and 58 ($3\underline{1}1'^*1$)-, 58 ($6\underline{1}1'-B$)-, and 58 ($^*6\underline{1}1'-B$)-intermediate groups (altogether $6\times 35 + 196\times 15 + 7\times 15 + 116\times 35 + 7 + 58\times 15 = 8192$ groups).

At the ($22\underline{1}1'^*1$)-symmetry, the category G_{30} generates 39 ($\underline{1}1'-B$)-intermediate, 104 ($2'\underline{1}-C$)-intermediate, 196 ($2\underline{1}-B$)-, 196 (22)-, 196 ($2\underline{2}-B$)-, and 196 ($\underline{2}2'-B$)-intermediate, 64 ($^*2\underline{1}1'-B$)-intermediate, 26 ($\underline{1}1'^*1$)-intermediate, 116 ($2\underline{1}1'-B$)-, 116 ($22\underline{1}-B$)-, 116 ($22'\underline{1}-C$)-, and 116 ($2'^*2\underline{1}-B$)-intermediate, and 58 ($2\underline{1}1'^*1$)-, 58 ($22\underline{1}1'-B$)-, and 58 ($2^*2\underline{1}1'-B$)-intermediate groups (altogether $39\times 7 + 104\times 21 + 196\times 22 + 26 + 64\times 7 + 116\times 42 + 58\times 15 = 12985$ groups). At the ($42\underline{1}1'^*1$)-symmetry, G_{30} generates 6 ($\underline{1}1'-B$)- and 6 ($2'\underline{1}-C$)-intermediate, 5 ($\underline{1}1'^*1$)- and 5 ($^*2\underline{1}1'-B$)-intermediate, 104 ($2\underline{1}1'-B$)- and 104 ($4'\underline{1}-C$)-intermediate, 196 ($22\underline{1}-B$)-, 196 ($22'\underline{1}-C$)-, 196 ($4\underline{1}-B$)-, 196 (42)-, 196 ($4\underline{2}-B$)-, 196 ($\underline{4}2-B$)-, and 196 ($\underline{4}2'-C$)-intermediate, 64 ($2\underline{1}1'^*1$)- and 64 ($^*4\underline{1}1'-B$)-intermediate, 116 ($22\underline{1}1'-B$)-, 116 ($2^*2\underline{1}1'-B$)-, 116 ($4\underline{1}1'-B$)-, 116 ($4\underline{2}\underline{1}-B$)-, 116 ($42'\underline{1}-C$)-, 116 ($4'\underline{2}\underline{1}-C$)-, and 116 ($4'^*2\underline{1}-C$)-intermediate, and 58 ($22\underline{1}1'^*1$)-, 58 ($4\underline{1}1'^*1$)-, 58 ($42\underline{1}1'-B$)-, 58 ($4^*2\underline{1}1'-B$)-, and 58 ($^*42\underline{1}1'-B$)-intermediate groups (altogether $6\times 28 + 5\times 8 + 104\times 28 + 196\times 71 + 64\times 8 + 116\times 91 + 58\times 23 = 29438$ groups). At the ($62\underline{1}1'^*1$)-symmetry, the category G_{30} generates 8 ($\underline{1}1'-B$)- and 8 ($2'\underline{1}-C$)-intermediate, 12 ($2\underline{1}-B$)-intermediate, 8 ($\underline{1}1'^*1$)- and 8 ($^*2\underline{1}1'-B$)-intermediate, 12 ($2\underline{1}1'-B$)-intermediate, 104 ($3\underline{1}1'-B$)- and 104 ($6'\underline{1}-C$)-intermediate, 196 ($6\underline{1}-B$), 196 ($32\underline{1}-B$)-, 196 (62)-, 196 ($6\underline{2}-B$)-, 196 ($\underline{6}2-B$)-, 196 ($32'\underline{1}-C$)-, and 196 ($\underline{6}2'-C$)-intermediate, 10 ($2\underline{1}1'^*1$)-intermediate, 64 ($3\underline{1}1'^*1$)- and 64 ($^*6\underline{1}1'-B$)-intermediate, 116 ($6\underline{1}1'-B$)-, 116 ($32\underline{1}1'-B$)-, 116 ($62\underline{1}-B$)-, 116 ($62'\underline{1}-C$)-, 116 ($6'2\underline{1}-C$)-, 116 ($3^*2\underline{1}1'-B$), and 116 ($6'^*2\underline{1}-C$)-intermediate, and 58 ($6\underline{1}1'^*1$)-, 58 ($32\underline{1}1'^*1$)-, 58 ($62\underline{1}1'-B$)-, 58 ($6^*2\underline{1}1'-B$)-, and 58 ($^*62\underline{1}1'-B$)-intermediate groups (altogether $8\times 28 + 12\times 7 + 8\times 8 + 12\times 7 + 104\times 28 + 196\times 71 + 10 + 64\times 8 + 116\times 91 + 58\times 23 = 29696$ groups).

At the ($23\underline{1}1'^*1$)-symmetry, the category G_{30} generates 1 ($\underline{1}1'-B$)-intermediate, 2 ($\underline{1}1'^*1$)-intermediate, 6 ($22\underline{1}-B$)-intermediate, 196 (23)-intermediate, 7 ($22\underline{1}1'-B$)-intermediate, 116 ($23\underline{1}-B$)-intermediate, 7 ($22\underline{1}1'^*1$)-intermediate, and 58 ($23\underline{1}1'-B$)-intermediate groups (altogether $1\times 7 + 2 + 6\times 7 + 196 + 7\times 7 + 116\times 7 + 7 + 58\times 7 = 1521$ groups). Finally, at the ($43\underline{1}1'^*1$)-symmetry, the category G_{30} generates 2 ($\underline{1}1'-B$)-intermediate, 3 ($\underline{1}1'^*1$)-intermediate, 12 ($22\underline{1}-B$)-intermediate, 12 ($22\underline{1}1'-B$)-intermediate, 196 (43)-, 196 ($\underline{4}3-B$)-, and 196 ($23\underline{1}-B$)-intermediate, 10 ($22\underline{1}1'^*1$)-intermediate, 116 ($43\underline{1}-B$)-, 116 ($23\underline{1}1'-B$)-, and 116 ($4'3\underline{1}-C$)-intermediate, and 58 ($43\underline{1}1'-B$)-, 58 ($23\underline{1}1'^*1$)-, and 58 ($^*43\underline{1}1'-B$)-intermediate groups (altogether $2\times 7 + 3 + 12\times 7 + 12\times 7 + 196\times 15 + 10 + 116\times 35 + 58\times 15 = 8065$ groups).

As a result, one obtains 32 generating + 19936 senior + 15964 junior + 778939 intermediate = 814871 groups G_{30}^P of the complete *P*-symmetry for 624 second-order hypercrystallographic *P*-symmetries. These groups model 814871 eight-dimensional symmetry groups of the category G_{87630}.

5. Using the properties of the strong group isomorphism and isomorphism of the *P*-symmetries ([2] and Sect. 2 of this paper), one can derive the universal formula for calculating the number of groups generated by any category of the classical symmetry groups with due regard for 624 second-order hypercrystallographic *P*-symmetries of the geometrical classification. Indeed, the generalization of any category $G_{mn\ldots}$ containing T symmetry groups with 624 *P*-symmetries yields T generating, $T \times 623$ senior groups $G^P_{mn\ldots}$, and $15 \times M_2 + M_3 + 8 \times M_4 + 15 \times M_6 + M_{22} + 8 \times M_{32} + 8 \times M_{42} + 8 \times M_{62} + 42 \times M_{2\underline{1}} + 7 \times M_{\underline{22}} + 28 \times M_{\underline{42}} + 56 \times M_{\underline{62}} + 28 \times M_{4\underline{1}} + 35 \times M_{6\underline{1}} + 7 \times M_{22\underline{1}} + 28 \times M_{42\underline{1}} + 28 \times M_{62\underline{1}} + M_{23} + 8 \times M_{43} + 7 \times M_{23\underline{1}} + 28 \times M_{43\underline{1}} + 22 \times M_{2\underline{1}1'} + 21 \times M_{22'\underline{1}} + 42 \times M_{4'2\underline{1}} + 56 \times M_{6'2\underline{1}} + 14 \times M_{4\underline{1}1'} + 15 \times M_{6\underline{1}1'} + 7 \times M_{22\underline{1}1'} + 14 \times M_{42\underline{1}1'} + 14 \times M_{62\underline{1}1'} + 7 \times M_{23\underline{1}1'} + 14 \times M_{43\underline{1}1'} + 7 \times M_{2^*2\underline{1}1'} + M_{2\underline{1}1'^*1} + 7 \times M_{*42\underline{1}1'} + 8 \times M_{*62\underline{1}1'} + M_{4\underline{1}1'^*1} + M_{6\underline{1}1'^*1} + M_{22\underline{1}1'^*1} + M_{42\underline{1}1'^*1} + M_{62\underline{1}1'^*1} + M_{23\underline{1}1'^*1} + M_{43\underline{1}1'^*1}$ junior groups $G^P_{mn\ldots}$.[2] The subscript at M denotes the *P*-symmetry considered, M together with this subscript indicates the number of junior groups $G^P_{mn\ldots}$ of this *P*-symmetry, the numerical factors indicate the number of *P*-symmetries in the isomorphism class for the corresponding *P*-symmetries. We also obtained $3099 \times M_2 + 82 \times M_3 + 120 \times M_4 + 260 \times M_6 + 15 \times M_{22} + 222 \times M_{32} + 120 \times M_{42} + 120 \times M_{62} + 3178 \times M_{2\underline{1}} + 361 \times M_{\underline{22}} + 112 \times M_{\underline{42}} + 378 \times M_{\underline{62}} + 112 \times M_{4\underline{1}} + 154 \times M_{6\underline{1}} + 28 \times M_{22\underline{1}} + 112 \times M_{42\underline{1}} + 112 \times M_{62\underline{1}} + 15 \times M_{23} + 43 \times M_{43} + 28 \times M_{23\underline{1}} + 49 \times M_{43\underline{1}} + 773 \times M_{2\underline{1}1'} + 364 \times M_{22'\underline{1}} + 42 \times M_{4'2\underline{1}} + 98 \times M_{6'2\underline{1}} + 14 \times M_{4\underline{1}1'} + 16 \times M_{6\underline{1}1'} + 7 \times M_{22\underline{1}1'} + 14 \times M_{42\underline{1}1'} + 14 \times M_{62\underline{1}1'} + 7 \times M_{23\underline{1}1'} + 7 \times M_{43\underline{1}1'} + 63 \times M_{2^*2\underline{1}1'} + 29 \times M_{2\underline{1}1'^*1} + 2 \times M_{*62\underline{1}1'} + 2 \times M_{2\hat{2}\underline{1}1'^*1}$ intermediate groups $G^P_{mn\ldots}$, where M with the subscript has the same meaning, and the numerical factors indicate the number of all possible factor-groups P/Q strongly isomorphic to the groups of substitutions characterizing the *P*-symmetries (see the calculation of the G^P_{30} groups in Sections 3 and 4).

The sum of the expressions for calculating all possible types of *P*-symmetry groups generated by T groups of the category $G_{mn\ldots}$ upon their generalization with 624 second-order hypercrystallographic *P*-symmetries yields the total number of groups $G^P_{mn\ldots}$, $T \times 624 + 3114 \times M_2 + 83 \times M_3 + 128 \times M_4 + 275 \times M_6 + 16 \times M_{22} + 230 \times M_{32} + 128 \times M_{42} + 128 \times M_{62} + 3220 \times M_{2\underline{1}} + 368 \times M_{\underline{22}} + 140 \times M_{\underline{42}} + 434 \times M_{\underline{62}} + 140 \times M_{4\underline{1}} + 189 \times M_{6\underline{1}} + 35 \times M_{22\underline{1}} + 140 \times M_{42\underline{1}} + 140 \times M_{62\underline{1}} + 16 \times M_{23} + 51 \times M_{43} + 35 \times M_{23\underline{1}} + 77 \times M_{43\underline{1}} + 795 \times M_{2\underline{1}1'} + 385 \times M_{22'\underline{1}} + 84 \times M_{4'2\underline{1}} + 154 \times M_{6'2\underline{1}} + 28 \times M_{4\underline{1}1'} + 31 \times M_{6\underline{1}1'} + 14 \times M_{22\underline{1}1'} + 28 \times M_{42\underline{1}1'} + 28 \times M_{62\underline{1}1'} + 14 \times M_{23\underline{1}1'} + 21 \times M_{43\underline{1}1'} + 70 \times M_{2^*2\underline{1}1'} + 30 \times M_{2\underline{1}1'^*1} + 7 \times M_{*42\underline{1}1'} + 10 \times M_{*62\underline{1}1'} + M_{4\underline{1}1'^*1} + M_{6\underline{1}1'^*1} + M_{22\underline{1}1'^*1} + M_{42\underline{1}1'^*1} + M_{62\underline{1}1'^*1} + M_{23\underline{1}1'^*1} + M_{43\underline{1}1'^*1} + 2 \times M_{2\hat{2}\underline{1}1'^*1}$. These groups model the symmetry groups of the category $G_{(m+5)(m+4)(m+3)mn\ldots}$.

Using the M_P values corresponding to the given category, one can check the numerical factors for the groups G^P_{20} and G^P_{21} from [3, 4] at $P \simeq G_{5430}$.

Thus, using the general theory of the *P*-symmetry as well as the properties of the strong group isomorphism and the isomorphism of the *P*-symmetries, we have derived the G^P_{30} groups for 624 second-order hypercrystallographic *P*-symmetries. These groups model all the eight-dimensional groups of the category G_{87630}. We have also obtained the formula for calculating new groups generated by any category of the symmetry groups with due regard for 624 second-order hypercrystallographic *P*-symmetries.

REFERENCES

1. A. M. Zamorzaev and A. F. Palistrant, Kristallografiya **44**, 976 (1999).
2. A. M. Zamorzaev, Izv. Akad. Nauk Resp. Mold. Mat., **1**, 75 (1994).
3. A. M. Zamorzaev, Izv. Akad. Nauk Resp. Mold. Mat., **2**(18), 3(19), 22 (1995).
4. A. M. Zamorzaev, Izv. Akad. Nauk Resp. Mold. Mat., 1(20), 65 (1996).
5. A. M. Zamorzaev, *Theory of Simple and Multiple Antisymmetry* [in Russian] (Shtiintsa, Kishinev, 1976).
6. A. M. Zamorzaev, Kristallografiya **12** (5), 819 (1967).
7. A. M. Zamorzaev, É. I. Galyarskii, and A. F. Palistrant, *Color Symmetry, Its Generalizations and Applications* [in Russian] (Shtiintsa, Kishinev, 1978).
8. A. M. Zamorzaev, Yu. S. Karpova, A. P. Lungu, and A. F. Palistrant, *P-symmetry and Its Further Development* [in Russian] (Shtiintsa, Kishinev, 1986).

[2] For the category G^P_{30} all the next M_P are zeroes. However, the formula is derived for any category $G^P_{mn\ldots}$.

Translated by A. Darinskiĭ

Crystallography Reports, Vol. 45, No. 1, 2000, pp. 10–12. Translated from Kristallografiya, Vol. 45, No. 1, 2000, pp. 16–18.

Method for Correction of a Two-Dimensional Image Reconstructed from Its Projections

Ya. A. Ilyushin

Physics Department, Moscow State University, Vorob'evy gory, Moscow, 119899 Russia

Received on March 27, 1998

Abstract—The reconstruction of a two-dimensional object by synthesis of its projections has been considered. The problem is solved with the aid of circular harmonic transforms. The formulas for tomographic reconstruction are obtained as expansions with respect to the systems of orthogonal functions outside the unit circle. These formulas are used for numerical simulation of image reconstruction. *© 2000 MAIK "Nauka/Interperiodica".*

The synthesis of projections is widely used in tomographic visualization of various objects [1, 2]. Projection and synthesis in a two-dimensional space is performed with the aid of rather simple photosummators. There exist tomographic devices that can directly perform such summation without the explicit representation of any information about the projections themselves. In some practical situations, only this approach can be used [3]. The thus reconstructed image is considerably distorted because it is related to the initial object by a certain integral transformation. Therefore, of great importance are various methods for correcting images reconstructed by the synthesis of their projections [1–3], i.e., the methods of reconstruction of an unknown function by the synthesis of its projections. Below, we describe the solution of this problem based on the expansion of the function into circular harmonics. This approach is more economical and allows a rather simple regularization of the reconstruction procedure. Moreover, it allows one to take into account the symmetry of an object under study in the natural way, which is of great importance for various crystallographic applications.

Consider the function $g(r, \varphi)$ defined on a unit circle. We assume that there exists the Radon transform of this function $f(p, \psi)$ and that it is possible to perform the synthesis of its projections, $\Sigma(r, \varphi)$. All these functions are expanded into Fourier series in terms of circular harmonics

$$g(r, \varphi) = \sum_{n=-\infty}^{\infty} \exp(in\varphi) g_n(r), \tag{1}$$

$$f(p, \psi) = \sum_{n=-\infty}^{\infty} \exp(in\psi) f_n(p), \tag{2}$$

$$\Sigma(r, \varphi) = \sum_{n=-\infty}^{\infty} \exp(in\varphi) \Sigma_n(r). \tag{3}$$

The radial components of harmonics are related by the Cormack transformation [4]:

$$f_n(p) = 2\int_p^1 \frac{T_n(p/r)}{\sqrt{r^2 - p^2}} g_n(r) r dr. \tag{4}$$

The synthesis of projections at the point (r, φ) can be described as equal to the sum of the integrals along all the lines passing through this point; i.e.,

$$\begin{aligned} \Sigma(r, \varphi) &= \int_{-\frac{\pi}{2}}^{\frac{\pi}{2}} f(p(\delta), \psi(\delta)) d\delta \\ &= \int_{\varphi - \frac{\pi}{2}}^{\varphi + \frac{\pi}{2}} f(r\cos(\psi - \varphi), (\psi - \varphi)) d\psi. \end{aligned} \tag{5}$$

The integral in the right-hand side of the above equation is an integral over the circumference passing through the origin of the coordinate system (Fig. 1) and is determined by the equation

$$p = r\cos(\psi - \varphi). \tag{6}$$

The above integral transformation was considered in [4]. It was shown that the radial components of circular harmonics are related by the transformation

$$\Sigma_n(r) = 2r\int_0^r \frac{T_n(p/r)}{\sqrt{r^2 - p^2}} f_n(p) dp. \tag{7}$$

Transformations (4) and (7) are conjugate operators with respect to scalar products $(\mathbf{x} \cdot \mathbf{y}) = \int_0^1 x(p) y(p) dp$

1063-7745/00/4501-0010$20.00 © 2000 MAIK "Nauka/Interperiodica"

and $(\mathbf{x} \cdot \mathbf{y}) = \int_0^1 x(r)y(r)dr$, respectively. Indeed,

$$\int_0^1 y(r)2r\int_0^r \frac{T_n(p/r)}{\sqrt{r^2-p^2}}x(p)(dp)dr = \int_0^1 x(p)2\int_p^1 \frac{T_n(p/r)}{\sqrt{r^2-p^2}}y(r)rdrdp. \quad (8)$$

Transforming these integrals to double ones and changing the integration order in (8), one can see that both sides of (8) are equal. Combining (4) and (7), we arrive at the expression relating the initial object and the synthesis of its projections

$$\Sigma_n(r) = 4r\int_0^r \frac{T_n(p/r)}{\sqrt{r^2-p^2}}\int_p^1 \frac{T_n(p/r')}{\sqrt{r'^2-p^2}}g_n(r')r'dr'dp. \quad (9)$$

Changing the integration order in the right-hand side, we reduce (9) to the form

$$\Sigma_n(r) = \int_0^1 K_n(r, r')g_n(r')dr', \quad (10)$$

where

$$K_n(r, r') = 4r'r\int_0^{\min(r, r')} \frac{T_n(p/r)}{\sqrt{r^2-p^2}}\frac{T_n(p/r')}{\sqrt{r'^2-p^2}}dp. \quad (11)$$

Obviously, the expression under the integral sign is symmetric; i.e., $K_n(r, r') = K_n(r', r)$. If $r' \longrightarrow r$, and the kernel of (11) has a singularity of the logarithmic type. The asymptotic behavior of $K_n(r, r')$ at $r' \longrightarrow r$ can be analyzed by the standard methods used for integrals with weak singularities [5]. Using the integral representation of the Bessel function [4]

$$J_{2n}(x) = \frac{(-1)^n 2}{\pi}\int_0^1 \frac{T_{2n}(y)\cos(xy)}{\sqrt{1-y^2}}dy \quad (12)$$

and a similar representation of the odd subscript, one can transform the kernel of the integral equation $K_n(r, r')$ to the form

$$K_n(r, r') = 2\pi r'\int_0^\infty J_n(rt)J_n(r't)dt. \quad (13)$$

The above integral can be expressed in terms of the hypergeometrical function [6]

$$K_n(r, r') = 2\pi\left(\frac{r'}{r}\right)^n r'\frac{\Gamma(n+1/2)}{\Gamma(n+1)\Gamma(1/2)} \times F\left(n+\frac{1}{2}, \frac{1}{2}; n+1; \left(\frac{r'}{r}\right)^2\right) \text{ if } r' < r, \quad (14)$$

$$K_n(r, r') = K_n(r', r) \text{ if } r' > r.$$

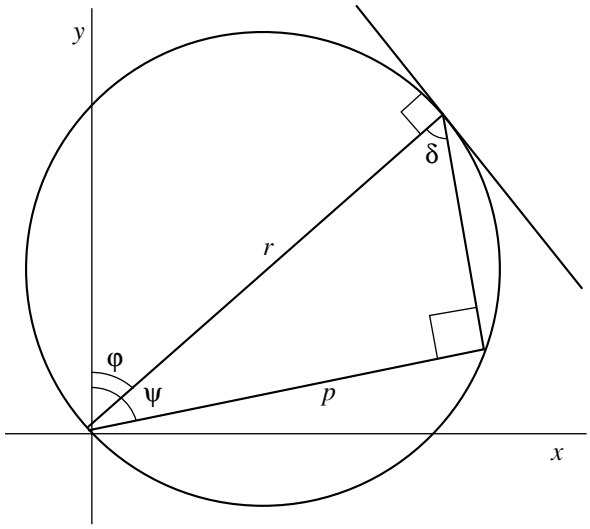

Fig. 1. Geometry of the procedure of synthesis of projections.

Thus, the transition from the Radon transform to the three-dimensional synthesis of projections reduces the problem of the reconstruction of the function $g(r, \varphi)$ to the solution of a system of ordinary integral Fredholm equations of the first kind and of type (10) having the symmetric kernel (14). Such a kernel possesses an orthonormalized system of eigenfunctions. Using the expansions in terms of these functions, one can construct an efficient numerical algorithm for solving the problem.

The three-dimensional synthesis of projections is a particular case of an operator introduced for the study of pairs of orthogonal sets that are transformed into one another by the Radon transform [7]. According the theorem proven in [7], the eigenfunctions of the kernel (14) are transformed by the Radon transform into the sets of functions orthogonal on a unit circle with a unit weight. However, this weight does not corresponds to any of the known pairs of orthogonal sets that can be represented in an explicit analytical form. The eigenfunctions can be calculated by approximate methods on a computer [8].

In some cases, it might be necessary to perform the tomographic reconstruction outside a certain closed domain which cannot be studied by a probe, e.g., in the studies of various surface structures, boundary layers, and, in particular, in the studies of the terrestrial atmo-

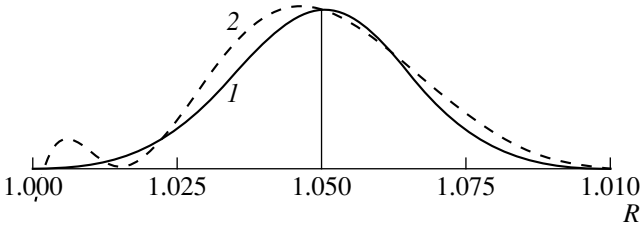

Fig. 2. (*1*) the initial profile of the density distribution in a thin layer and (*2*) the reconstructed density distribution.

sphere from the data of radiosonde observations. The orthonormalized functions for a circular domain can be calculated from the known solutions for the internal domain of a unit circle. Perform the following coordinate transformation: $s = 1/r$, $q = 1/p$, which transforms the straight line $r = p/\cos(\varphi - \psi)$ into a circumference $s = q\cos(\varphi - \psi)$. In this case, integral transformation (4) takes the form

$$f_n(q) = 2\int_0^q \frac{q}{s^2} g_n(s) \frac{T_n(s/q)}{\sqrt{q^2 - s^2}} ds. \quad (15)$$

Multiplying both sides by the Zernike polynomial $R_n^l(q)$ [4] and integrating the result with respect to q from 0 to 1, we obtain

$$\int_0^1 f_n(q) R_n^l(q) dq = 2\int_0^1 R_n^l(q) \int_0^q \frac{q}{s^2} g_n(s) \frac{T_n(s/q)}{\sqrt{q^2 - s^2}} ds dq. \quad (16)$$

Changing the order of integration in the right-hand side, we arrive at

$$\int_0^1 \frac{g_n(s)}{s^2} 2\int_s^1 q R_n^l(q) \frac{T_n(s/q)}{\sqrt{q^2 - s^2}} dq ds = 2\int_0^1 \frac{g_n(s)}{s^2} \frac{U_{n+2l+1}(s) ds}{(n + 2l + 1)}, \quad (17)$$

where $U_m(s) = \sin(m\arccos(s))$ is the Chebyshev function of the second kind. Taking into account the orthogonality properties of the Chebyshev functions and Zernike polynomials and returning to the old variables, one can show that

$$g_n(r) = \frac{2}{\pi r^2} \sum_{l=0}^{\infty} \frac{U_{n+2l+1}(1/r)}{\sqrt{1 - (1/r)^2}} (n + 2l + 1) \times \int_1^{\infty} f_n(p) R_n^l(1/p) \frac{dp}{p^2}. \quad (18)$$

Figure 2 illustrates numerical simulation of tomographic reconstruction of a thin spherically symmetric layer from 60 terms of series (18) (the initial layer profile and result of its reconstruction, respectively). The somewhat deteriorated convergence of the series in the close vicinity of the surface is associated with the fact that summation of the Fourier series with the approximate coefficients is an ill-posed problem. This shortcoming can be eliminated by regularization of the series summation by invoking the known information on the boundary values of the function to be reconstructed at the surface that can be obtained, e.g., from some additional measurements, physical considerations, etc.

REFERENCES

1. B. K. Vaĭnshteĭn and A. M. Mikhaĭlov, Kristallografiya **17** (2), 258 (1972).
2. B. K. Vaĭnshteĭn, Usp. Fiz. Nauk **109** (3), 455 (1973).
3. V. V. Pikalov and N. G. Preobrazhenskiĭ, *Reconstructive Tomography in Gas Dynamics and Plasma Physics* [in Russian] (Nauka, Novosibirsk, 1987).
4. A. M. Cormack, J. Appl. Phys. **34** (9), 2722 (1963), *ibid.*, **35** (10), 2908 (1964).
5. M. V. Fedoryuk, *Asymptotic Functions. Integrals and Series* [in Russian] (Nauka, Moscow, 1987).
6. I. S. Gradshteĭn and I. M. Ryzhik, *Tables of Integrals, Sums, Series, and Products* (Nauka, Moscow, 1971; Academic, New York, 1980).
7. R. B. Marr, J. Math. Anal. Appl. **45**, 357 (1974).
8. A. B. Vasil'eva and N. A. Tikhonov, *Integral Equations* [in Russian] (MGU, Moscow, 1989).

Translated by L. Man

Crystallography Reports, Vol. 45, No. 1, 2000, pp. 103–104. Translated from Kristallografiya, Vol. 45, No. 1, 2000, pp. 108–110.

X-ray Mapping in Heterocyclic Design: II. Diffractometric Study of Crystalline 2-Oxo-2,3-Dihydroimidazo[1,2-*a*]pyridine Hydrochloride

V. B. Rybakov, S. G. Zhukov, E. V. Babaev, O. S. Mazina, and L. A. Aslanov

Chemistry Department, Moscow State University, Vorob'evy gory, Moscow, 119899 Russia
e-mail: rybakov@biocryst.phys.msu.su

Received May 13, 1999

Abstract—The crystal structure of 2-oxo-2,3-dihydroimidazo[1,2-*a*]pyridine hydrochloride, $C_7H_7ClN_2O$, is determined by X-ray diffraction. The structure is solved by the direct method and refined by the least-squares procedure to $R = 0.0408$. The alternation of bond lengths in the molecule is inconsiderable, but does not disappear completely, since no aromatization occurs upon formation of the bicycle from the molecule. This structural change is apparently due to the increased conjugation of the NH group with the pyridine residue of the bicycle. One of the specific structural features of the salt is the formation of the N^+–H··Cl^- hydrogen bond (N–H, 0.792 Å; H···Cl, 2.260 Å; and N–H···Cl, 171.2). © *2000 MAIK "Nauka/Interperiodica".*

This work continues a series of investigations of heterocyclic compounds that enter into reactions of cyclization and ring transformation [1–5]. The structure of 1,2-dihydro-2-imino-1-carboxymethylpyridine (**I**) was studied in the preceding paper [5]. In the present work, we determined the structure of a product of its cyclization, 2-oxo-2,3-dihydroimidazo[1,2-*a*]pyridine hydrochloride (**II**).

The **I** ⟶ **II** cyclization was first carried out by Reindel in 1924 [6]. However, the compound obtained was by mistake assigned the structure of pyrrolo[2,3-*b*]pyridine. Tschitschibabin showed [7] that, in the course of cyclization, the imidazolone fragment is formed. No data on the crystal structure of **II** is present in the Cambridge Structural Database [8]. The synthesis of **II** was performed according to the procedure described in [6]

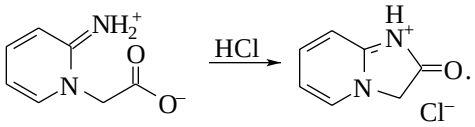

I **II**

Recrystallization from a 1 : 1 isopropanol–water solution yields transparent colorless crystals with a platelike habit.

EXPERIMENTAL

Crystals **II**, $C_7H_7ClN_2O$, are triclinic. The unit-cell parameters were determined and refined on a CAD4 automated diffractometer using 25 reflections in the θ range 11°–14° [9] (λMoK_α, graphite monochromator). The crystal data are $a = 7.121(2)$ Å, $b = 7.621(2)$ Å, $c = 8.312(2)$ Å, $\alpha = 65.69(2)°$, $\beta = 67.45(2)°$, $\gamma = 70.24(2)°$, $V = 370.9(2)$ Å^3, $d_{calcd} = 1.528$ g/cm^3, $\mu(\lambda Mo) = 0.450$ mm^{-1}, $Z = 2$, and space group $P\bar{1}$. A set of 2187 unique reflections with $I \geq 2\sigma(I)$ was collected in the range $\theta \leq 26°$ on the same diffractometer by the ω-scan technique. The processing of the diffraction data measured was performed with the WinGX96 program package [10]. The coordinates of the non-hydrogen atoms were found by the direct method, and the structure was refined in the anisotropic approximation by the least-squares procedure using the SHELX97 program package [11]. All the hydrogen atoms were located from the difference synthesis of electron density and

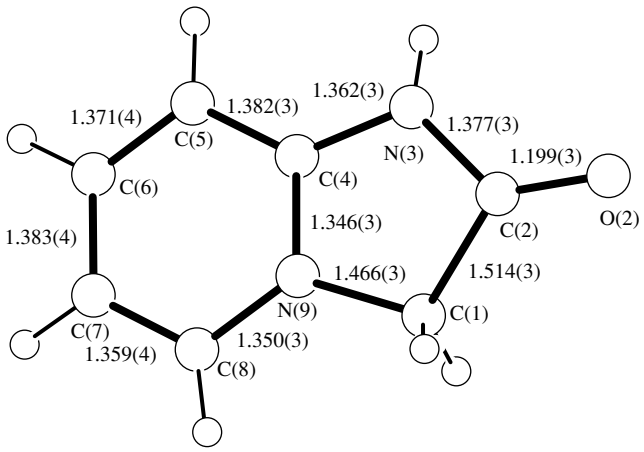

The structure of the molecule studied and atomic numbering.

1063-7745/00/4501-0103$20.00 © 2000 MAIK "Nauka/Interperiodica"

Atomic coordinates ($\times 10^4$) and equivalent (isotropic) thermal parameters U_{eq}/U_{iso} ($Å^2 \times 10^3$) for molecule **II**

Atom	*x*	*y*	*z*	U_{eq}/U_{iso}
Cl	3283(1)	1424(1)	8058(1)	44(1)
C(1)	1527(5)	8296(3)	2928(3)	40(1)
C(2)	1959(4)	7252(3)	4782(3)	40(1)
O(2)	1793(3)	7963(3)	5889(3)	58(1)
N(3)	2584(3)	5279(3)	4961(3)	40(1)
C(4)	2623(3)	4945(3)	3459(3)	34(1)
C(5)	3171(4)	3200(3)	3088(3)	42(1)
C(6)	3022(4)	3304(4)	1453(4)	44(1)
C(7)	2365(4)	5090(4)	219(4)	43(1)
C(8)	1866(4)	6783(4)	613(3)	38(1)
N(9)	2016(3)	6668(2)	2226(2)	31(1)
H(11)	2420(39)	9159(37)	2174(35)	41(7)
H(12)	108(49)	8941(42)	3078(39)	55(8)
H(3)	2762(43)	4332(42)	5847(40)	51(8)
H(5)	3563(40)	2025(38)	3951(36)	40(6)
H(6)	3492(40)	2152(39)	1119(35)	47(7)
H(7)	2256(44)	5137(42)	–911(42)	62(8)
H(8)	1490(39)	8035(38)	–119(35)	41(7)

included in the refinement in the isotropic approximation. The final discrepancy factors are $R1 = 0.0408$ and $wR2 = 0.0930$. The atomic coordinates and thermal parameters are listed in the table. The residual electron density lies between $\Delta\rho_{max} = 0.253$ and $\Delta\rho_{min} = -0.255$ e/Å^3. The organic cation shown in the figure was drawn with the PLUTON96 program [12].

RESULTS AND DISCUSSION

The chloride anion serves as a counterion in compound **II**. The heterocyclic cation is planar. The largest atomic deviation from the plane of the bicycle is 0.011(2) Å. In theory, three tautomeric forms of **II** are possible: *A*, *B*, and *C*

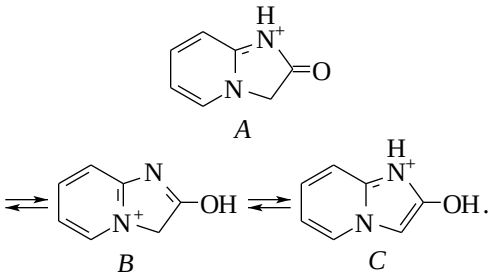

However, the C(1)–C(2) bond (figure) is a single C–C bond (1.51 Å), which eliminates the *C* tautomer. The C(2)–O(2) bond is the normal double bond C=O (1.20 Å), which eliminates the *B* tautomer. Therefore, the structure of cation **II** is unambiguously described by the *A* tautomer.

It is interesting to reveal the structural changes upon the **I** ⟶ **II** cyclization. As we already noted in [5], the bond lengths in the ring of **I** distinctly alternate: actually, molecule **I** contains a quazi-diene fragment. In the course of cyclization, the bonds in the six-membered fragment tend to become equal, and the alternation of bond lengths in **II** becomes inconsiderable.

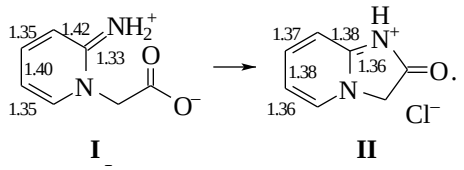

This structural feature is remarkable, since no aromatization occurs upon formation of the bicycle from the monocycle. The above structural change is apparently due to the increased conjugation of the NH group with the pyridine residue of the bicycle.

Another structural feature of salt **II** is the formation of the $N(3)^+$–H(3)··Cl^- hydrogen bond [N(3)–H(3), 0.79 Å; H(3)··Cl, 2.26 Å; and N(3)–H(3)··Cl, 171°].

ACKNOWLEDGMENTS

This work was supported by the Russian Foundation for Basic Research, project no. 99-03-33076a. We also acknowledge the support of this Foundation in the payment of the licence for using the Cambridge Structural Database, project no. 99-07-90133.

REFERENCES

1. E. V. Babaev, A. V. Efimov, S. G. Zhukov, *et al.*, Khim. Geterotsikl. Soedin., No. 7, 983 (1998).
2. E. V. Babaev, S. V. Bozhenko, D. A. Maiboroda, *et al.*, Bull. Soc. Chim. Belg. **106** (11), 631 (1997).
3. S. G. Zhukov, V. B. Rybakov, E. V. Babaev, *et al.*, Acta Crystallogr., Sect. C: Cryst. Struct. Commun. **53**, 1909 (1997).
4. E. V. Babaev, S. V. Bozhenko, S. G. Zhukov, *et al.*, Khim. Geterotsikl. Soedin., No. 8, 1105 (1997).
5. V. B. Rybakov, S. G. Zhukov, E. V. Babaev, *et al.*, Kristallografiya **44** (6), 1067 (1999).
6. F. Reindel, Chem. Ber. **57,** 1381 (1924).
7. A. E. Tschitschibabin, Chem. Ber. **57,** 2092 (1925).
8. F. H. Allen and O. Kennard, Chem. Des. Autom. News **8**, 31 (1993).
9. Enraf–Nonius, *CAD4 Software: Version 5.0* (Enraf–Nonius, Delft, 1989).
10. L. J. Farrugia, *WinGX96: An Integrated System of Publicly Available Windows Programs for the Solution, Refinement, and Analysis of Single-Crystal X-ray Diffraction Data* (Univ. of Glasgow, Glasgow, 1996).
11. G. M. Sheldrick, *SHELX97: Programs for the Solution and Refinement of Crystal Structures* (Univ. of Göttingen, Göttingen, 1997).
12. A. L. Spek, *PLUTON96: Molecular Graphics Program* (Univ. of Utrecht, Utrecht, 1996).

Translated by I. Polyakova

Crystallography Reports, Vol. 45, No. 1, 2000, pp. 105–116. Translated from Kristallografiya, Vol. 45, No. 1, 2000, pp. 111–122.

STRUCTURES OF MACROMOLECULAR COMPOUNDS

Three-Dimensional Structure of the Enzyme Dimanganese Catalase from *Thermus Thermophilus* at 1 Å Resolution

S. V. Antonyuk*, V. R. Melik-Adamyan*, A. N. Popov*, **, V. S. Lamzin, P. D. Hempstead***, P. M. Harrison***, P. J. Artymyuk***, and V. V. Barynin*,*****

**Shubnikov Institute of Crystallography, Russian Academy of Sciences, Leninskiĭ pr. 59, Moscow, 117333 Russia*

***European Molecular Biology Laboratory, EMBL Hamburg Outstation, c/o DESY, Notkestrasse 85, Hamburg, 22603 Germany*

****Krebs Institute for Biomolecular Research, Department of Molecular Biology and Biotechnology, University of Sheffield, P.O. Box 594, First Court, Western Bank, Sheffield, S10 2TN UK*

Received August 25, 1999

Abstract—The crystal structures of two forms of the enzyme dimanganese catalase from *Thermus Thermophilus* (native and inhibited by chloride) were studied by X-ray diffraction analysis at 1.05 and 0.98 Å resolution, respectively. The atomic models of the molecules were refined to the *R* factors 9.8 and 10%, respectively. The three-dimensional molecular structures are characterized in detail. The analysis of electron-density distributions in the active centers of the native and inhibited enzyme forms revealed that the most flexible side chains of the amino acid residues Lys162 and Glu36 exist in two interrelated conformations. This allowed us to obtain the structural data necessary for understanding the mechanism of enzymatic activity of the dimanganese catalase. *© 2000 MAIK "Nauka/Interperiodica".*

INTRODUCTION

Catalase ($H_2O_2 : H_2O_2$ oxidoreductase, E.C. 1.11.1.16) is an enzyme with the molecular weight of 250–400 kDa, present in cells of almost all living organisms, which catalyzes disproportionation of hydrogen peroxide into water and molecular oxygen. The major physiological function of catalases consists in protection the cell components against the oxidative action of hydrogen peroxide formed in the course of metabolism. Most catalases studied to date are tetrameric heme-containing proteins participating in the enzymatic reaction proceeding in two stages:

(1) $E–Fe + H_2O_2 = E–Fe–O + H_2O$,

(2) $E–Fe–O + H_2O_2 = E–Fe + H_2O + O_2$.

At the first stage, a hydrogen peroxide molecule oxidizes the iron atom of a heme group located in the active center of the enzyme to yield the oxidized form of the enzyme (Compound **I**). At the second stage, the second hydrogen peroxide molecule reduces Compound **I** to its initial state [1]. Presently, the three-dimensional structures of six heme catalases isolated from organisms of different types and are studied by X-ray diffraction analysis [2–7]. Dimanganese catalases from bacteria *Thermus thermophilus*, *Lactobacillus plantarum*, and *Thermoleophilum Album* are studied insufficiently [8, 9]. These catalases cannot be inhibited by cyanide, contain no heme group, and have two manganese ions in the active center.

Earlier, the three-dimensional structure of dimanganese catalase from *Thermus thermophilus* has been determined at a 3 Å resolution [10] and, more recently, at a 1.4 Å resolution [11, 12]. It was established that the enzyme molecule with the weight 200 kDa consists of six identical subunits. The major motif of the secondary structure of the subunit can be described as two neighboring pairs of antiparallel helices with the active center of the enzyme containing two Mn ions in between. The sequence of 302 amino acid residues in the polypeptide chain of the subunit of dimanganese catalase from *Thermus thermophilus* has been determined by chemical methods [13].

Table 1. Statistical characteristics of X-ray diffraction data collected from crystals of native dimanganese catalase and its complex with Cl^- ions

Characteristic	Form of the enzyme	
	native	complex with Cl^- ions
Maximum resolution, Å	1.05	0.98
Unit-cell parameters $a = b = c$, Å	132.3	132.07
Total number of reflections	354906	413309
Number of reflections with $I > 2\sigma(I)$	267199	353229
Completeness of the set, %	99.9	98.5
Completeness in the last resolution shell, %	98.9	98.8
$R(I)_{\text{total}} = \Sigma\|I - \langle I\rangle\|/\Sigma I$, %	7.0	3.6

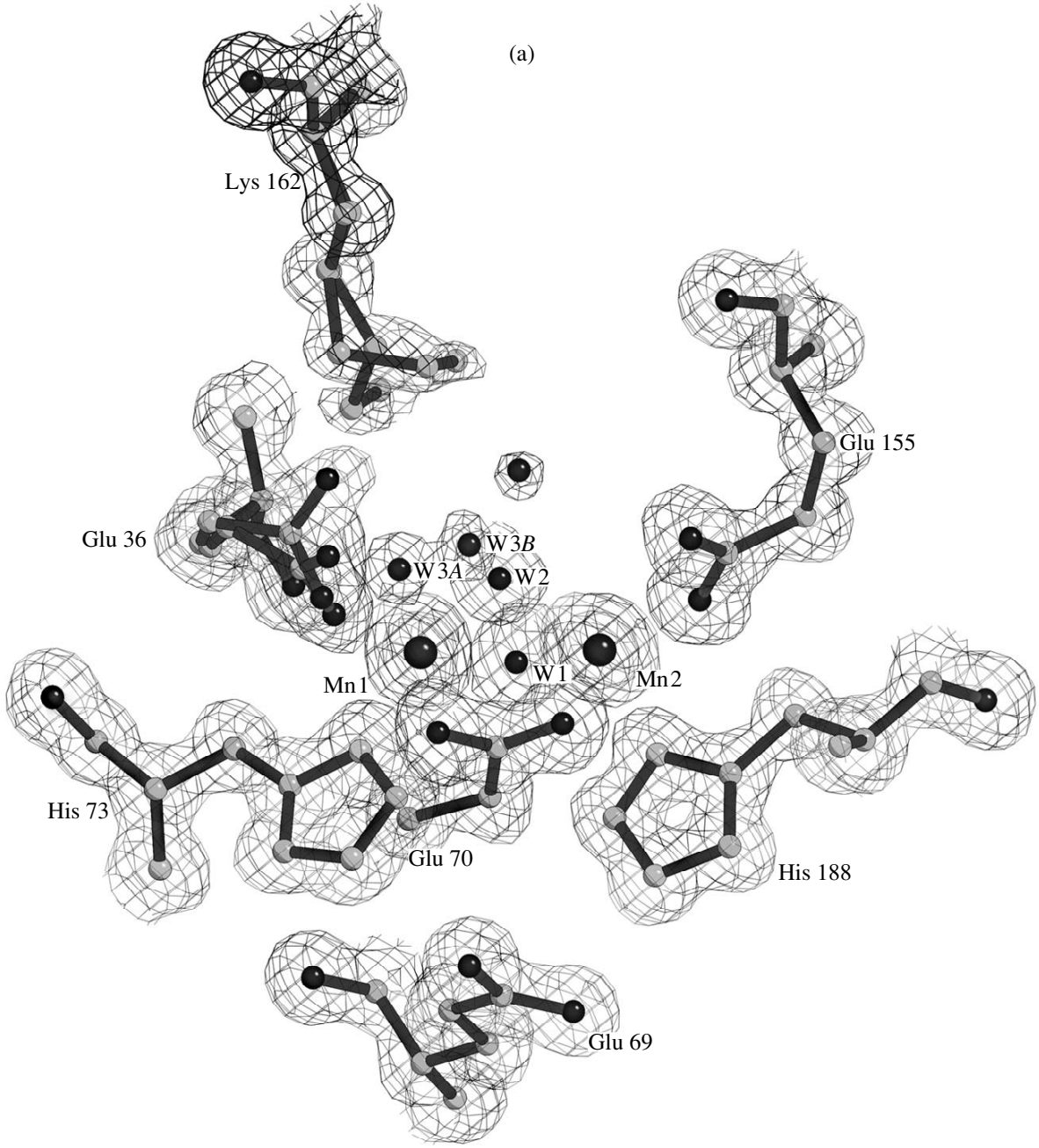

Fig. 1. The $2F_o - F_c$ electron density distribution in the active center of the enzyme (the contours are drawn at the 1σ and 8σ levels) (a) in the native structure (W3A is conformation **II** and W3B is conformation **I**) and (b) in the complex with Cl^- ions (Cl1 and Cl2 are Cl^- ions). The figures are drawn with the use of the BOBSCRIPT program [29].

It was established (EPR spectroscopy) that two Mn ions in the active center of the enzyme can exist in different oxidation states, namely, as (Mn^{2+}, Mn^{2+}), (Mn^{2+}, Mn^{3+}), and (Mn^{3+}, Mn^{4+}), and can be transformed into one another with the use of various reducing and oxidizing agents. The presence of the active state (Mn^{3+}, Mn^{3+}) in the native enzyme was confirmed spectrophotometrically [14]. It was shown that the enzyme in the (Mn^{2+}, Mn^{2+}) state is reversibly inhibited by monovalent negatively charged ligands, such as Cl^-, N_3^-, NO_2^-, NO_3^-, and F^- [15]. The EPR and EXAFS spectroscopic studies demonstrated that the (Mn^{2+}, Mn^{2+}) oxidation state of manganese ions can be transformed into the (Mn^{3+}, Mn^{3+}) oxidation state and back in the course of the enzymatic reaction of dimanganese catalases [14, 16, 17].

We studied the three-dimensional structure of dimanganese catalase from *Thermus thermophilus* by

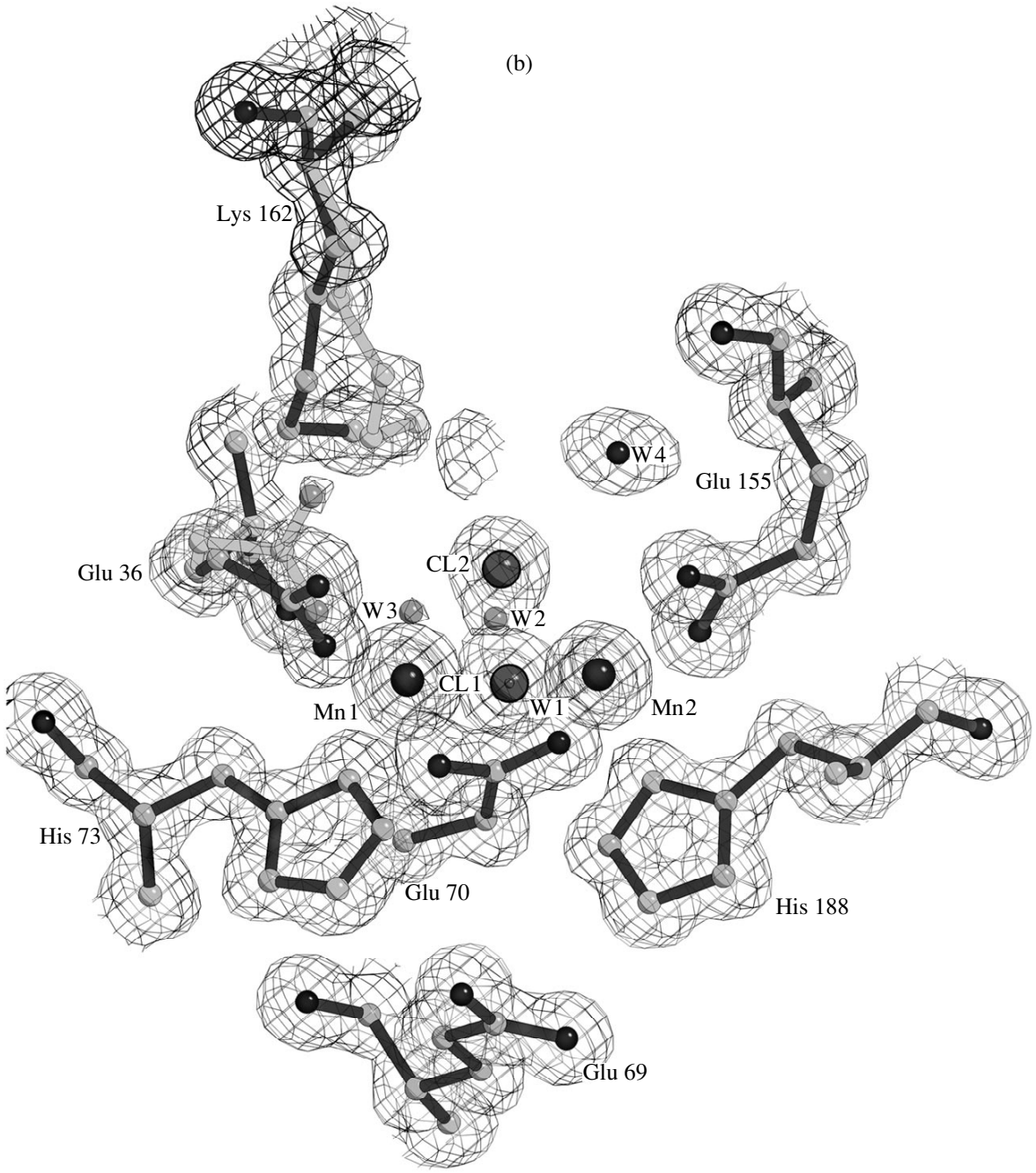

Fig. 1. (Contd.)

methods of X-ray protein crystallography with the use of synchrotron radiation. The experimental data sets were collected on enzyme crystals at low temperature. This allowed us to obtain X-ray data at about a 1.0 Å resolution, to calculate the electron density distribution, and to construct and refine atomic models of the enzyme in the native and inhibited forms. The analysis of the electron density distribution in the active center of the enzyme in two oxidation states enabled us to reveal several possible side-chain positions and to draw some preliminary conclusions on binding sites of hydrogen peroxide molecules in the course of the enzymatic reaction of dimanganese catalase.

MATERIALS AND METHODS

Crystallization of the Enzyme and Treatment of Crystals

Crystals of dimanganese catalase from the extremethermophilic bacterium *Thermus thermophilus* [9]

Table 2. Statistical characteristics of the refined models of the native catalase and its complex with Cl^- ions

Characteristic	Form of the enzyme	
	native	complex with Cl^- ions
R-factor, %	9.8	10.0
R-free factor, %	11.0	11.2
Dispersion precision index (DPI), Å [26, 27]	0.014	0.013
G factor (PROCHECK [28])	0.04	0.04
Number of atoms	5864	5871
Number of water molecules	880	922
Number of atoms of side chains in the K (L) subunits disordered over two positions	27(28)	32(33)
Number of water molecules disordered over two positions	37	54
Number of sulfate ions	6	6
Number of lithium ions	3	3
Rms of 1–2 bond lengths, Å	0.014	0.013
Rms of 1–4 bond lengths, Å	0.027	0.027
Rms of 1–4 bond lengths, Å	0.036	0.037
Rms of the chiral volume, $Å^3$	0.127	0.127
Deviations from the planarity, Å	0.006	0.02
B factor for the atoms of the main chain, $Å^2$	9.7	9.8
B factor for the atoms of the side chains, $Å^2$	12.2	12.7
B factor for water molecules, $Å^2$	26.5	26.7

Note: DPI is calculated by the formula $\sigma(x) = (N_a/(N_o - N_p))^{1/2} Rd_{\min} C^{-1/3}$, where C is the completeness of the data set, R is the standard R factor, $d_{\min}$ characterizes the maximum resolution, N_a is the number of atoms included in the refinement, N_o is the number of the observed reflections, and N_p is the number of the parameters to be refined.

were grown by the method of vapor diffusion in the hanging-drop modification at 37–46°C. The crystals of native catalase were grown with the use of a reservoir solution consisting of a 1.4 M ammonium sulfate solution in a 0.05 M AMPSO buffer at pH 9.0. The droplets had equal volumes (4 μL) of the protein solution (20–24 mg/mL of the protein in a 0.05 M AMPSO buffer at pH 9.0) and the reservoir solution. The crystals grew for about one week and had the shape of a 1.0–1.5 mm long rhombododecahedra, sp. gr. $P2_13$, and unit cell parameters $a = b = c = 134.3$ Å. The asymmetric part of the unit cell contains 1/3 of the protein molecule, i.e., two subunits.

The native enzyme crystals had a brownish-pink color, which confirmed the expected (Mn^{3+}, Mn^{3+}) oxidation state of the Mn ions in the crystals (it is well known that the (Mn^{2+}, Mn^{2+}) ions stored under alkaline conditions are oxidized to (Mn^{3+}, Mn^{3+})) [18].

Crystals of the enzyme inhibited by Cl^- ions were prepared by 30 min-soaking of native enzyme crystals in a solution of 1 mM hydroxylamine sulfate and 1.7 M ammonium sulfate in a 0.1 M HEPES buffer at pH 7.2. This resulted in the reduction of the oxidation state of the Mn ions to (Mn^{2+}, Mn^{2+}). Then the crystals were transferred for 1 h to a solution containing 100 mM NaCl and 1.7 M ammonium sulfate in a 0.1 M HEPES buffer at pH 7.2 and then to a stabilizing solution of the same composition at pH 5.5.

Crystal Flash-Cooling

With the aim of collecting low-temperature X-ray diffraction data, the crystals of native catalase were transferred to a stabilizing solution containing 30% PEG400 and 0.36 M lithium sulfate in a 0.1 M AMPSO buffer at pH 8.5. For the crystals of the complex with Cl^- ions, the stabilizing solution contained 40% PEG400, 0.36 M lithium sulfate, and 0.1 M NaCl in a 0.1 M MES buffer at pH 5.5.

The crystals were kept in the stabilizing solution for 10–20 s. Then the crystals were "caught" by a loop and were flash-cooled in a stream of nitrogen at 100 K (an Oxford Cryosystem low-temperature attachment). The crystals of the complex with chloride ions were flash-cooled to the cryogenic temperature and then "defreezed" to the ambient temperature; this procedure was repeated until the corresponding diffraction patterns contained no rings due to ice and attained the maximum resolution [19].

Experimental Data Collection and Data Processing

The X-ray intensity data sets were collected with the use of an Imaging Plate detector (MAR Research) from crystals of the native and inhibited forms of catalase using synchrotron radiation (the wavelength was 0.98 Å, the DORIS storage ring, the beam energy 4.5 GeV; EMBL, Hamburg) at 100 K. The experimental data were preliminarily processed using the DENZO program [20]. The data-collection statistics are given in Table 1.

Calculations of Electron Density Distributions and Refinement of the Atomic Models

The calculation of electron-density distributions and the refinement of the models were performed using the CCP4 [21], REFMAC [22], and SHELX [23] program packages. Two subunits (denoted here as *K* and *L*) located in the asymmetric part of the unit cell were refined independently. The construction and refinement of the atomic models were made by the "O" graphic program package [24], modified for an interactive *Sili-*

con Graphics station. The manual improvement of the models was based on the analysis of the Fourier difference syntheses calculated with the $(2F_o - F_c\varphi_c)$ and $(F_o - F_c\varphi_c)$ coefficients, where F_o and F_c are the observed and the calculated moduli of the structure factors, respectively, and φ_c are the phases of the structure factors calculated for the atomic model.

The atomic coordinates of the model of the native dimanganese catalase and the corresponding temperature factors were refined in several stages using the REFMAC [22] and SHELX [23] program packages. The atomic coordinates of dimanganese catalase, earlier determined at a 1.6 Å resolution on the basis of the X-ray diffraction data collected at room temperature [11] were used as the starting model coordinates for calculating the phases of the structure factors. The initial *R* factor was 47% for the X-ray data obtained at the resolution ranging from 15 to 2.0 Å. In the course of the refinement, the X-ray data set was gradually extended to the affainment of the 1.05 Å resolution. To model the solvent structure, each refinement cycle was completed with an automated procedure of the incorporation into the model of bound water molecules (the ARP program [25]). The total sum of the occupancies for the amino acid residues having several conformations was taken to be unity. The occupancies for different conformations of the side chains of the disordered amino acid residues were refined using the SHELX97 program. Then, these data were used in the subsequent refinement by the anisotropic version of the REFMAC program. The positions of hydrogen atoms were calculated from the geometric considerations and were not refined. The atomic model of the complex with chloride ions was refined using the REFMAC program and the atomic coordinates of the native enzyme (R = 9.8%) as the starting parameters. Both structures were refined with the use of anisotropic *B* factors.

The electron density distributions in the active centers of the native enzyme and its complex with chloride ions are shown in Fig. 1. The statistical characteristics of the refined models of the native enzyme and its complex are given in Table 2.

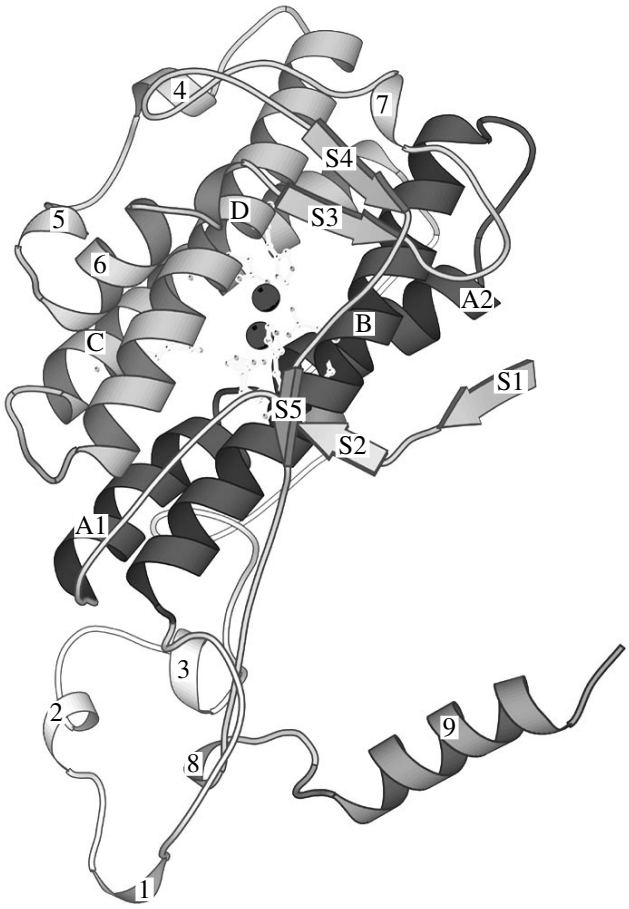

Fig. 2. Schematic of the spatial arrangement of the elements of the secondary structure of the subunit of the dimanganese catalase. The active center of the enzyme with two Mn ions is located between the long A, B, C, and D helices in the vicinity of the bending of the A helix and is formed by the amino acid residues of these four helices. The shorter helices are numbered and the elements of the β structure are labelled by S. For the amino acid residues and their numbers in the secondary-structural elements see Table 3.

RESULTS AND DISCUSSION

Analysis of Models

The validity of the refined models of the native and inhibited forms of the enzyme is supported by the statistical characteristics given in Table 2 and by the final electron-density maps $2F_o - F_c$ where all the amino acid residues of the polypeptide chain are reflected by the clear electron-density maxima. The exceptions are the last two C-terminal residues (Ala301 and Lys302) and several terminal atoms of the side chains of the Lys residues located on the molecule surface. The torsion angles at the Cα atoms of all residues are within the energetically allowed regions. The analysis of the electron density distribution shows that three of the total 15 proline residues (Pro209, Pro211, and Pro283) in the subunit have the *cis* conformation.

Secondary and Tertiary Structures of the Subunit of the Dimanganese Catalase

The three-dimensional structure of the enzyme has been described elsewhere [10–12]. The results of our study allow a more detailed characterization of the secondary structure of the molecule based on the analysis of hydrogen bonding. It was demonstrated that 42.7% of the amino acid residues belong to the α helices, 8.8% of the residues belong to the 3/10 helices, and 4.3% of the residues belong to the β strands (Figs. 2, 3; Table 3). The spatial arrangement of the structural elements of the secondary structure of the monomer is shown in Fig. 2.

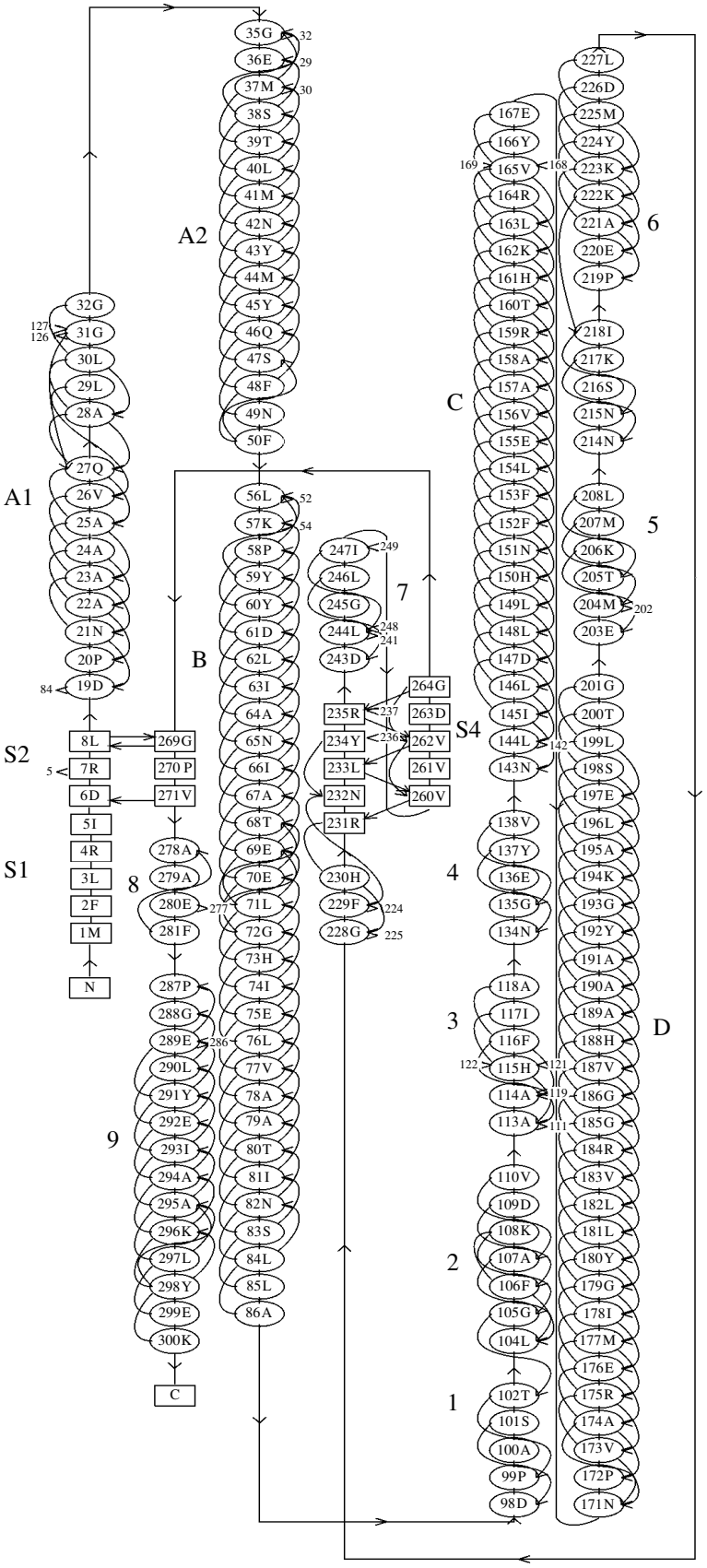

Fig. 3. Schematic of hydrogen bonds in the subunit of the molecule (obtained using the PROMOTIF program [30]).

Table 3. Secondary-structural elements of dimanganese catalase

Structural element	Type	Amino acid residues	Number of residues	Structural characteristic features
S1	β	1–5	5	The element forms an antiparallel β sheet with the analogous strand *S*1 of the second subunit
S2	β	7–8	2	The element is antiparallel to S5; Arg7 is bound to Phe236 and Ile8 is bound to Leu7 of the second subunit
A1	α	19–32	13	The helix is followed by the 3/10 helix
A2	α	35–50	16	The helix is linked to the second portion of the A2 helix through the type **I** β turn
B	α	56–89	35	The helix is preceded by the type **II** β turn and is followed by the type **IV** β turn
1	3/10	98–102	5	The helix is followed by the type **I** β turn
2	3/10	104–110	7	The helix is followed by the type **VII** β turn
3	α	113–118	6	The helix is preceded by the type **VII** β turn
4	3/10	134–138	4	
C	α	143–169	27	The helix is followed by the type **I** β turn
D	α	171–201	33	The helix is preceded by the type **I** β turn
5	3/10	203–208	4	The helix is followed by the type **IVb** β turn
6	α	214–230	17	The α helix is preceded by and is followed by 3/10 helices
S3	β	232–235	4	The element is parallel to S4
7	3/10	241–249	9	The helix is preceded by the type **I** β turn and is followed by the type **VI** β turn
S4	β	260–263	4	The strand is preceded by the β pin (251–253) and (255–257)
S5	β	269–270	2	The element is antiparallel to S2
8	3/10	278–284	8	The element is followed by the type **IVa** β turn
9	α	284–300	13	The helix is preceded by the type **VIII** β turn

Quaternary Structure of the Molecule

Six subunits of the dimanganese catalase form a hexamer with the symmetry 32. The hexamer has the shape of a hexagonal prism with the maximum dimensions 69 and 95 Å along the threefold axis and the perpendicular direction, respectively (Fig. 4).

There are two subunits per asymmetric part of the unit cell. These subunits are related by a noncrystallographic twofold symmetry axis. The rms deviation of the Cα atoms of the *K* subunit from the corresponding atoms of the *L* subunit is 0.2 Å. The most pronounced differences in the positions of the Cα atoms (0.4–1.5 Å) are observed in the regions characterized by moderate differences in the environments of the *K* and *L* subunits (residues 14–17, 169–172, 220–223, 263, and 268).

Three-Dimensional Structure of the Active Center of Dimanganese Catalase

The active center with two Mn ions is located deeply inside the monomer between four major helices (A, B, C, and D) and has access to the surrounding solution through two channels. The first 22 Å-long channel emerges to the molecule surface, whereas the second 16 Å-long channel is connected with the central channel of the hexamer (Fig. 5).

The Mn1- and Mn2-ions, which play the most important role in the active center of the enzyme, form the coordination bonds with the nitrogen atoms of the side chains of the His73 and His188 residues and with the oxygen atoms of the side chains of the Glu36, Glu70, and Glu155 residues (Fig. 6). The analysis of the electron-density distributions for the active centers in the native enzyme and in its complex with chloride ions demonstrated that the side chains of two amino acid residues (Glu36 and Lys162) in both crystallographically independent subunits, *K* and *L*, occupy two mutually dependent positions each. In this case, the terminal atoms of the Glu36 and Lys162 residues are shifted by 1.5–2.0 Å, and between the OE2 atom of the Glu36 residue and the Mn1 ion, the W3 water molecule appears. This water molecule occupies the sixth coordination position about the Mn1 ion (Fig. 6). The lengths of the coordination bonds of the manganese ions and the angles between these bonds differ from the corresponding ideal geometric characteristics (see Table 4). Thus, the active center can have two conformations. The occupancies of conformation **I** of the active center in the crystals of the native enzyme are 0.5 and 0.6 for the *L* and *K* subunits, respectively. In the crystals of the complex with Cl^- ions, the occupancies equal 0.85 for both subunits. The corresponding occupancies of conformation **II** are 0.5, 0.4, and 0.15, respectively.

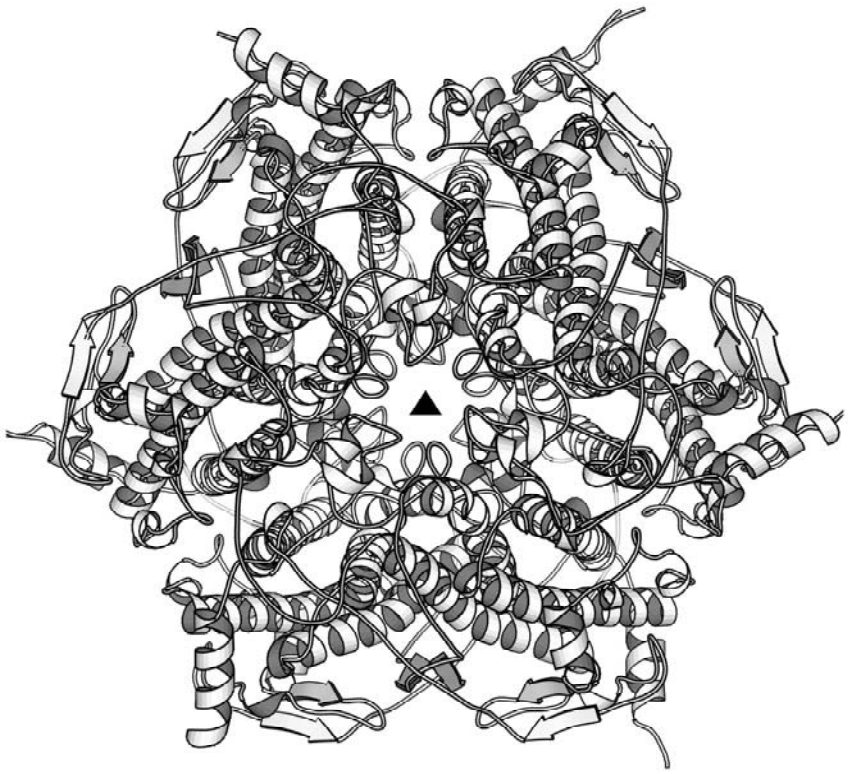

Fig. 4. Quaternary structure of dimanganese catalase. The threefold axis is indicated by a triangle.

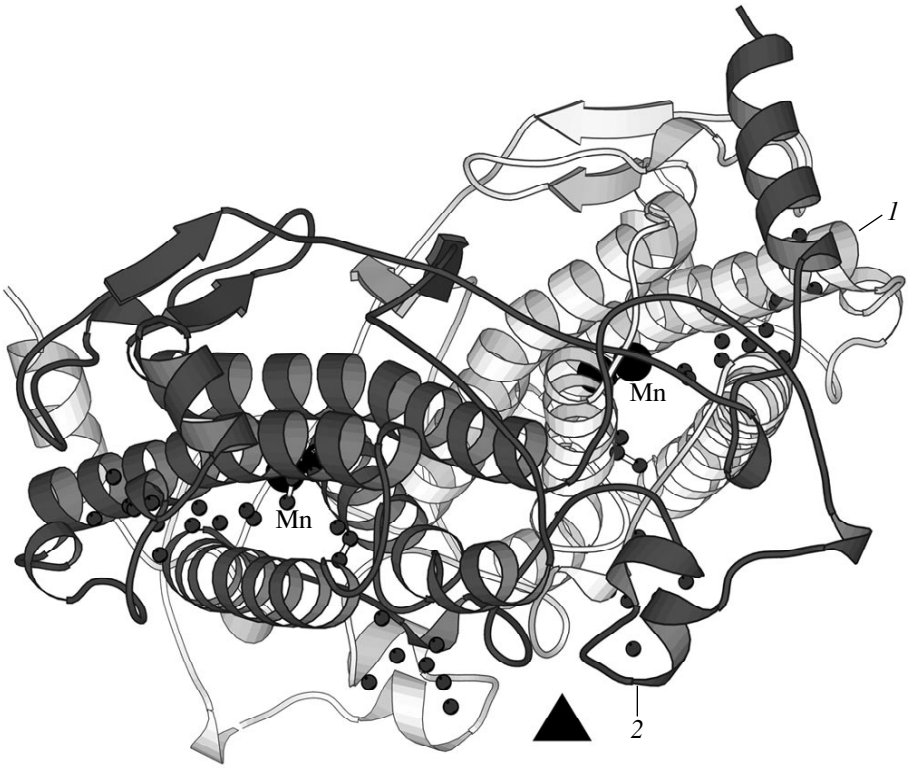

Fig. 5. Two subunits per asymmetric unit. One can see the channels leading to the active center of the molecule 22 Å-long channel *1* and the 16 Å-long channel *2*. The directions of the channels are indicated by arrows.

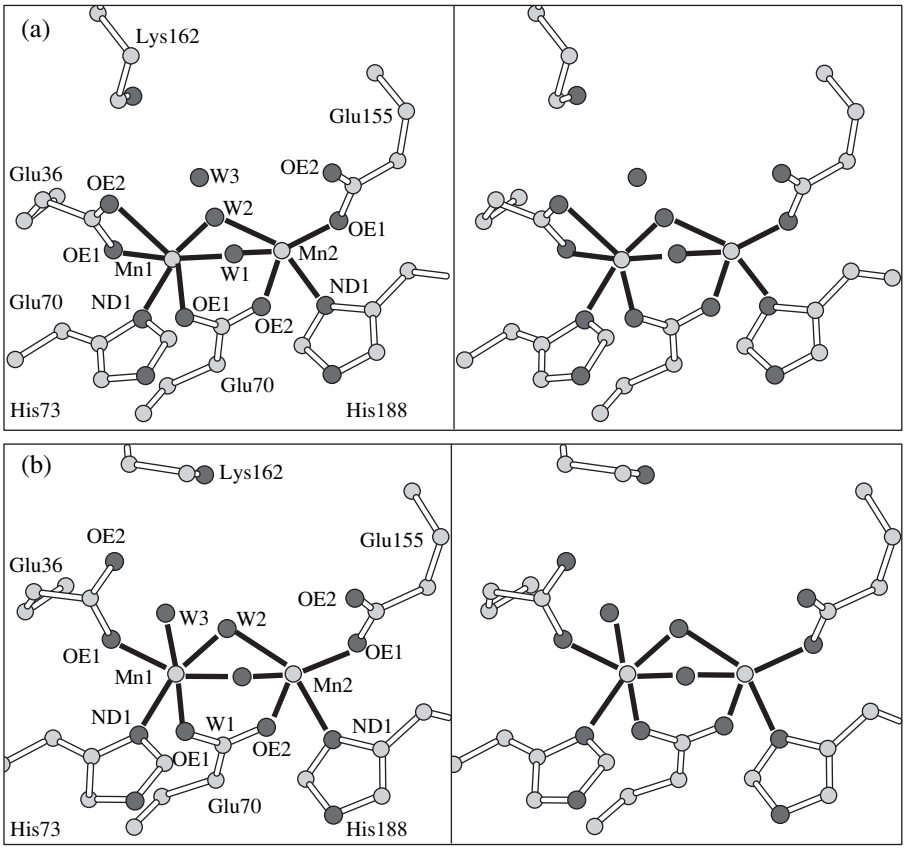

Fig. 6. Stereoview of the active center of the native enzyme: (a) conformation **I** and (b) conformation **II**.

The manganese ions in the native enzyme are linked via two oxygen atoms. Hereinafter, they are called the bridging atoms (W1 and W2 atoms in Figs. 1, 6 and in Table 5). The nature of the two atoms bridging the Mn ions has not been reliably established as yet. There are grounds to believe [14, 15] that oxygen atoms of water molecules or hydroxyl groups can bridge the Mn ions in the reduced (Mn^{2+}, Mn^{2+}) state, whereas in the oxidized (Mn^{3+}, Mn^{3+}) state, one of the bridges is formed by oxygen atoms. The bond lengths of the bridging W1 atom in the structure of the native dimanganese catalase shortened in comparison with the bonds formed by the W2 atom lead to an assumption that in the oxidized (Mn^{3+}, Mn^{3+}) dimanganese catalase, this W1 atom is replaced by the oxygen atom. In the complex with Cl^- ions, these ions are located in the vicinity of the W1 and W2 positions (Figs. 1, 6), and their refined occupancies are 1.0 and 0.85, respectively. The temperature factors of the Cl^- ions located in the vicinity of the W1 and W2 positions are 8.0 and 8.4 $Å^2$, respectively and, thus, are comparable with the temperature factors of the Mn1 and Mn2 ions (7.7 and 7.3 $Å^2$, respectively).

It is highly probable that conformation **I** of the active center in the complex with chloride ions, with the occupancies of the positions of the Glu36 and Lys162 residues equal to 0.85, corresponds to the reduced state of the enzyme with two Cl^- ions occupying the W1 and W2 positions. Conformation **II** corresponds to the enzyme state, in which the first bridge is formed by the Cl^- ion, and the second one, by the oxygen atom of the water molecule.

The positions of the bridging W1 and W2 ligands, occupied by Cl ions in the enzymatic reaction, can also be occupied by the oxygen atoms of hydrogen peroxide molecules, located, similar to an azide ion, in the above complex; i.e., they are almost perpendicular to the Mn1W2Mn2 plane [12]. It should be noted that, within the above assumptions, a hydrogen peroxide molecule in conformation **I** can replace W1 and W2, whereas in conformation **II**, this molecule can replace only W2 because of the presence of the water molecule in the W3 position hindering the replacement of the W1 ligand by a hydrogen peroxide molecule (Fig. 6). Since hydrogen peroxide decomposition proceeds in two stages with the participation of two hydrogen peroxide molecules [14] (the first hydrogen peroxide molecule in conformation **I** occupies the W2 position), the next hydrogen peroxide molecule is bound to replace the W1 ligand in conformation **II**, which is sterically impossible. Thus, it is most likely that the reaction

Table 4. Coordination environment around the manganese ions and some principal distances in the active centers of the native dimanganese catalase and its complex with chloride Å

Characteristic	Form of enzyme			
	native		complex with Cl^- ions	
conformation	**I**	**II**	**I**	**II**
Mn1–Mn2	3.13		3.30(3.32)	
Coordination about Mn1	6(5)	6	6	6
Mn1–OE1Glu36	2.10(2.13)	2.05(2.03)	2.16(2.14)	2.16(2.16)
Mn1–OE2Glu36	2.35(2.89)	3.39(3.36)	2.28(2.26)	3.55
Mn1–OE2Glu70	2.12		2.12	
Mn1–ND1His73	2.22(2.20)		2.21(2.22)	
Mn1–W1	2.03(2.06)		2.50(2.51)	
Mn1–W2	2.07(2.07)		2.6(2.59)	2.1(2.11)
Mn1–W3		2.27(2.29)		2.22(2.26)
Coordination around Mn2	5		5	
Mn2–OE2Glu70	2.12(2.13)		2.12	
Mn2–ND1His188	2.26(2.25)		2.24(2.23)	
Mn2–OE1Glu155	2.17(2.17)		2.20(2.22)	
Mn2–OE2Glu155	2.64(2.63)		2.43(2.45)	
Mn2–W1	2.12(2.13)		2.60(2.58)	
Mn2–W2	2.18(2.21)		2.50(2.52)	2.12(2.14)

Note: The data are given for the K subunit; the characteristics for the L subunit different from the corresponding characteristics for the K subunit are given in parentheses.

Table 5. Selected angles (deg) between the coordination bonds of the manganese ions in native dimanganese catalase and chloride-inhibited catalase

Characteristics	Form of the enzyme			
	native		complex with Cl^- ions	
conformation	**I**	**II**	**I**	**II**
Mn1–W1–Mn2	98.6(96.6)		80.8(81.3)	
Mn1–W2–Mn2	93.7(94.5)		80.4(81.2)	101.2(102.5)
OE1Glu36–Mn1–W1	165.4(161.9)	151.9(134.3)	165.4(165.1)	145.1(146.2)
OE1Glu36–Mn1–W2	89.6(92.4)	98.0(103.4)	90.9(90.2)	89.3(100.0)
OE1Glu36–Mn1–ND1His73	100.5(99.9)	95.1(91.5)	102.2(102.8)	105.8(99.8)
W1–Mn1–OE1Glu70	105.4(105.2)		106.4(106.7)	
OE1Glu36–Mn1–OE1Glu70	80.1(88.4)	102.0(120.6)	83.7(83.6)	106.8(106.8)
OE1Glu36–Mn1–OE2Glu36	56.5(48.0)		59.1(57.7)	
OE1Glu36–Mn1–W3		77.9(60.6)		95.2(95.3)
W2–Mn1–W1	77.1(76.2)		77.8(77.8)	82.2(81.1)
W2–Mn1–OE2Glu36	96.4(91.4)		87.2(87.7)	
W2–Mn1–ND1His73	165.8(165.1)		167.5(166.8)	157.4(156.4)
W2–Mn1–W3		93.0(92.5)		98.2(98.3)
W1–Mn1–W3		74.9(73.7)		52.1(51.6)
W3–Mn1–OE1Glu70		178.2(178.1)		158.2(157.9)
W1–Mn2–OE2Glu70	106.4(107.2)		113.4(113.2)	
W2–Mn2–OE2Glu155	98.5(99.1)		88.8(89.5)	109.2(109.3)
W2–Mn2–OE1Glu155	107.0(107.9)		101.0(100.9)	108.7(109.1)
W2–Mn2–OE2Glu70	84.9(84.5)		92.8(92.3)	73.6(73.9)
W2–Mn2–W1	72.9(71.7)		77.8(78.0)	79.3(78.9)
W2–Mn2–ND1His188	154.1(152.6)		160.9(160.6)	147.7(147.3)

Note: The angles are given for the K subunit; the corresponding angles for the L subunit are given in parentheses.

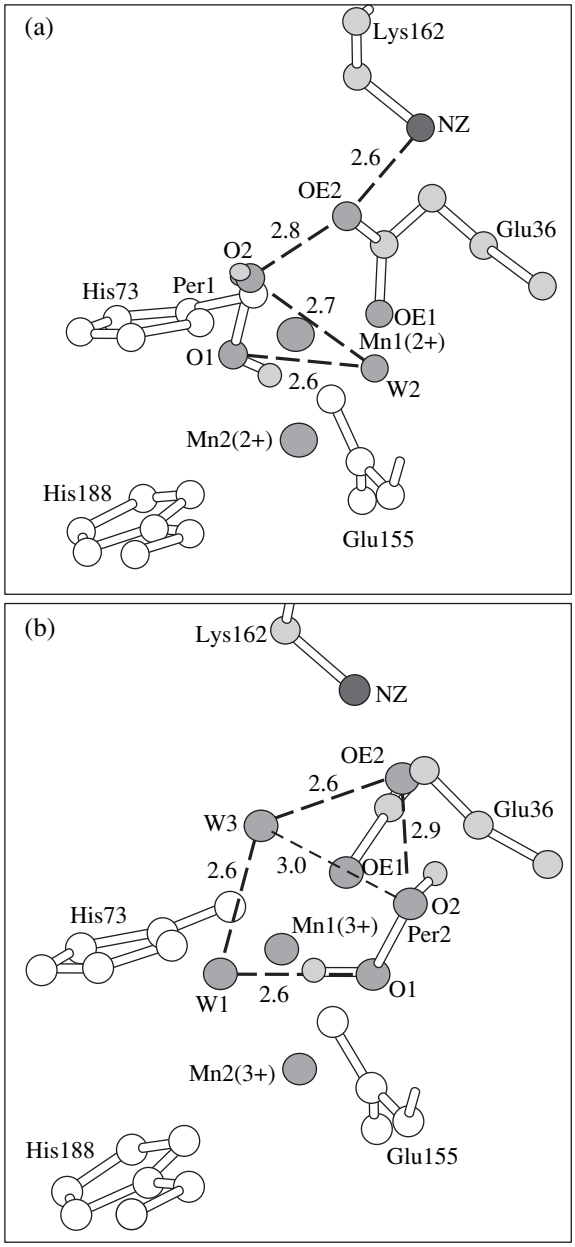

Fig. 7. Possible bonding of hydrogen peroxide molecules in the active center in (a) **I** and (b) **II** conformations. The distances between the atoms are given in Å.

begins with the replacement of the W1 position in conformation **I**.

The distances between the atoms in hypothetical hydrogen peroxide positions and the atoms of the active center in two conformations are indicated in Fig. 7. The redistribution of a proton between the O1 and O2 atoms of hydrogen peroxide during the enzymatic reaction can occur with the participation of water molecules in the W1, W2, and W3 positions and the OE2 atom of the amino acid residue Glu36. Electrostatic interactions between hydrogen peroxide molecules and the Lys162 residue may become essential if the O–O bond in the first hydrogen peroxide molecule breaks and thus facilitates deprotonation of the second hydrogen peroxide molecule at the second stage of the reaction.

The precision structural data on the arrangement of the amino acid residues in the active center obtained in this study provide a reliable structural basis for the construction of the detailed stereochemical mechanism of the catalase action. Some additional data can be obtained from the structural studies of the catalase in which the amino acid resides Glu36, Lys162, and Thr39 in the active center are replaced using the methods of gene engineering.

ACKNOWLEDGMENTS

This study was supported by EMBL, the Governmental Program of the Russian Federation “Leading Scientific Schools” (project no. 96-15-96427), by the Russian Foundation for Basic Research (project no. 99-02-16191), and by BBSRC (grant no. 50/B05117).

REFERENCES

1. G. R. Schonbaum and B. Chance, in *The Enzymes*, 3d ed., Ed. by P.D. Boyer (Academic Press, New York, 1976), Vol. 13, Part C, pp. 363–408.
2. I. Fita, A. M. Silva, M. R. N. Murthy, *et al.*, Acta Crystallogr., Sect. B: Struct. Sci. **42**, 497 (1986).
3. G. N. Murshudov, W. R. Melik-Adamyan, A.I. Grebenko, *et al.*, FEBS Lett. **312**, 127 (1992).
4. J. Bravo, N. Verdaguer, J. Tormo, *et al.*, Structure **3**, 491 (1995).
5. B. K. Vainshtein, W. R. Melik-Adamyan, V. V. Barynin *et al.*, J. Mol. Biol. **188**, 49 (1986).
6. P. Gouet, H.-M. Jouve, and O. Dideberg, J. Mol. Biol. **249**, 933 (1995).
7. M. J. Mate, M. Zamocky, L. M. Nykyri, *et al.*, J. Mol. Biol. **268**, 135 (1999).
8. V. V. Barynin and A. I. Grebenko, Dokl. Akad. Nauk SSSR **286**, 461 (1986).
9. Y. Kono and I. Fridovich, J. Biol. Chem. **258**, 6015 (1983).
10. V. V. Barynin, A. A. Vagin, W. R. Melik-Adamyan, *et al.*, Dokl. Akad. Nauk SSSR **288**, 877 (1986).
11. V. V. Barynin, P. D. Hempstead, A. A. Vagin, *et al.*, J. Inorg. Biochem. **67**, 196 (1997).
12. V. V. Barynin, P. D. Hempstead, A. A. Vagin, *et al.*, in *EMBL Hamburg Outstation Annual Report* (EMBL, Hamburg, 1999), p. 283.
13. S. V. Shlyapnikov, A. A. Dement’ev, A. J. G. Moir, *et al.*, Biokhimiya (in press).
14. S. V. Khangulov, V. V. Barynin, and S.V. Antonyuk-Barynina, Biochim. Biophys. Acta **1020**, 25 (1990).
15. S. V. Khangulov, V. V. Barynin, N. V. Voevodskaya, *et al.*, Biochim. Biophys. Acta **1020**, 305 (1990).
16. G. S. Waldo, R. M. Fronko, and J. E. Penner-Hahn, Biochemistry **30**, 10486 (1991).
17. G. S. Waldo and J. E. Penner-Hahn, Biochemistry **34**, 1507 (1995).

18. F. A. Cotton and G. Wilkinson, *Advanced Inorganic Chemistry*, 2nd ed. (John Wiley, New York, 1969).
19. S. V. Antonyuk, V. V. Barynin, A. N. Popov, *et al.*, in *Proceedings of XVIIIth European Crystallographic Meeting* (1998), Vol. 5, Part B, p. 493.
20. Z. Otwinowski and V. Minor, *DENZO: Oscillation Data Processing Program for Macromolecular Crystallography* (Yale University, New Haven, 1993), p. 56.
21. CCP4—Collaborative Computational Project No. 4, Acta Crystallogr., Sect. D: Biol. Crystallogr. **50**, 760 (1994).
22. G. N. Murshudov and A. A. Vagin, Acta Crystallogr., Sect. D: Biol. Crystallogr. **53**, 240 (1997).
23. G. M. Sheldric and T. R. Schneider, Methods Enzymol. **277**, 319 (1997).
24. T. A. Jones, J. Y. Zou, and S. W. Cowan, Acta Crystallogr., Sect. A: Found. Crystallogr. **47**, 110 (1991).
25. V. S. Lamzin and K. S. Wilson, Acta Crystallogr., Sect. D: Biol. Crystallogr. **49**, 129 (1993).
26. W. J. Cruickshank, Acta Crystallogr. **13**, 774 (1960).
27. W. J. Cruickshank, in *Macromolecular Refinement: Proceedings of the CCP4 Study Weekend* (1996), pp. 11–22.
28. R. A. Laskovski, M. W. MacArthur, D. S. Moss, *et al.*, J. Appl. Crystallogr. **26**, 283 (1993).
29. R. M. Esnouf, J. Mol. Graph. **15**, 133 (1997).
30. E. G. Hutchinson and J. M. Thornton, Protein Sci. **5**, 212 (1996).

Translated by T. Saphonova

Crystallography Reports, Vol. 45, No. 1, 2000, pp. 117–121. Translated from Kristallografiya, Vol. 45, No. 1, 2000, pp. 123–127.

PHASE TRANSITIONS

EPR Study of Kinetic Properties of a Weak Polar Ferroelectric $Li_2Ge_7O_{15}$

M. P. Trubitsyn, M. D. Volnyanskiĭ, and A. Yu. Kudzin

Physics Faculty, Dnepropetrovsk State University, per. Nauchnyĭ 13, Dnepropetrovsk, 320625 Ukraine

Received February 24, 1998

Abstract—The EPR spectra of Mn^{2+} ions have been studied in the vicinity of the phase transition to the ferroelectric phase in lithium heptagermanate crystals. The anomalous broadening of the resonance lines observed in the vicinity of the transition temperature T_C was attributed to an increase of the contribution of low-frequency ($\omega < 10^7$ Hz) fluctuations of the local order parameter. The critical index of the correlation length is determined to be $\nu \approx 0.63$, which indicates the Ising-type critical behavior of the crystal. The experimental data obtained in the vicinity of T_C were interpreted with due regard for long-range dipole interactions. According to our estimates, the forces of dipole interactions are prevalent only in the close vicinity of the transition point, $|T - T_C| \ll 0.1$ K. © *2000 MAIK "Nauka/Interperiodica".*

INTRODUCTION

The use of magnetic resonance methods provided for the experimental detection and study of a large number of critical phenomena accompanying structural phase transitions [1, 2]. A very promising application of the radiospectroscopic methods to weak polar ferroelectrics [3], whose physical properties in the vicinity of the phase transition are determined by the effect of the fluctuations in the order parameter, was reported in [4, 5]. One of the representatives of the group of weak polar ferroelectrics is lithium heptagermanate (LHG) of the composition $Li_2Ge_7O_{15}$ with the phase transition from the paraelectric (sp. gr. D_{2h}^{14}) to the ferroelectric phase (sp. gr. C_{2v}^5) at $T_C = 283.5$ K [6, 7].

Below, we report the study of the widths and the shapes of the EPR lines in the vicinity of the phase transitions in LHG crystals doped with paramagnetic Mn^{2+} ions (0.06 and 9.2 wt %). Earlier [8], we observed considerable broadening of the resonance lines and their crossover in the vicinity of T_C. We performed computer modeling of the spectral contour providing the separation of the local order parameter and the width of EPR lines and studied its temperature behavior.

The studies were performed on a Radiopan SE/X 2547 spectrometer (with the klystron width ~9 GHz). The temperature of the specimens was maintained at ±0.02 K by heating them in nitrogen vapors with the use of a conventional cryostat.

EXPERIMENTAL RESULTS

We measured and studied the line $m_j = -5/2$ of the high-field electron sextet $M_S = -3/2 \longleftrightarrow -5/2$, whose superfine components are the most sensitive to the structural distortions during the phase transition. The width of the line, δH, was determined as a distance between the extrema of the first derivative of the absorption line. The δH measurements and the subsequent analysis of the line shape presented no difficulties because the neighboring components were not superimposed, and the superfine splitting of the high-field sextet (~6.9 mT) exceeded the width of the individual line for more than an order of magnitude (~0.5 mT far from the T_C).

Figure 1 shows the temperature dependences of the experimental line widths obtained in the external magnetic fields differently oriented with respect to the crystallographic axes: $\mathbf{H} \parallel \mathbf{b}$ and $\angle\mathbf{Hb} = 7°$ at $\mathbf{H} \perp \mathbf{c}$. For the main orientation $\mathbf{H} \parallel \mathbf{b}$, no noticeable changes of δH in the vicinity of T_C were observed. The line shape was almost independent of the distance to the transition point and was characterized by the contour intermediate between the Lorentzian and Gaussian ones. For the field orientation $\angle\mathbf{Hb} = 7°$ at $\mathbf{H} \perp \mathbf{c}$, the line width was considerably broadened with an approach to the T_C point: δH increased from ~0.53 mT (far from the transition point, $T = 303.1$ K) up to ~1.4 mT (in the vicinity of the transition point T_C, $T = 283.90$ K). In this case, the experimental line contour is also considerably transformed and, in the vicinity of T_C, acquires an almost Gaussian shape.

The study of the line-width anisotropy in the vicinity of T_C and the angular dependences of the spectral-component splitting below T_C [8] showed that the anomalous line broadening in the vicinity of the phase transition was caused by fluctuations in the local order parameter. To single out the contribution of fluctuations into δH, we modeled on a computer the experimental contour of the spectrum line by the convolution of the Lorentzian derivative with the Gaussian $S(H)$ =

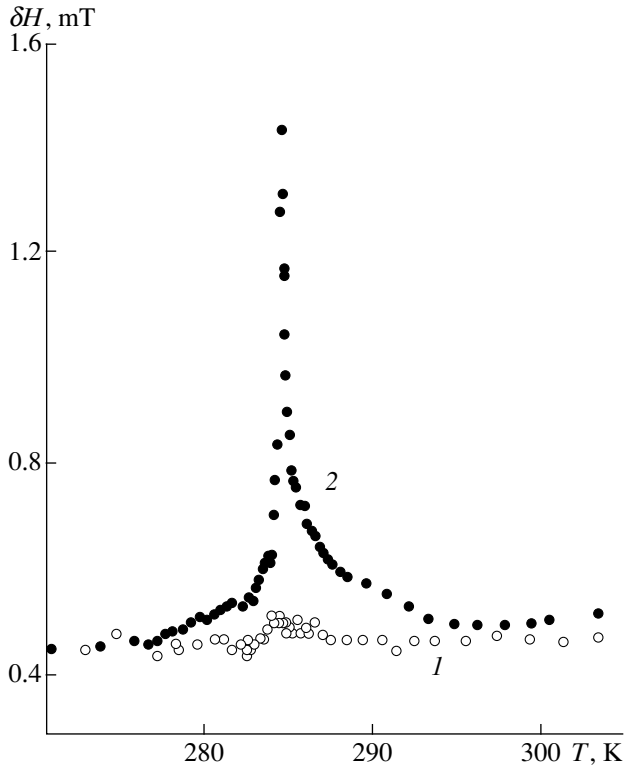

Fig. 1. Temperature dependence of the width of the hyperfine line $m_j = -5/2$, $M_S = -3/2 \longleftrightarrow -5/2$ in the vicinity of the phase transition for two orientations of the external magnetic field (*1*) **H** || **b**, (*2*) ∠**Hb** = 7°, **H** ⊥ **c**. For the second orientation, the line is split into a doublet below T_C. The line width is indicated only for the high-field component.

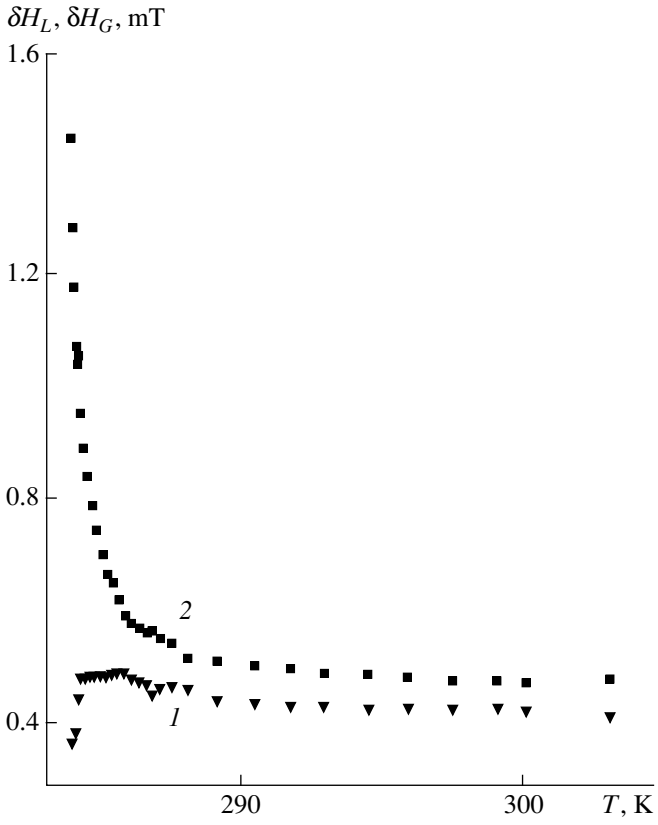

Fig. 2. (*1*) Homogeneous δH_L and (*2*) inhomogeneous δH_G contributions to the resulting line width in the high-temperature region around T_C; ∠**Hb** = 7°, **H** ⊥ **c**.

$\int L(H - H_C/\delta H_L)G(H_C - H_0/\delta H_G)dH_C$ under the assumption that a line due to an individual paramagnetic ions can be described by the Lorentzian with the center at H_C and that the H_C values are normally distributed about the experimentally determined center of the H_0 line because of the action of the static mechanisms.

The temperature dependences of the fitting parameters δH_L and δH_G obtained by the least squares method are shown in Fig. 2 at $T > T_C$. It is seen that the uniform component of the line width δH_L is almost temperature independent, whereas the Gaussian line width δH_G noticeably increases with an approach to T_C. Comparing the data in Figs. 1 and 2, one can conclude that the broadening of the resonance lines in the vicinity of T_C is determined by an increase of the inhomogeneous component δH_G. Thus, the critical contribution due to the fluctuations in the local-order parameter can be attributed to the Gaussian component and determined from the relationship

$$\delta H_{CR}(T) = (\delta H_G^2(T) - \delta H_G^2(T^*))^{\frac{1}{2}}.$$

It was also assumed that the value δH_G (T^* = 303.1 K) = 0.35 mT measured far from the phase transition is provided by insignificant inhomogeneous contributions. The dependence $\delta H_{CR}(T)$ obtained is plotted on a double logarithmic scale in Fig. 3.

DISCUSSION

Evolution of the EPR spectra during the phase transition is caused by the atomic displacements in the local environment of a paramagnetic probe and the specific mechanisms of the spin–lattice interactions. The resonance fields for which the "absorption" of the SHF-power is recorded are the functions of the time-dependent local order parameter $\eta(t) = \langle\eta\rangle + \delta\eta(t)$. In the vicinity of the phase transitions, these fields can be expanded into a series

$$H_R(t) = H_0 + A\eta(t) + \frac{1}{2}B\eta^2(t) + \ldots$$
$$= \left\{H_0 + A\langle\eta\rangle + \frac{1}{2}B\langle\eta^2\rangle\right\} + \left\{A\delta\eta + \frac{1}{2}B(\eta^2 - \langle\eta^2\rangle)\right\}. \quad (1)$$

Here, H_0 describes the line position in the paraelectric phase; the coefficients A and B are dependent on the position of the paramagnetic center in the lattice and the magnetic field orientation with respect to the crystal axes. The braces in the above expression single out the static and the time-dependent contributions to the resonance fields. The static part, $H_0' = H_0 + A\langle\eta\rangle + \frac{1}{2}B\langle\eta^2\rangle$, describes the displacement of the line because of the nonzero value of $\pm\langle\eta\rangle$ and the mean square fluctuations $\langle\delta\eta^2\rangle$. The dynamic part determines the fluctuation effect on the width and the shape of the resonance line.

According to [9], the local symmetry of the Mn^{2+} centers in the paraelectric phase of the LHG crystals is characterized by a twofold axis $C_2 \parallel \mathbf{b}$, which disappears upon the phase transition. Thus, if the magnetic field is parallel to **b**, the resonance fields H_R are the even functions of the local order parameter, whereas the coefficient A before the linear term in expansion (1) equals zero. The absence of noticeable anomalies in the experimental dependence $\delta H(T)$ for the main orientation (Fig. 1) leads to a conclusion that the squared contribution to broadening the EPR line is insignificant and can be ignored. The fluctuation contribution to the line width can be expressed in terms of the second moment of the line [10] as

$$\delta H_{CR}^2 \sim \langle (H_R - H_0')^2 \rangle = A^2 \sum_q \langle \delta\eta_q^2 \rangle, \qquad (2)$$

where the summation is performed with due regard for the local nature of the magnetic resonance over all the allowed values of the wave vectors in the Brillouin zone. In [11], the fluctuation contribution to the widths of the resonance lines was considered for the limiting case, where the fluctuation frequencies considerably exceeded the characteristic experimental frequency ω_1. Neglecting the critical index of the pair correlation function η [12], whose small value is usually beyond the accuracy limit of the radiospectroscopic measurements, the critical line width in the dynamic limit can be represented as [11, 13]

$$\delta H_{CR} \sim A^2 k_B T \tau^{-\nu} \arctan\left\{\frac{\pi}{k_0 a}\tau^{-\nu}\right\}. \qquad (3)$$

Here k_B is the Boltzmann constant, $\tau = |T - T_C|/T_C$ is the reduced temperature, $k = k_0\tau^\nu$ is the reciprocal correlation length, ν is the corresponding critical index, and a is the lattice constant.

If fluctuations are characterized by frequencies considerably lower than ω_1, they can be interpreted as quasistatic displacements in the local environment of the paramagnetic center. In this case, the critical line width is [13]

$$\delta H_{CR}^2 \sim A^2 k_B T\left[1 - \frac{k_0 a}{\pi}\tau^\nu \arctan\left(\frac{\pi}{k_0 a}\tau^{-\nu}\right)\right]. \qquad (4)$$

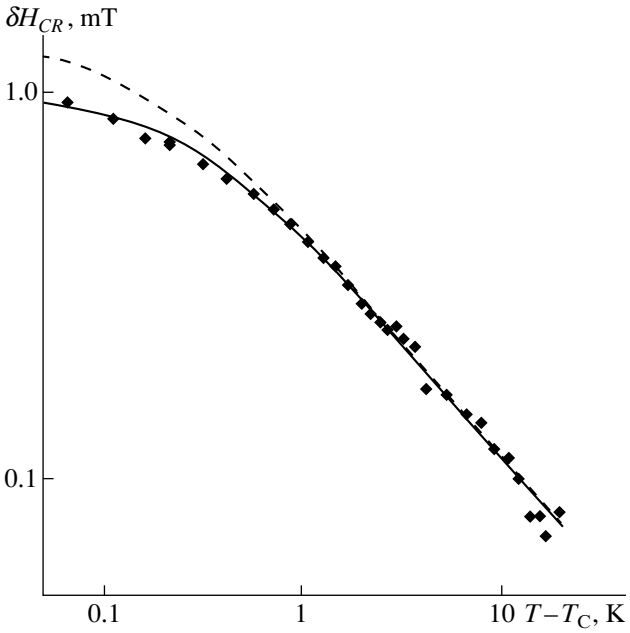

Fig. 3. Temperature dependence of the critical contribution to the line width. Points indicate the experimental data, the dashed line indicates the data calculated by (5), and the solid line indicates the data calculated by (7).

According to [3], in the dynamic limit, δH_{CR} is divergent by the power law, whereas in the static limit (4), it takes a finite value. At the same time, analysis of the experimental dependences based on the consideration of the temperature-dependent parts of (3) and (4) does not allow a reliable determination of the applicability ranges of the above approximations in all the cases. The best way to solve this problem is to establish the character of the δH_{CR} dependence on the parameter A of the expansion [14]. The study of the orientation and temperature dependences of the Mn^{2+} spectra in LHG crystals showed that the linear relationship $\delta H_{CR} \sim A$ is observed in the broad neighborhood of the phase transition [15]. Such behavior corresponds to (4) and indicates that the broadening of the resonance lines is caused by the fluctuations occurring with frequencies lower than the measurement frequency of the experiment (i.e., the frequency analog of the line width $\omega^1 \sim 10^7$ Hz). Therefore, the temperature dependence of the critical line width (Fig. 3) should necessarily be considered within the framework of static approximation (4). To describe the experimental data, we used the relation-

ship

$$\delta H_{CR}^2 = CT\left\{1 - D(T - T_C)^{\nu}\arctan\left(\frac{1}{D(T - T_C)^{\nu}}\right)\right\}, \quad (5)$$

which includes three fitting parameters C, D, and ν. The transition temperature T_C = 283.83 K was determined from splitting the spectral components in the ferroelectric phase [16]. The calculated dependence is shown by a dashed line in Fig. 3. It is seen that at $T_C + 1\ \text{K} \lesssim T \lesssim T_C + 20$ K, the theoretically calculated curve agrees quite well with the experimental data. The slope of the dependence in the aforementioned range is determined by the critical index of the correlation length with the value of $\nu \approx 0.63$. Approaching further to the transition point in the $T_C < T \lesssim T_C + 1$ K range, relationship (5) predicts higher values of the critical width than those observed experimentally (Fig. 3). At the transition point, expression (5) yields an overestimated value $((\delta H_{CR})^{\max} = (CT_C)^{\frac{1}{2}} \sim 1.6$ mT). The $T_C < T \lesssim T_C + 1$ K interval considerably exceeds the accuracy of thermostating and the temperature gradients in the nitrogen-vapor flow. Therefore, this deviation cannot be caused by the experimental errors in the temperature mode, which should have led to a considerable spread of the $\delta H(T)$, whereas the experiment shows a considerable anomaly in the line width (Fig. 1). Now, assume that the systematic deviation of the experimental points from the calculated curve toward lower values is associated with the suppression of the fluctuation contributions by the long-range dipole interactions. Then, in order to describe the experimental behavior, one has to take into account the dipole–dipole term in the expression for the qth component of the mean-square fluctuation

$$\langle \delta\eta_q^2 \rangle = k_B T\chi(q = 0)\frac{k^2}{q^2 + \Delta^2(\mathbf{q}_z/\mathbf{q})^2 + k^2}, \quad (6)$$

where $\chi(q = 0) = \chi_0\tau^{-\gamma}$ is the static susceptibility at the critical magnitude of the wave vector, $\Delta^2 = 4\pi e^2/\delta$, e is the effective charge of the soft mode, δ is the coefficient before the gradient term in the free-energy expansion, and $\mathbf{q}_z$ is the wave-vector component along the polar axis. The integration over the Brillouin zone in (2) with due regard for (6) is complicated by the anisotropy that appeared in the dispersion relationship. At the same time, the tendency to fluctuation suppression can be seen if one neglects the angular dependence of the dipole term. Assuming that $(\mathbf{q}_z/\mathbf{q})^2 = 1$ in (6), we obtain for the static case

$$\delta H_{CR}^2 = CT\left\{1 - (D^2(T - T_C)^{2\nu} + \tilde{\Delta}^2)^{\frac{1}{2}} \times \arctan\left(\frac{1}{(D^2(T - T_C)^{2\nu} + \tilde{\Delta}^2)^{\frac{1}{2}}}\right)\right\}. \quad (7)$$

In the above expression, an additional parameter $\tilde{\Delta} = \Delta a/\pi$, absent in (5), is introduced. The curve calculated by (7) with the same C, D, and ν values as those used in (5) is shown by a solid line in Fig. 3. It is seen that expression (7) for longitudinal fluctuations qualitatively reflects the effect of the relative suppression of the critical contributions by the dipole–dipole interactions and, thus, allows one to describe the experimental data in the vicinity of T_C^+. At the transition point, expression (7) yields the value $(\delta H_{CR})^{\max} \sim 0.99$ mT.

CONCLUSION

The study of the EPR spectra of Mn^{2+} centers allowed us to single out the fluctuation contribution to line broadening in the vicinity of the phase transition in the LHG crystals. A nonclassical value of the critical index of the correlation length, $\nu \approx 0.63$, agrees quite well with the value $\beta \approx 0.32$ obtained in the studies of the temperature behavior of the local order parameter below T_C by the EPR method below T_C [16]. The indices obtained correspond to the Ising-type critical behavior and indicate the existence of short-range forces responsible for the phase transition [17]. Obviously, the Ising nature of the critical properties of LHG crystals is explained by the small effective charge of the soft mode and, therefore, the weak dipole–dipole interactions [3]. This conclusion, drawn from the study of the local characteristics qualitatively, agrees with the macroscopic properties of LHG crystals [4, 5].

In the narrow (~1 K) temperature range above T_C, we observed a slower increase of the critical contribution to δH_{CR} in comparison with that for the curve calculated by (5). We believe that this deviation (Fig. 3) is caused by the suppression of fluctuations in the local order parameter by the long-range Coulomb interactions, which can also change the type of the critical behavior with an approach to T_C [17]. The possibility of observing the crossover in the transition from the Ising to the dipole behavior in weak polar dielectrics was discussed in [3] and then was experimentally confirmed by the studies of the dielectric susceptibility and thermal capacity of TSCC crystals [18]. As far as we know, no logarithmic analomalies in LHG crystals have been reported. We believe that this can be explained as follows. The logarithmic corrections can be obtained from

(2) and (6) under the assumption that $q^2 + k^2 \ll \Delta^2$. The fitting parameters used in (7) to describe the experimental data (Fig. 3) indicate that this condition is fulfilled in the temperature range $T - T_C \ll (\tilde{\Delta}/D)^{1/\nu} \sim 0.14$ K. Fitting the calculated dependences to the experimental data by the numerical integration of (2), with due regard for all the possible directions of the wave vector (6), yields a somewhat overestimated value but one that has the same order of magnitude (~0.7 K). These estimates show that the temperature range of the true logarithmic behavior can hardly be attained in the experiments because of a too small amplitude of dipole interactions, Δ.

REFERENCES

1. F. Borsa and A. Rigamonti, *Magnetic Resonance of Phase Transitions*, Ed. by F.J. Owens, Ch.P. Poole, H. A. Farach, *et al.* (Academic, San Francisco, 1979), p. 79.
2. K. A. Muller and J. C. Fayet, in *Structural Phase Transitions II*, Ed. by K.A. Muller and H. Thomas (Berlin, Springer, 1991), Vol. 45, p. 1.
3. A. K. Tagantsev, I. G. Siniĭ, and S. D. Prokhorova, Izv. Akad. Nauk SSSR, Ser. Fiz. **51** (12), 2082 (1987).
4. B. A. Strukov, M. Yu. Kozhevnikov, M. D. Volnyanskiĭ, *et al.*, Kristallografiya **36** (4), 942 (1991).
5. B. A. Strukov, M. Yu. Kozhevnikov, Kh. A. Nizomov, *et al.*, Fiz. Tverd. Tela (Leningrad) **33** (10), 2962 (1991).
6. H. Volenkle, F. Wittman, and H. Nowotny, Monatsch. Chem. **101**, 46 (1970).
7. S. Hausssuhl, F. Wallrafen, K. Recker, *et al.*, Z. Kristallogr. B **153**, 329 (1980).
8. M. P. Trubitsyn, M. D. Volnyanskiĭ, A. Yu. Kudzin, *et al.*, Fiz. Tverd. Tela (Leningrad) **34** (6), 1746 (1992).
9. M. P. Trubitsyn, M. D. Volnyanskiĭ, and A. Yu. Kudzin, Kristallografiya **36** (6), 1472 (1991).
10. A. Abragam, *The Principles of Nuclear Magnetism* (Oxford, 1961, IL, 1963).
11. F. Schwabl, Phys. Rev. Lett. **28** (8), 500 (1972).
12. H. Stanley, *Introduction to Phase Transitions and Critical Phenomena* (Pergamon, 1971; Mir, Moscow, 1973).
13. Th. Waldkirch, K. A. Muller, and W. Berlinger, Phys. Rev. B **7** (3), 1052 (1973).
14. G. F. Reiter, W. Berlinger, K. A. Muller, *et al.*, Phys. Rev. B: Condens. Matter **21** (1), 1 (1980).
15. M. P. Trubitsyn, M. D. Volnyanskiĭ, A. Yu. Kudzin, *et al.*, Fiz. Tverd. Tela (Leningrad) **40** (1), 111 (1998).
16. M. P. Trubitsyn, Fiz. Tverd. Tela (Leningrad) **40** (1), 114 (1998).
17. A. Brause and R. Cowley, *Structural Phase Transitions* (Taylor and Francis, London, 1981; Mir, Moscow, 1984).
18. E. Sandvold and E. Courtens, Phys. Rev. B: Condens. Matter **27** (9), 5660 (1983).
19. M. J. Tello, M. A. Pérez-Jubindo, and A. López-Echarri, Solid State Commun. **50** (11), 957 (1984).

Translated by L. Man

Crystallography Reports, Vol. 45, No. 1, 2000, pp. 122–127. Translated from Kristallografiya, Vol. 45, No. 1, 2000, pp. 128–133.

PHASE TRANSITIONS

Gorsky–Bragg–Williams Theory of Phase Transitions in the Approximants of Icosahedral Quasicrystals

V. A. Chizhikov

Shubnikov Institute of Crystallography, Russian Academy of Sciences, Leninskiĭ pr. 59, Moscow, 117333 Russia

Received April 13, 1999

Abstract—The Gorsky–Bragg–Williams (GBW) theory has been modified to describe phase transitions caused by the ordering of two kinds of atoms in the even and the odd sublattices of the structures of icosahedral quasicrystals with the dodecahedral local order (DLO) and their approximants. The modified method is exemplified by numerical calculations of such phase transitions in the structures of several simplest approximants. © *2000 MAIK "Nauka/Interperiodica".*

INTRODUCTION

In 1984, Shechtman, Bleach, Gratias, and Cahn obtained diffraction patterns with a system of sharp Bragg reflections characterized by the icosahedral symmetry from the $Al_{86}Mn_{14}$ alloy [1]. They came to the following conclusions: (a) the point symmetry of the alloy is inconsistent with the periodicity, and (b) the narrow sharp diffraction reflections indicate the existence of the long-range order in the alloy. Prior to the publication of these results, diffraction patterns with Bragg reflections were usually interpreted as an indication of the existence of the translation symmetry in the crystals. Therefore it was assumed that the $Al_{86}Mn_{14}$ alloy has a certain "latent" symmetry similar to periodicity. Such a symmetry received the name of quasiperiodicity. The $Al_{86}Mn_{14}$ alloy and other similar substances were called icosahedral quasicrystals [2–5].

At present, the ideal structure of a quasicrystal is usually modeled by the projection method in which the sites of atom location in the substance are determined as points of the intersection of the physical space and the three-dimensional atomic surfaces normal to this space in a certain six-dimensional supraspace in which these atomic surfaces form a certain six-dimensional hypercubic lattice [3–5]. The direction of the physical space on the basis of the six-dimensional lattice is irrational and is determined from the condition of the existence of the icosahedral symmetry. Another method of derivation of an ideal quasilattice is based on a postulate about the existence of a certain local order, e.g., a dodecahedral local order (DLO) in the arrangement of atoms. Such an order is characterized by the location of the nearest neighbors of each atom at several vertices of a dodecahedron whose center coincides with this atom [6, 7]. The dodecahedral local order can be considered as the microscopic interpretation of the projection method. Therefore it was used for the creation of a realistic model of quasicrystal growth [8, 9]. Using the DLO concept, one can also model approximants—crystals with large unit cells whose microstructures are close to those of quasicrystals. In order to describe the approximants by the projection method, the corresponding physical space should be rationally inclined with respect to the basis of the six-dimensional lattice.

It was established that the Bragg reflections of the diffraction pattern from an icosahedral quasicrystal can be indexed using six conventional Miller indices [2, 3]. Then, the basis of the reciprocal lattice is represented by six vectors connecting the center of an icosahedron with its vertices. The reciprocal lattice in this basis can be a six-dimensional primitive, face- or body-centered hypercubic lattice [10–12]. Using the analogy with cubic crystals, icosahedral quasicrystals with such reciprocal lattices can be called primitive, body-, and face-centered icosahedral quasicrystals.

Below, we consider a phase transition from a primitive icosahedral quasicrystal (or its approximant) to a face-centered icosahedral quasicrystal (or its approximant). The preliminary results were published elsewhere [13].

TRANSITIONS BREAKING THE SYMMETRY RELATING THE EVEN AND THE ODD SUBLATTICES

The motif most often encountered in quasicrystals and approximants is that of the dodecahedral local order (DLO) [6, 7]. Earlier [14], it was shown that the DLO-structure can be considered as consisting of two sublattices with any two neighboring atoms in the structure belonging to different sublattices. These sublattices are equivalent if the symmetry group of the quasicrystal includes a symmetry element providing the interchange of these sublattices. A simple quasicrystal and those of its approximants which belong to the space groups $Pa\bar{3}$, $Im\bar{3}$, $I23$, $Pn\bar{3}$, and $I2_13$ have the equiva-

1063-7745/00/4501-0122$20.00

lent sublattices [14]. One of the possible micromechanisms of a phase transition from a primitive to a face-centered quasicrystal (or their approximants) proceeds via ordering in the equivalent sublattices built by atoms of different kinds. In the phenomenological approximation, this transition can be described as the change in the symmetry of a certain density function $\rho(\mathbf{r})$ [15, 16], which, in the vicinity of the critical point, can be written as

$$\rho(\mathbf{r}) = \rho_s(\mathbf{r}) + \delta\rho_a(\mathbf{r}), \tag{1}$$

where $\rho_s(\mathbf{r})$ and $\delta\rho_a(\mathbf{r}) = \eta g(\mathbf{r})$ are the symmetric and antisymmetric components of this function with respect to the interchange of the sublattices. The expansion of the free energy into a series with respect to a small parameter η has the form

$$F = F_0 + ak_B(T - T_c)\eta^2 + b\eta^4, \tag{2}$$

where T_c is the temperature of the second-order phase transition.

THE GORSKY–BRAGG–WILLIAMS APPROXIMATION

Unlike the phenomenological Landau theory with emphasis on the change of the symmetry during phase transformations, the Gorsky–Bragg–Williams approximation is focused on possible microstructural factors that may cause phase transitions and are associated with atomic ordering in alloys [17–19]. The simplest example is a binary AB alloy with equal concentrations of both components (the number of atoms of each kind are equal to $N/2$, with the total number of all the atoms in the crystal being N). The atoms are located at the sites of a certain lattice which can be divided into two equivalent sublattices, α and β, with the α-sites being surrounded with the β-sites and *vice versa*. The degree of the alloy order is characterized by fractions of atoms of kind A in the α and the β sublattices, f^α and f^β, respectively. From the condition of equal concentrations of both kinds of atoms, it follows that $f^\beta = 1 - f^\alpha$. In a completely disordered phase, $f^\alpha = f^\beta = 1/2$.

The energy of such an alloy is determined in the approximation of interactions between the nearest neighbors. The interaction energies for the AA, BB, and AB pairs are denoted as $-v_{AA}$, $-v_{BB}$, and $-v_{AB}$, respectively. Then, an ordering phase transition can occur only if the energy of ordering, $v = (v_{AB} - (v_{AA} + v_{BB})/2)$, is positive.

The free energy can be written in terms of the total energy and the entropy as

$$F = E - TS, \tag{3}$$

$$\begin{aligned} S &= k_B \ln W \\ &= -k_B \sum_{p \in \{\alpha, \beta\}} (N/2)(f^p \ln f^p + \bar{f}^p \ln \bar{f}^p), \end{aligned} \tag{4}$$

where W is the number of possible ways of arranging the $f^\alpha(N/2)$ A atoms at the sites of the α-sublattice, and the $f^\beta(N/2)$ A atoms at the sites of the β-sublatice, $\bar{f} = 1 - f$. Thus, the Bragg–Williams approximation reduces to the substitution of the total energy by the energy averaged over the configuration at the given value of f^α, namely

$$\begin{aligned} E = -(N/2)z(&v_{AA} f^\alpha f^\beta + v_{BB} \bar{f}^\alpha \bar{f}^\beta \\ &+ v_{AB}(f^\alpha \bar{f}^\beta + \bar{f}^\alpha f^\beta)), \end{aligned} \tag{5}$$

where z is the number of the nearest neighbors of each site. The thermodynamic equilibrium is determined by the minimum free energy. At the point of a phase transition, $\dfrac{\partial^2 F}{(\partial f^\alpha)^2} = 0$, which allows one to determine the temperature of the phase transition as

$$\frac{k_B T_c}{2v} = \frac{z}{4}. \tag{6}$$

The GBW theory described above can be directly applied to those structures, where all the sites have the same number of the nearest neighbors, e.g., to the DLO-structures of the CsCl ($z = 8$) and the FeSi ($z = 7$) types.

THE MODIFIED GORSKY–BRAGG–WILLIAMS APPROXIMATION

In more complicated structures, different sites have different numbers of nearest neighbors. Moreover, the sites with the equal numbers of nearest neighbors within the first coordination sphere can have different numbers of neighbors within the following coordination spheres. Generally speaking, in quasicrystals, the position of each site is unique. In the corresponding approximants, the numbers of various types of sites are limited by the number of atoms in the unit cell. Below, we consider the necessary modification of the GBW approximation which takes into account the nonequivalence of the lattice sites.

As earlier, consider a binary alloy with equal concentrations of the atoms of kinds A and B occupying the sites of a certain lattice with two equivalent sublattices. It is possible to select several types of sites in these sublattices in such a way that any two sites of one type would be crystallographically equivalent. The lattice is characterized by the number N_i of sites of type i in each of the sublattices and the number N_{ij} of bonds between the sites of the type i of one sublattice with the sites of

the type j of the other sublattice. These numbers are related as $\Sigma_j N_{ij} = z_i N_i$, where z_i is the number of the nearest neighbors for a site of the ith type. In a crystal, one can consider the numbers N_i and N_{ij} for one unit cell. Then the state of the alloy under study is determined by the probabilities f_i^α and f_i^β to encounter atoms A at the sites of type i in the sublattices α and β, which can be determined from the condition of the minimum free energy and an additional condition that

$$\sum_i N_i(f_i^\alpha + f_i^\beta) = \sum_i N_i, \tag{7}$$

which signifies that the concentrations of the A and B atoms are equal. The energy and the entropy are given by the expressions similar to (5) and (4)

$$\begin{aligned} E = -\sum_{ij} N_{ij}(&v_{AA} f_i^\alpha f_j^\beta + v_{BB}\bar{f}_i^\alpha \bar{f}_j^\beta \\ &+ v_{AB}(f_i^\alpha \bar{f}_j^\beta + \bar{f}_i^\alpha f_j^\beta)), \end{aligned} \tag{8}$$

$$S = -k_B \sum_{i,\, p \in \{\alpha,\beta\}} N_i(f_i^p \ln f_i^p + \bar{f}_i^p \ln \bar{f}_i^p). \tag{9}$$

Since any thermodynamically equilibrium state is characterized by the minimum free energy, it is possible to increase the free energy by a value determined by the constant combination of the probabilities $\Lambda\Sigma_{i,p} N_i f_i^p$ and to assume that all f_is are independent variables. Then the condition of the extreme free energy is determined by the equalities

$$\begin{cases} \dfrac{\partial F}{\partial f_i^\alpha} = 2v\sum_j N_{ij} f_j^\beta \\ \quad + N_i(\Lambda + z_i d + k_B T \ln(f_i^\alpha/\bar{f}_i^\alpha)) = 0 \\ \dfrac{\partial F}{\partial f_i^\beta} = 2v\sum_j N_{ij} f_j^\alpha \\ \quad + N_i(\Lambda + z_i d + k_B T \ln(f_i^\beta/\bar{f}_i^\beta)) = 0, \end{cases} \tag{10}$$

where $d = ((v_{BB} - v_{AA})/2 - v)$.

Now, we can pass to new variables $f_i^+ = (f_i^\alpha + f_i^\beta)/2$ and $f_i^- = (f_i^\alpha - f_i^\beta)/2$. At temperatures exceeding the critical one, $f_i^\alpha = f_i^\beta$ and the equilibrium condition takes the form

$$\begin{cases} f_i^- = 0 \\ \dfrac{\partial F}{\partial f_i^+} = 2v\sum_j N_{ij} f_j^+ \\ \quad + N_i(\Lambda + z_i d + k_B T \ln(f_i^+/\bar{f}_i^+)) = 0 \end{cases} \tag{11}$$

with the positively-defined matrix of coefficient before the second-order terms in the expansion of the free energy. The corresponding matrix has the form

$$\begin{pmatrix} 2vR^+(T) & 0 \\ 0 & 2vR^-(T) \end{pmatrix},$$

$$\begin{aligned} 2vR^+ &= \frac{1}{2}\left\| \frac{\partial^2 F}{\partial f_i^+ \partial f_j^+} \right\| \\ &= \left\| 2vN_{ij} + k_B T \delta_{ij} N_i \left(\frac{1}{f_i^+} + \frac{1}{1 - f_i^+} \right) \right\|, \\ 2vR^- &= \frac{1}{2}\left\| \frac{\partial^2 F}{\partial f_i^- \partial f_j^-} \right\| \\ &= \left\| -2vN_{ij} + k_B T \delta_{ij} N_i \left(\frac{1}{f_i^+} + \frac{1}{1 - f_i^+} \right) \right\|. \end{aligned} \tag{12}$$

At the transition point, the matrix is not positively defined any more and the determinant at the transition point is equal to zero (see Appendix 1), which fact allows one to determine the transition temperature. In the case of a phase transition of the two structure sublattices making them nonequivalent, the critical temperature is determined from the equality

$$\begin{aligned} &\det R^-(T_c) \\ &= \det\left\| -N_{ij} + (k_B T_c/(2v))\delta_{ij} N_i L_i^{(1)} \right\| = 0, \end{aligned} \tag{13}$$

where $L_i^{(1)} = ((f_i^+(T_c))^{-1} + (1 - f_i^+(T_c))^{-1})$.

In order to compare the GBW and the phenomenological theories, we have to represent the antisymmetric component of the density function in the form

$$\delta\rho_a(\mathbf{r}) = \sum_{i,k} f_i^-(\delta(\mathbf{r} - \mathbf{r}_{ik}^\alpha) - \delta(\mathbf{r} - \mathbf{r}_{ik}^\beta)), \tag{14}$$

where $\mathbf{r}_{ik}^\alpha$ and $\mathbf{r}_{ik}^\beta$ are the coordinates of the kth sites of the type i in the α and β sublattices. The final step necessary for comparing these theories is the representation of the free energy given by (3), (8), and (9) in form (2) (see Appendix 2).

CALCULATION OF TRANSITION TEMPERATURES

Now calculate the dependence of the temperature of a phase transition on the energy of the pair interactions of the nearest neighbors in a crystal. With this aim, we use condition (13) obtained in the previous section. Consider, e.g., the AlPd alloy having three modifications in the vicinity of the point of equal concentrations of Al and Pd atoms, cubic crystals of the CsCl- and the

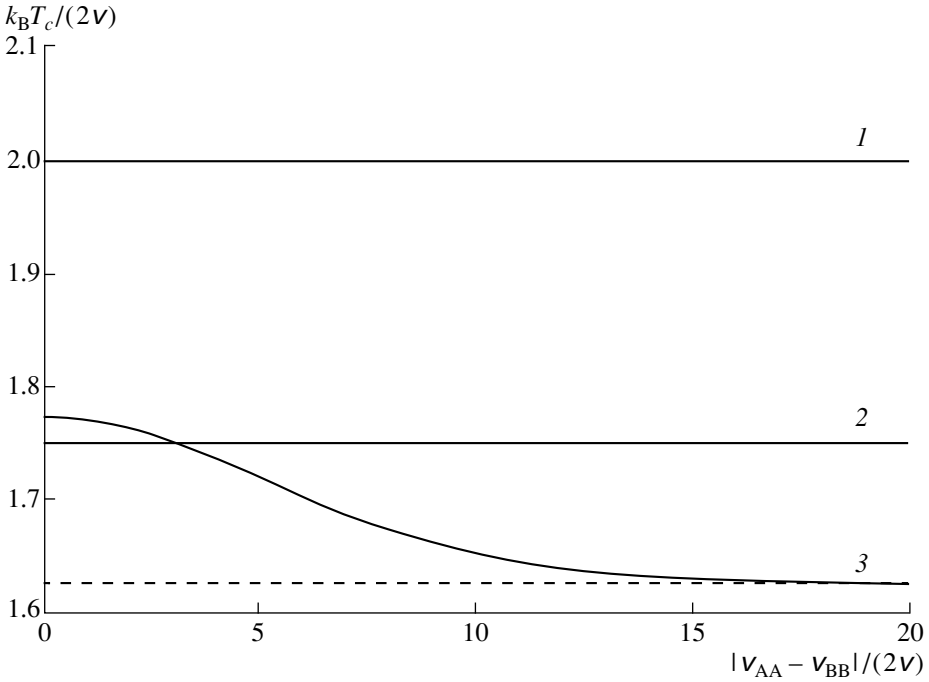

Fig. 1. Dependence of the temperature T_c of the ordering phase transition on the pair-interaction energies $-v_{AA}$, $-v_{BB}$, and $-v_{AB}$ calculated for the structures of the types (*1*) CsCl ($Im\bar{3}m$) and (*2*) FeSi ($Pa\bar{3}$) by the GBW method and (*3*) for the structure of the AlPd-type ($R\bar{3}$) by the modified GWB method; $v = v_{AB} - (v_{AA} + v_{BB})/2$ is the energy of ordering.

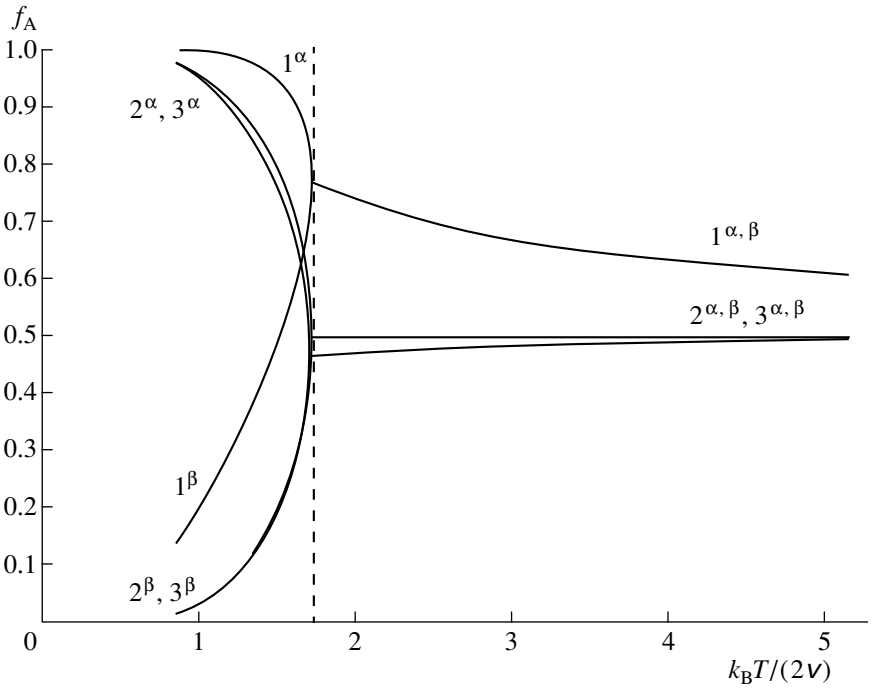

Fig. 2. Temperature dependences of the probabilities f_A to encounter the atoms of kind A at the sites of the first, second, and third kinds in the α- and β-sublattices of the AlPd-type structures ($R\bar{3}$) calculated by the modified GBW method at the interaction constant $(v_{BB} - v_{AA})/(2v) = 5.0$. The vertical dashed line corresponds to the point of the second-order phase transition.

FeSi-types described by the space groups $Pm\bar{3}m$ and $P2_13$, and a rhombohedral crystal described by the sp. gr. $R\bar{3}$. All these crystals are characterized by a certain DLO and have two symmetric sublattices, the first one being filled with Al atoms and the second one, with Pd atoms (the AlPd alloy). Therefore possible phase transitions to these phases from the phases with the equivalent sublattice characterized by higher symmetries [space groups $Im\bar{3}m$, $Pa\bar{3}$, and $R\bar{3}$ (the latter with the smaller unit cell)] can be studied by the GBW method. The dependence of T_c on the constants of pair interactions is shown in Fig. 1. In this example, both cubic crystals consists of only one type of site in each sublattice; therefore, they can be studied by the conventional GBW method. The AlPd alloy ($R\bar{3}$) has three types of sites:

$(N_1, N_2, N_3) = (1, 6, 6)$, $(z_1, z_2, z_3) = (8, 7, 7)$, and

$$||N_{ij}|| = \begin{pmatrix} 2 & 6 & 0 \\ 6 & 24 & 12 \\ 0 & 12 & 30 \end{pmatrix}. \quad (15)$$

If $v_{AA} = v_{BB}$, then $k_BT_c/(2v) = \langle z\rangle/4$, where $\langle z\rangle$ is the arithmetic mean of the numbers of the nearest neighbors for all the atoms. If $(v_{AA} - v_{BB})/(2v) \longrightarrow \infty$, then $k_BT_c/(2v) \longrightarrow 1.6192$.

In addition to the transition temperature, one can also calculate the temperature dependence of the probabilities f_i using equation (7) and (10). The typical dependence calculated for the parameter $(v_{AA} - v_{BB})/(2v) = 5.0$ is shown in Fig. 2.

DISCUSSION

The modified GBW approximation suggested in this article is an approximate method for studying the thermodynamic properties of alloys in the vicinity of the phase transition based on a number of assumptions about the character of atomic interactions, etc. Although the method cannot be used for reliable quantitative estimates, it yields rather good qualitative results. Consider, e.g., the dependence of the phase-transition temperature on the energy of pair interactions for the AlPd alloy (sp. gr. $R\bar{3}$). If $v_{AA} = v_{BB}$, then the critical temperature is determined by formula (6) obtained for the case, where all the atoms have the same number of nearest neighbors. The change of the v_{AA}/v_{BB} ratio results in a decrease of the phase-transition temperature, which is explained by the fact that, in the absence of phase transitions, the system acquires the additional possibility of lowering its free energy. The probability of encountering atoms of different kinds at the structure sites differs from 1/2 still at temperatures exceeding the critical one (Fig. 2). Thus, if $v_{AA} > v_{BB}$, the AA bond becomes energetically more advantageous that the BB bond. Therefore the atoms of kind A have the tendency to fill the sites with the maximum number of the nearest neighbors.

The ordering mechanism considered in this study was experimentally observed for compounds of the CsCl type. In complicated structures such as those of quasicrystals and high-order approximants, one can hardly expect ordering at all the sites without structural changes. A more realistic mechanism for such structures is the ordering of atoms of various kinds only at a small number of their sites, whereas all the other sites of the structure can be filled with atoms of the third kind. The role of the sites at which the ordering process occurs can also be played by the so-called icosahedral holes.

Second-order phase transitions occur in primitive quasicrystals and their approximants. For crystals, the necessary condition for occurrence of such transitions is the existence of two equivalent sublattices. This condition is automatically met for approximants described by some specific space groups. The approximants described by other space groups (e.g., by the sp. gr. $Pm\bar{3}$) have *a priori* nonequivalent sublattices. However, one cannot exclude the possibility that some of these crystals are the approximants of primitive quasicrystals. If these crystals have sufficiently large unit cells, their physical properties should be close to the properties of quasicrystals. In particular, these approximants can undergo "pseudotransitions" corresponding to the transitions from primitive approximants to the approximants of face-centered quasicrystals. Similar to second-order phase transitions, these pseudotransitions occurring without the change in the symmetry (the space group) should be accompanied by an anomalous jump in the heat capacity, whereas the corresponding diffraction patterns should show drastic changes in the intensities of some reflections.

APPENDIX 1

The necessary and sufficient condition of positive definability of a certain matrix A is its representation in the form $A = C^TC$, where C is a nondegenerate matrix. Therefore the matrix A stops being positively defined at the moment when the matrix C becomes degenerate; i.e., $\det C = 0$. However, $\det A = (\det C)^2$, and therefore the determinant of the matrix A becomes zero at the point where this matrix stops being positively defined.

APPENDIX 2

In the vicinity of the phase transition, the antisymmetric component of the density function is determined by the following probabilities:

$$f_i^- = \eta g_i + O(|T - T_c|)^{3/2}, \quad R^-\mathbf{g} = 0, \quad |\mathbf{g}| = 1, \quad (16)$$

where η is the order parameter. Performing minimization with respect to f_i^+ and expanding the density function into a Taylor series with respect to a small parameter η, one can reduce the free energy to form (2) with the coefficients

$$a = \left(\frac{k_B T_c}{2v}\right)\sum_{ij} N_i L_i^{(2)} g_i^2 K_{ij} N_j L_j^{(0)},$$

$$b = (k_B T_c)\left[-\frac{1}{2}\sum_i N_i L_i^{(3)} g_i^4 + 2\left(\frac{k_B T_c}{2v}\right)\sum_{ij} N_i L_i^{(2)} g_i^2 K_{ij} N_j L_j^{(2)} g_j^2\right], \quad (17)$$

where

$$K_{ij} = (R^+(T_c))_{ij}^{-1} - \frac{\Sigma_{mn}(R^+(T_c))_{im}^{-1} N_m N_n (R^+(T_c))_{nj}^{-1}}{\Sigma_{mn} N_m (R^+(T_c))_{mn}^{-1} N_n}, \quad (18)$$

$$L_i^{(n)} = \frac{1}{n!}\frac{d^n}{(dx)^n}\ln\frac{x}{1-x}, \quad x = f_i^+(T_c).$$

ACKNOWLEDGMENTS

I am grateful to V. E. Dmitrienko for numerous useful discussions and valuable remarks. The study was supported by the Russian Foundation for Basic Research, project no. 95-02-05746-a.

REFERENCES

1. D. Shechtman, I. Blech, D. Gratias, *et al.*, Phys. Rev. Lett. **53**, 1951 (1984).
2. D. Levine and P. J. Steinhardt, Phys. Rev. Lett. **53**, 2477 (1984).
3. P. A. Kalugin, A. Yu. Kitaev, and L. S. Levitov, Pis'ma Zh. Éksp. Teor. Fiz. **41**, 145 (1985).
4. M. Duneau and A. Katz, Phys. Rev. Lett. **54**, 2688 (1985).
5. V. Elser, Phys. Rev. Lett. **54**, 1730 (1985).
6. V. E. Dmitrienko, Acta Crystallogr., Sect. A: Found. Crystallogr. **50**, 515 (1994).
7. V. E. Dmitrienko, Mater. Sci. Forum **151**, 199 (1994).
8. V. E. Dmitrienko and S. B. Astaf'ev, JETP Lett. **61**, 331 (1995).
9. V. E. Dmitrienko and S. B. Astaf'ev, Phys. Rev. Lett. **75**, 1538 (1995).
10. T. Janssen, Acta Crystallogr., Sect. A: Found. Crystallogr. **42** (2), 61 (1986).
11. D. S. Rokhsar, N. D. Mermin, and D. C. Wright, Phys. Rev. B: Condens. Matter. **35**, 5487 (1987).
12. L. S. Levitov and J. Rhyner, J. Phys. (Paris) **49**, 1853 (1988).
13. V. A. Chizhikov and V. E. Dmitrienko, in *Proceedings of Int. Conf. on Aperiodic Crystals, Aperiodic'97* (1997), p. 581.
14. V. A. Chizhikov, Kristallografiya **44** (5), 814 (1999) [Crystallogr. Rep. **44**, 755 (1999)].
15. L. D. Landau, Zh. Éksp. Teor. Fiz. **7**, 19 (1937).
16. L. D. Landau and E. M. Lifshitz, *Theoretical Physics. vol. 5. Statistical Physics* [in Russian] (Nauka, Moscow, 1975; Pergamon, New York, 1980), Chap. 14.
17. W. Gorsky, Z. Phys. **50**, 64 (1928).
18. W. L. Bragg and E. J. Williams, Proc. R. Soc. London A: **145**, 699 (1934).
19. T. Muto and Y. Takagi, *The Theory of Order–Disorder Transitions in Alloys* (Academic, New York, 1955; IL, Moscow, 1959).

Translated by L. Man

Crystallography Reports, Vol. 45, No. 1, 2000, pp. 128–132. Translated from Kristallografiya, Vol. 45, No. 1, 2000, pp. 134–138.

Valence States and Coordination of Titanium Ions in Beryl Crystals

V. P. Solntsev and A. M. Yurkin

Institute of Mineralogy and Petrography, Siberian Division, Russian Academy of Sciences, Universitetskiĭ pr. 3, Novosibirsk, 630090 Russia

Received July 28, 1997

Abstract—The valence states and coordination of titanium ions in beryl crystals grown from flux and by gas-transport reactions have been studied by the methods of electron paramagnetic resonance (EPR) and optical spectroscopy. The parameters of the EPR spectra for Ti^{3+} in the Al^{3+} and Si^{4+} sites are determined. It is found that at concentrations exceeding 0.1–0.15 wt %, the EPR-spectra have additional lines due to exchange-bonded pairs of Ti^{3+} ions. It is shown that the two-humped absorption band with the maxima at 495 (π), 545 (π), and 495 (σ) nm are formed due to Ti^{3+} ions located in the octahedral position. *© 2000 MAIK "Nauka/Interperiodica".*

INTRODUCTION

The latest achievement in the studies of $BeAl_2O_4 : Cr^{3+}$ [1], Ti^{3+} [2], and $Be_3Al_2Si_6O_{18} : Cr^{3+}$ [3] tunable lasers have stimulated investigation of titanium-doped beryl ($Be_3Al_2Si_6O_{18}$). The preliminary EPR and absorption spectra data [4] for titanium-doped beryls grown from flux indicate the existence of two valence states of Ti ions occupying two different structural sites. In the present paper, we studied the EPR and electron spectra of the optical absorption of Ti^{3+} ions in synthetic beryls. The crystals were grown by the method of gas-transport reactions [5] and from flux [6]. The titanium content in the specimens attained 0.0–2.1 and 0.0–0.3 wt % in the gas-transport reactions and in growth from flux, respectively. The EPR spectra were studied at a frequency of 9.3 GHz and at temperatures of 300 and 77 K. The polarized absorption spectra were recorded on the plates cut off parallel to the $\{10\bar{1}0\}$ face at 300 K on an SF-20 spectrophotometer.

EXPERIMENTAL RESULTS

When the titanium content in the specimen (up to 0.1 wt. % TiO_2), the EPR spectra had a single fine-structure line ($S = 1/2$) attributed to Ti^{3+} in the Al^{3+} site (Fig. 1a, Ti^{3+}_{Al}). The spectral parameters are close to those of Ti^{3+} in natural beryl [7].

The spectra from beryls with high TiO_2 content (0.3 wt % and higher) showed the presence of two additional weak centers, I and II, described by $S = 1$ (Fig. 1c) and possessing one and three magnetic complexes per unit cell, respectively. The analysis of the angular dependence of the above centers and their characteristic dependence on Ti concentration indicate that these centers correspond to different pairs of Ti^{3+}_{Al} ions with the dipole–dipole and exchange interactions. Center I is associated with the $Ti^{3+}_{Al}-Ti^{3+}_{Al}$ pairs located along the *c*-axis and spaced by the distance $r = 4.597$ Å. The symmetry of this pair is C_{3h}. Center II is formed by the perpendicular $Ti^{3+}_{Al}-Ti^{3+}_{Al}$ pairs (Ti^{3+} ions occupy two closest Al sites in the (0001) plane with $r = 5.319$ Å, $\theta = 90°$, the symmetry of the pair is D_2). The radius-vectors of such pairs form angles of 120° in the (0001) plane.

The EPR spectra of centers I and II are described by the Hamiltonian

$$\hat{H} = \hat{H}_0(\mathrm{I}) + \hat{H}_0(\mathrm{II}) + JS_1S_2 + D(3S_{1z}S_{2z} - S_1S_2) + \hat{H}_{\mathrm{HFS}},$$

where $S_1 = S_2 = 1/2$; $\hat{H}_0(\mathrm{I}) + \hat{H}_0(\mathrm{II})$ is the part of the Hamiltonian that takes into account the energy of isolated ions, and JS_1S_2 describes the isotropic exchange interaction. The two last terms describe the anisotropic and hyperfine interactions, respectively. The exchange interactions result in the formation of the singlet and triplet states. Magnetic resonance transitions are allowed only within the triplet [8], which can be considered as a state with the resultant effective spin $S = 1$. The anisotropic interaction causes the zero-field splitting of the triplet. Therefore, the EPR spectrum shows two transitions. Knowing the interval between these transitions, one can calculate D for pairs I and II by the formula $D_{\mathrm{dip}} = -\beta(2g_{\parallel} + g_{\perp})/2r^3$ [8] under the assumption of pure dipole–dipole interactions ($D_{\mathrm{dip}}(\mathrm{I}) = 271.4$ G; $D_{\mathrm{dip}}(\mathrm{II}) = 179.0$ G). The calculated data are somewhat different from the experimental ones (see table); $D(\mathrm{I}) = 220$ G; $D(\mathrm{II}) = 191.0$ G. This discrepancy

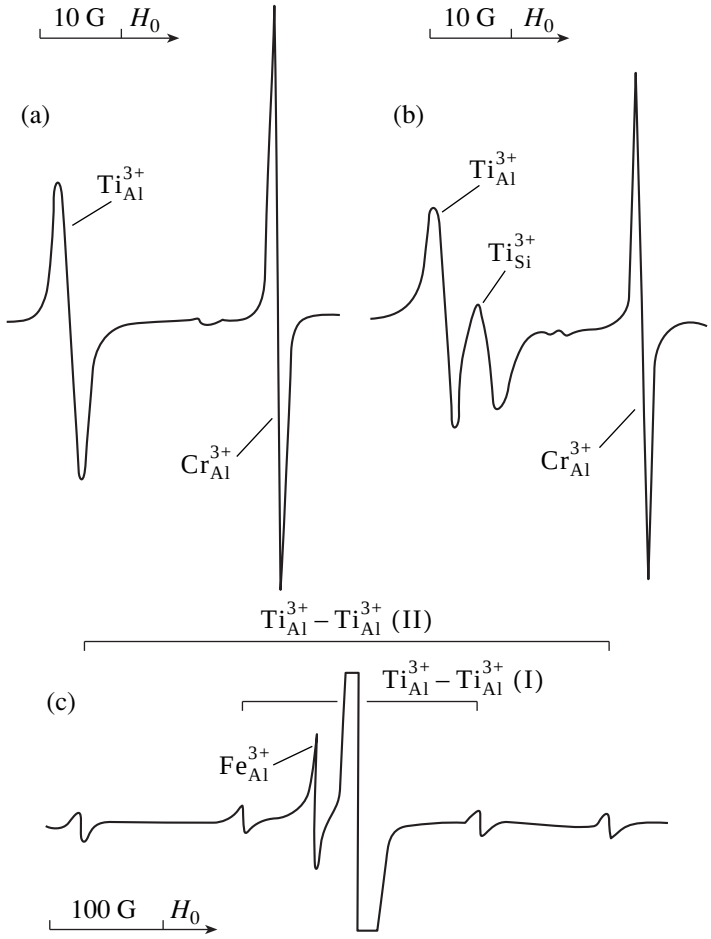

Fig. 1. EPR spectra of Ti^{3+} ions in beryl obtained at $H \parallel c$ and 77 K; (a, b) beryl crystals grown from flux (TiO_2 ~ 0.05 wt %) (a) before and (b) after irradiation; (c) – spectra of the Ti^{3+}–Ti^{3+} ion pairs in beryl grown by the gas-transport reaction (TiO_2 ~ 0.25 wt %). Additional lines on the spectra are attributed to noncontrollable impurities Cr^{3+}_{Al} or Fe^{3+}_{Al}. H_0 is the magnetic field (G).

may be attributed to the effect of the anisotropic exchange ($D_{ex} = D - D_{dip}$). The anisotropic and isotropic exchange constants (D_{ex} and J, respectively) have not been determined, because we did not study the temperature dependence of D and, thus, did not know its sign.

In order to change the charge state of titanium ions in beryl, the specimens with low TiO_2 content (less than 0.1 wt %) were subjected to γ-irradiation (^{60}Co, 2 Mrad, 77 K). After irradiation, beryls grown from flux showed the lines due to Ti^{3+}_{Al} at 77 K and also intense additional lines due to extra centers Al^{2+}_{Be} and O^{-}_{II} and a center consisting of 12 magnetically nonequivalent complexes (K_M = 12) in the unit cell. The former two centers were thoroughly analyzed in [9]. Being heated to 300 K, the crystal emitted crimson light, whereas the intensities of Al^{2+} and O^{-} decreased by a factor of 2–3. After heating, the crystal acquired a yellowish–brown color. The absorption spectrum of the crystals had wide bands with the maxima at 360–390 and at about 530 nm. Heating to 430 K resulted in the annealing of the Al^{2+} and O^{-} centers, the decoloration of crystals, and the disappearance of the absorption bands at 360–390 nm. It was difficult to detect the band at 530 nm against the background of the more intense band at 495–545 nm. At the same time, the intensities of the Ti^{3+}_{Al} centers and the center with K_M = 12 decreased by factors of 1.1 and 1.5, respectively. With the further increase of the temperature to 430–820 K, the intensity of Ti^{3+}_{Al} increased proportionally to a decrease of the intensity due to the center with K_M = 12 (which was annealed at 820 K).

The center with K_M = 12 is described by the Hamiltonian of orthorhombic symmetry with S = 1/2 and the hyperfine structure due to $^{47, 49}Ti$ (Fig. 2) characteristic of Ti^{3+}. At $H \parallel [0001]$, the center is represented by a single line (Ti^{3+}_{Si} center in Fig. 1b). In an arbitrarily ori-

Parameters of the EPR spectra of Ti^{3+} ions in some crystals

Center	g_z	g_y	g_x	A, D	Position	Calculated field V, cm^{-1}	
						weak trigonal	strong trigonal
Beryl, 300 K							
Ti^{3+}_{Al}	1.9887	1.8423	1.8423		$Ti^{3+} \longrightarrow Al^{3+}_6$		
Beryl, 77 K							
Ti^{3+}_{Al}	1.9895	1.8416	1.8416	$A_{\parallel} = -2.0$ $A_{\perp} = 19.5$	$Ti^{3+} \longrightarrow Al^{3+}_6$	−1780	−2564
Ti^{3+}_{Si}	1.9880	1.9073	1.8656	$A_y = 20.5$	$Ti^{3+} \longrightarrow Si^{4+}_4$		
Ti^{3+}_{Al}–Ti^{3+}_{Al} (I)	1.9910	1.8420	1.8420	D(I) = 204.6	$Ti^{3+} \longrightarrow Al^{3+}_6$		
Ti^{3+}_{Al}–Ti^{3+}_{Al} (II)	1.8420	1.9910	1.9910	D(II) = 184.3	$Ti^{3+} \longrightarrow Al^{3+}_6$		
Cordierite, 77 K							
Ti^{3+}_{Mg}	1.9720	1.8050	1.7820		$Ti^{3+} \longrightarrow Mg^{2+}_6$	−1280	−1980
Ti^{3+}_{Al}	1.9947	1.9135	1.9010	$A_y = 21.4$	$Ti^{3+} \longrightarrow Al^{3+}_4$		
Chrysoberyl, 77 K							
$Ti^{3+}(C_S)$	1.9320	1.7480	1.7100		$Ti^{3+} \longrightarrow Al^{3+}_6$	−740	−1500

Note: Subscripts "6" and "4" indicate the coordination numbers of the ion to be substituted. The g-factors were measured with an accuracy of ±0.001. The parameters of hyperfine (A) and fine (D) splittings of Ti^{3+} levels are determined with an accuracy of $\pm 0.5 \times 10^{-4}$ cm^{-1}.

ented magnetic field (H), this line is split into 12 lines. However, twelve lines degenerate into 3 lines in the fields $H \parallel [2\bar{1}\bar{1}0]$ or $[01\bar{1}0]$ and into 6 lines in the $(2\bar{1}\bar{1}0)$, $(01\bar{1}0)$, or (0001) planes. The angular dependence of lines due to the Ti^{3+}_{Si} center in the (0001) plane is shown in Fig. 3. The analysis of the angular dependence of the g-tensor of this center showed that Ti^{3+} is most likely located in the Si^{4+} site. However, we expected that Ti^{3+} ions in this site (Ti^{3+}_{Si}) should have the C_S-symmetry ($K_M = 6$). The Z-axis of each complex should coincide with the [0001] direction, whereas the X_1- and Y_1-axes should lie in the (0001) plane forming the angles of 196° and 106° with the $[2\bar{1}\bar{1}0]$-direction, respectively. The X- and Y-axes of the other complexes are obtained by rotating the axes of the first complex through angles of ±60°, ±120°, and 180°. The experimentally determined directions are fairly close to the expected ones: g_z ($\theta = 7°$, $Y = 6°$), g_x ($\theta = 90°$, $Y = 186°$), and g_Y ($\theta = 83°$, $Y = 96°$). The lowering of the symmetry of the SiO_4-tetrahedron from C_S to C_1 upon the substitution $Ti^{3+} \longrightarrow Si^{4+}$ seems to be caused by the local compensation of the charge in the nearest Al and Be cationic positions.

In the visible range, the absorption spectrum of titanium-doped beryl obtained by gas-transport reactions has a two-humped band (Fig. 4) with the maxima at 495 (π), 545 (π), and 495 (σ) nm. This spectrum is characteristic of a Ti^{3+} ion in the octahedral coordination in which the upper ^2E level of the ion, not split in a trigonal field, is split because of the Jahn–Teller effect and spin-orbital interaction (beryl, corundum) or due to low-symmetry effects and spin-orbital interaction (chrysoberyl, two-humped band with the maxima at 497 and 542 nm [10]). The band intensities (495 and 545 nm) correlate with the intensity of the Ti^{3+}_{Al} center in the EPR spectrum and the density of pinkish–red coloration of the specimens. We failed to detect the bands due to Ti^{3+}_{Si} ions because of the low intensity of the bands due to the Ti^{3+}_{Si} centers in comparison with those due to the Ti^{3+}_{Al} centers and additional absorption in the irradiated specimens. The polarization properties of the Ti^{3+}_{Al} spectrum are explained by the $^2E_{1/2} \longrightarrow {}^2E_{1/2}$ $(\pi + \sigma)$ and $^2E_{1/2} \longrightarrow {}^2E_{3/2}$ (σ) transitions.

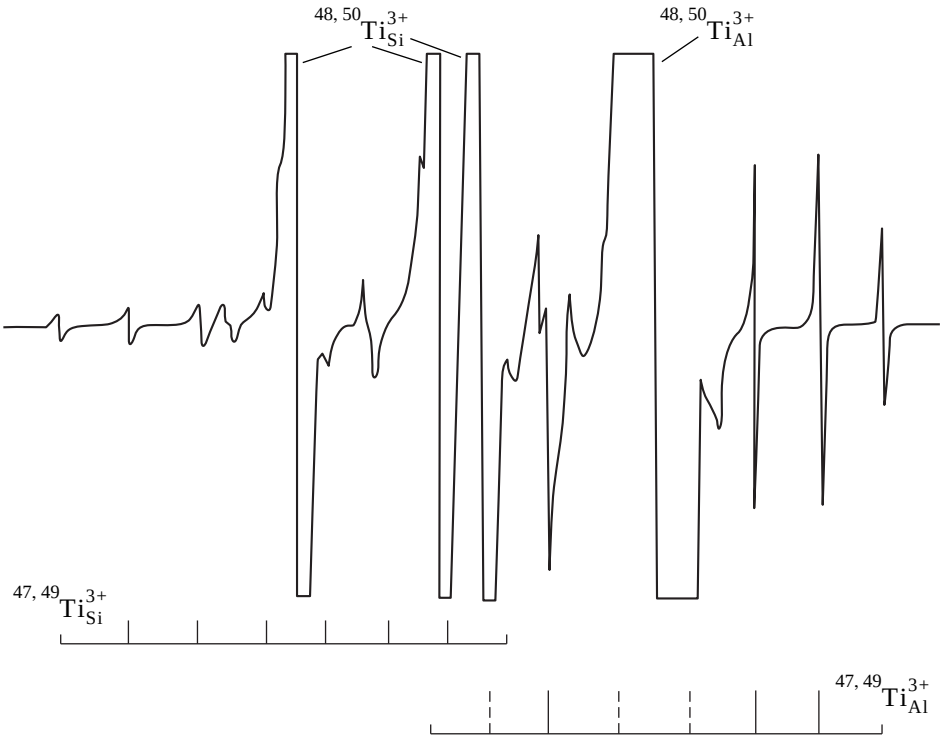

Fig. 2. Hyperfine structure of EPR spectra of Ti^{3+}_{Si} and Ti^{3+}_{Al} ($H \perp c$, 77 K).

ANALYSIS OF PARAMETERS OF ABSORPTION AND EPR SPECTRA

In a trigonal field of the D_3 symmetry, the ^2D term of the Ti^{3+} ion is split into the upper $^2E(e)$ and lower $^2E(t)$ doublets and the $^2A_1(t)$ singlet. The splitting constant for Cr^{3+} in beryl in the trigonal field is known to be negative ($v = -2000$ cm^{-1} [11]). By analogy, the splitting constant for Ti^{3+}, v, should also be negative. Then, the lower level is $^2A_1$. The optical transitions $^2A_1 \longrightarrow {}^2E$ are allowed only for σ-polarization. The spin-orbit interaction provides the splitting of the ^2E levels into $E_{1/2} + E_{3/2}$. In this case, the $^2E_{1/2}(^2A_1) \longrightarrow {}^2E_{1/2}$ and $^2E_{1/2} \longrightarrow {}^2E_{3/2}$ transitions are allowed for π + σ- and σ-polarizations, respectively. The spin-orbital interactions for Ti^{3+} are rather weak ($\lambda = 154$ cm^{-1}), and therefore the splitting of the $^2E(e)$ band (~1850 cm^{-1}) should be attributed to the dynamic Jahn–Teller effect [12].

The negative v value also follows from the analysis of the g-factors for Ti^{3+} in a trigonal field. Indeed, for positive v values and the lower $E_{3/2}$ level, the g-factors are given by the formula: $g_\parallel = 2(1 - P)$, $g_\perp = 0$ [13]. The obtained values are inconsistent with the experimental data, $g_\parallel = 1.9895$, $g_\perp = 1.8416$. In the case of negative v for the $E_{1/2}$ level: $g_\parallel = 2|\sin^2\alpha - (1 - P)\cos^2\alpha|$, $g_\perp = 2|\sqrt{2}\,Q\sin\alpha\cos\alpha + sm^2\alpha|$. The fact that the EPR spectrum of Ti^{3+} was observed at 300 K indicates that the excited levels are located far away from the ground state. Assuming that the trigonal field is strong ($P = 1$, $Q = 3$), one can estimate v using formula (22) from [13],

$$\tan\alpha = -\frac{1}{2\lambda}\left|v + \frac{\lambda}{2} + \left(v^2 + \frac{9}{4}\lambda^2 - v\lambda\right)^{1/2}\right|$$

to obtain $v = -2564$ cm^{-1} (λ was taken to be equal to 120 cm^{-1}). For comparison, the table lists the parameters of the EPR spectrum and the estimated v for octahedral Ti^{3+} complexes in cordierite [14] and chrysoberyl [10]. Apparently, the values obtained should be considered as the upper limit. The estimates of v for Ti^{3+} in beryl, cordierite, and chrysoberyl in the approx-

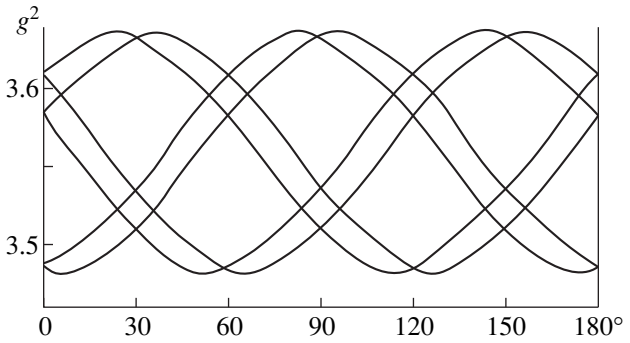

Fig. 3. Angular dependence of EPR lines due to the Ti^{3+}_{Si} center in the (0001) plane.

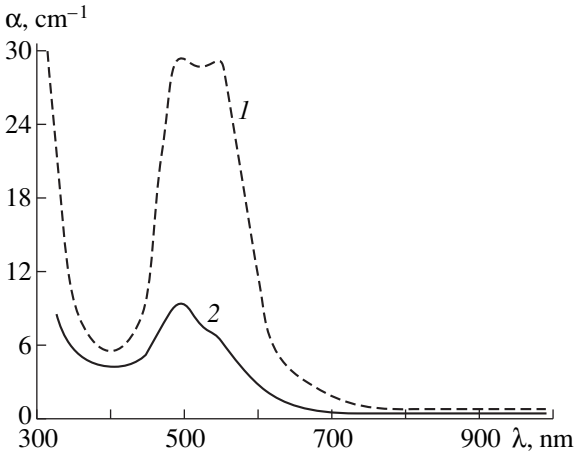

Fig. 4. Absorption spectrum of Ti_{Al}^{3+} in beryl obtained in the polarized light at 300 K: (*1*) π, (*2*) σ-polarization.

imation of a weak trigonal field with due regard of the contribution that comes to the wave function of the ground state from the upper doublet yields –1780, –1280, and –740 cm^{-1}, respectively. These results qualitatively explain the large width of the lines due to Ti^{3+} ions in the EPR spectra of cordierite (~50 G) and chrysoberyl (~70–100 G) in comparison with the corresponding lines in beryl (~10–15 G) at comparable TiO_2 concentrations (0.2 wt %).

Using formula (20) [13], we estimated the distances between the ground and excited levels in the triplet due to Ti^{3+} in beryl at $\nu = -1780$ and -2564 cm^{-1}. These values are $\delta_1(E_{1/2} - E_{1/2})$ 1848, 2529 cm^{-1} and $\delta_2(E_{3/2} - E_{1/2})$ 1709, 2507 cm^{-1} and are within the range of natural lattice vibrations. Qualitatively, the data obtained explain the splitting scheme proposed and the observation of the EPR spectrum of the Ti^{3+} at room temperature.

Thus, the data obtained indicate that the Ti_{Al}^{3+} ions are responsible for absorption in the vicinity of 495 (σ, π) and 545 (π) nm. This fact is adequately interpreted within the splitting scheme of Ti^{3+} levels in the trigonal field with allowance for the Jahn–Teller effect and spin-orbital interactions leading to the lower $E_{1/2}$ ground level in full agreement with EPR spectra.

Our study shows that the Ti impurity can have different valence states (Ti^{3+} and Ti^{4+}) and occupy both the Al and Si sites. It has been established that Ti_{Si}^{3+} can explain the observed nonstoichiometry of beryls. Indeed, all the beryl specimens containing Ti_{Si}^{3+} ions showed an excess in Al. The characteristic compositions of such beryls are 2.97 BeO, 2.05 Al_2O_3, 5.92 SiO_2, and 0.05 TiO_2. Note that the Ti_{Si}^{3+} center was observed in the specimens in which some Be and Si ions were substituted by Al^{3+}. This fact was confirmed by observations upon the irradiation of Al_{Be}^{2+} and O_{II}^{-} centers (the O^- ion stabilized in the vicinity of the Si site occupied by Al) [9]. In other words, the crystal irradiation and annealing result in the charge transfer between the centers according to the scheme

$$Ti_{Al}^{3+} + nTi_{Si}^{4+} + Al_{Be}^{3+} \underset{\text{annealing}}{\overset{\gamma\text{-irradiation}}{\rightleftarrows}} Ti_{Si}^{3+} + (1-n)Ti_{Al}^{3+} + nTi_{Al}^{4+} + Al_{Be}^{2+} + O_{II}^{-}.$$

REFERENCES

1. J. C. Walling, O. G. Peterson, H. P. Jenssen, *et al.*, IEEE J. Quantum Electron. **QE-16**, 1302 (1980).
2. A. I. Alimpiev, G. V. Bukin, V. N. Matrosov, *et al.*, Kvantovaya Élektron. **13** (5), 885 (1986).
3. V. S. Gulev, A. P. Eliseev, V. P. Solntzev, *et al.*, Kvantovaya Élektron. **14** (10), 1990 (1987).
4. V. P. Solntsev, A. Ya. Rodionov, and G. G. Khranenko, *Growth and Properties of Crystals* [in Russian] (Nauka, Novosibirsk, 1988), p. 100.
5. A. Ya. Rodionov and V. S. Pavlyuchenko, *Growth of Crystals of Minerals of the Beryl Group and Study of Their Properties* [in Russian] (Novosibirsk, 1980), p. 62.
6. G. G. Khranenko and V. P. Solntsev, *Growth and Properties of Crystals* [in Russian] (Nauka, Novosibirsk, 1988), p. 88.
7. L. V. Bershov, Zh. Strukt. Khim. **10**, 141 (1969).
8. A. Abragam and B. Bleaney, *Electron Paramagnetic Resonance of Transition Ions* (Oxford, Clarendon, 1970).
9. V. P. Solntsev, *Studies on Theoretical and Genetic Mineralogy* [in Russian] (Nauka, Novosibirsk, 1981), p. 92.
10. V. P Solntsev, V. N. Matrosov, and E. G. Tsvetkov, Zh. Prikl. Spektrosk. **37**, 839 (1982).
11. R. M. Macfarlane, Phys. Rev. **1**, 989 (1970).
12. R. M. Macfarlane, J. Y. Wong, and M. D. Stuge, Phys. Rev. **166**, 250 (1968).
13. D. K. Rey, Fiz. Tverd. Tela (Leningrad) **3** (9), 2525 (1961).
14. V. P Solntsev, T. V. Demina, and M. A. Mikhailov, *X-ray and Molecular Spectroscopy of Minerals* [in Russian] (Nauka, Novosibirsk, 1985), p. 121.

Translated by A. Darinskiĭ

Crystallography Reports, Vol. 45, No. 1, 2000, pp. 13–20. Translated from Kristallografiya, Vol. 45, No. 1, 2000, pp. 19–26.

STRUCTURES OF INORGANIC COMPOUNDS

Crystal Structures of Double Calcium and Alkali Metal Phosphates $Ca_{10}M(PO_4)_7$ (M = Li, Na, K)

V. A. Morozov*, A. A. Belik*, R. N. Kotov*, I. A. Presnyakov*, S. S. Khasanov, and B. I. Lazoryak***

** Moscow State University, Vorob'evy gory, Moscow, 119899 Russia*

*** Institute of Solid State Physics, Russian Academy of Sciences, Chernogolovka, Moscow oblast, 142432 Russia*

Received October 22, 1997

Abstract—Crystal structures of double calcium and alkali metal phosphates described by the general formula $Ca_{10}M(PO_4)_7$ (M = Li, Na, K) have been studied by the Rietveld method. The lattice parameters are a = 10.4203(1) and c = 37.389(1) Å (for M = Li), a = 10.4391(1) and c = 37.310(1) Å (for M = Na), and a = 10.4229(1) and c = 37.279(2) Å (for M = K); sp. gr. $R3c$, Z = 6. The specific features of the distribution of alkali metal cations over the structure positions are discussed. © *2000 MAIK "Nauka/Interperiodica".*

INTRODUCTION

Double calcium and alkali metal phosphates described by the general formula $Ca_{10}M(PO_4)_7$ [M = Li (**I**), Na (**II**), and K (**III**)] are crystallized in the trigonal system [1] and are isostructural to β-$Ca_3(PO_4)_2$ [2]. The variations of the unit-cell parameters and the volumes (a, c, and V) as functions of the radius of the alkali metal cation for these compounds are similar to the variations of these parameters for the compounds of the composition $Ca_9MgM(PO_4)_7$ (M = Li, Na, K) [3]. The IR-spectroscopy [3], luminescence [4], and Mössbauer spectroscopy [5] data indicate that chemical bonding in the compounds described by the general formula $Ca_9M^{2+}M(PO_4)_7$ (where M^{2+} = Ca, Mg and M = Li, Na, K) are of different natures. The intensity and the number of bands on the IR and luminescence spectra of these phases depend on the size of the alkali metal cation [3, 4]. The X-ray diffraction and Mössbauer spectroscopy data showed that in the $Ca_9MgM(PO_4)_7$ structures (M = Li, Na, K), the alkali metal cations are distributed over the $M(4)O_{15}$ cavities in a rather complicated way [6]. The structures of the $Ca_{10}M(PO_4)_7$ compounds (M = Li, Na, K) have not been determined as yet.

EXPERIMENTAL

Synthesis and methods of study. Compounds **I**–**III** were synthesized by the method described elsewhere [1]. The compounds of the composition $Ca_{10}M(PO_4)_7$: ^{57}Fe (1 at.%) (where M = Li, Na, K) studied by the method of Mössbauer probe spectroscopy were synthesized as was described in our previous study [5].

The structures of compounds **I**–**III** were refined using the sets of experimental data collected on a SIEMENS D500 powder diffractometer [CuK_α radiation, λ = 1.5406 Å, SiO_2-monochromator, BRAUN position-sensitive detector, scan step 0.01 (2θ)].

The conditions of the diffraction experiment and the main parameters of the structure refinement of the compounds studied are listed in Table 1. Full-matrix refinement by the Rietveld method [7] was performed using the RIETAN [8, 9] and GSAS [10] packages of programs.

Refinement of crystal structures. We used the coordinates determined for the β-$Ca_3(PO_4)_2$ structure (sp. gr. $R3c$) as the initial coordinates for the structure determination of compounds **I**–**III** [2]. As in the case of triple phosphates of the composition $Ca_9MgM(PO_4)_7$ (M = Li, Na, K) [6], we "placed" the alkali metal cation into the six-fold position M(4).

At the first stage of the structure determination, the profile, positional, and thermal atomic parameters were refined by the RIETAN program up to the values R_{wp} = 5.14–5.88, R_p = 3.97–4.54, R_E = 3.12–3.46, R_I = 2.07–2.94, and R_F = 1.22–1.69. The thermal parameters (B_{iso}) of calcium (0.2–1.3 Å^2), phosphorus (0.2–1.5 Å^2), and oxygen (0.2–2.0 Å^2) atoms corresponded to the values usually obtained in the structure refinement by the full-profile analysis. At the same time, the thermal parameter of lithium atoms [B_{iso}(Li) = 1.6 Å^2) was considerably lower than those of the sodium and potassium atoms [B_{iso}(Na) = 3.0 Å^2 and B_{iso}(K) = 4.0 Å^2, respectively].

The atomic coordinates of structures **II** and **III** refined by the RIETAN program were then used to calculate the electron-density distribution maps ρ(xyz) and Δρ(xyz) by the GSAS program. Contrary to the electron density in the vicinity of Ca^{2+} cations, the electron den-

Table 1. Experimental conditions and results of the structure refinement of double phosphates **I**–**III**

Characteristic	**I**	**II**	**III**
Range of measurements of 2θ, deg	10–140	10–140	2–67
I_{max}	44926	52297	21573
Unit-cell parameters (sp. gr. *R*3*c*, *Z* = 6):			
a, Å	10.4203(1)	10.4391(1)	10.4729(1)
c, Å	37.3895(1)	37.3096(1)	37.2787(1)
V, Å^3	3516(1)	3521(1)	3541(1)
Number of reflections	752	751	173
Pseudo-Voight profile function, η	0.545(1)	0.604(4)	0.621(6)
Profile parameters:			
U	0.0209(5)	0.0301(5)	0.104(3)
V	0.0121(2)	0.0192(2)	0.042(1)
W	0.01317(6)	0.01456(8)	0.0140(2)
Reliability factors* (*R*)			
R_{WP}	5.88	5.31	5.14
R_P	4.54	4.06	3.97
R_E	3.36	3.12	3.46
R_I	2.94	2.07	2.24
R_F	1.69	1.29	1.22

* Calculated by the following formulas [18]: $R_{WP} = [(\Sigma w[y_{i\,obs} - y_{i\,calc}]^2/(\Sigma w_i[y_{i\,obs}]^2)]^{1/2}$; $R_P = (\Sigma|y_{i\,obs} - y_{i\,calc}|)/(\Sigma y_{i\,obs})$, $R_I = (\Sigma|I_{obs} - I_{calc}|)/(\Sigma I_{obs})$; $R_F = (\Sigma|[I_{obs}]^{1/2} - [I_{calc}]^{1/2}|)/(\Sigma[I_{obs}]^{1/2})$; $R_E = R_{WP}/S(S = [(\Sigma w_i[y_{i\,obs} - y_{i\,calc}]^2/(N–P)]^{1/2}$; *N* is the number of experimental points and *P* is the number of the parameters to be refined.

sity in the vicinity of the alkali metal cation (K^+ or Na^+) was noticeably elongated in the direction of the threefold axis (Figs. 1a, 1b) as in triple $Ca_9Mg*M*(PO_4)_7$ (*M* = Na, K) phosphates [6]. This spread of the electron density indicates that both sodium and potassium cations in the structures under study statistically occupy two close positions above and below the triangular face formed by O(21) atoms located in a large $*M*(4)O_{15}$ cavity and elongated in the direction of the threefold axis (see the corresponding figure in [6]). An attempt to refine the structure of compound **III** by the RIETAN program with the use of the split potassium position has failed, whereas a similar attempt for compound **II** was rather successful. The sodium position is split into two positions with the simultaneous reduction of the thermal parameter B_{iso} (Na) down to 2.0 Å^2 and with the occupancies of the $*M*(4_1)$ and $*M*(4_2)$ positions being 80 and 20%, respectively. The effective $*M*(4_1)$–$*M*(4_2)$ distance was determined as ~0.6 Å.

The Fourier maps ρ(*xyz*) and Δρ(*xyz*) for compound **I** had an electron-density maximum (~5 $\bar{e}$/Å^3) with the coordinates 0, 0, 0.19 in the vicinity of the lithium position (Fig. 1c). If this position was filled only with lithium cations, the electron density would not have exceeded 3 $\bar{e}$/Å^3. A high value of the electron density can indicate the statistical filling of the position with lithium and calcium atoms simultaneously. This is also confirmed by the variation of the O(21)–O(21) distance in the $*M*(4)O_{15}$ cavity in the transition from potassium to lithium in double phosphates of the composition $Ca_{10}*M*(PO_4)_7$. The shortest *M*(4)–O(21) distance in the $*M*(4)O_{15}$ cavity is observed for whitlockite-type structures. In triple phosphates of the composition $Ca_9Mg*M*(PO_4)_7$ (*M* = Li, Na, K), the O(21)–O(21) distance in the plane of the triangular face and therefore also the distance from the O(21) oxygen atom to the threefold axis regularly decreases with a decrease of the radius of the alkali metal cation [6]. The O(21)–O(21) distance in double phosphates of the composition $Ca_{10}*M*(PO_4)_7$ also decreases in the transition from potassium to sodium from the value 4.53 Å in compound **III** to 4.21 Å in compound **II** (Figs. 2b, 2c). However, in the model of structure **I**, where the *M*(4) position is fully occupied by lithium, this distance equals 4.33 Å (Fig. 2a) and is close to the analogous distance in the β-$Ca_3(PO_4)_2$ structure (4.36 Å) (Fig. 2d).

The refinement of the model in which the position *M*(4) filled with both Ca^{2+} and Li^+ cations yielded a high value of the thermal parameter of the "effective" atom $*n*Li^+ + (1 - *n*)Ca^{2+}$ ($B_{iso} \approx 12$ Å). The refinement of

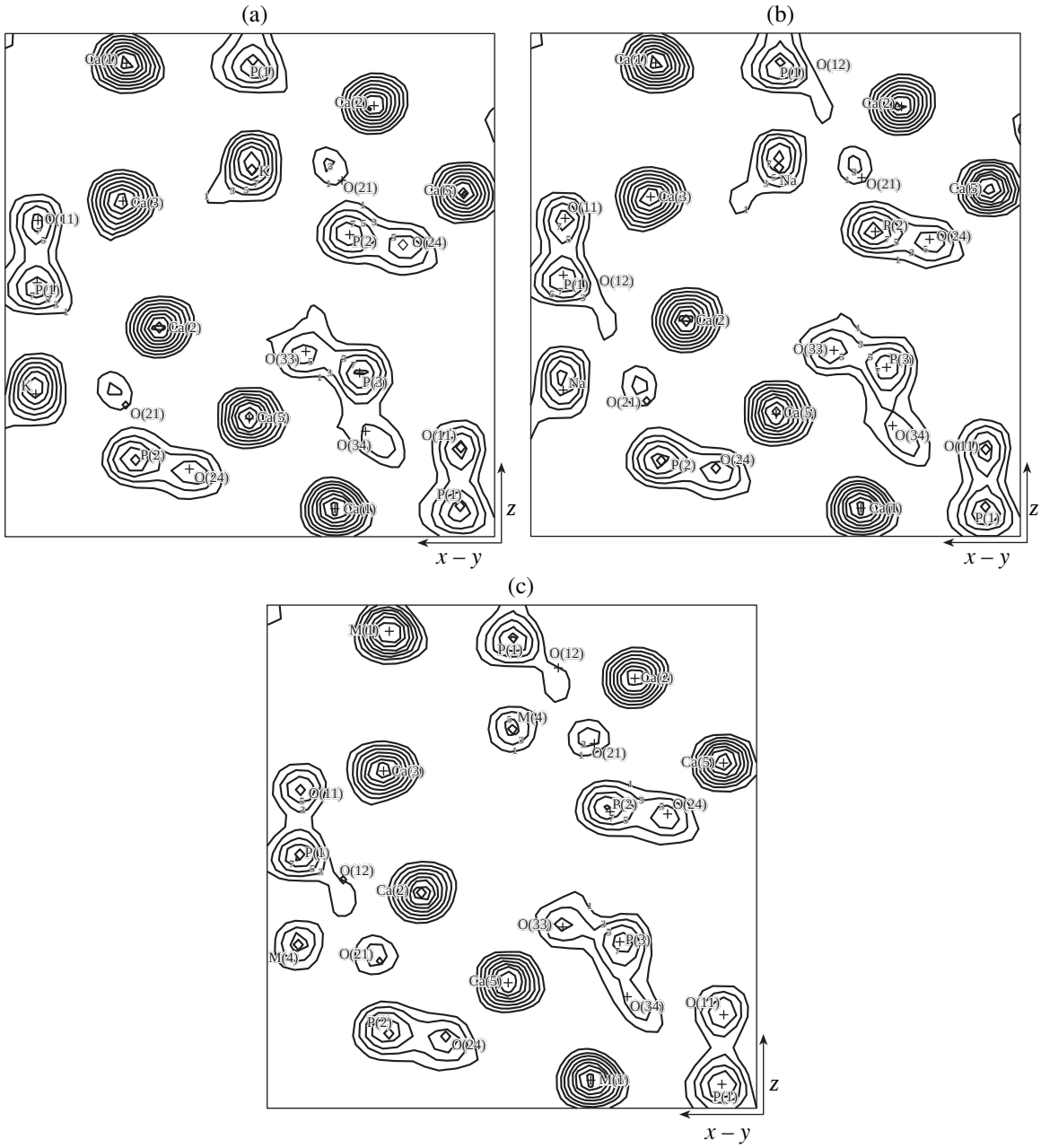

Fig. 1. Fourier-map of the electron density distribution ($\rho_{obs}(xyz)$) in the $(1\bar{1}1)$ plane. A 14×14 Å-large fragment is shown (the coordinate of the square center is 0, 0, 0.1). (a) $Ca_{10}K(PO_4)_7$, (b) $Ca_{10}Na(PO_4)_7$, and (c) $Ca_{10}Li(PO_4)_7$.

the model in which lithium and calcium atoms occupy two close positions, $M(4_1)$ and $M(4_2)$, along the *z*-axis in the $M(4)O_{15}$ cavity reduced the thermal parameter down to $B_{iso} \approx 2.4$ Å^2 and showed the positional separation of lithium and calcium atoms. The occupancies are 87% (~5 lithium atoms in the position $M(4_1)$) and 13% (~1 calcium atom in the position $M(4_2)$). The effective $M(4_1)$–$M(4_2)$ distance equals ~1 Å.

The refinement of the Ca(1)–Ca(3) and Ca(5) occupancies in the $Ca_{10}Li(PO_4)_7$ structure showed that the Ca(2), Ca(3), and Ca(5) positions are fully occupied by calcium cations (with the occupancies being close to unity). The occupancy of the position Ca(1) with calcium cations does not exceed 0.94. According to the crystallochemical formula, if the *M*(4) position is occupied with both Ca^{2+} (~1 cations) and Li^+ (~5 cations), the unit cell of the crystal is lacking one Li^+ cation. Taking into account that the occupancy of the Ca(1) position is underestimated, we assumed that it should also be filled with both Ca^{2+} and Li^+ cations [$M(1)$ = 0.94 Ca^{2+} + 0.06 Li^+).

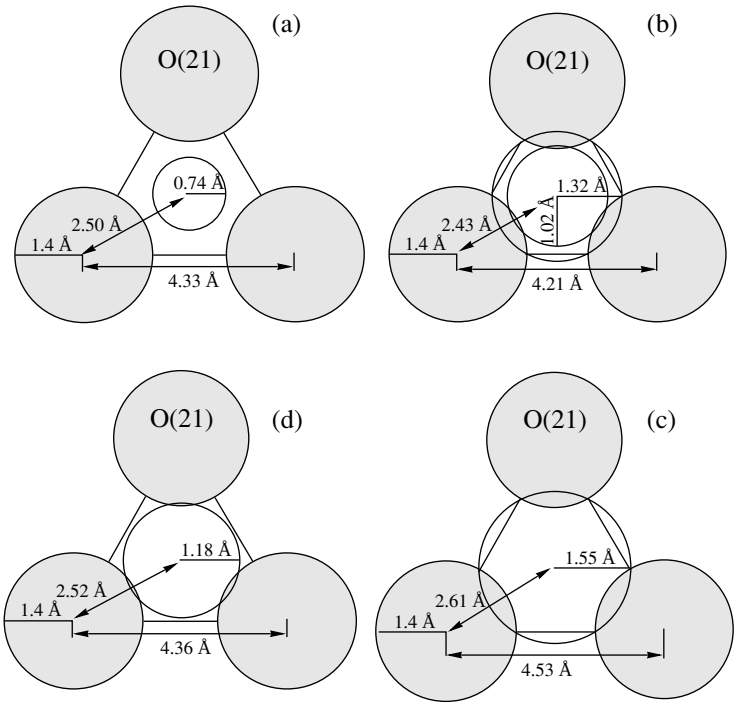

Fig. 2. Free space on a triangular face formed by O(21) atoms located in the $M(4)O_{15}$ cavity for the $Ca_{10}M(PO_4)_7$ structures (M = Li, Na, K). (M = (a) Li, (b) Na, (c) K, and (d) β-$Ca_3(PO_4)_2$). The interatomic distances are given in angstroms.

Upon the refinement of all the parameters for the selected models, the observed and the calculated diffraction patterns agreed quite well. The residual electron-density level on the difference Fourier maps $\Delta\rho(xyz)$ of all the three structures did not exceed $\pm 0.8\,\bar{e}/\text{Å}^3$. The atomic coordinates and the isotropic thermal parameters for structures **I**–**III** are listed in Table 2. The average interatomic distances only slightly differ from the analogous distances usually observed in diffraction studies of both single [11–14] and polycrystals [6, 15].

Mössbauer spectroscopy studies. The Mössbauer spectra from $Ca_{10}M(PO_4)_7$: 1 at. % $^{57}Fe^{2+}$ (M = Li, Na, K) at different temperatures show a quadrupole doublet with the broadened components. At the first stage, the experimental spectra were treated under an assumption of the continuous distribution of the electric-field gradient at the $^{57}Fe^{2+}$ nuclei. The profile analysis of the obtained $P(e^2qQ)$ distributions allowed us to single out at least two groups of quadrupole splitting. Similar to [5], the relative contributions of both groups of quadrupole splitting to the experimental spectra were determined by representing the spectra as the superpositions of two broadened quadrupole doublets (Fig. 3). The spectrum parameters obtained are listed in Table 3. The experimental data indicate that (i) similar to the case of $Ca_9MgM(PO_4)_7$ (M = Li, Na, K), the impurity Fe^{2+} ions occupy two octahedral positions characterized by different distortions of the oxygen polyhedra; (ii) the number of differently distorted octahedra in $Ca_9MgLi(PO_4)_7$ is temperature-dependent and almost constant for potassium- and sodium-containing compounds in the whole temperature range studied; (iii) the numbers of differently distorted octahedra for compounds **I**–**III** are almost composition-independent at room temperature, and (iv) the noticeable broadening of the doublets on the Mössbauer spectra indicate that each of these spectra is, in fact, the superposition of several quadrupole doublets with close values of the chemical shift δ and quadrupole splitting Δ.

DISCUSSION

The compounds **I**–**III** belong to the structure type of the natural mineral whitlockite [14]. Earlier [6], we showed that alkali metal cations in this structure type are located in a large $M(4)O_{15}$ cavity elongated in the direction of the threefold axis. The structural study of the $Ca_9MgM(PO_4)_7$ compound (M = Li, Na, K) showed that alkali metal cations occupy two positions in this cavity, $M(4_1)$ and $M(4_2)$, i.e., are located in distorted $M(4_1)O_3(12)O_3(21)$- and $M(4_2)O_3(21)O_3(22)$-octahedra. With the change of the temperature, alkali metal cations (Li^+ or Na^+) start migrating from one octahedron to another only through the shared face formed by three O(21) atoms (Fig. 2).

The free region on this shared face for double phosphates **I**–**III** is shown in Fig. 2. Calculating this free region, we used the ionic radia at the c.n. = 6 (Li^+ =

Table 2. Atomic coordinates and isotropic thermal parameters (B_{iso}) in the structures of double phosphates

Atom	*M*	*x*	*y*	*z*	B_{iso}, Å^2	Atom	*M*	*x*	*y*	*z*	B_{iso}, Å^2
M(1)*	Li	0.7257(6)	0.8603(7)	0.4316(4)	0.2(1)	O(12)	Li	0.008(2)	0.861(2)	0.2555(8)	1.3(4)
	Na	0.7260(6)	0.8589(6)	0.4316(3)	0.6(1)		Na	0.010(2)	0.863(1)	0.2542(6)	0.7(3)
	K	0.726(2)	0.858(2)	0.432(1)	0.2(1)		K	0.010(4)	0.864(3)	0.256(3)	0.7
Ca(2)	Li	0.6182(6)	0.8242(8)	0.2317(4)	0.8(1)	O(21)	Li	0.728(2)	0.913(2)	0.1743(7)	1.9(5)
	Na	0.6160(5)	0.8244(7)	0.2320(3)	0.6(1)		Na	0.737(2)	0.918(2)	0.1753(5)	1.0(4)
	K	0.615(2)	0.8233(8)	0.2337(7)	0.5(4)		K	0.717(4)	0.906(4)	0.176(2)	1.0
Ca(3)	Li	0.1208(7)	0.2670(5)	0.3261(4)	1.7(1)	O(22)	Li	0.771(3)	0.787(3)	0.1214(6)	2.0(5)
	Na	0.1208(6)	0.2664(4)	0.3254(3)	0.91(1)		Na	0.766(2)	0.780(2)	0.1216(6)	0.6(4)
	K	0.118(2)	0.265(1)	0.3265(8)	1.2(5)		K	0.766(7)	0.778(6)	0.124(1)	0.6
$M(4_1)$**	Li	0.0	0.0	0.191(4)	3(2)	O(23)	Li	0.726(2)	0.009(2)	0.1131(6)	0.3(3)
	Na	0.0	0.0	0.185(1)	2.0(5)		Na	0.727(2)	0.012(2)	0.1136(6)	0.6(4)
	K	0.0	0.0	0.1822(9)	4.0(8)		K	0.729(5)	0.012(4)	0.115(1)	0.6
$M(4_2)$***	Li	0.0	0.0	0.166(2)	3(2)	O(24)	Li	0.521(2)	0.761(2)	0.1290(6)	0.8(3)
	Na	0.0	0.0	0.169(6)	2.0(5)		Na	0.521(2)	0.763(2)	0.1290(6)	0.6(3)
Ca(5)	Li	0.0	0.0	0.0	1.3(2)		K	0.520(5)	0.760(5)	0.129(1)	0.6
	Na	0.0	0.0	0.0	0.5(1)	O(31)	Li	0.599(2)	0.951(2)	0.0444(6)	0.4(3)
	K	0.0	0.0	0.0	0.2(4)		Na	0.600(2)	0.952(2)	0.0451(6)	0.8(4)
P(1)	Li	0.0	0.0	0.2656(4)	1.5(2)		K	0.596(5)	0.954(5)	0.046(1)	0.8
	Na	0.0	0.0	0.2667(4)	1.0(2)	O(32)	Li	0.573(2)	0.692(2)	0.0514(6)	0.2(3)
	K	0.0	0.0	0.269(1)	1.5(6)		Na	0.570(2)	0.691(2)	0.0513(6)	1.0(4)
P(2)	Li	0.6896(8)	0.865(1)	0.1343(4)	1.0(2)		K	0.571(6)	0.692(5)	0.053(1)	1.0
	Na	0.6903(7)	0.8645(9)	0.1340(4)	0.7(1)	O(33)	Li	0.821(2)	0.919(2)	0.0439(6)	0.8(3)
	K	0.688(2)	0.865(2)	0.1359(9)	1.5(7)		Na	0.820(1)	0.921(2)	0.0439(6)	0.4(3)
P(3)	Li	0.6532(9)	0.8474(9)	0.0327(4)	0.8(2)		K	0.820(4)	0.918(6)	0.0472(1)	0.4
	Na	0.6516(8)	0.8469(8)	0.0324(3)	0.7(2)	O(34)	Li	0.628(1)	0.827(2)	0.9922(5)	1.2(4)
	K	0.655(3)	0.849(2)	0.0335(9)	0.2(2)		Na	0.631(1)	0.828(2)	0.9921(5)	0.7(3)
O(11)	Li	0.0	0.0	0.310(1)	2.0(9)		K	0.634(3)	0.832(4)	0.993(1)	0.7
	Na	0.0	0.0	0.3098(8)	0.4(5)						
	K	0.0	0.0	0.312(2)	0.4****						

Note: Notation for oxygen atoms: the first number indicates the sequential number of the tetrahedron, the second number indicates the sequential number of an oxygen atom in the tetrahedron.

* M(1) = 0.94Ca + 0.06Li for **I** and 1.00Ca for **II** and **III**.

** $M(4_4)$ = 0.87(3)Li for **I**, 0.8(1)Na for **II,** and 1.00K for **III**.

*** $M(4_2)$ = 0.13(3)Ca for **I** and 0.2(1)Na for **II**.

**** B_{iso} was not refined.

0.74 Å), Na^+ = 1.02 Å) and c.n. = 9 (Na^+ = 1.32 Å, Ca^{2+} = 1.18 Å), and K^+ = 1.55 Å [16]. It is seen from Fig. 2 that the dimensions of the free region depend on the cations located in the structure. Lithium (calcium) and sodium cations can be located in the face plane, whereas potassium cations can be located only either above or below the face formed by the O(21) atoms (Fig. 2).

In the $Ca_9MgLi(PO_4)_7$ structure, lithium cations occupy two positions, Li(1) and Li(2), in the $M(4_1)O_6$- and $M(4_2)O_6$-octahedra, respectively [6]. Lithium cations in these positions are spaced by an effective distance of ~1.5 Å comparable with the sum of the radii of two neighboring lithium cations, $2r_{VI}(Li^+) = 2 \times 0.74 = 1.48$ Å [16]. Such a short distance between two super-

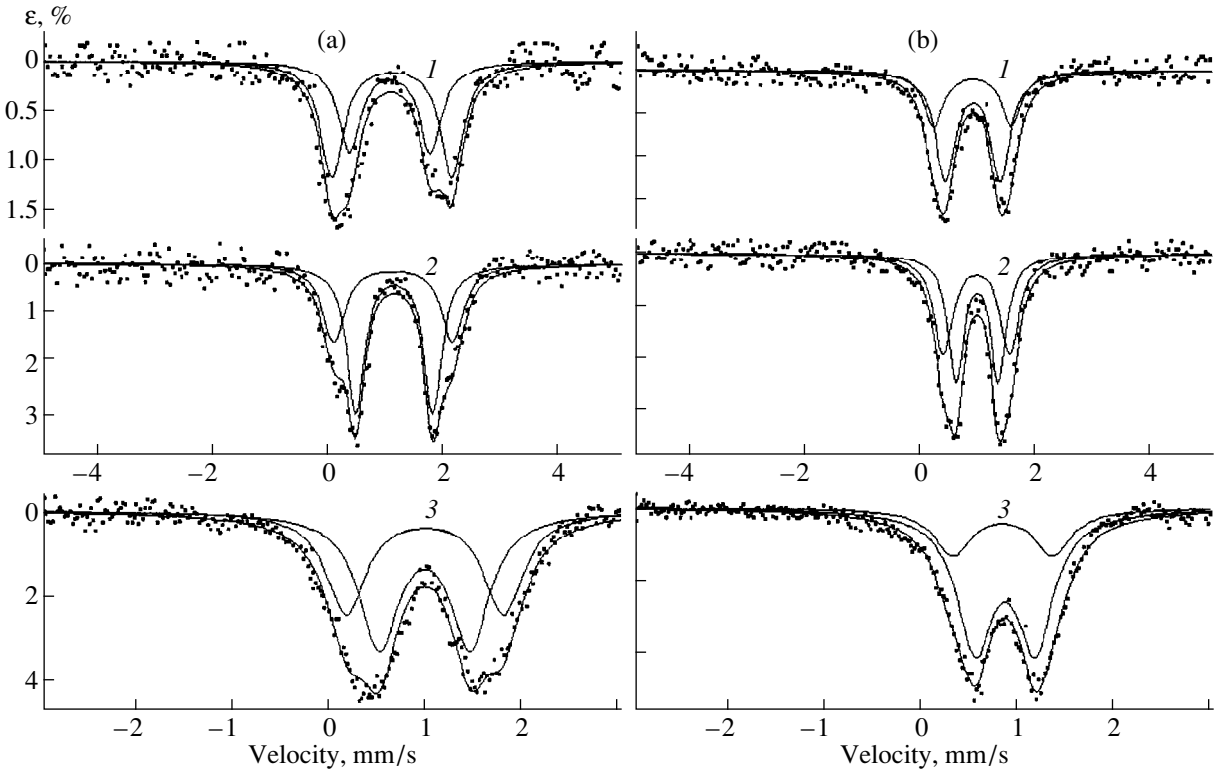

Fig. 3. Mössbauer spectra of ^{57}Fe in the $Ca_{10}M(PO_4)_7$: ^{57}Fe compounds (M = L i(*1*), Na (*2*), K (*3*)) at (a) 77 and (b) 300 K; ε denotes absorption.

imposed lithium ions in the subcell does not lead to any overlap in their electron densities. In double phosphates **I** and **II**, the distance between the $M(4_1)$ and $M(4_2)$ positions equals ~1.0 Å (structure **I**) and 0.6 Å (structure **II**), which is considerably less than $2r_{VI}(Na^+)$ = 2.04 Å or $r_{VI}(Li^+) + r_{IX}(Ca^{2+}) = (0.74 + 1.18)$ Å = 1.92 Å. Therefore, on the electron density maps ρ(*xyz*) and Δρ(*xyz*), the maxima due to these two atoms occupying the $M(4)$ position overlap. The existence of two positions for alkali metal cations in the structure is indirectly confirmed by the Mössbauer spectroscopy data (Table 3).

Table 3. Parameters of the ^{57}Fe Mossbauer spectra of the compounds $Ca_{10}M(PO_4)_7$: 1 at.% ^{57}Fe (M = Li, Na, K)

M	T, K	δ, mm/s	Δ, mm/s	I*, mm/s	S_j/S**, %
Li	300	1.19 ± 0.02	1.37 ± 0.08	0.42 ± 0.04	35 ± 9
		1.19 ± 0.01	0.87 ± 0.06	0.42 ± 0.04	65 ± 9
	77	1.35 ± 0.01	1.81 ± 0.04	0.48 ± 0.06	63 ± 6
		1.31 ± 0.01	1.29 ± 0.06	0.48 ± 0.06	37 ± 6
Na	300	1.24 ± 0.02	1.20 ± 0.02	0.33 ± 0.02	40 ± 9
		1.25 ± 0.01	0.75 ± 0.02	0.33 ± 0.02	60 ± 9
	77	1.37 ± 0.01	2.09 ± 0.02	0.38 ± 0.02	34 ± 8
		1.39 ± 0.01	1.35 ± 0.02	0.38 ± 0.02	66 ± 8
K	300	1.10 ± 0.01	1.04 ± 0.05	0.47 ± 0.04	30 ± 7
		1.12 ± 0.01	0.63 ± 0.03	0.47 ± 0.04	70 ± 6
	77	1.21 ± 0.01	1.65 ± 0.02	0.50 ± 0.02	44 ± 6
		1.21 ± 0.01	0.97 ± 0.01	0.50 ± 0.02	56 ± 8

* Γ is the half-width.

**S_j/S is the relative area of the spectrum component. Chemical shifts are given with respect to α-Fe.

Similar to the case of triple phosphates $Ca_9MgM(PO_4)_7$ (M = Li, Na, K), the Mössbauer spectra of impurity Fe^{2+} ions in double phosphates **I**–**III** are described as superpositions of at least two broadened quadrupole doublets (Fig. 3). In the structures of triple phosphates $Ca_9MgM(PO_4)_7$ (M = Li, Na, K), the probe ^{57}Fe atoms are located in octahedra of two types. On the Mössbauer spectra, this is reflected by two doublets with different values of quadrupole splitting [6]. The cation in the position $M(4_2)$ distorts the $M(5)O_6$-octahedron containing the probe ^{57}Fe atoms to a larger degree than the cation in the position $M(4_1)$ [15]. The latter fact is also reflected in the Mössbauer spectra at the ^{57}Fe nuclei: the quadrupole splitting of one of the spectrum components is much more pronounced. The distribution of alkali metal cations in the $M(4)$ position characterizes the relative areas of the doublets in the Mössbauer spectra of impurity Fe^{2+} ions, and, therefore, also the numbers of differently distorted octahedra [6]. The

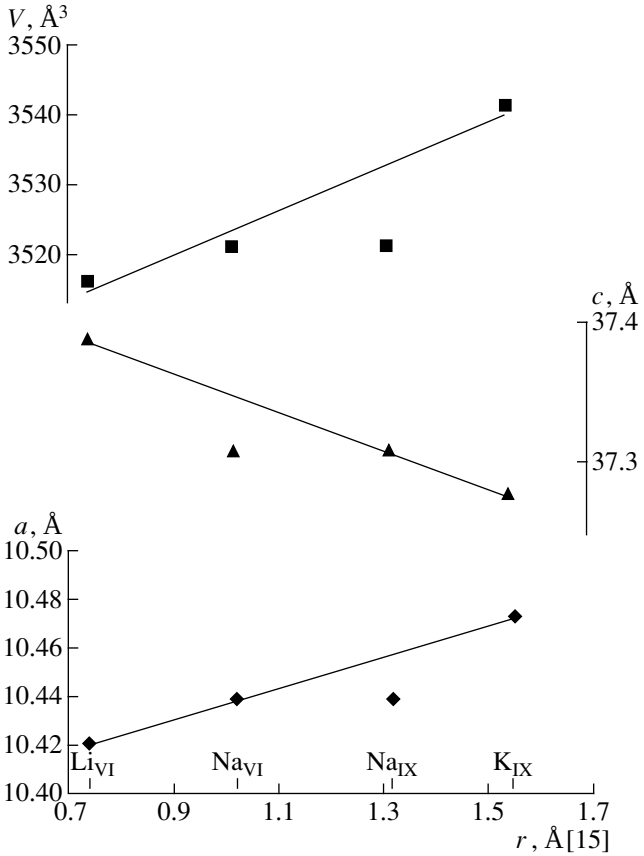

Fig. 4. Variations of lattice constants as functions of the radius of the alkali metal cation [15] in double phosphates $Ca_{10}M(PO_4)_7$ (**M** = Li, Na, K).

considerable broadening of the spectrum components is explained by the fact that the real crystal structures of double phosphates **I**–**III** have four types of the environment of the $M(5)O_6$-octahedron with the $M(4_1)$ and $M(4_2)$ positions, namely, $M(5)O_6M_3(4_1)$, $M(5)O_6M_2(4_1)M(4_2)$, $M(5)O_6M(4_1)M_2(4_2)$, and $M(5)O_6M_3(4_2)$. Using the Mössbauer spectroscopy data, one can estimate the occupancies of the $M(4_1)$ and $M(4_2)$ positions (Table 3) in double phosphates **I**–**III** that cannot be estimated from the structural data. The occupancy of the position $M(4_1)$ corresponds to the relative area of the Mössbauer-spectrum component with small quadrupole splitting Δ, whereas the occupancy of the position $M(4_2)$ corresponds to the relative area of the Mössbauer spectra component with more pronounced quadrupole splitting.

As is seen from Table 4, the relative contributions of the doublets with the pronounced and weak distortions for compound **I** and, therefore, also the occupancies of the positions $M(4_1)$ and $M(4_2)$ are temperature dependent in the temperature range 77–300 K. In other words, with the change in the temperature, lithium cations in the position $M(4)$ start migrating from one site to another. At 300 K, the component areas in the Mössbauer spectra of $^{57}Fe^{2+}$ with different distortions for compounds **I**–**III** are almost the same (within the experimental error). Thus, the nature of an alkali metal cation at room temperature does not affect the occupancies of the $M(4_1)$ and $M(4_2)$ positions with these cations (Table 3). For compounds **II**–**III**, the occupancies of the $M(4_1)$ and $M(4_2)$ positions are also temperature independent.

The analysis of the *M*–O distances and the variation of the unit-cell parameters depending on the ionic radii of the alkali cations in double phosphates **I**–**III** does not allow one to determine the coordination numbers of sodium cations (Fig. 4). On the one hand, the Na–O(22) distances (3.36 Å) considerably exceed the Na–O(12) (2.98 Å) and Na–O(21) (2.45 Å) distances, thus indicating that the most probable coordination number is six. For a potassium cation, the difference between the K–O(12) and K–O(22) distances is much lower (3.13 and 3.23 Å, respectively), and therefore its coordination number should equal nine. On the other hand, at the coordination number of sodium cations equal to six, one observes the linear dependence of the lattice parameter *a* and *V* on the ionic radius of an alkali cation in double phosphates **I**–**III**. The linear dependence of the parameter *c* is observed at the coordination number of sodium equal to nine (Fig. 4). We believe that such indeterminacy for the coordination number of sodium cations in **II** indirectly confirms the mobility of the alkali metal cation in the $M(4)$ position in whitlockite-type structures.

In whitlockite-type structures, alkali metal cations occupy two close positions, $M(4_1)$ and $M(4_2)$, both statistically and nonequivalently. Nonequivalent filling of two close positions observed earlier for α-$Na_3Sc_2(PO_4)_3$ [17] results in the appearance of ferroelectric properties in these crystals [18]. One one can also expect the manifestation of ferroelectric properties in double phosphates **I**–**III** within a wide temperature range. In terms of crystal chemistry, these assumptions are quite realistic; however, they should be confirmed experimentally.

ACKNOWLEDGMENTS

This study was supported by the Russian Foundation for Basic Research, project no. 97-03-33224a.

REFERENCES

1. S. Yu. Oralkov, B. I. Lazoryak, and R. G. Aziev, Zh. Neorg. Khim. **33** (1), 73 (1988).
2. B. Dickens, L. W. Schroeder, and W. E. Brown, J. Solid State Chem. **10** (3), 232 (1974).
3. B. I. Lazoryak, S. V. Khoĭna, V. N. Golubev, *et al.*, Zh. Neorg. Khim. **35** (6), 137 (1990).
4. B. I. Lazoryak, S. V. Khoĭna, V. N. Golubev, *et al.*, Zh. Neorg. Khim. **36** (3), 702 (1991).

5. V. A. Morozov, B. I. Lazoryak, K. V. Pokholok, *et al.*, Kristallografiya **40** (3), 523 (1995) [Crystallogr. Rep. **40** (3), 478 (1995)].
6. V. A. Morozov, I. A. Presnyakov, A. A. Belik, *et al.*, Kristallografiya **42** (5), 825 (1997) [Crystallogr. Rep. **42** (5), 751 (1997)].
7. H. M. Rietveld, Acta Crystallogr. **22** (1), 151 (1967).
8. F. Izumi, J. Crystallogr. Jpn. **27** (1), 23 (1985).
9. F. Izumi, *The Rietveld Method*, Ed. by R. A. Young (University Press, Oxford, 1993), Ch. 13.
10. A. C. Larson and R. B. Von Dreele, *Generalized Crystal Structure Analysis System (GSAS)*, *LAUR 86-748* (Los Alamos, 1988).
11. L. W. Schroeder, B. Dickens, and W. E. Brown, J. Solid State Chem. **22** (3), 253 (1977).
12. R. Gopal, C. Calvo, J. Ito, *et al.*, Can. J. Chem. **52** (7), 1155 (1974).
13. E. Kostiner and J. R. Rea, Acta Crystallogr., Sect B: Struct. Sci. **32** (1), 250 (1976).
14. C. Calvo and R. Gopal, Am. Mineral. **60** (1), 120 (1975).
15. B. I. Lazoryak, V. A. Morozov, A. A. Belik, *et al.*, J. Solid State Chem. **122** (1), 15 (1996).
16. R. D. Shannon, Acta Crystallogr., Sect. A: Cryst. Phys., Diffr., Theor. Gen. Crystallogr. **32** (5), 751 (1976).
17. V. A. Efremov and V. B. Kalinin, Kristallografiya **23** (4), 703 (1978).
18. S. A. Okopenklo, S. Yu. Stefanovich, V. B. Kalinin, *et al.*, Fiz. Tverd. Tela (Leningrad) **20**, 2846 (1978).

Translated by L. Man

Crystallography Reports, Vol. 45, No. 1, 2000, pp. 133–137. Translated from Kristallografiya, Vol. 45, No. 1, 2000, pp. 139–143.

Calculation of Local Electric Fields in Displacive-Type Ferroelectrics: $LiNbO_3$

A. V. Yatsenko

Simferopol State University, Yaltinskaya ul. 4, Simferopol 36, 333036 Ukraine

Received May 14, 1998; in final form, October 1, 1998

Abstract—The method is suggested for calculating the intensity and potential of a local electric field in displacive-type ferroelectrics which is based on the introduction of a transitional zone between the region of the discrete localization of ions and the homogeneously polarized medium. The method is exemplified on the calculation of the contribution of Li^+ ions to the local electric field in the lithium niobate structure. It is shown that the method provides fast convergence of the results in the calculation of the field intensity and high relative accuracy of the calculated electric-field potential inside the crystal. The contribution of the induced dipoles to the local electric field is calculated, and it is shown that the stability of the $LiNbO_3$ structure is provided by considerable anisotropy in the polarizability of Nb–O bonds. The method is applicable to any ionic crystal. © *2000 MAIK "Nauka/Interperiodica".*

Recently, the real (defect) structure of $LiNbO_3$ single crystals grown from congruent melts has been widely discussed. This is explained by the commercial use of lithium niobate crystals especially in programmed ultrasonic delay lines. Today, there are three major models of the defect structure of congruent $LiNbO_3$ crystals [1]. One of these models contains the oxygen (V_O) and lithium (V_{Li}) vacancies. Now, it is believed that the intrinsic defects are present only in the cationic sublattice [2, 3].

Modeling of the NMR spectra of ^7Li and ^{93}Nb nuclei based on the calculations of the parameters of the electric-field gradient (EFG) tensor in the lithium niobate defect structure has shown [4, 5] that the shape of the central-transition line in the NMR spectrum of ^{93}Nb is very sensitive to the type of the defects and their concentrations. However, even the allowance for the random spatial distributions of defects and defect complexes in the crystal lattice in the models of the defect structure did not provide complete agreement between the calculated and the experimental data (more than 20000 random implementations of the EFG tensor at ^{93}Nb nuclei were considered).

Most probably, this can be explained by the fact that in these calculations, the local distortions of the structure due to defects in the cationic sublattice were ignored. The strong dependence of the parameters of the EFG tensor on the local environment of Nb^{5+} ions and, especially, on the length and orientation of Nb–O bonds dictates the accurate determination of the displacements of ions in the first coordination sphere caused by defects. However, no acceptable method of such calculations has been developed as yet. Thus, the energy of defect formation in $LiNbO_3$ was determined without the allowance for possible variations in the interionic distances [6, 7].

The method for estimating local distortions in the $LiNbO_3$ structure caused by intrinsic defects can be based, e.g., on the calculations of the intensity of the local electric field, E_{loc}, at the ions of the crystal lattice. The E_{loc}-fields in homogeneously polarized dielectrics are usually calculated by the Lorenz method as

$$E_{loc} = E_i + E_d + E_p + E_{dep}, \quad (1)$$

where E_i is the contribution of the point charges of ions within a sphere of radius R_1, E_d is the contribution of the induced dipole moments of the ions located within the same sphere, E_p is the Lorenz field induced by the polarized medium outside the sphere of radius R_1, and E_{dep} is the depolarization field. Expression (1) is valid if $d_m \ll R_1$, where d_m is the maximum arm of the dielectric dipoles. The ionic contribution E_i in the structure consisting of n kinds of ions is calculated by the standard formula

$$E_i = \frac{1}{4\pi\varepsilon_0}\sum_{k=1}^{n}\sum_{j=1}^{m_k}\frac{q_k}{R_{0jk}^3}R_{0jk}, \quad (2)$$

where j are the ordinal numbers of the charges of one sign, $R_{0\,jk}$ is the radius–vector between the point at which the calculation is performed E_i and the jth ion of the kth kind, q_k are the effective charges of the ions of the kth kind, and m_k is the total number of ions of the kth kind within the sphere of radius R_1.

The dependence of the zth component E_{iz} of the field E_i at the Li^+ ions in $LiNbO_3$ (the Z-axis coincides with the threefold symmetry axis of the crystal) on the summation radius R_1 is shown in Fig. 1a. The calculations

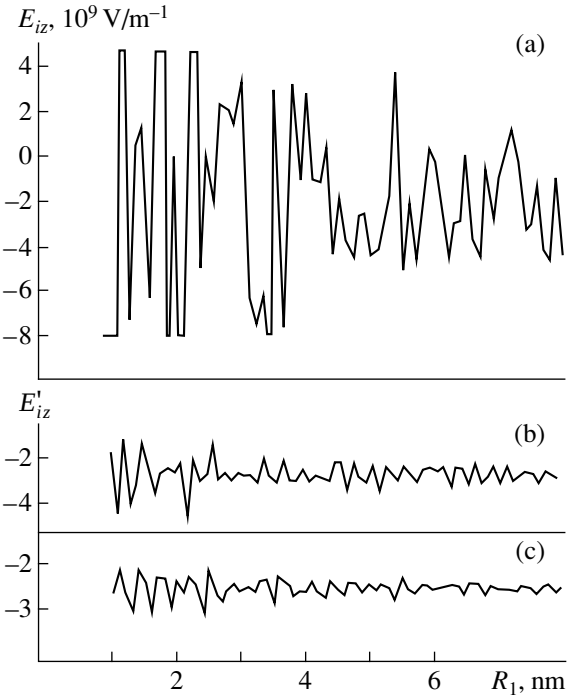

Fig. 1. Dependences of the components (a) E_{iz} and (b, c) E'_{iz} on the summation radius R_1 at Li^+ ions in the $LiNbO_3$ structure; (b) Q (R_{0jk}) is calculated by formula (6a), (c) Q (R_{0jk}) is calculated by formula (6b); σ = 0.2 nm.

were made by formula (2) (with the use of the following effective charges of the lattice ions: $q_{Li} = 0.98$, $q_{Nb} = 3.67$, and $q_0 = -1.55$ in the units of the electron charge) were determined by the LCAO MO method in [8]. As is seen from Fig. 1a, despite considerable R_1 values (the total number of ions exceeds 2×10^5 at $R_1 = 8$ nm), the convergence of the function $E_{iz}(R_1)$ is far from being satisfactory.

To improve the convergence of the lattice sums, several methods can be used, of which the most widespread is the Ewald method [9]. However, the Ewald method and its modifications are based on the essential simplification of the charge distribution in the crystal lattice. To maintain the electrical neutrality of the ensemble of ions as a whole, the volume under consideration should be multiple to the unit-cell volume, which considerably complicates the calculation of the E_p field and limits the applicability of the Ewald method to ferroelectrics.

Below, we suggest another approach to the calculation of the local electric fields in ionic crystals, which provides a fast convergence of the lattice sums. Since the spontaneous polarization P in displacive-type ferroelectrics is determined mainly by the displacement of cations with respect to the oxygen sublattice, we introduce into consideration a transitional region between the region of discrete localized ions and the homogeneously polarized medium in the shape of a spherical layer of the internal radius R_1 and the external radius R_2. Then, the local field E_{loc} at the center of the spherically symmetric specimen of radius R_3 can be written as

$$E_{loc} = E_i + E_{add} + E_d + E_{dep},$$

where

$$E_{add} = \frac{1}{4\pi\varepsilon_0}\sum_{k=1}^{n}\sum_{j=m_k+1}^{l_k}\frac{q_k Q(R_{0jk})}{R_{0jk}^3}R_{0jk} + \int_{R_1}^{R_2}\int_{0}^{\pi}\frac{P(1-Q(R_{0jk}))(3\cos^2\theta-1)\sin\theta}{\varepsilon_0 r}dr d\theta \qquad (3)$$

$$+ \int_{R_2}^{R_3}\int_{0}^{\pi}\frac{P(3\cos^2\theta-1)\sin\theta}{\varepsilon_0 r}dr d\theta$$

and l_k is the number of ions of the kth kind within the sphere of the radius R_2, θ is the spherical angle between P and the radius–vector r, and $Q(R_{0jk})$ is the coefficient, which is a function of R_{0jk} and is responsible for the type of the transitional region ($0 \le Q(R_{0jk}) \le 1$). Both integrals in (3) are identical zeroes and therefore

$$E'_i = E_i + E_{add} = \frac{1}{4\pi\varepsilon_0}\sum_{k=1}^{n}\sum_{j=1}^{l_k}\frac{q_k Q(R_{0jk})}{R_{0jk}^3}R_{0jk}, \qquad (4)$$

where $Q(R_{0jk}) = 1$ at $R_{0jk} \le R_1$. If $R_{0jk} \ge R_1$, the function $Q(R_{0jk})$ should be chosen in the analytical form to provide the fast convergence of E'_i. Thus, the expression for E_{loc} at the center of the spherical specimen takes the form

$$E_{loc} = E'_i + E_d + E_{dep}, \qquad (5)$$

where E_{dep} takes into account only the effect of the charges on the specimen surface and the internal depolarizing charge.

We analyzed the following expressions for the function $Q(R_{0jk})$:

$$Q(R_{0jk}) = \exp\left[-\frac{(R_{0jk}-R_1)}{\sigma}\right], \qquad (6a)$$

$$Q(R_{0jk}) = \exp\left[-\frac{(R_{0jk}-R_1)^2}{2\sigma^2}\right], \qquad (6b)$$

where σ is the parameter to be determined.

The corresponding dependences of the zth component, E'_{iz}, of the field E'_i at Li^+ ions in $LiNbO_3$ on the summation radius R_1 at $(R_2 - R_1) = 4$ nm are also shown in Fig. 1. It is seen that the choice of $Q(R_{0jk})$ in the form of the Gaussian function (6b) provides a faster convergence of E'_{iz} than the use of the function (6a), the σ

value being the same. If $Q(R_{0jk})$ is chosen in form (6b), the effect of σ on $\langle E'_{iz} \rangle$ determined within the interval $4.0 \le R_1 \le 8.0$ nm and the root-mean square deviation $\delta E'_{iz}$ of E'_{iz} from $\langle E'_{iz} \rangle$ are illustrated by Fig. 2. It is seen that in the latter case, $\langle E'_{iz} \rangle$ has a good convergence with $\delta E'_{iz}$, rapidly decreasing with an increase in σ.

The E'_{iz} values were calculated for all structurally nonequivalent ions of the $LiNbO_3$ crystal lattice in the range of R_1 up to 80 nm (the total number of ions exceeded 3×10^8). However, no tendency to divergence of the lattice-sum was observed (σ = 1.0 nm, the relative accuracy 5×10^{-5}). Despite the rather good results, the choice of $Q(R_{0jk})$ in the form (6b) was, to a large extent, intuitive, and the optimization of this function presents a problem by itself.

Of course, the above approach can also be used to calculate the electric-field potential φ inside the crystal. The contribution of the point charges of the lattice ions to φ is

$$\varphi_i = \frac{1}{4\pi\varepsilon_0} \sum_{k=1}^{n} \sum_{j=1}^{l_k} \frac{q_k Q(R_{0jk})}{R_{0jk}}.$$

Figure 3 shows φ_i for the classical position of Li^+ ions in the $LiNbO_3$ structure as a function of R_1. The $Q(R_{0jk})$ function was chosen in the form (6b); $(R_2 - R_1) = 4\sigma$. It is seen that within the range of the studied σ values, the relative accuracy of the φ_i determination increases with σ, and, at σ = 1.5 nm, attains the value sufficient for solving many problems, e.g., for calculating local potential reliefs [10].

The calculation of E'_i at all the structurally nonequivalent Li^+, Nb^{5+}, and O^{2-} ions provides the determination of the induced dipole moments p_k of these ions and, thus, also of E_d. The p_k values can be calculated either analytically [11] or by the iteration method [12], with the latter method being preferable for numerical calculations. The classical values of the polarizability of lattice ions in $LiNbO_3$ are: α_{Li} = 0.029, α_{Nb} = 0.220, and α_0 = 2.405 (in the units of 10^{-24} cm^3) [13]. However, in the calculation of the dipole component of the local field, these values are usually either increased or decreased by a factor ranging from 2 to 4 [11]. Below, we use the iteration procedure and take into account the contribution of the moments p_k within the sphere of radius R_1 = 5 nm. It was established that the thus calculated E_d values only slightly depend on α_{Li} and α_{Nb}, but are very sensitive to α_0. The dependences of the z-component of the total electric field at the Li^+, Nb^{5+}, and O^{2-} ions on α_0 are shown in Fig. 4.

One of the conditions providing for the stability of the $LiNbO_3$ structure is the requirements that E_{loc} at the

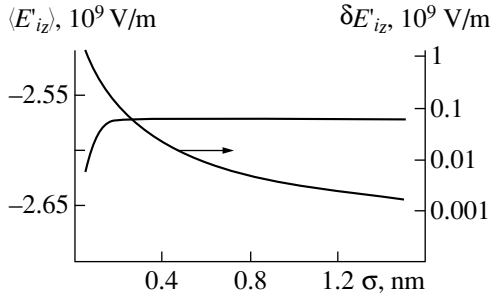

Fig. 2. Dependences of $\langle E'_{iz} \rangle$ and $\delta E'_{iz}$ on σ; $Q(R_{0jk})$ is the Gaussian function ($(R_2 - R_1) = 4\sigma$).

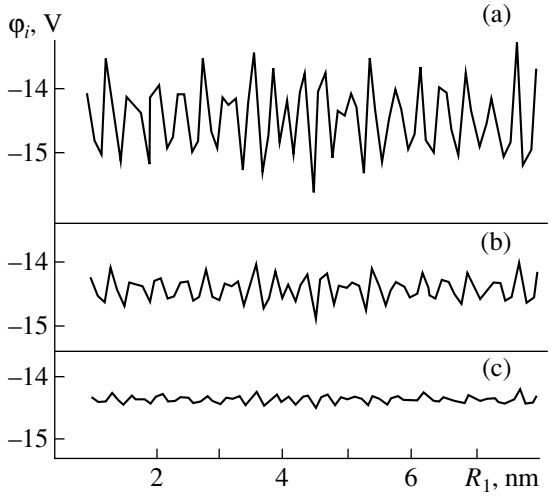

Fig. 3. Dependence of the ionic contribution to φ on R_1 at various values of σ; $Q(R_{0jk})$ is the Gaussian function, the difference ($(R_2 - R_1) = 4\sigma$) equals (a) 0.3, (b) 0.5, (c) 1.0 nm.

Li^+ ions should be antiparallel to the polar z-axis. It is seen from Fig. 4 that this condition is fulfilled only at anomalously low α_0 values, which is inconsistent with the dielectric susceptibilities measured and calculated in the optical range. It should also be indicated that the variations of the effective charges of Nb^{5+} and O^{2-} ions do not affect the dependence of E_{loc} at the Li^+ ions on α_0. This inconsistency can be interpreted with the invocation of the fact that the overlap of the electron shells of the Nb^{5+} and O^{2-} ions results in considerable anisotropy in the polarizability of O^{2-} ions. Therefore, one should take into account the polarizability of the Nb–O bonds described by the second-rank tensor or the polarizability of the NbO_3 cluster and not the polarizabilities of individual ions.

Below, we consider the limiting variant of anisotropy in the polarizability of the Nb–O bonds. It was assumed that the components of the polarizability tensor of O^{2-} ions in the system of its axes are $\alpha_{11} = \alpha_{22} =$

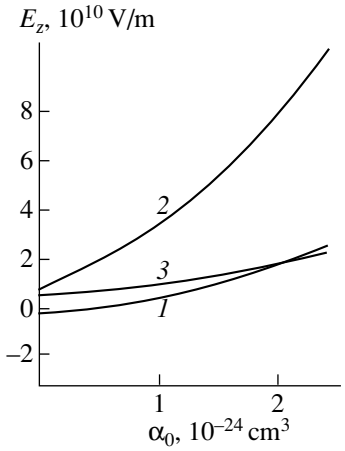

Fig. 4. Dependence of the *z*th component of the local electric field at (*1*) Li^+, (*2*) Nb^{5+}, and (*3*) O^{2-} ions on α_0 in the $LiNbO_3$ structure.

0, and $\alpha_{33} = 2.405 \times 10^{-24}$ cm^3, with the *3* axis coinciding with the direction of the Nb–O bond.

For simplicity, the polarizability of Nb^{5+} ions was assumed to be isotropic. The calculated ionic contribution and the total value of E_{loc} (neglecting the depolarization field) at the Nb^{5+}, Li^+, and O^{2-} ions and the calculated components of the induced dipole moments of these ions obtained upon four iteration cycles are listed in the table (in the Cartesian coordinate system, in which the *x*-axis coincides with the *a*-axis and the *z*-axis coincides with the *c*-axis of the hexagonal system). As is seen from the table, the results obtained are qualitatively consistent with the data on the $LiNbO_3$ structure.

The verification of the absolute accuracy of the above method of calculating local electric fields in $LiNbO_3$ can be made by two methods. In particular, knowing the values of the ionic and dipole contributions to E_{loc}, one can calculate the force acting onto each ion. Since in $LiNbO_3$ crystals, $E_{dep} \cong 10^5$ V/cm [14], then, in the first approximation, this field can be ignored. The analysis of the interactions in the ideal $LiNbO_3$ structure leads to the following expression for the force balance along the *z*-direction:

$$F_z(\mathrm{Nb}) + 3F_z(0) + F_z(\mathrm{Li}) + p_z(\mathrm{Nb})V_{zz}(\mathrm{Nb}) + 3p_z(0)V_{zz}(0) = 0,$$

where F_z(Nb), F_z(0), and F_z(Li) are the *z*-components of the Coulomb forces acting onto the point charges of the corresponding ions; $p_z(0)$ and p_z(Nb) are the *z*th components of the induced dipole moments of the O^{2-} and Nb^{5+} ions, and V_{zz} are the components of the EFG tensor with due regard for possible antiscreening. The calculations showed that $V_{zz}(\mathrm{O}) = 1.33 \times 10^{20}$ V/m^2 and $V_{zz}(\mathrm{Nb}) = -3.94 \times 10^{21}$ V/m^2. Thus, the condition of force balance is fulfilled within 17% of the maximum term. The analysis of possible interactions in the *xy*-plane yields similar results. One can also estimate the

Components of the local electric field at the ions of the $LiNbO_3$ crystal lattice and the induced dipole moments

Ion	Coordinates, nm			E_i'-components, 10^{10} V/m		
	x	*y*	*z*	E_{ix}	E_{iy}	E_{iz}
Nb^{5+}	0	0	0	0.000	−0.000	0.720
Li^+	0	0	−3.009	−0.000	0.000	−0.257
O_I^2	−1.014	−1.317	0.897	−0.787	−4.328	0.514
O_{II}^2	1.648	−0.219	0.897	4.142	1.483	0.514
O_{III}^2	−0.634	1.537	0.897	−3.355	2.846	0.514
Ion	$(E_d + E_i')$-components, 10^{10} V/m			*p*-components, |*e**| nm		
	x	*y*	*z*	p_x	p_y	p_z
Nb^{5+}	0.000	−0.000	4.937	0.000	−0.000	0.0075
Li^+	0.000	0.000	−1.040	0.000	0.000	−0.0002
O_I^2	−0.375	−4.757	2.268	−0.4112	−0.5342	0.0364
O_{II}^2	4.307	2.057	2.268	0.6682	−0.0890	0.0364
O_{III}^2	−3.932	2.703	2.268	−0.2571	0.6263	0.0364

* *e* is the electron charge.

repulsion forces due to overlap of the electron shells of the ions in the Nb–O pair: $F_r \simeq 1.69 \times 10^{-8}$ N.

The thus determined induced dipole moments can be used to calculate the macroscopic polarization of the crystal

$$P \cong n[q_{\mathrm{Li}}\Delta_{\mathrm{Li}} + q_{\mathrm{Nb}}\Delta_{\mathrm{Nb}} + 3p_z(0) + p_z(\mathrm{Nb})],$$

where Δ_{Li} and Δ_{Nb} are the displacements of the Li and Nb ions from the symmetric positions and n is the volume concentration of Li^+ ions. Using the values of the effective charges [8], the data listed in table, and the standard crystallographic data, we obtain P = 81.5 μC/cm^2, i.e., a value close to the classical value (71 μC/cm^2) [14]. Thus, despite the somewhat simplified allowance for anisotropy in the polarizability of the Nb–O bonds, the method suggested above provides satisfactory accuracy in the determination of the local electric field E_{loc}.

We believe that the application of the suggested method to $LiNbO_3$ will provide reliable information on the local distortions of the crystal structure by intrinsic and extrinsic defects and the model study of the effect of macroscopic electric fields on the cationic sublattice. Of course, a similar method for calculating E_{loc} and φ can be applied not only to ferroelectrics, but also to any ionic crystal. The analysis of the shape of the polarized specimen as a function of E_{loc} and the optimization of the $Q(R_{0jk})$ function for the suggested method would be the subject of a separate article.

REFERENCES

1. O. F. Shirmer, O. Thiemann, and M. Wöhlecke, J. Phys. Chem. Solids **52**, 185 (1991).
2. Y. Watanabe, T. Sota, K. Suzuki, *et. al*., J. Phys.: Condens. Matter **7**, 3627 (1995).
3. N. Zotov, F. Frey, H. Boysen, *et al*., Acta Crystallogr., Sect. B: Struct. Sci. **51**, 961 (1995).
4. E. M. Ivanova, N. A. Sergeev, and A. V. Yatsenko, Ukr. Fiz. Zh. **42**, 47 (1997).
5. A. V. Yatsenko, H. M. Ivanova, and N. A. Sergeev, Physica B (Amsterdam) **240**, 254 (1997).
6. H. Donnerberg, S. M. Tomlinson, C. R. A. Catlow, and O. F. Shirmer, Phys. Rev. B: Condens. Matter **40**, 11909 (1989).
7. H. Donnerberg, S. M. Tomlinson, C. R. A. Catlow, *et al*., Phys. Rev. B: Condens. Matter **44**, 4877 (1991).
8. W. Y. Ching, Gu Zong-Quan, and Xu Yong-Nian, Phys. Rev. B: Condens. Matter **50**, 1992 (1994).
9. D. Fincham, Mol. Simulation **13**, 1 (1994).
10. A. V. Yatsenko and N. A. Sergeev, in *Proceedings of 28th Congress AMPERE* (Canterbury, England, 1996), p. 279.
11. Yu. N. Venevtsev, E. D. Politova, and S. A. Ivanov, *Ferro- and Antiferroelectrics of the Barium Titanate Family* [in Russian] (Khimiya, Moscow, 1985).
12. V. M. Buznik, *Nuclear Resonance in Ionic Crystals* [in Russian] (Nauka, Novosibirsk, 1981).
13. M. Levalois and G. Allais, Phys. Status Solidi A **40**, 181 (1977).
14. Yu. S. Kuz'minov, *Electrooptical and Nonlinear-Optical Lithium Niobate Crystal* [in Russian] (Nauka, Moscow, 1987).

Translated by L. Man

Crystallography Reports, Vol. 45, No. 1, 2000, pp. 138–144. Translated from Kristallografiya, Vol. 45, No. 1, 2000, pp. 144–150.

Spatial Distribution of Piezoinduced Change in the Optical Pathlength in Lithium Niobate Crystals

O. G. Vlokh*, B. G. Mytsyk, A. S. Andrushchak*, and Ya. V. Pryriz****

** Institute of Physical Optics, L'viv, Ukraine*

*** L'viv Center of the Institute of Space Research, L'viv, Ukraine*

Received May 14, 1997

Abstract—For the first time, the "indicative" surfaces of the constants of the piezooptic effect and their stereographic projections have been constructed with due regard for crystal elasticity for lithium niobate crystals described by the symmetry class 3*m*. The comparative analysis of these surfaces and the corresponding surfaces of the *true* piezooptic effect has been performed. *© 2000 MAIK "Nauka/Interperiodica".*

In [1–4], the *indicative* surfaces of the piezooptic effect (the POE surfaces) describing the variation of the refractive index n_i under the effect of normal mechanical stress σ_m (unidirectional pressure) were constructed with the use of the full matrices of the piezooptic coefficients π_{im}. The effect of the elastic properties of a crystal on the measured π_{im} coefficients was neglected.

In the present study, we constructed the indicative surfaces of the piezoinduced variation of the optical pathlength in lithium niobate crystals. We took into account the variations of both the refractive index n_i and the specimen length d_k along the direction of light propagation. The indicative surfaces are of great importance for the practical use of various optical materials, because the change in the intensity of the light transmitted by the specimen under the effect of σ_m is provided by the change in the optical pathlength $\Delta_{ik} = n_i d_k$ in the specimen. The dependence of Δ_{ik} on σ_m is well known [5]. This dependence calculated for the unit length of the specimen along the direction of the light propagation and per unit mechanical stress σ_m has the form

$$\delta\Delta = \frac{\delta\Delta_{ikm}}{d_k\sigma_m} = -\frac{1}{2}\pi_{im}n_i^3 + S_{km}(n_i - 1), \qquad (1)$$

where the subscripts *i*, *k*, and *m* correspond to three principal directions of an electrooptic experiment—polarization of light **i**, the direction of light propagation **k**, and the direction of the pressure application **m** (S_{km} are the coefficients of elastic compliance).

The right-hand side of (1) consists of two terms responsible for the contribution of "true" piezooptic (the first term) and elastic (the second term) effects to the change in the optical pathlength in the specimen.

It should be emphasized that relationship (1) is valid only for one-path interferometers used in the piezooptic experiments (see, e.g., [5–9]). For two-path interferometers [10–12], formula (1) has an additional factor 2 in each term in the right-hand side. For Fizeau interferometers [13–15], the factor $(n_i - 1)$ in the second term of (1) should be substituted by n_i.

In order to write the relationships for the spatial distribution of piezoinduced change in the optical pathlength (i.e., the equations of the piezooptic surfaces with due regard for elasticity), the quantities π_{im}, S_{km}, and n_i in (1) should be substituted by the corresponding expressions from the equations of the spatial distribution of the piezooptic effect π'_{im} (the equations of the POE surface), the spatial distribution of the elastic effect S'_{km} (the equation of the elastic-effect surface), and the equation of the spatial distribution of the refractive index n'_i (the optical indicatrix). Then, equation (1) acquires the form

$$\delta\Delta' = -\frac{1}{2}\pi'_{im}n_i'^3 + S'_{km}(n'_i - 1). \qquad (2)$$

It follows from (2) that the magnitude of the radius–vector **r** which describes the surface of the piezoinduced change in the optical pathlength $\delta\Delta'$ can be determined by substituting the magnitudes of the radius-vectors of the π'_{im}, S'_{km} surfaces and the values of n'_i along the directions of the radius–vector **r**. Equation (2) is valid for any symmetry class. We limit our consideration to the symmetry class 3*m*, which also describes lithium niobate crystals.

The equations of the indicative POE surfaces (the π'_{ii} surface for longitudinal POE and $\pi'^{(i)}_{im}$ and the $\pi'^{(m)}_{im}$ surfaces for the transverse POE for crystals of the symmetry class 3*m*) were considered elsewhere [1, 4]. The elastic-effect surfaces were considered in [16–18], but the cited works provided no equations of the transverse components of the elastic-compliance tensor for crystals described by the symmetry class 3*m*. In these studies, only the sections were analyzed. Therefore, we

1063-7745/00/4501-0138$20.00

write here these equations using the method for the construction of the POE surfaces described in [1–4].

The principal components of the elastic-compliance tensor S'_{km} ($k, m \le 3$) in the Cartesian coordinates for the crystals of the symmetry class 3*m* can be written as [16, 19]:

$$\begin{aligned} S'_{km} &= S_{11}(\alpha_{k1}\alpha_{m1} + \alpha_{k2}\alpha_{m2})^2 \\ &+ S_{12}(\alpha_{k1}\alpha_{m2} - \alpha_{k2}\alpha_{m1})^2 + S_{13}[(\alpha_{k1}^2 + \alpha_{k2}^2)\alpha_{m3}^2 \\ &+ \alpha_{k3}^2(\alpha_{m1}^2 + \alpha_{m2}^2)] + S_{33}\alpha_{k3}^2\alpha_{m3}^2 \\ &+ S_{14}[(\alpha_{k1}^2 - \alpha_{k2}^2)\alpha_{m2}\alpha_{m3} + \alpha_{k2}\alpha_{k3}(\alpha_{m1}^2 - \alpha_{m2}^2) \\ &+ 2\alpha_{k1}\alpha_{k2}\alpha_{m1}\alpha_{m3} + 2\alpha_{k1}\alpha_{k3}\alpha_{m1}\alpha_{m2}] \\ &+ S_{44}(\alpha_{k2}\alpha_{k3}\alpha_{m2}\alpha_{m3} + \alpha_{k1}\alpha_{k3}\alpha_{m1}\alpha_{m3}), \end{aligned} \tag{3}$$

where α_{k1}, …, α_{m3} are the directional cosines of the vectors **k** and **m** in the crystallophysical coordinate system.

In order to construct the surfaces of various optical quantities, one has to pass to the spherical coordinate system, where the directions of the pressure application, **m**, and the light propagation, **k**, coincide with the axes of a mobile coordinate system $X'_1X'_2X'_3$ (Fig. 1) and are set by the spherical coordinates θ and φ. Now, write the expressions for the directional cosines for the directions **k** and **m** in terms of θ and φ for the same three cases for which the POE surfaces were constructed in [1–4].

For the π'_{ii} surfaces at (**i** ∥ **m** ∥ X'_3 ∥ **r**) and of the $\pi'^{(m)}_{im}$ surface at (**m** ∥ X'_3 ∥ **r**; **i** ∥ X'_2) (Fig. 1), the spatial distribution of the elastic effect is determined from the conditions **k** ∥ X'_1 and **m** ∥ X'_3 ∥ **r**, and therefore

$$\begin{aligned} \alpha_{k1} &= \cos\theta\cos\varphi, \quad \alpha_{k2} = \cos\theta\sin\varphi, \\ \alpha_{k3} &= -\sin\theta, \\ \alpha_{m1} &= \sin\theta\cos\varphi, \quad \alpha_{m2} = \sin\theta\sin\varphi, \\ \alpha_{m3} &= \cos\theta. \end{aligned} \tag{4}$$

Substituting (4) into (3), we arrive at the equation

$$\begin{aligned} S'_{km} &= S_{13} + (S_{11} + S_{33} - 2S_{13} - 2S_{44})\sin^2\theta\cos^2\theta \\ &+ (S_{14}/4)\sin 4\theta\sin 3\varphi. \end{aligned} \tag{5}$$

For the $\pi'^{(i)}_{im}$ surfaces (**i** ∥ X'_3 ∥ **r**; **m** ∥ X'_2), the elasticity contribution can be calculated by substituting directional cosines into (4) for the same direction **k** ∥ X'_1, whereas the directional cosines of **m** should be written for the case **m** ∥ X'_2. We obtain

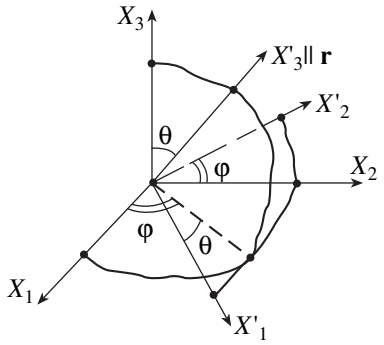

Fig. 1. Spatial position of the coordinate system $X'_1X'_2X'_3$ moving with respect to the crystallophysical coordinate system $X_1X_2X_3$.

$$\begin{aligned} \alpha_{k1} &= \cos\theta\cos\varphi, \quad \alpha_{k2} = \cos\theta\sin\varphi, \\ \alpha_{k3} &= -\sin\theta, \\ \alpha_{m1} &= -\sin\varphi, \quad \alpha_{m2} = \cos\varphi, \quad \alpha_{m3} = 0. \end{aligned} \tag{6}$$

Substituting (6) into (3), we obtain the surface of the elastic effect for crystals described by the symmetry class 3*m*:

$$S''_{km} = S_{12}\cos^2\theta + S_{13}\sin^2\theta + S_{14}\sin\theta\cos\theta\sin 3\varphi. \tag{7}$$

For uniaxial crystals, the expression for n'_i has the form [19]:

$$n'_i = (\sin^2\theta/n_e^2 + \cos^2\theta/n_o^2)^{-\frac{1}{2}}, \tag{8}$$

where n_o and n_e are the principal refractive indices of the ordinary and the extraordinary beams in the crystal, respectively.

Now, using (2) and the POE surfaces [1] [expressions (5) or (7) and (8)], we arrive at three equations for δΔ' describing the spatial distribution of the piezoinduced changes of the optical pathlengths in crystals of the symmetry class 3*m*, namely:

1. For the surface of the longitudinal component of the POE tensor, π'_{ii} (**i** ∥ **m** ∥ X'_3 ∥ **r**; **k** ∥ X'_2, Fig. 1), we have:

$$\begin{aligned} \delta\Delta'_1 &= -\frac{1}{2}\pi'_{ii}n_i'^3 + S'_{km}(n'_i - 1) \\ &= -\frac{1}{2}\{\pi_{11}\sin^4\theta + (\pi_{13} + \pi_{31} + 2\pi_{44})\sin^2\theta\cos^2\theta \\ &+ \pi_{33}\cos^4\theta + (\pi_{14} + 2\pi_{41})\sin^3\theta\cos\theta\sin 3\varphi\} \\ &\times [\sin^2\theta/n_o^2 + \cos^2\theta/n_e^2]^{-\frac{3}{2}} \end{aligned} \tag{9}$$

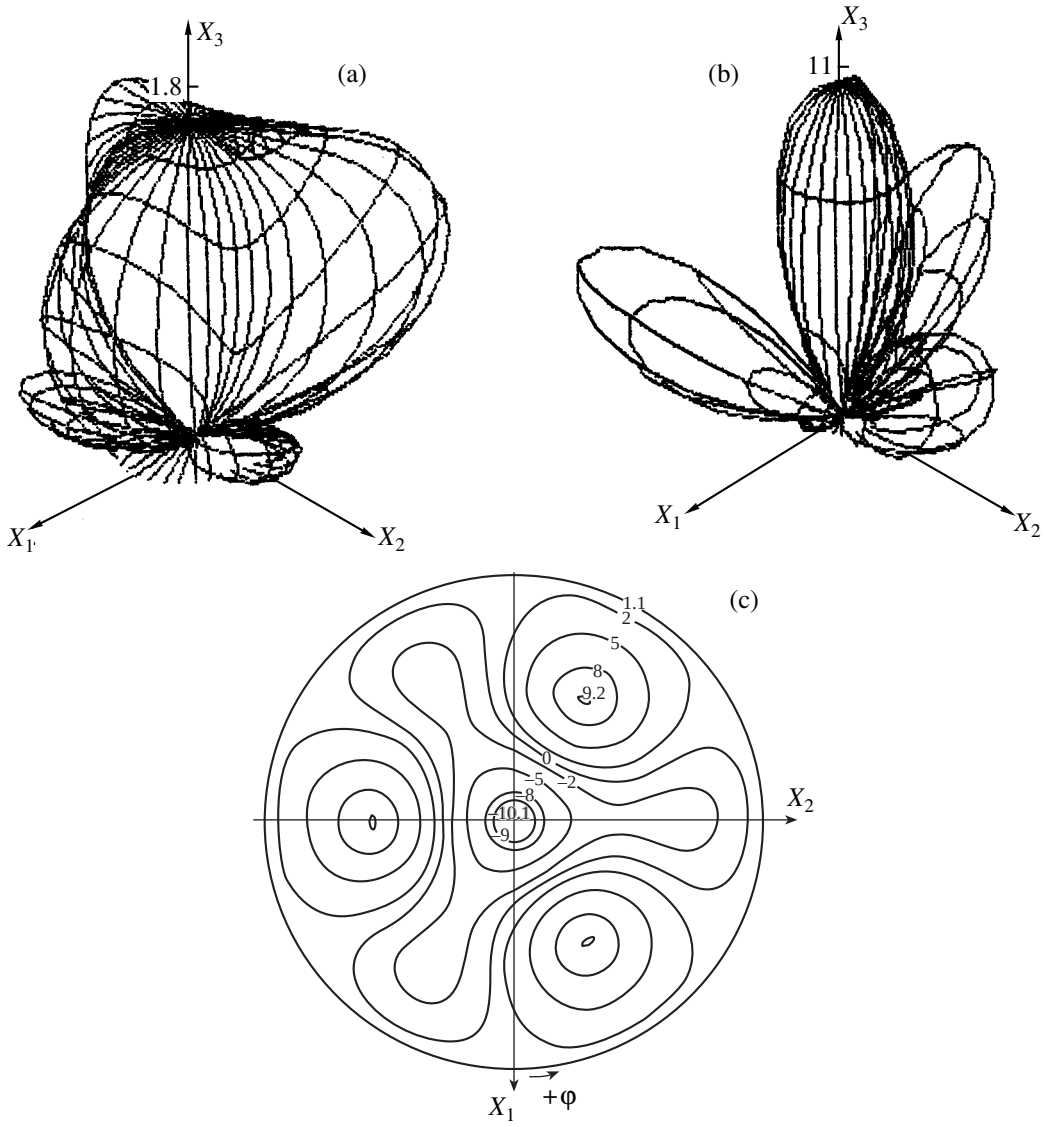

Fig. 2. The general views of (a) the indicative surface of longitudinal POE, π'_{ii}, (b) the corresponding surface of the piezoinduced optical pathlengths $\delta\Delta'_1$, and (c) its stereographic projection for lithium niobate crystals; $\lambda = 0.6328$ μm, $T = 20$°C. All the values are given in 10^{-12} m^2/N; the light and dark regions have the opposite signs.

$$+\{S_{13}(S_{11}+S_{33}-2S_{13}-2S_{44})\sin^2\theta\cos^2\theta$$

$$+(S_{14}/4)\sin 4\theta\sin 3\varphi\}$$

$$\times\left[(\sin^2\theta/n_o^2+\cos^2\theta/n_e^2)^{-\frac{1}{2}}-1\right].$$

2. For the piezooptic surface of light polarization $\pi'^{(i)}_{im}$ (**i** ∥ X'_3 ∥ **r**; **k** ∥ X'_1; **m** ∥ X'_2), we have

$$\delta\Delta'_2 = -\frac{1}{2}\pi'^{(i)}_{im}n'^3_i + S''_{km}(n'_i-1)$$

$$= -\frac{1}{2}\{\pi_{12}\sin^2\theta+\pi_{31}\cos^2\theta-\pi_{41}\sin 2\theta\sin 3\varphi\}$$

$$\times[\sin^2\theta/n_o^2+\cos^2\theta/n_e^2]^{-\frac{3}{2}} \qquad (10)$$

$$+\{S_{12}\cos^2\theta+S_{13}\sin^2\theta+S_{14}\sin\theta\cos\theta\sin 3\varphi\}$$

$$\times\left[(\sin^2\theta/n_o^2+\cos^2\theta/n_e^2)^{-\frac{1}{2}}-1\right).$$

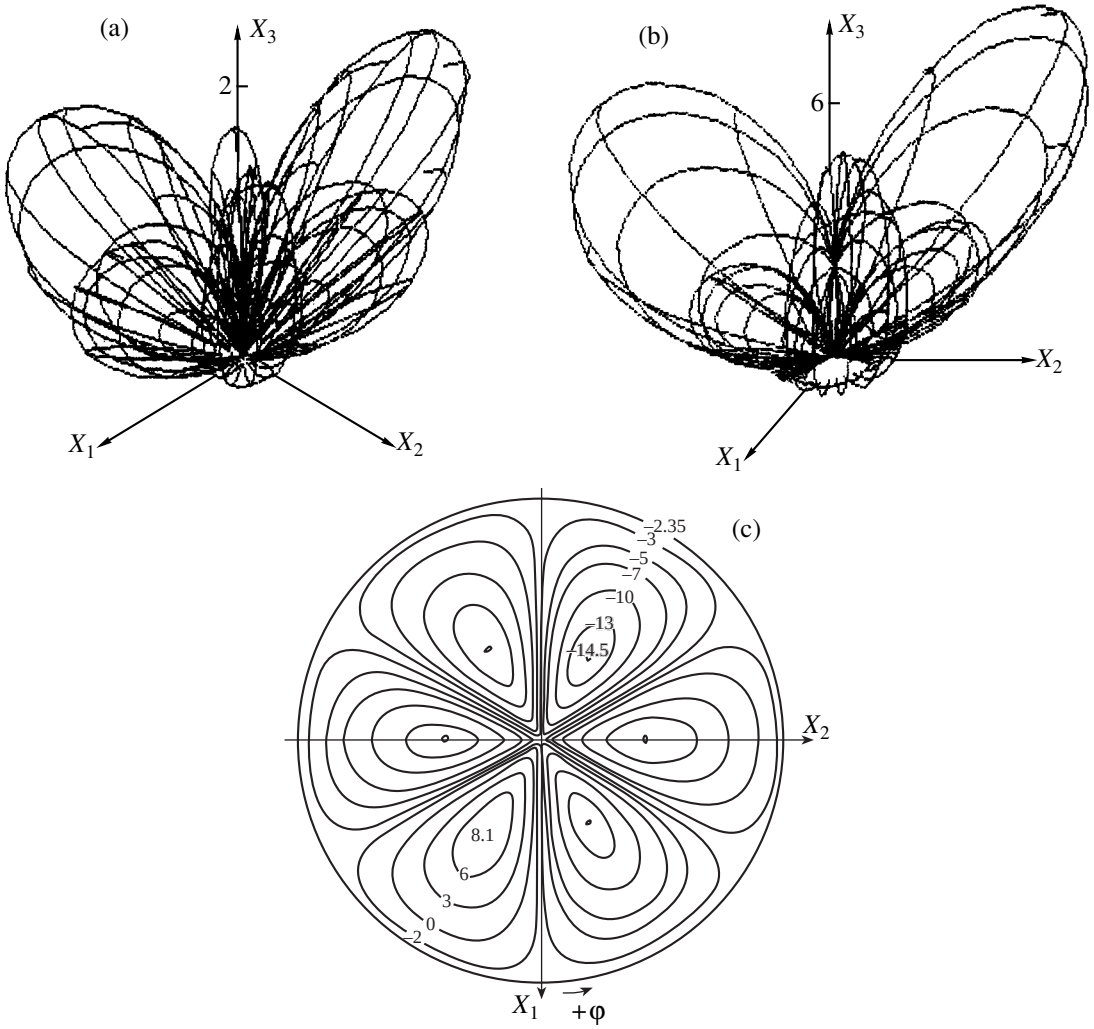

Fig. 3. The same as in Fig. 2 for (a) the indicative piezooptic surface of light polarizations $\pi'^{(i)}_{im}$ and (b) the corresponding $\delta\Delta'_2$ surface. For notation, see Fig. 1.

3. For the piezooptic surface of the mechanical stress $\pi'^{(m)}_{im}$ (**i** ∥ X'_2; **k** ∥ X'_1; **m** ∥ X'_3 ∥ **r**), we have

$$\delta\Delta'_3 = -\frac{1}{2}\pi'^{(m)}_{im} n_o^3 + S'_{km}(n_o - 1)$$

$$= -\frac{1}{2}\{\pi_{12}\sin^2\theta + \pi_{13}\cos^2\theta - \pi_{14}\sin\theta\cos\theta\sin 3\varphi\} n_o^3 \quad (11)$$

$$+ \{S_{13} + (S_{11} + S_{33} - 2S_{13} - 2S_{44})\sin^2\theta\cos^2\theta$$

$$+ (S_{14}/4)\sin 4\theta\sin 3\varphi\}(n_o - 1).$$

Using relationships (9)–(11), we constructed the surfaces of the piezoinduced change in the optical pathlengths in lithium niobate crystal shown in Figs. 2b, 3b, and 4b. In the corresponding calculations, the following values of the piezooptic coefficients (at 10^{-12} m^2/N) were used: $\pi_{11} = -0.47$, $\pi_{12} = 0.11$, $\pi_{13} = 2.0$, $\pi_{31} = 0.47$, $\pi_{33} = 1.6$, $\pi_{14} = 0.7$, $\pi_{41} = -1.9$, $\pi_{44} = 0.21$ from [20], the elastic-compliance coefficients $S_{11} = 5.77$, $S_{12} = -1.77$, $S_{13} = -1.32$, $S_{33} = 4.92$, $S_{14} = -0.853$, $S_{44} = 16.6$ from [21], and the refractive indices $n_o = 2.285$ and $n_e = 2.200$ from [22]. Figures 2c, 3c, and 4c show the stereographic projections of these surfaces (the method of their construction was described in [1]), which allow the quantitative estimation of the effect. For comparison, Figs. 2a, 3a, and 4a show the surfaces of the true piezooptic effects π'_{ii}, $\pi'^{(i)}_{im}$, and $\pi'^{(m)}_{im}$ for lithium niobate crystals [1].

In order to exclude the errors associated with the nonuniqueness of the selection of the coordinate system [24], all the measurements of the piezooptic coefficients, the construction of the surfaces of the piezoinduced change in the optical pathlengths, and the further use of the results obtained should necessarily be performed in the same crystallophysical coordinate system (with due regard for the positive directions of the ayes [23]). It should also be indicated that all the surfaces

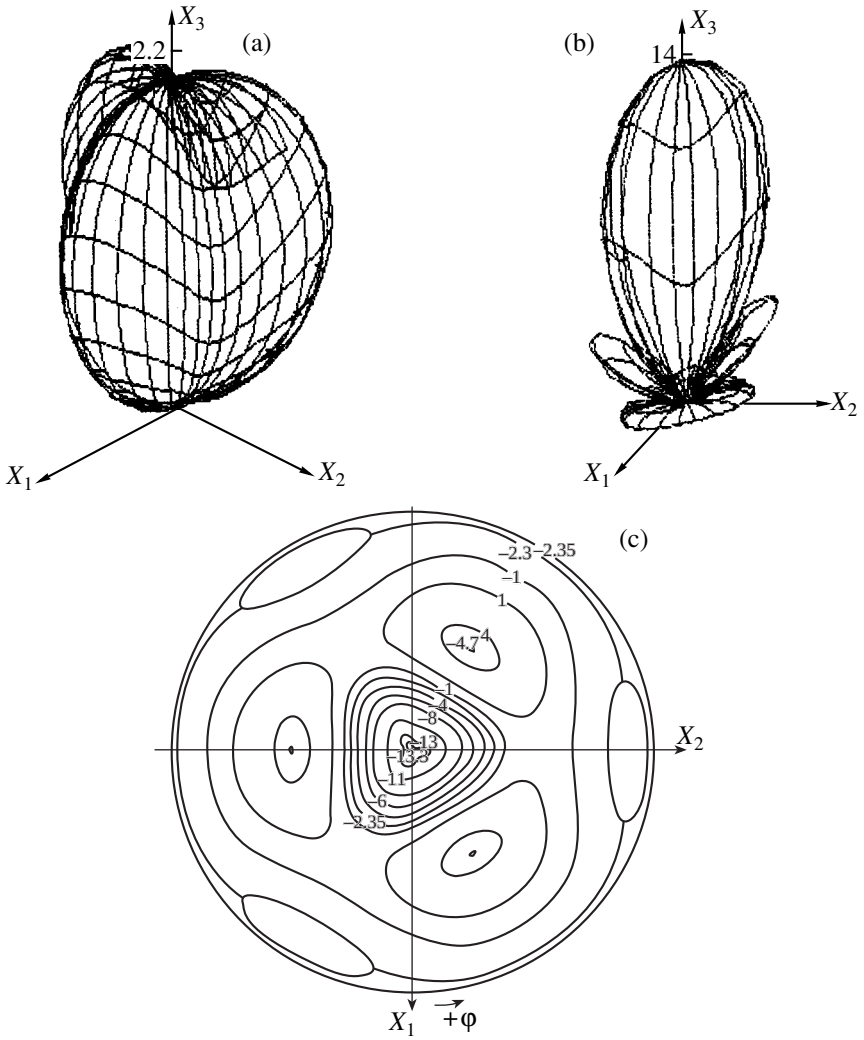

Fig. 4. The same as in Figs. 2 and 3 for (a) the indicative piezooptic surface of the mechanical stress $\pi'^{(m)}_{im}$ and (b) the corresponding $\delta\Delta'_3$ surface. For notation see Fig. 1.

were constructed by the method of the meridian (φ = const) and the equatorial (θ = const) sections in the frontal dimetric (Figs. 3b, 4b) or isometric (all the other figures) view with their subsequent mapping onto the drawing plane. The selection of the image type was dictated by the strive to have the most clear representation of images of each surface. In order to exclude the overlap of invisible lines of the lower and the back parts of the surfaces, only the frontal upper parts of these surfaces are shown in the figures. One can reconstruct the complete three-dimensional view of these surfaces by mapping the figures obtained via the center of the coordinate system.

We should like to emphasize that π'_{im} enters equation (2) with the negative sign, and therefore, in order to compare the π'_{im} and $\delta\Delta'$ surfaces, we changed the signs of the positive and negative effects for the latter surface.

Now, perform comparative analysis of the $\delta\Delta'$ and π'_{im} surfaces for lithium niobate crystals. Since the spatial variation of the refractive index n'_i is insignificant (<4% of n_o), its effect can be ignored in the comparative analysis of the $\delta\Delta'$ and π'_{im} surfaces.

As is seen from the figures, all the surfaces of the piezoinduced optical pathlength in lithium niobate crystals are characterized by considerable anisotropy of the POE effect including the sign reversal.

Similar to the surfaces of the true POE (Figs. 2a, 3a, 4a), the $\delta\Delta'$ surfaces under consideration are not figures of rotation, in full correspondence with the well known German theorem [25]. In accordance with the Curie–Neumann principle [16], these surfaces preserve the main symmetry elements (see the corresponding stereographic projections), namely, a threefold symmetry axis and three symmetry planes normal to the drawing plane, which is characteristic of the crystals of the sym-

Maximum values of the surfaces of piezoinduced change in the optical pathlengths

Surface	Extreme value of $\delta\Delta'$ and its piezooptic and elastic components, 10^{-12} m^2/N			Angular coordinates of the directions of the extreme $\delta\Delta'$ values					
				light polarization, **i**		light propagation, **k**		unidirectional pressure, **m**	
	$\delta\Delta'$	$-\frac{1}{2}\pi'_{im}n'^{3}_{i}$	$S'_{km}(n_i - 1)$	θ	φ	θ	φ	θ	φ
$\delta\Delta'_1$, Fig. 2b	−10.1	−8.5 (84%)	−1.6 (16%)	0°	–*	90°	Arbitrary	0°	–*
$\delta\Delta'_2$, Fig. 3b	−14.5	−12.5 (86%)	−2.0 (14%)	45°	30° 150° 270°	135°	30° 150° 270°	90°	120° 240° 360°
$\delta\Delta'_3$, Fig. 4b	−13.5	−11.9 (88%)	−1.6 (12%)	90°	Arbitrary	90°	Arbitrary	0°	–*

* At $\theta = 0$, the radius-vector **r** coincides with the X_3-axis and therefore no projection of **r** onto the X_1X_2 plane determining the angle φ can exist.

metry class 3*m*. The presence of the threefold axis also follows from the analysis of relationships (10)–(12), where each term includes the factor sin 3φ with a period of 120°.

The analysis of the POE surfaces (Figs. 2a–4a) and the corresponding surface with due regard for elasticity (Figs. 2b–4b) leads to the conclusion that the contribution of elasticity to $\delta\Delta'$ for most of the arbitrary directions, including the principal directions, is comparable with the piezoelectric contribution. In [20], this statement was confirmed only for the principal directions X_1, X_2, X_3 in the crystal. A more pronounced anisotropy is caused by the elasticity contribution, which is seen from the comparison of the π'_{im} and $\delta\Delta'$ surfaces (Figs. 2a, 2b). It is also seen that the negative sheets of the $\delta\Delta'$ surface are much larger than the other ones, whereas the positive part of the surface is elongated. This can be explained by the subtraction of the piezooptic and elastic contributions to $\delta\Delta'$, the radius-vector of this surface, in the vicinity of the isotropic X_1OX_2 plane (this is also confirmed by the calculations performed in [20] for the piezooptic coefficients π_{11} and π_{22}) and *vice versa*, by summation of the contributions from π'_{im} and S'_{km} for the radius-vector located in the vicinity of the optical axis X_3 (this is also confirmed by the calculation of these contributions for the coefficient π_{33} in [20]). The considerable change in anisotropy associated with allowance for the elasticity contribution is also seen from the comparison of Figs. 4a and 4b. Figure 4b shows the changes in the optical pathlengths having different signs, whereas the optical pathlengths on the surface in Fig. 4a have the same signs.

The $\delta\Delta'$ dependences are described by rather complicated equations, and therefore we failed to calculate the corresponding extreme values that were for the $\pi'^{(i)}_{im}$ and $\pi'^{(m)}_{im}$ surfaces as we did in [1]. Therefore, these values were determined with the aid of the Wulff nets from the corresponding stereographic projections (Figs. 2c–4c) and then were tabulated. It is seen from this table that the maximum piezoinduced change in the optical pathlength is observed for the dependence $\delta\Delta'_2$. At the same time, it is seen that the maximum values of all three dependences are comparable. However, in practice, the most important dependences are $\delta\Delta'_1$ and $\delta\Delta'_3$, because their maximum values correspond to the experimental geometry, where the directions of **i**, **m**, and **k** coincide with the directions of the principal axes. It is remarkable that the elastic and piezooptic contributions for the extreme values of all the dependences are also comparable, with the latter contribution being six–seven times higher than the others ones. Moreover, the analysis of the extreme values of the π'_{im} [1] and $\delta\Delta'$ [1] dependences shows that the extreme values of the longitudinal piezooptic effect θ and the correspondent π'_{ii} dependence are characterized by different $\delta\Delta'_1$ values ($\theta \approx 40°$, Fig. 2a and $\theta = 0°$, Fig. 2b).

For all three $\delta\Delta'$ surfaces considered in this article, there exist numerous directions and experimental piezooptic conditions for which the effect has the zero value (this corresponds to zero isolines on the stereographic projections). This signifies that one can always set experimental conditions such that the piezoinduced change in the optical pathlength would be zero.

Concluding the article, we should like to indicate that the approach based on the spatial summation or separation of two different simultaneously induced effects in anisotropic materials can also be used for other purposes, e.g., for taking into account the electrically-induced deformation of specimens in electrooptic studies.

REFERENCES

1. A. S. Andrushchak, B. G. Mytsyk, and O. V. Lyubich, Ukr. Fiz. Zh. (Russ. Ed.) **37** (8), 1217 (1992).
2. A. S. Andrushchak and B. G. Mytsyk, Ukr. Fiz. Zh. (Russ. Ed.) **40** (11), 1222 (1995).
3. B. G. Mytsyk, A. S. Andrushchak, N. V. Dem'yanishin, *et al.*, Kristallografiya **41** (3), 500 (1996) [Crystallogr. Rep. **41** (3), 472 (1996)].
4. B. G. Mytsyk and A. S. Andrushchak, Kristallografiya **41** (6), 1054 (1996) [Crystallogr. Rep. **41** (6), 1001 (1996)].
5. N. A. Romanyuk, B. G. Mytsyk, and L. N. Kulyk, Ukr. Fiz. Zh. (Russ. Ed.) **31** (3), 354 (1986).
6. F. Pockels, *Lehrbuch der Kristallooptik* (Teubner, Berlin, 1906).
7. B. R. Eppendahl, Ann. Phys. **4–61** (2), 591 (1920).
8. S. Haussuhl and K. Uhl, Z. Kristallogr. **128**, 418 (1969).
9. K. Shahabuddin and T. S. Narasimhamurty, Solid State Commun. **43** (12), 941 (1982).
10. H. E. Pettersen, J. Opt. Soc. Am. **63** (10), 1243 (1973).
11. A. Feldman, Opt. Eng. **17** (5), 453 (1978).
12. A. Wardzynski, J. Phys. C: Solid State Phys. **3** (6), 1251 (1970).
13. T. S. Narasimhamurty, J. Opt. Soc. Am. **59** (6), 682 (1969).
14. K. Vedam, Proc. Ind. Acad. Sci. A **34**, 161 (1951).
15. R. M. Waxler and E. N. Zarabaugh, J. Res. Nat. Bur. Stand.–J. Phys. Chem. A. **74** (2), 215 (1970).
16. Yu. I. Sirotin and M. P. Shaskol'skaya, *Foundations of Crystal Physics* [in Russian] (Nauka, Moscow, 1979).
17. Sh. M. Butabaev, N. V. Perelomova, and I. I. Smyslov, Kristallografiya **17** (3), 678 (1972).
18. Sh. M. Butabaev and I. I. Smyslov, Kristallografiya **16** (4), 796 (1971).
19. A. A. Chernov, E. I. Givargizov, Kh. S. Bagdasarov, *et al.*, *Modern Crystallography. vol. 3. Crystal Growth* (Nauka, Moscow, 1981; Springer, Berlin, 1984).
20. B. G. Mytsyk, Ya. V. Pryriz, and A. S. Andrushchak, Cryst. Res. Technol. **26** (7), 931 (1991).
21. U. A. Weakliem, W. J. Burke, D. Redfield, *et al.*, RCA Rev. **36** (1), 149 (1975).
22. D. Smith and N. Riccius, Opt. Commun. **17** (3), 332 (1976).
23. B. G. Mytsyk and A. S. Andrushchak, Ukr. Fiz. Zh. (Russ. Ed.) **38** (7), 49 (1993).
24. B. G. Mytsyk and A. S. Andrushchak, Kristallografiya **35** (6), 1574 (1990).
25. V. L. German, Dokl. Akad. Nauk SSSR **48** (2), 95 (1945).

Translated by L. Man

Crystallography Reports, Vol. 45, No. 1, 2000, pp. 145–147. Translated from Kristallografiya, Vol. 45, No. 1, 2000, pp. 151–153.

Elastic, Piezoelectric, and Dielectric Properties of α-GeO_2 Single Crystals

D. B. Balitskiĭ*, O. Yu. Sil'vestrova, V. S. Balitskiĭ***, Yu. V. Pisarevskiĭ**, D. Yu. Pushcharovskiĭ*, and E. Philippot******

** Moscow State University, Vorob'evy gory, Moscow, 119899 Russia*

*** Shubnikov Institute of Crystallography, Russian Academy of Sciences, Leninskiĭ pr. 59, Moscow, 117333 Russia*

**** Institute of Experimental Mineralogy, Russian Academy of Sciences, Chernogolovka, Moscow oblast, 142432 Russia*

***** Laboratoire de Physicochemie des Materiaux Solides, Montpellier Cedex 5, F-34095 France*

Received June 18, 1999

Abstract—The elastic, piezoelectric, and dielectric characteristics of α-GeO_2 crystals are studied at room temperature. The measurements were performed by the resonance method on crystals grown on α-quartz seeds from solutions in the recirculating mode. In germanium dioxide crystals, the piezoelectric moduli have high values. The characteristic features of variations of the electromechanical and elastic properties in crystals with the quartzlike structure observed earlier are confirmed. *© 2000 MAIK "Nauka/Interperiodica".*

The trigonal α-phase of germanium dioxide crystals is similar to the well-studied α-phase of quartz and other compounds described by this structural type (berlinite, gallium phosphate, etc.) All these materials, first and foremost α-quartz, are widely used in piezoelectric technology. Up to now, in spite of the great importance of germanium and silicon for geochemistry and crystal chemistry, the properties of germanium dioxide crystals have not been sufficiently studied because of the difficulties encountered in the growth of α-GeO_2 single crystals. Recently, a special method for the growth of these crystals from solutions in the recirculating mode has been developed [1]. In turn, this allowed the measurements of the elastic parameters of α-GeO_2 crystals by the Mandel'shtam–Brillouin method [2]. According to [3], the α-modifications of SiO_2 and GeO_2 are characterized by compressibility higher than in comparison with many other oxides.

All these facts explain a considerable interest to the study of elastic, piezoelecrtic, and dielectric properties of the α-GeO_2. Below, we report the results of such a study.

Germanium dioxide crystals for experiments were grown by the hydrothermal method on silicon dioxide seeds (α-quartz) [1]. The crystals grown had the dimensions 12–4 × 6–10 × 4–8 mm. The specimens were the *X*-, *Y*-, and *Z*-cuts of the crystals and also the rods oriented as is shown in the figure. All the specimens had silver electrodes applied as is shown in figure.

The dielectric constants were calculated from the measured capacitance of *X*-, *Y*- and *Z*-cuts on an automated capacitance bridge in a 100–200 V/cm electric field at a frequency of 1 kHz. Simultaneously, the tangent of the angle dielectric losses was also measured.

The electromechanical properties of α-GeO_2 crystals were studied by resonance methods [1]. The application of HF electromagnetic signals to the electrodes excites the oscillation modes related to certain piezoelectric moduli or constants, in full accordance with the matrix of piezoelectric constants. Measuring the resonance and antiresonance frequencies of the correspond-

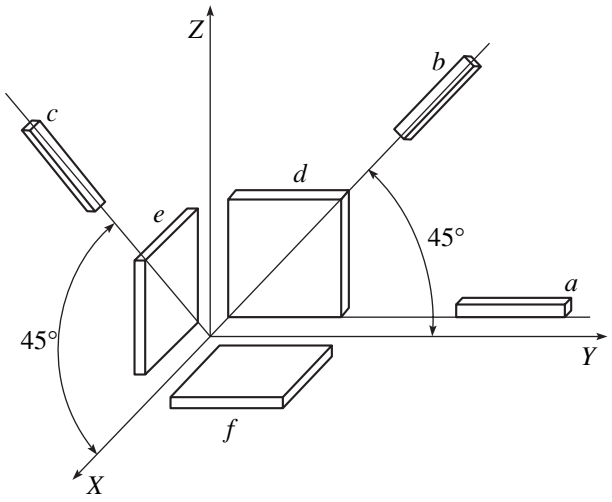

Shape and orientation of the specimens of α-GeO_2 crystals used for electromechanical measurements by the resonance method and dielectric measurements: *a*—(*XYtwl*)-0°/0°/0°; *b*—(*XYtwl*)-45°/0°/0°; *c*—(*YZtwl*)-45°/0°/0°; *d*—*X*-cut; *e*—*Y*-cut; and *f*—*Z*-cut.

1063-7745/00/4501-0145$20.00 © 2000 MAIK "Nauka/Interperiodica"

Table 1. Electromechanical properties of α-GeO_2 crystals

Oscillation mode (figure)	Frequency constant, kHz mm	s^E_{ik}, 10^{-12} m^2/N	c^D_{ik}, 10^{10} N/m^2	$10^2\,k_{cm}$
Compression-extension oscillations of the rod *Y*-cut (*XYtwl*) – 0°/0°/0°	1876.5	s_{11} = 16.588		k_{12} = 15.4*
Compression-extension oscillations of the rod cut (*XYtwl*) – 45°/0°/0°	2074.4	s'_{22} = 13.574		k_{12} = 21.2*
Compression-extension oscillations of the rod cut (*YZtwl*) – 45°/0°/0°	2341.2	s'_{11} = 10.656		k_{23} = 8.9*
Compression-extension oscillations of the *X*-cut	1935.5–1974.8		c^D_{11} = 6.413	k_t = 3.4**
Shear oscillations along the thickness of the *Y*-cut	1206.1–1211.7		c^D_{66} = 2.490–2.514	k_{26} = 7.01**

* $k^2_{cm}/(k^2_{cm}-1) = (\pi f_{aR}/2f_R)\,\mathrm{cotan}(\pi f_{aR}/2f_R)$.

** k^2_t and $k^2_{26} = (\pi f_{aR}/2f_R)\tan(\pi\Delta f/2f_{aR})$, where $\Delta f = f_{aR} - f_R$.

Table 2. Comparison of the properties of quartzlike materials

Parameters	SiO_2	$AlPO_4$	$GaPO_4$	GeO_2
a, *c*, Å	4.9121	4.937	4.899	4.984
	5.4044	10.926	11.034	5.660
ρ, g/cm^3	2.655	2.640	3.570	4.28
⟨*r*⟩-averaged ionic radius	0.26	0.28	0.32	0.39
T–*O*–*T*, deg	143.7	142.4	134.6	130.0
d_{11}, 10^{-12} C/N	2.31	3.30	4.5	4.04
d_{14}, 10^{-12} C/N	0.727	1.62	1.94	3.82
c_{11}, 10^9 N/m^2	86.79	64.88	66.6	66.4*
				64.8
c^{12}, 10^9 N/m^2	6.79	8.98	21.8	21.3*
c_{13}, 10^9 N/m^2	12.01	14.6	24.9	32*
c^{33}, 10^9 N/m^2	105.79	87.4	102.1	118*
c_{44}, 10^9 N/m^2	58.21	43.12	37.7	36.8*
				37.4
c_{14}, 10^9 N/m^2	18.12	–12.17	3.9	2.2*
				11.7
c_{66}, 10^9 N/m^2	40.0	27.95	22.4	22.53*
				21.10
$\varepsilon_{11}/\varepsilon_0$	4.45		5.2	7.43
$\varepsilon_{33}/\varepsilon_0$	4.6		5.1	6.65

* Data [2].

ing oscillation modes (the frequencies of "in-parallel" and "in-series" resonances), we also determined the frequency constants, the acting elastic moduli, and the coefficients of the electromechanical coupling (Table 1). Using the dielectric constants determined, the data listed in Table 1, and the relationships [4]

$$d_{11} = -d_{12} = k_{12}(s^E_{11}\varepsilon^T_{11})^{1/2},$$

$$d_{14} = 2k_{23}(s^E_{33}\varepsilon^T_{11})^{1/2},$$

$$e_{11} = e_{26} = k_{26}(c^D_{66}\varepsilon^S_{11})^{1/2} = k_t(c^D_{11}\varepsilon^S_{11})^{1/2},$$

$$e_{14} = d_{14}c^E_{44} + 2d_{11}c^E_{14},$$

we determined the components of the tensor of piezoelectric moduli and the constants. These data are listed

in Table 2 together with the dielectric and elastic parameters of the α-phase of germanium dioxide. For comparison, the same data for quartz and other crystals of the berlinite group with the quartzlike structure are also indicated in Table 2. The structural parameters of α-GeO_2 in Table 2 were obtained in the refinement of the crystal structure based on the X-ray diffraction data (Sintex *P*-1 diffractometer, 446 reflections with $|F| > 3\sigma|F|$, $R = 0.041$) and are in agreement with the known data.

Table 2 indicates the *T–O–T* angle formed by the tetrahedrally coordinated cations, which determines, according to [5], the possible changes in the elastic and piezoelectric properties of quartzlike materials.

The data listed in Table 2 show a considerable increase of the piezoelectric moduli d_{11} and d_{14} in GeO_2 crystals in comparison with their values in quartz. Different properties of these compounds are not accidental, because the *c*/*a* ratio for GeO_2, 1.1356, considerably exceeds this value for SiO_2, 1.1007, thus indicating a more pronounced distortion of Ge-tetrahedra [3]. It was indicated in [5] that the *T–O–T* angle can be used as a criterion of the structural distortion of quartzlike compounds, because it is a linear function of the *c*/*a* ratio: a decrease in the *T–O–T* angle is accompanied by an increase of the *c*/*a* ratio and the angle of rotation of the tetrahedra around the two-fold axes. According to [4], the density and the elastic and the piezoelectric constants of compounds with the α-quartz structure show the linear correlation with the *T–O–T* angles. However, an assumption [5] about an increase of the coefficient of electromechanical coupling with a decrease of the angle between the tetrahedra is not quite correct for GeO_2, which, we believe, is associated with its considerably higher dielectric constant.

On the whole, the correlation between the physical properties and structural characteristics can be interpreted on the basis of simple crystallochemical principles: an increase of the mean radius of a tetrahedral cation (*T*) [6] provides the baric deformation of the α-quartz structure, which is accompanied by an increase of the piezoelectric moduli for compounds of this series.

Thus, we revealed that the piezoelectric moduli of germanium dioxide crystals are very high. We also confirmed the specific features of the changes in the electromechanical and elastic properties of quartzlike compounds established earlier.

REFERENCES

1. D. V. Balitskiĭ, D. Yu. Pyshcharovskiĭ, and V. S. Balitskiĭ, in *Proccedings of the International Conference on Crystals: Growth, Properties, Structure, and Application* (Aleksandrov, Russia, 1997), Vol. 1, p. 512.
2. M. Glimsditch, A. Polian, V. Brazhkin, *et al.*, J. Appl. Phys. **83**, 3018 (1998).
3. J. Glinnemann, H. E. King, H. Schulz, *et al.*, Z. Kristallogr. **198**, 177 (1992).
4. A. A Kaminskiĭ, I. M. Sil'vestrova, S. E. Sarkisov, *et al.*, Phys. Status Solidi A **80**, 607 (1983).
5. E. Philippot, D. Palmier, M. Pintard, *et al.*, J. Solid State Chem. **123**, 1 (1996).
6. R. D. Shannon, Acta Cryst. A **32**, 751 (1976).

Translated by A. Zalessky

Crystallography Reports, Vol. 45, No. 1, 2000, pp. 148–149. Translated from Kristallografiya, Vol. 45, No. 1, 2000, pp. 154–155.

Anisotropy of the Optical Suppression of the Magnetoplastic Effect in NaCl Single Crystals

Yu. I. Golovin*, R. B. Morgunov*, A. A. Dmitrievskiĭ*, and S. Z. Shmurak**

** Derzhavin Tambov State University, Tambov, 392622 Russia*
e-mail: victor@tgpi.tambov.ru

*** Institute of Solid-State Physics, Russian Academy of Sciences, Chernogolovka, Moscow oblast, 142432 Russia*

Received April 8, 1998

Abstract—Anisotropy of the plane-polarized light effect on magnetosensitive point defects in NaCl crystals has been observed. The data obtained may yield the information on the symmetry of the electronic states of these defects. © *2000 MAIK "Nauka/Interperiodica".*

Earlier, we have established that the paths of magnetically induced dislocations (the field induction B = 7 T) in crystals preliminarily exposed to a monochromatized light of a certain wavelength [1]. It was shown [2] that this magnetoplastic effect is associated with the change of states of photo- and magnetosensitive point defects. At present, there is no information about the atomic and electronic states of these defects. However, if is well known that they are metastable [3]. Usually, metastable defects in ionic crystals have a complex structure; i.e., they can consist of several extrinsic or intrinsic defects and contain impurity-vacancy dipoles. The defects of such types are usually characterized by the anisotropy of their physical properties. Therefore, it can be assumed that the efficiency of the photoexcitation of magnetosensitive centers and the dislocation mobility in crystals is dependent on the orientation of the polarization plane of light. We had the aim to study the dependence of the efficiency of the optical suppression of the magnetoplastic effect on the orientation of the polarization plane of the light with respect to the main crystallographic directions.

In the experiments, we used nominally pure $3 \times 3 \times$ 5-mm-large NaCl single crystals. Prior to the introduction of dislocations and the application of a magnetic field, the crystals were exposed for 15 min to polarized and nonpolarized light at the wavelength of 350 nm, which provided the maximum suppression of magnetoplasticity in the NaCl crystals. Then, edge dislocations were induced by a conventional technique of scratching crystal surfaces. The field-induced dislocation displacements were revealed by the method of double chemical etching. Magnetic-field pulses had the shape of a half-period of the sinusoid with an amplitude of 7 T and a duration of 10^{-2} s. We studied the mobility of only those edge dislocations whose Burgers vector was perpendicular to the direction of light propagation. The numbers N_1, N_2, N_3, and N_4 of dislocations displaced under the effect of the magnetic field along the $[\bar{1}10]$, [110], $[1\bar{1}0]$, and $[\bar{1}\bar{1}0]$ directions were normalized to the total number of displaced dislocations ΣN_i and, thus, the numbers of dislocations moving in each slip plane were determined.

In the first series of experiments, the crystals were exposured to the nonpolarized light and the numbers of dislocations displaced along all the above directions [perpendicular to the direction of light propagation (Fig. 1a)] were the same. In the second series of experiments, we used the polarized light, and it was found that the numbers of dislocations displaced along the $[\bar{1}10]$ and $[1\bar{1}0]$ directions are equal to $n_1 = (N_1 + N_3)/\Sigma N_i$; the numbers of dislocations displaced along the [110] and $[\bar{1}\bar{1}0]$ directions are equal to $n_2 = (N_2 + N_4)/\Sigma N_i$ (Fig. 1b). The ratio n_1/n_2 depends on the angle α formed by the polarization plane of light and the (100) plane of the crystal (Fig. 2). The maximum difference between the n_1 and n_2 values is observed at $\alpha = 45°$,

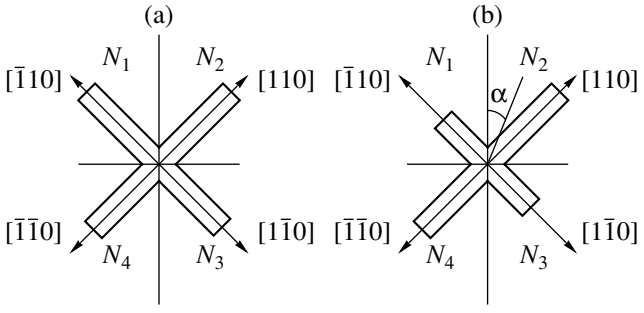

Fig. 1. Illustration of the displacements of N_i dislocations along four crystallographic directions in crystals in a magnetic field: (a) not exposed to light; (b) preliminarily exposed to a polarized light with the polarization plane forming an angle of $\alpha = 45°$ with the (100) plane.

1063-7745/00/4501-0148$20.00 © 2000 MAIK "Nauka/Interperiodica"

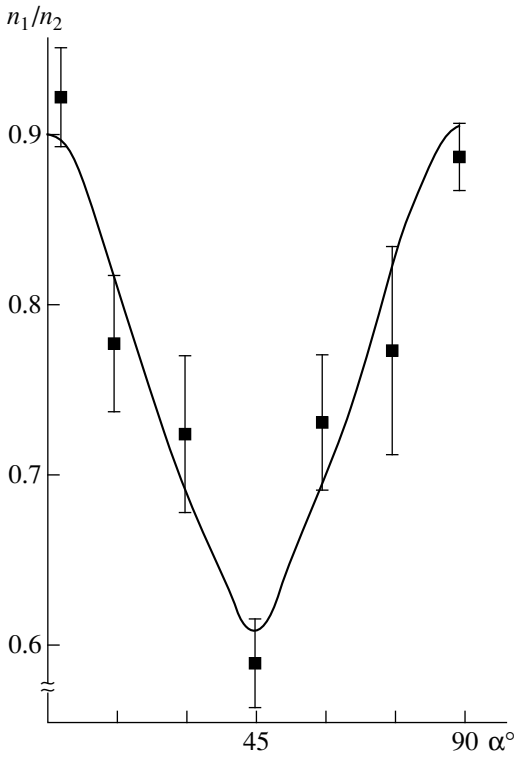

Fig. 2. Total number n of dislocations displaced along the $[\bar{1}10]$ and $[1\bar{1}0]$ directions normalized to the total number n_2 of dislocations displaced along the [110] and $[\bar{1}\bar{1}0]$ directions as a function of angle α formed by the plane of the light polarization with the (100) plane.

$n_1 \approx 0.4$, and $n_2 \approx 0.6$. At $\alpha = 0°$, $n_1 = n_2 \approx 0.5$. There were no noticeable changes in the dislocation paths with the change in the polarization-plane orientation. Thus, the orientation of the polarization plane of light during photoexposure affects only the fraction of dislocations displaced in an applied magnetic field.

Since the crystals were exposed to light prior to the introduction of fresh dislocations, the observed anisotropy of the magnetoplastic effect can be attributed to the anisotropy of magnetosensitive point defects, which seem to possess a lower symmetry than the crystal lattice. Under this assumption, the observed anisotropy in dislocation displacements can be interpreted as follows. Polarized light affects only those chaotically oriented anisotropic defects which possess the orientation favorable for excitation. Therefore, a certain time after light irradiation for the destruction of light-induced order in the defect subsystem by thermal fluctuations, dislocations are decelerated only by some of the initially oriented defects. Since the efficiency of dislocation interactions with the anisotropic defects depends on their orientation with respect to the slip plane [4], one can expect the anisotropy in the dislocation motion determined by the orientation of the polarization plane with respect to the crystallographic axes.

As was shown in [2], the influence of the preliminary light irradiation on the magnetoplastic effect can be explained by a reconstruction of the electronic state of the point defects, therefore, the experimental data described above can be considered as information on the symmetry of this state.

ACKNOWLEDGMENTS

This study was supported by the Russian Foundation for Basic Research, project no. 97-02-16074.

REFERENCES

1. Yu. I. Golovin, R. B. Morgunov, and S. E. Zhulikov, Vestn. Tambovskogo Gos. Universiteta, Ser. Estestvenno-Tekhnicheskaya **2**, 101 (1997).
2. Yu. I. Golovin, R. B. Morgunov, M. V. Badylevich, and S. Z. Shmurak, Fiz. Tverd. Tela (St. Petersburg) **39**, 1389 (1997).
3. Yu. I. Golovin, R. B. Morgunov, and V. E. Ivanov, Fiz. Tverd. Tela (St. Petersburg) **39**, 2016 (1997).
4. M. Czapelski and M. Suszynska, Phys. Status Solidi B **132**, 409 (1985).

Translated by V. Tokarev

Crystallography Reports, Vol. 45, No. 1, 2000, pp. 150–153. Translated from Kristallografiya, Vol. 45, No. 1, 2000, pp. 156–159.

PHYSICAL PROPERTIES OF CRYSTALS

Effect of Magnetic Field on Anelasticity of KBr Crystals

N. A. Tyapunina[1], V. L. Krasnikov[2], and É. P. Belozerova[2]

[1] *Moscow State University, Vorob'evy gory, Moscow, 119899 Russia*

[2] *Kostroma State Technological University, Kostroma, Russia*

Received May 20, 1998

Abstract—The effect of a weak (0.2 T) magnetic field on the amplitude dependences of the internal friction and the defect of Young's modulus in KBr crystals has been studied. It is shown that, under the action of the magnetic field, the internal friction increases and the effective elastic modulus decreases, thus indicating an increase of sample plasticity. The preliminary treatment of the samples in a magnetic field results in the inverse effect—hardening. © *2000 MAIK "Nauka/Interperiodica".*

1. INTRODUCTION

At present, much attention is paid to the effect of magnetic fields on the mechanical properties of dielectrics, semiconductors, and metals. Most of the experiments study the behavior of dislocations during the active loading of crystals or creeping (see, for example, [1, 2] and review [3]).

We studied the effect of a weak magnetic field on anelasticity of KBr crystals during their sign-reversed loading in the kilohertz frequency range. Anelasticity of crystals in this frequency range are controlled by the dislocation mechanisms, and the effect of a magnetic field was studied under the conditions when dislocation segments are forced to oscillate under the effect of ultrasound.

2. EXPERIMENTAL

Anelasticity of KBr crystals were studied by the method of a two-component resonance oscillator [4]. Sample vibrations excited a longitudinal ultrasonic standing wave along sample length. We used a frequency of 54 kHz; the strain amplitudes ε_0 ranged from 10^{-6} to 10^{-3}. The internal friction, δ, and the defect of Young's modulus $\Delta M/M$ (hereafter called modulus defect) were measured in vacuum under a residual air pressure of 0.13 Pa at room temperature. The measurement error did not exceed 2%. The magnetic field was created by a permanent magnet with the induction B = 0.2 T.

The state of the sample was checked by performing selective etching and constructing the current–voltage characteristics of an oscillator. The current–voltage characteristic $I(V)$ of a two-component oscillator is, in fact, the dependence of the current I in quartz (for "in-series resonance") on the voltage V applied to its contacts. The current I is proportional to the strain amplitude, ε_0, and the tangent of the slope of the current–voltage characteristic with respect to the current axis is proportional to the internal friction [5]. Using the $I(V)$ curve, one can determine (with a high accuracy) the amplitudes ε_0 giving rise to changes in the dislocation behavior. Comparing the current–voltage characteristics for various samples, one can compare the plasticity of various samples. The analysis of the current–voltage characteristics also provides the determination of some quantitative parameters of the dislocation structure in the crystal [5].

The studies were performed in two modes. In the first one, both magnetic field and ultrasonic fields were applied simultaneously. In the second mode, the samples were preliminarily treated in a magnetic field. Then, the current–voltage characteristics were measured and the internal friction and defect of Young's modulus were measured at the zero field. The results thus obtained were compared with the corresponding data for a control sample not treated in a magnetic field.

The yield point of KBr samples was 9×10^5 Pa, the initial dislocation density was equal to 3×10^9 m^{-2}. The total amount of bivalent impurities calculated from the temperature dependence of conductivity was equal to 8.2×10^{-7} mol parts. The spectral analysis showed that the main bivalent impurity was Ca.

3. RESULTS

3.1. Effect of Magnetic Field on Current–Voltage Characteristics Oscillator with KBr Crystal

The typical current–voltage characteristics for an oscillator with KBr crystal obtained under (curve *1*) the simultaneous effect of a magnetic field and the ultrasound (curve *2*) in the zero field and (curve *3*) after the preliminary 3.5 h-treatment of the samples in a magnetic field are shown in Fig. 1. It is seen that curve *1* (the simultaneous action of a magnetic field and the ultrasound) is located much lower than the two other curves, thus indicating that the magnetic field increases the sample plasticity.

1063-7745/00/4501-0150$20.00

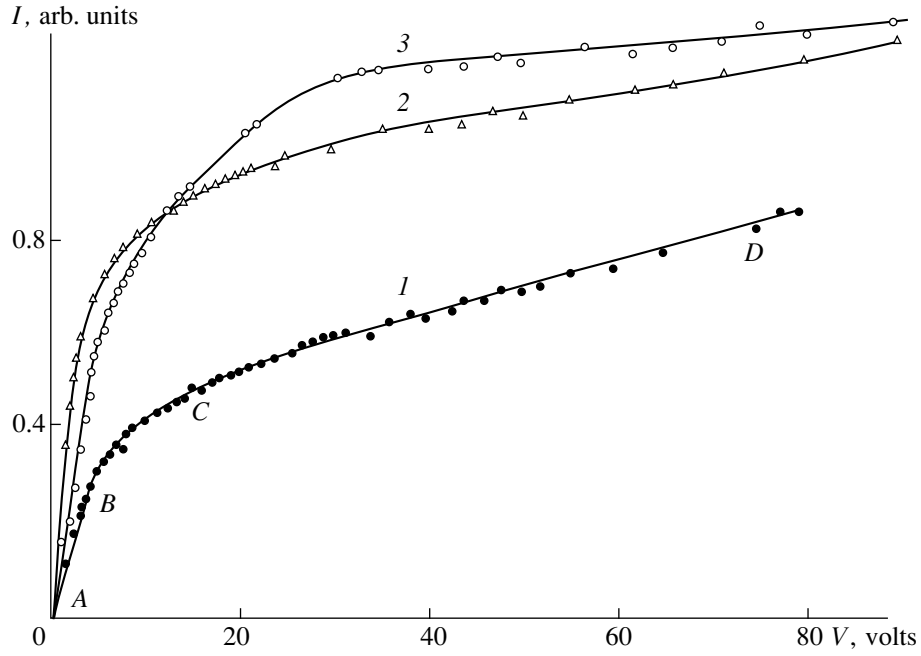

Fig. 1. Current–voltage characteristics $I(V)$ of the two-component oscillator with KBr samples: (*1*) a sample in the magnetic field during measurements; (*2*) a sample in the initial state; (*3*) a sample treated in a magnetic field prior to measurements.

The preliminary 3.5 h exposure of the sample to the magnetic field (curves *3*, *2*) provided its strengthening. It should be indicated that the corresponding samples (curves *1*, *2*) had mirror-smooth cleavages. All these curves (Fig. 1) had three segments. We consider them for curve *1*. The linear part *AB* of curve *1* corresponds to low values of the applied voltage *V*. The nonlinear segment *BC* is smoothly transformed into the asymptotic segment *CD*. Using the method from [5] and extrapolating this segment of the curve to the *I*-axis, one can estimate the stress τ^{st} that should be overcome by dislocation segments at this stage of ultrasound application. According to [6], τ^{st} are the values of the generalized Peierls–Nabarro barriers (their estimated values are listed in table). It is seen that the application of the magnetic field reduces the τ^{st} values. Since τ^{st} is proportional to the yield point [7], one can state that the magnetic field decreases the yield stress. On the other hand, the preliminary treatment of samples in magnetic fields strengthen the sample, so the τ^{st} value of the magnetically treated sample exceeds the corresponding value of the control sample.

3.2. The Effect of Magnetic Field on the Amplitude Dependence of Internal Friction in KBr

The current–voltage characteristics show that the effect of a magnetic field on the amplitude-dependent internal friction depends on the experimental conditions. Figure 2 shows typical amplitude dependences $\delta(\varepsilon_0)$ for KBr samples obtained in the 0.2 T magnetic field and in the zero field, and also for samples treated in a magnetic field prior to measurement (curves *1*, *2*, *3*, respectively).

As was shown above, the simultaneous effect of the magnetic and ultrasonic fields plasticizes the sample.

Starting stresses τ^{st}, amplitudes ε_0 corresponding to the beginning of the amplitude dependence of internal friction, characteristic unpinning strain Γ, and the average displacements of oscillating dislocation segments $\langle u \rangle$ under various experimental conditions

Parameters	Experimental conditions		
	B = 0.2 T	B = 0	3.5 h treatment in a 0.2 T magnetic field prior to measurements
τ^{st}, MPa^2	26.4	57.7	67.8
ε_0, 10^{-4}	1.2	2.8	3.4
Γ, 10^{-4}	6.2	21.7	9.0
$\langle u \rangle$, μm	1.1	0.37	0.14

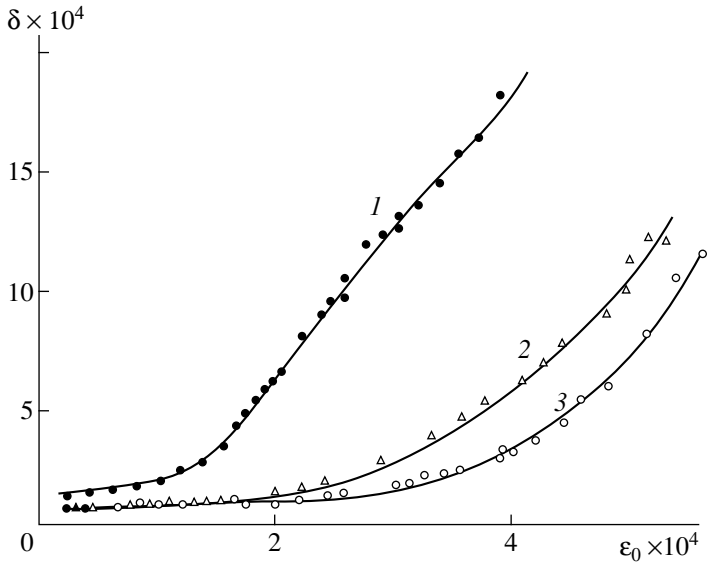

Fig. 2. Effect of a magnetic field on the variations of the internal-friction amplitude for KBr samples. For notation, see Fig. 1.

Figure 2 shows that the amplitude dependence of the internal friction for such a sample shifts towards lower amplitudes ε_0, whereas the amplitude-dependent internal friction becomes considerably higher than the internal friction of the control sample.

Comparing curves *2* and *3* in Fig. 2, we see that the preliminary treatment for 3.5 h of the sample in a 0.2 T magnetic field reduces its amplitude-dependent internal friction in comparison with the internal friction of the control sample. The amplitude dependence shifted towards higher ε_0 values. This confirms once again the fact of sample strengthening upon the preliminary treatment in a magnetic field.

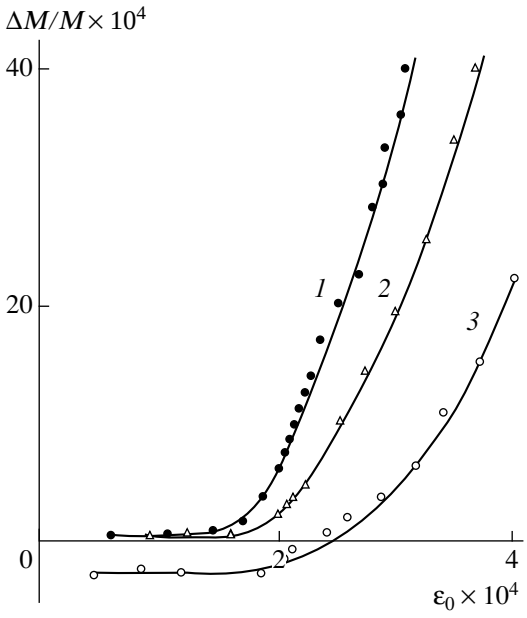

Fig. 3. Effect of a magnetic field on the amplitude variations of the defect of Young's modulus for KBr samples. For notation, see Fig. 1.

The amplitudes of relative stresses ε_0 at the antinode of an ultrasound standing wave, which provide the amplitude dependence on the internal friction in KBr samples under various conditions of the tests, are indicated in the table.

The decrease of internal friction in samples preliminary treated in a pulsed magnetic field was also observed for stannic bronze at the frequency of 1 Hz [8]. It was assumed [8] that this effect was determined by the change in the "impurity–defect atmosphere" around the dislocation caused by the magnetic field. In the Granato–Lücke coordinates [9], the $\delta(\varepsilon_0)$ curves become straight lines, which indicates that internal friction is controlled by interactions between dislocations and pinning centers. Processing of the data obtained by the method of linear regression with the use of the theory developed in [9] provides the determination of $\Gamma \sim F_m/l_c$ from the slope of the approximating curves, where F_m is the maximum force of interaction between a dislocation with a pinning center and l_c is the average distance of an oscillating segment. The Γ values are given in the table. It is seen that the application of a magnetic field reduces the value of Γ by a factor exceeding three in comparison with the control sample. However, these data cannot give an unambiguous answer to the question of whether the maximum interaction force F_m is reduced and of whether the length of oscillating segment l_c increases. It seems that both parameters are changing.

3.3. Effect of Magnetic Field on the Modulus Defect

The modulus defect measured as a function of ε_0 is shown in Fig. 3. It is seen that both control sample and the sample under study show no amplitude dependence of the modulus defect up to $\varepsilon_0 = 1.8 \times 10^{-4}$. For the sample preliminarily treated in a magnetic field at low ε_0 values, the defect is negative, which shows once again that the magnetic field provides sample strengthening. An increase in the ultrasound amplitude changes the negative sign of the modulus defect to positive one.

In accordance with measurements of the modulus defect and following [10], we estimated the averaged displacement of the dislocation segments $\langle u \rangle$ during oscillations. The results of estimation, $\langle u \rangle$, corresponding to the strain amplitude $\varepsilon_0 = 2.3 \times 10^{-4}$, are given in table. It is seen that the average displacements $\langle u \rangle$ in the magnetic fields are three times higher than the displacements of the dislocation segments in the control samples. At the same amplitude ε_0, the displacements of the oscillating dislocation segments are proportional to $\langle l_c^2 \rangle$ [11], whence $\langle l_c^2 \rangle$ increases in the tests in magnetic fields; in other words, an ever increasing number of segments "is liberated" from the stoppers. These conclusions are in accordance with the idea that a magnetic field promotes the unpinning of dislocations from paramagnetic centers [12].

CONCLUSION

The experimental data obtained and their analysis conclusively prove the existence of the effect of a weak magnetic field on anelasticity of alkali-halide crystals. The simultaneous action of magnetic and ultrasound fields is not equivalent to their successive application. The results obtained quantitatively agree with the effects observed in alkali-halide crystals in magnetic fields for other loading modes.

ACKNOWLEDGMENTS

We are grateful to V.I. Alshits for constant interest in our work and useful discussions.

REFERENCES

1. A. A. Urusovskaya, V. I. Alshits, A. E. Smirnov, *et al.*, Pis'ma Zh. Éksp. Teor. Fiz. **65**, 470 (1997).
2. Yu. I. Golovin, R. B. Morgunov, and S. E. Zhulikov, Izv. Akad. Nauk, Ser. Fiz. **60**, 174 (1996).
3. Yu. I. Golovin and R. B. Morgunov, Izv. Akad. Nauk, Ser. Fiz. **61**, 850 (1997).
4. J. Marx, Rev. Sci. Instrum. **22**, 503 (1951).
5. E. K. Naimi, *Measurements of Internal Friction, Modulus Defect and Starting Dislocation Stresses by the Method of Current–Voltage Characteristics of a Combined Vibrator*, deposited to VINITI, no. 2589 (1985).
6. E. K. Naimi, *Ultrasonic Determination of Peierls–Nabarro Stresses in Crystals*, Review of Progress in Quantitative NDE (University of California, La Tolla, 1986), p. 232.
7. J. J. Gilman, Progr. Ceramic Sci. **1**, 146 (1961) [Usp. Fiz. Nauk **LXXX**, 455 (1963)].
8. O. I. Datsko and V. I. Alekseenko, Fiz. Tverd. Tela (St. Petersburg) **39**, 1234 (1997).
9. A. V. Granato and K. Lücke, J. Appl. Phys. **27**, 583 (1956) [IL, Moscow (1963), p. 27].
10. R. V. Whitworth, Phil. Mag. **5**, 425 (1960).
11. D. Niblett, J. Wilks, Advances in Physics **9**, 1 (1960) [Usp. Fiz. Nauk **LXXX**, 125 (1963)].
12. V. I. Alshits, E. V. Darinskaya, O. L. Kazakova, *et al.*, Izv. Akad. Nauk, Ser. Fiz. **57**, 2 (1993).

Translated by A. Zalessky

Crystallography Reports, Vol. 45, No. 1, 2000, pp. 154–156. Translated from Kristallografiya, Vol. 45, No. 1, 2000, pp. 160–162.

PHYSICAL PROPERTIES OF CRYSTALS

Bulk Photovoltaic and Photorefractive Effects in a Piezoelectric $La_3Ga_5SiO_{14}$: Fe Crystal

T. M. Batirov*, K. A. Verkhovskaya, R. K. Dzhalalov*, E. V. Dubovik**, B. V. Mill***, and V. M. Fridkin***

** Dagestan State University, Makhachkala, Dagestan, Russia*

*** Shubnikov Institute of Crystallography, Russian Academy of Sciences, Leninskiĭ pr. 59, Moscow, 117333 Russia*

**** Moscow State University, Vorob'evy gory, Moscow, 119899 Russia*

Received May 20, 1998

Abstract—The linear and the circular bulk photovoltaic and photorefractive effects in a piezoelectric $La_3Ga_5SiO_{14}$: Fe crystal have been studied. It is shown that the photorefractive effect is induced by generation of the photovoltaic voltage. © *2000 MAIK "Nauka/Interperiodica".*

A piezoelectric lanthanum gallium silicate of the composition $La_3Ga_5SiO_{14}$ has a trigonal symmetry and is described by the point group 32. The crystal is noncentrosymmetric and optically active. The crystal symmetry does not contradict the existence of the linear and the circular bulk photovoltaic effects. Since the crystal has a pronounced band gap ($E_g > 5$ eV), the intrinsic effects can be observed only is the far ultraviolet range. The linear and circular bulk photovoltaic effects in the visible range of the spectrum can be observed only in doped crystals. We studied these effects in a praseodymium-doped lanthanum gallium silicate $La_3Ga_5SiO_{14}$: Pr^{3+} [1, 2]. We also studied the photorefractive effect and its possible mechanisms in these crystals [3]. The intrinsic bulk photovoltaic effect and the induced photorefractive effect were also observed in another piezoelectric, $Pr_3Ga_5SiO_{14}$ [4].

Below, we describe the study of the photovoltaic effect and the photorefractive effect in a Czochralski-grown piezoelectric $La_3Ga_5SiO_{14}$: Fe crystal. The $3 \times 3 \times 2$ mm-large specimens doped with iron to the concentration 0.5% were oriented along the *X*-, *Y*-, and *Z*-axes. Both linear and circular bulk photovoltaic effects were generated by an Ar-laser (λ = 488.0–514.5 nm) with the light intensity $I = 0.25$ W/cm^2 at room temperature. The method used for photovoltaic measurements was described earlier [5].

As is well known, the linear bulk photovoltaic effect is described by a third-rank tensor β_{ijk} [5] similar to the piezoelectric tensor, namely

$$j_i^L = \frac{1}{2} I \beta_{ijk}^L (e_j e_k^* + e_j^* e_k), \quad (1)$$

where j_i^L is the component that describes the current density in the linear bulk photovoltaic effect, I is the intensity of the incident light, and e_j and e_k are the projections of the polarization vector of the incident light. Knowing the nonzero components of the tensor β_{ijk}^L for the point group 32, one can obtain from formula (1) the current density of the linear bulk photovoltaic effect j_y^L along the *Y*-axis of the crystals for a linearly polarized light propagating along the *Z*-axis in the form

$$j_y^L = \beta_{11}^L I \sin 2\varphi, \quad (2)$$

where φ is the angle formed by the polarization vector of the incident light and the *Y*-axis of the crystal.

The specific rotation of the polarization plane of light, ρ, changes the amplitude of the current density of a linear photovoltaic effect and gives rise to the phase shift of its angular dependence [1]:

$$j_y^L = \beta_{11}^L I \frac{\sin(\rho d/2)}{\rho d/2} \sin(2\varphi + \rho d/2), \quad (3)$$

where $d = 2$ mm is the crystal thickness along the optical axis *Z*. For the $La_3Ga_5SiO_{14}$ crystal, $\rho \cong 5.8°$/mm at λ = 500 nm [6], which gives rise to the phase shift $\rho d/2 \cong 5.8°$ and a decrease of the amplitude of the current density of the linear bulk photovoltaic effect by 0.4% $\left(\frac{\sin(\rho d/2)}{\rho d/2} \cong 0.996\right)$. With due regard of all the above stated, the effect of the optical activity on the bulk photovoltaic effect can be ignored.

The circular bulk photovoltaic effect is described by a second-rank tensor β_{il}^C [5]

$$j_i^C = \beta_{il}^C \kappa_l I, \quad (4)$$

1063-7745/00/4501-0154$20.00

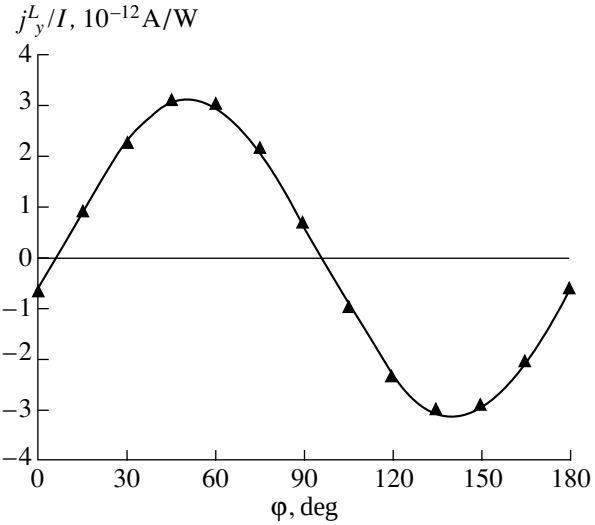

Fig. 1. Ratio of the current density of the bulk photovoltaic effect j_y^L to the intensity I of the incident light as a function of the angle φ formed by the *Y*-axis of the crystal and the polarization vector of the incident light for a $La_3Ga_5SiO_{14}$: Fe crystal.

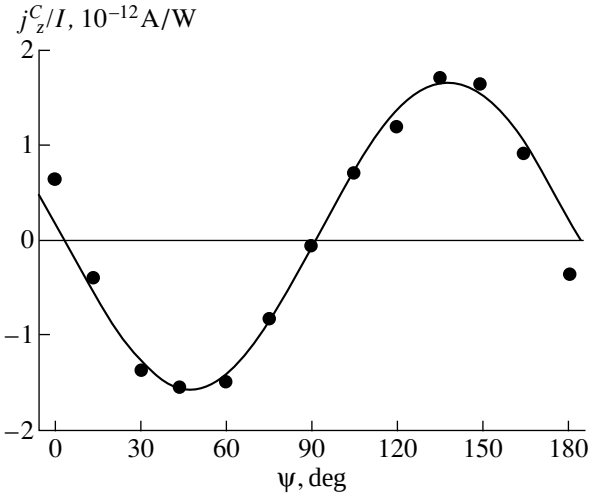

Fig. 2. Ratio of the current density of a circular bulk photovoltaic effect j_z^C to the intensity I of the incident light as a function of the angle ψ formed by the optical axis of a quarter-wave plate and the polarization vector of the incident light for a $La_3Ga_5SiO_{14}$: Fe crystal.

where j_i^C is the component of the current density due to the circular photovoltaic effect and $\boldsymbol{\kappa} = \boldsymbol{\kappa}^* = i[\mathbf{e} \cdot \mathbf{e}^*]$ is the degree of ellipticity of the incident light wave. The eliptically polarized light was generated by transmitting a linearly polarized light wave through a λ/4 plate. In this case, $\kappa_1 = \sin 2\psi$, where ψ is the angle between the optical axis of a quarter-wave plate and the polarization vector of the incident laser beam. Thus, illuminating the crystal along the *Z*-axis (through semitransparent electrodes), we obtain the current density of the circular bulk photovoltaic effect along the same direction in the form

$$j_z^C = \beta_{33}^C I \sin 2\psi. \quad (5)$$

Figure 1 shows the angular dependence of the current density of the linear bulk photovoltaic effect j_y^L divided into the intensity of the incident light for a $La_3Ga_5SiO_{14}$: Fe crystal. The points indicate the experimentally measured values of j_y^L/I; the solid line is obtained by the least squares method. The approximating function was the theoretical dependence described by (3). It is seen that the phase shift of the dependence $j_y^L(I)$ caused by the optical activity of the crystal is approximately equal to the above value of $\rho d/2$. Comparing the experimental results with formula (2), we obtain $\beta_{11}^L = 3.1 \times 10^{-12}$ V^{-1}. Since the absorption coefficient is known ($\alpha \approx 0.36$ cm^{-1}), we can calculate the Glass tensor component characterizing the photovoltaic sensitivity of the crystal, $G_{11}^L = \beta_{11}^L \alpha^{-1} = 8.6 \times 10^{-12}$ cm V^{-1}.

Figure 2 shows the dependence of j_z^C on the angle formed by the optical axis of the half-wave plate and the polarization vector of the laser beam. The points indicate the experimentally measured values of j_z^C/I, the solid line is obtained by the least squares method. The approximating function is the theoretical dependence calculated by (5). The phase shift of the curve in Fig. 2 is caused by the error inherent in the method used for measuring the angular dependence of the current of the circular photovoltaic effect. Comparing the experimental data for the circular bulk photovoltaic effect with formula (5), one obtains the components of the photovoltaic ($\beta_{33}^C = 1.6 \times 10^{-12}$ V^{-1}) and Glass ($G_{33}^C = 4.4 \times 10^{-12}$ cm V^{-1}) tensors.

The electric field generated by the bulk photovoltaic effect was determined from the current–voltage characteristic obtained for a crystal illuminated along the *Z*-axis with the aim to provide the maximum photovoltaic current, $E_{ph} \approx 5.35$ kV/cm. Taking into account the considerable strength of the photovoltaic field in a $La_3Ga_5SiO_{14}$: Fe crystal, we also measured photorefraction by the compensation method described elsewhere [7]. A crystal was illuminated with a linearly polarized light along the *Z*-axis at two different angles (φ_1 and φ_2) between the polarization vector of the light **e** and the *Y*-axis of the crystal, i.e., at the maximum values of the photovoltaic currents flowing in opposite directions. The angles φ_1 and φ_2 were selected with due regard for the rotation of the polarization plane of light caused by the optical activity of the crystal.

Figure 3 illustrates the kinetics of photorefraction recording in a $La_3Ga_5SiO_{14}$: Fe crystal at $\varphi_1 = 45°$ and

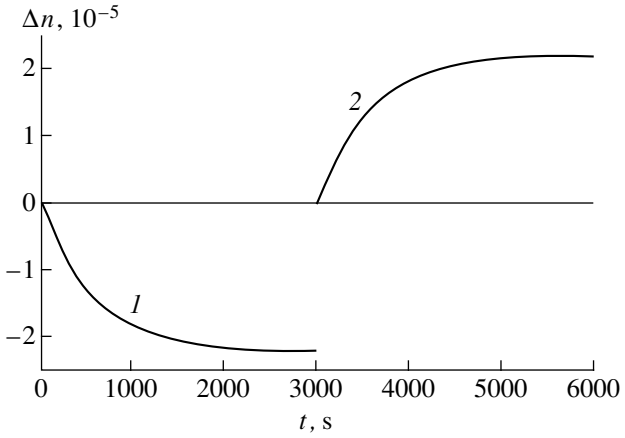

Fig. 3. Illustrating the kinetics of photorefraction recording in a $La_3Ga_5SiO_{14}$: Fe crystal for two polarization states of the light of intensity I = 19.64 W/cm^2. (*1*) $\varphi_1 = 45°$ and (*2*) $\varphi_2 = 135°$.

$\varphi_2 = 135°$ (positive and negative currents, respectively). The thus measured photorefraction is $\Delta n \approx 2.3 \times 10^{-5}$.

Taking into account the crystal symmetry and the geometry of the experiment, we have

$$\Delta n = -r_{11} n_0^3 E_{ph}, \quad (6)$$

where n_0 is the refractive index of the ordinary wave, E_{ph} is the photoinduced field, and r_{11} is the coefficient of the linear electrooptical effect. The electrooptical coefficient at $\Delta n = 2.3 \times 10^{-5}$, $n_0 = 1.9$ [6], and $E_{ph} = 5.35$ kV/cm equals $r_{11} = 6.3 \times 10^{-10}$ cm/V.

The results obtained, i.e., the pronounced photoinduced fields generated by the bulk photovoltaic effect and the dependence of the magnitude and the sign of photorefraction observed on the radiation polarization, indicate that photorefraction in a piezoelectric $La_3Ga_5SiO_{14}$: Fe crystal is caused by the linear bulk photovoltaic effect. This phenomenon makes $La_3Ga_5SiO_{14}$: Fe crystals promising materials for recording holographic gratings using the bulk photovoltaic effect.

REFERENCES

1. V. M. Fridkin, A. A. Kaminskiĭ, V. G. Lazarev, *et al.*, Appl. Phys. Lett. **55** (6), 545 (1989).
2. G. Dalba, E. Doubovik, V. M. Fridkin, *et al.*, Ferroelectrics Lett. **21**, 61 (1996).
3. C. Dam-Hansen, P. M. Johansen, and V. M. Fridkin, Appl. Phys. Lett. **69**, 2003 (1996).
4. T. Batirov, R. Djalalov, E. Doubovik, *et al.*, Ferroelectrics Lett. **23**, 95 (1997).
5. B. Sturman and V. Fridkin, *The Photovoltaic and Photorefractive Effects in Noncentrosymmetric Materials* (Nauka, Moscow, 1992; Gordon and Breach, Philadelphia, 1992).
6. O. A. Baturina, B. N. Grechushnikov, A. A. Kaminskiĭ, *et al.*, Kristallografiya **32** (2), 406 (1987).
7. M. Lains and A. Glass, *Principles and Applications of Ferroelectrics and Related Materials* (University Press, Oxford, 1977; Mir, Moscow, 1981).

Translated by L. Man

Crystallography Reports, Vol. 45, No. 1, 2000, pp. 157–160. Translated from Kristallografiya, Vol. 45, No. 1, 2000, pp. 163–166.

THIN FILMS

Isothermal Liquid Phase Epitaxy of A^3B^5 Compounds under Excessive Vapor Pressure of the B^5 Component

Yu. P. Khukhryanskiĭ, V. A. Savchenko, V. V. Emel'yanov, and V. N. Ermilin

Voronezh State Technical University, Moskovskiĭ pr. 14, Voronezh, 394026 Russia

Received April 8, 1998; in final form, October 13, 1998

Abstract—A mathematical model has been developed of isothermal epitaxial growth of A^3B^5 films on the A^3B^5 substrates from flux by creating the excessive pressure of diatomic vapors of the B^5 component. The model is based on the diffusion equation with the nonlinear boundary condition at the evaporation surface and the third-kind condition at the crystallization surface. The problem is solved numerically on a computer. *© 2000 MAIK "Nauka/Interperiodica".*

The isothermal methods of liquid-phase epitaxy of elementary and complex semiconductors [1, 2] have been insufficiently studied both in the theoretical and experimental aspects. However, in practice, these methods are rather attractive, since, first, they provide the use of a rather wide range of growth rates and, second, the technologies of isothermal methods are usually rather simple because it is much easier to maintain the growth system at the given level than to change it according to a certain program.

Consider one of the methods of the isothermal liquid-phase epitaxy of A^3B^5 compounds for the diffusion model based on the creation of an excessive pressure of the element B of the fifth group over the flux. Let a plane layer of B of component thickness l in the melt of metal A saturated at the temperature T be in contact with the substrate of a binary A^3B^5 compound consisting of the same elements. We assume that the substrate is horizontal and that its upper surface lies in the plane $z = 0$. The vertical z-axis is directed upward. The concentration of the component B in the saturated flux equals C_{10}, mol/cm^3. In turn, the flux layer is in equilibrium with the gas phase—the vapor of the element B (with the concentrations of B_2 dimers equal to C_{20} mol/cm^3) and the gas carrier (e.g., hydrogen). The solubility of hydrogen in the melt and its interaction with the vapor of the element B are ignored.

Now, consider a boundary layer of thickness Δ in the gas phase above the flux surface in which the transport of the volatile components proceeds by the diffusion mechanism. Outside this layer, the gas phase is force or convection stirred and therefore is homogeneous.

It should be emphasized that at the concentration of the B element in the flux of metal A characteristic of the epitaxy of gallium and indium phosphides and arsenides, the element B in the liquid phase is in the atomic state [3, 4], so that C_{10} is the atomic concentration of the element B in the melt A. However, as the mass-spectrometry data show [5, 6], only the dimers of the element B and atoms of the element A are transported to the vapor phase from the saturated flux. The equilibrium vapor phase above the saturated B solutions in the melt of the metal A consists mainly of B_2 and B_4 molecules [7]. Unfortunately, we still do not know in what molecular form the element B is transported from the vapor phase to the flux. However, since the epitaxy proceeds at temperatures $T \approx 800$–1000 K, the concentration of the B-dimers in the vapor phase considerably exceeds the concentration of B-tetramers, and therefore one can assume that only B_2 dimers are transported from the vapor phase to the flux. The further modeling of the epitaxial process was made under this assumption.

Let us take it that the partial pressure of the B vapors above the flux at the moment $t = 0$ is changed in a jumpwise manner so that the concentration of B_2-dimers in the vapor phase attains the value $C_2(l + \Delta)$ everywhere except in the boundary layer, $t \geq 0$. Since the ratio D_2/Δ has high values (where D_2 is the diffusion coefficient of dimers B_2 in the gas phase), the linear distribution of dimer concentration $C_2(z, t)$ readily attains the steady state value in the boundary layer $l < z \leq l + \Delta$.

Thus, a flow of B-dimers,

$$j_g(t) = -2D_2\frac{C_2(l+\Delta) - C_2(l, t)}{\Delta} \qquad (1)$$

is directed from the gas phase to the flux.

Hereafter, the dimer flows are recalculated to the flows of B-monomers.

Now, denote the concentration of the B atoms in the flux layer at $t > 0$ by $C_1(z, t)$. Then two expressions follow from the continuity condition for the B flow at the gas–solution interface:

$$j_g(t) = -D_1\frac{\partial C_1(z, t)}{\partial z}\bigg|_{z = l}, \qquad (2)$$

1063-7745/00/4501-0157$20.00 © 2000 MAIK "Nauka/Interperiodica"

$$j_g(t) = 2\left[-\frac{H_2(T)M_g}{\rho_g}C_2(l,t) + G_2(T)\left(\frac{M_s}{\rho_s}\right)^2 C_1^2(l,t)\right], \quad (3)$$

where D_1 is the diffusion coefficient of B atoms in the flux (in cm^2/s), M_g and M_s are the molecular masses of the gas–carrier and the solvent (A element) (in g/mol), ρ_g and ρ_s are the densities of the gas–carrier and the solvent (in g/cm^3), and $H_2(T)$ and $G_2(T)$ are the rates of specific absorption and evaporation for dimers of the element B in the melt of the element A (in mol/(cm^2 s)).

The squared concentration in (3) reflects the fact of dimer molecule formation on the flux surface caused by pair collisions of the atoms of the element B. Relationship (3) shows that the parameters of the system $G_2(T)$ and $H_2(T)$ are related as

$$H_2(T)\frac{M_g}{\rho_g} = G_2(T)\frac{C_{10}^2}{C_{20}}\left(\frac{M_s}{\rho_s}\right)^2. \quad (4)$$

Expressions (1)–(3) allow one to write the following boundary condition at the surface of the solution–gas phase interface

$$\left.\frac{\partial C_1(z,t)}{\partial z}\right|_{z=l} = \frac{2}{D_1\left(1+\frac{H_2(T)M_g\Delta}{D_2\rho_g}\right)} \times\left\{\frac{H_2(T)M_g}{\rho_g}C_2(l+\Delta) - G_2(T)C_1^2(l,t)\left(\frac{M_s}{\rho_s}\right)^2\right\}. \quad (5)$$

The evaporation of the component A is neglected and therefore the concentration of the B atoms over the liquid-phase layer is set by the one-dimensional diffusion equation

$$\frac{\partial C_1(z,t)}{\partial t} = D_1\frac{\partial^2 C_1(z,t)}{\partial z^2} \quad (6)$$

with the initial condition

$$C_1(z,0) = C_{10}. \quad (7)$$

The condition at the substrate surface is formulated in the same way as in [8]

$$D_1\left.\frac{\partial C_1(z,t)}{\partial z}\right|_{z=0} = \frac{D_1^*}{\delta}C_1(0,t), \quad (8)$$

where δ is the thickness of the boundary flux layer on the substrate surface ($\delta \ll l$), D_1^* is the diffusion coefficient in the boundary layer of the solution, and $\Lambda = D_1^*/\delta$ is the kinetic crystallization coefficient. For the A^3B^5 compounds, germanium, and silicon, the numerical value of Λ is equal to 5×10^{-3}–10^{-2} cm/s [8, 9].

Thus, boundary-value problem (4)–(7) describes the kinetics of epitaxial growth of A^3B^5 films under the isothermal conditions and excessive pressures of the vapors of the B element above the flux.

Now, reduce the boundary-value problem (5)–(8) to the dimensionless form. With this aim, introduce the following dimensionless parameters:

$$\frac{z}{l} = \zeta, \quad \frac{D_1 t}{l^2} = \tau, \quad (9)$$

$$\frac{C_1(z,t)}{C_{10}} = 1 + U_1(\zeta,\tau), \qquad \frac{C_2(l+\Delta)}{C_{20}} = 1 + U_{20}, \quad (10)$$

$$L = \frac{D_1^* l}{D_1\delta}, \quad Q = \frac{H_2(T)M_g\Delta}{D_2\rho_g}, \quad R = 2\frac{C_{20}D_2 l}{C_{10}D_1\Delta}. \quad (11)$$

It should be noted that the system parameters Q and R can be represented as the ratios of the characteristic flows

$$Q = \frac{H_2(T)C_{20}M_g}{\rho_g}\left(\frac{D_2C_{20}}{\Delta}\right)^{-1}, \qquad R = 2\frac{D_2C_{20}}{\Delta}\left(\frac{D_1C_{10}}{l}\right)^{-1}. \quad (12)$$

With due regard for relationships (9)–(11), the problem can be written in the dimensionless form

$$\frac{\partial U_1(\zeta,\tau)}{\partial\tau} = \frac{\partial^2 U_1(\zeta,\tau)}{\partial\zeta^2}, \quad U_1(\zeta,0) = 0, \quad (13)$$

$$\left.\frac{\partial U_1(\zeta,\tau)}{\partial\zeta}\right|_{\zeta=0} = LU_1(0,\tau), \quad (14)$$

$$\left.\frac{\partial U_1(\zeta,\tau)}{\partial\zeta}\right|_{\zeta=1} = \frac{QR}{1+Q}[1+U_{20}-(1+U_1(1,\tau))^2]. \quad (15)$$

The thickness of the epitaxial film h (in cm) grown for the time τ_0 is given by the formula

$$h = h_0\int_0^{\tau_0}\left.\frac{\partial U_1(\zeta,\tau)}{\partial\zeta}\right|_{\zeta=0}d\tau = h_0L\int_0^{\tau_0}U_1(0,\tau)d\tau, \quad (16)$$

$$h_0 = \frac{C_{10}lM_{AB}}{\rho_{AB}}, \quad (17)$$

where ρ_{AB} and M_{AB} are the density and the molecular mass of the binary A^3B^5 compound to be crystallized, respectively.

Since boundary condition (15) is nonlinear, the solution of the boundary-value problem (13)–(15) is obtained by numerical methods.

The film thicknesses h calculated by (16) on a computer as a function of the dimensional parameters Q, R, and τ_0 at $h_0 = 1.0$, $U_{20} = 3.0$ m, and $L = 100$ are shown

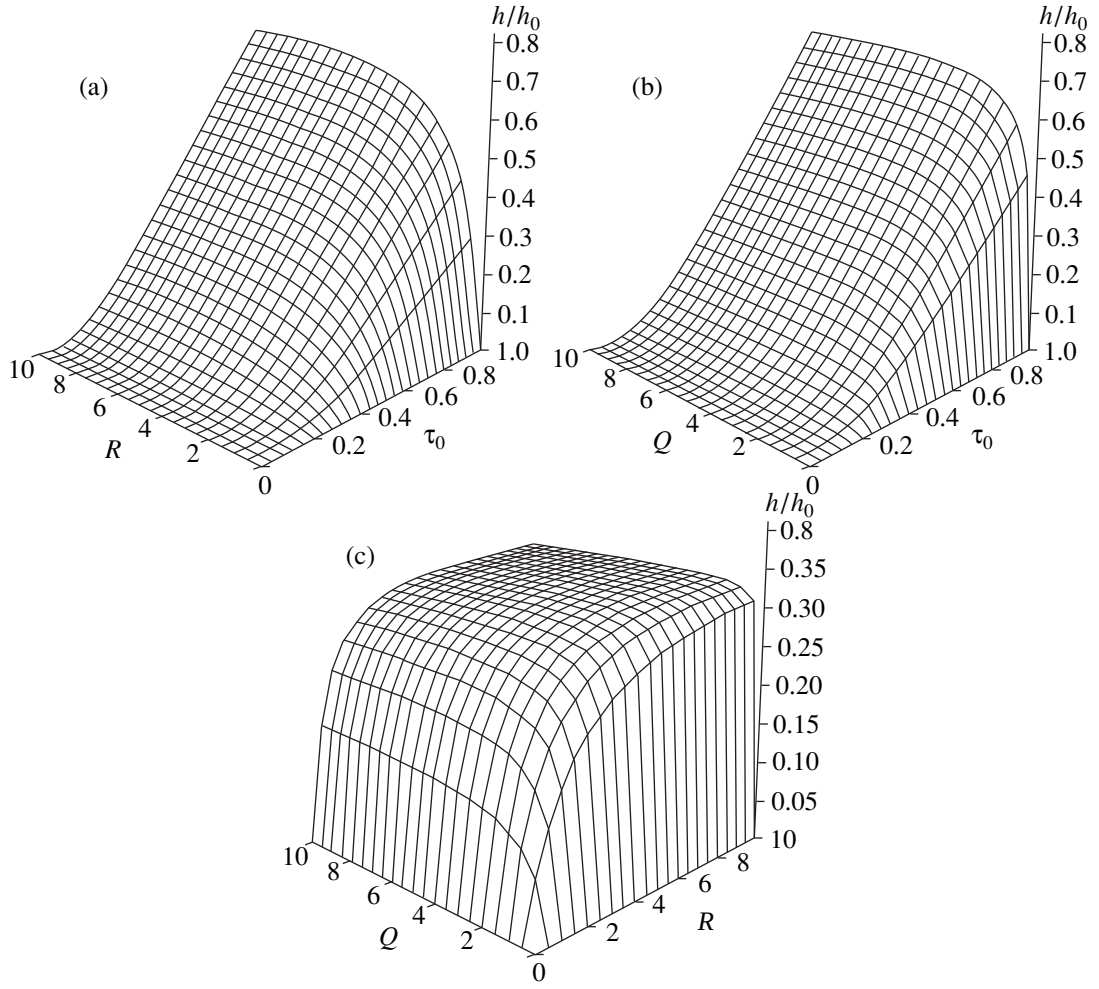

Fig. 1. Thickness of the epitaxial film, h/h_0, as a function of the dimensionless parameters Q, R, and τ_0 at $h_0 = 1.0$, $U_{20} = 3.0$, and $L = 100$: (a) $Q = 1.0$, (b) $R = 1.0$, and (c) $\tau_0 = 0.5$.

in Figs. 1a–1c. It is seen that the film thickness considerably increases with an increase of the parameters Q and R in the range of their variations $0 < Q \le 2$ and $0 < R \le 5$.

We also studied the dependence of the deposition rate of the film as a function of the Q, R, U_{20}, and L parameters. The deposition rate $V(\tau)$ (in cm/s) was calculated by the formulas

$$V(\tau) = V_0 \frac{\partial U_1(\zeta, \tau)}{\partial \zeta}\bigg|_{\zeta = 0} = V_0 L U_1(0, \tau), \quad (18)$$

$$V_0 = \frac{D_1 C_{10}}{l} \frac{M_{AB}}{\rho_{AB}}. \quad (19)$$

As was to be expected, an increase of the B vapor pressure above the flux increases the crystallization rate of the film on the substrate with a certain delay, $\sim 0.05\tau$. Obviously, growth of the film can be controlled by changing both the temperature and the vapor pressure. Combining these two factors, one can considerably increase the possibilities provided by the liquid-phase epitaxy.

One has to pay attention to the fact that at $U_{20} < 1$, the epitaxial method considered here allows the attainment of very low rates of film growth ($\sim 10^{-8}$ cm/s), which makes this method very promising for nanotechnologies.

The dependence of the growth rate of the film on the parameter L is quite conventional [8]: with an increase of L, the growth rate also increases and attains a constant value at $L > 100$.

The deposition rate is also strongly dependent on the parameters Q and R: with an increase of Q and R, the deposition rate $V(\tau)$ increases and attains a steady-state value at $\tau \sim 1$ (Fig. 2).

For the quantitative verification of the model relationships obtained, we performed an experiment on the growth of the indium phosphide film on the (100)InP substrate from the solution of phosphorus in the indium melt at $U_{20} = 0.3$ and $T = 973$ K. Using a special attach-

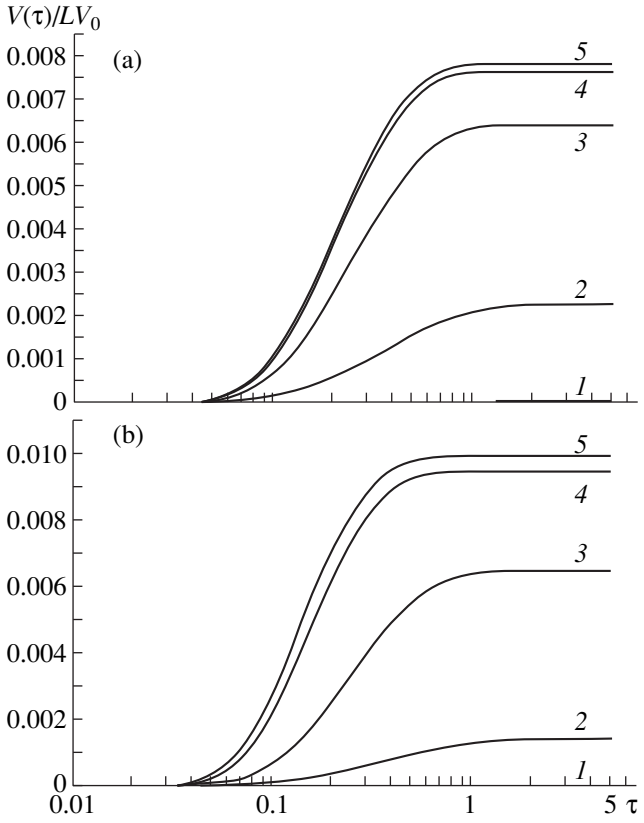

Fig. 2. Deposition rate $V(\tau)/LV_0$ of the film as a function of time at certain values of the dimensionless parameters Q and R: (a) $L = 100$, $U_{20} = 3.0$, and $R = 1$; curves *1–5* correspond to the following Q values: 10^{-3}; 10^{-1}; 10^0; 10^1, and 10^3. (b) $L = 100$, $U_{20} = 3.0$, and $Q = 1$; curves *1–5* correspond to the following R values: 10^{-3}; 10^{-1}; 10^0; 10^1, and 10^3.

ment, we managed to form a flat flux layer of the thickness $(5–6) \times 10^{-2}$ cm on the substrate surface. Within 60 and 90 min, the films attained the thicknesses of $\sim 2 \times 10^{-5}$ and 4×10^{-5} cm, respectively. The calculated film thicknesses, 2×10^{-5} and 3.1×10^{-5} cm, are quite consistent with the experimental data. In our calculations, we used the following numerical values of the parameters of the "vapor–solution" system: $C_{10} = 9 \times 10^{-4}$ mol/cm^3 [10], $C_{20} = 6.7 \times 10^{-11}$ mol/cm^3, $G_2(973) = 7.5 \times 10^{-3}$ mol/(cm^2 s) [11], $\Delta = 10^{-2}$ cm, $D_1 = 10^{-5}$ cm^2/s, $D_2 = 5$ cm^2/s, $\Lambda = 10^{-2}$ cm/s, $Q = 48.3$, $R = 4.5 \times 10^{-2}$, and $L = 60$.

Thus, the macroscopic model of the isothermal method of the liquid-phase epitaxy of the A^3B^5 compounds allows one to predict the characteristic features of the film deposition and also interpret the well-known experimental data on the indium phosphide epitaxy.

ACKNOWLEDGMENTS

The study was supported by the State Committee on Higher Education of the Russian Federation in the Field of Fundamental Problems of Metallurgy, project no. 94-3.5-41 in 1995.

REFERENCES

1. V. M. Andreev, L. M. Dolginov, and D. N. Tret'yanov, *Liquid Epitaxy in Technology of Semiconductor Devices* [in Russian] (Sov. Radio, Moscow, 1975).
2. V. B. Ufimtsev and R. Kh. Akchurin, *Physicochemical Foundations of Liquid-Phase Epitaxy* [in Russian] (Metallurgiya, Moscow, 1983).
3. Yu. P. Khukhryanskiĭ and V. N. Ermilin, Izv. Akad. Nauk SSSR. Neorg. Mater. **16** (3), 380 (1980).
4. Yu. P. Khukhryanskiĭ, V. N. Ermilin, and M. S. Tulinova, Izv. Akad. Nauk SSSR. Neorg. Mater. **17** (10), 1733 (1981).
5. C. T. Foxon, B. A. Joyce, and R. F. C. Farrow, J. Phys. D: Appl. Phys. **7**, 2422 (1974).
6. C. T. Foxon, L. A. Harvey, and B. A. Joyce, J. Phys. Chem. Solids **34**, 1693 (1973).
7. S. I. Gorbov, *Itogi Nauki Tekh. Ser. Khim. Termod. Ravnovesiya* (VINITI, Moscow, 1975), Vol. 3.
8. Yu. P. Khukhryanskiĭ, Kristallografiya **37** (5), 1275 (1992).
9. Y. Inatomi and K. Kuribayashi, J. Cryst. Growth **114**, 380 (1991).
10. C. D. Thurmond, J. Phys. Chem. Solids **26**, 785 (1965).
11. Yu. P. Khukhryanskiĭ, L. N. Verem'yanina, I. V. Kombarova, *et al.*, Zh. Fiz. Khim. **71** (5), 870 (1997).

Translated by L. Man

Crystallography Reports, Vol. 45, No. 1, 2000, pp. 161–168. Translated from Kristallografiya, Vol. 45, No. 1, 2000, pp. 167–174.

CRYSTAL GROWTH

Anomalous Effects in Dopant Distribution in Ge Single Crystals Grown by the Floating Zone Technique Aboard Spacecrafts

A. V. Kartavykh, É. S. Kopeliovich, M. G. Milvidskiĭ, and V. V. Rakov

Institute of Chemical Problems of Microelectronics, Bol'shoĭ Tolmachevskiĭ per. 5, Moscow, 109017 Russia

Received April 8, 1998; in final form, April 13, 1999

Abstract—Specific features of Ga-dopant distribution in Ge single crystals grown by the floating zone technique from lightly and heavily Ga-doped Ge melts aboard the *Photon* spacecrafts have been studied. An anomalously strong concentration dependence of the effective coefficient of Ga distribution in Ge crystallized from melts with a well-developed free surface, which has no analogues under the terrestrial conditions, has been established for the first time. This anomaly is interpreted as a consequence of specific concentration-dependent processes of heat and mass transfer in the molten zone, and, first of all, the intensification of the concentration–capillary convection with an increase of the doping level. The quantitative characteristics of the crystallization parameters necessary for the construction and verification of hydrodynamic models are obtained experimentally. The effect of the observed phenomena on the electrophysical homogeneity of the grown single crystals and possible methods for the control of dopant distribution in such crystals are discussed. © *2000 MAIK "Nauka/Interperiodica"*.

INTRODUCTION

Capillary convection (CC, Marangoni convection) has a special place among the processes determining characteristics of heat and mass transfer in melts during their crystallization under conditions of weightlessness. The physical mechanism of capillary convection (CC) is based on the dependence of the surface-tension forces in the melt on its temperature and composition. One distinguishes between the thermally induced capillary (TCC) and concentration-induced capillary (CCC) convections. The driving force of the TCC is the temperature gradient on a free melt surface. The driving force of the CCC is the concentration gradient of the surface-active dopant in the vicinity of the melt surface.

The Marangoni convection is one of the most important factors determining the quality of semiconductor single crystals grown in space by the floating zone techniques. Earlier [1], we showed that the effect of capillary convection on the thermocapillary convection in melts observed in the processes of floating-zone growth in space results in the characteristic axisymmetric inhomogeneity of the dopant distribution in the transverse cross sections of the crystals. This inhomogeneity is caused by the intensification of the melt stirring in the subsurface layer and a decrease of the effective distribution coefficient in the corresponding local regions of the crystallization front. However, it is still unclear which type of Marangoni convection (TCC or CCC) makes the determining contribution to formation of such inhomogeneity in doped semiconductor crystals.

Proceeding from the considerable experience of performing space experiments and processing their results, we assumed that the *concentration* Marangoni convection produces a strong (probably prevalent) effect on the hydrodynamic situation in heavily doped (with the dopant content exceeding 10^{17} cm^{-3}) melts of semiconductor materials [2]. However, the question about the effect of CCC on the dopant distribution and the appearance of anisotropic electrophysical properties in grown crystals can be answered only upon analysis of the results obtained in deliberate space experiments. The correct methodical performance of such experiments requires crystallization of a representative set of specimens from melts at different concentrations of the same dopant in identical thermal fields and at the equivalent minimum possible microgravitation levels. Taking into account the fine nature of the effects to be studied, the real conditions aboard spacecrafts, and the insufficient quality of the growth apparatus used in space experiments, one has to foresee special measures for excluding various systematic methodical errors. The present article describes such experiments and analyzes and discusses the results obtained.

METHODS OF PERFORMING GROWTH EXPERIMENTS

The experiments were performed aboard automatic spacecrafts of the *Foton* series [3]. The choice of gallium-doped germanium as a model material was dictated by the fact that Ga-impurity in Ge-melts is not volatile and has high surface activity [4] and the distribution coefficient $k \ll 1$. Zone recrystallization of Ge both in space and in the control terrestrial experiments was performed in *Zone*-type apparatus [5]. The initial specimens were 110 mm long ⟨100⟩-oriented single-

1063-7745/00/4501-0161$20.00

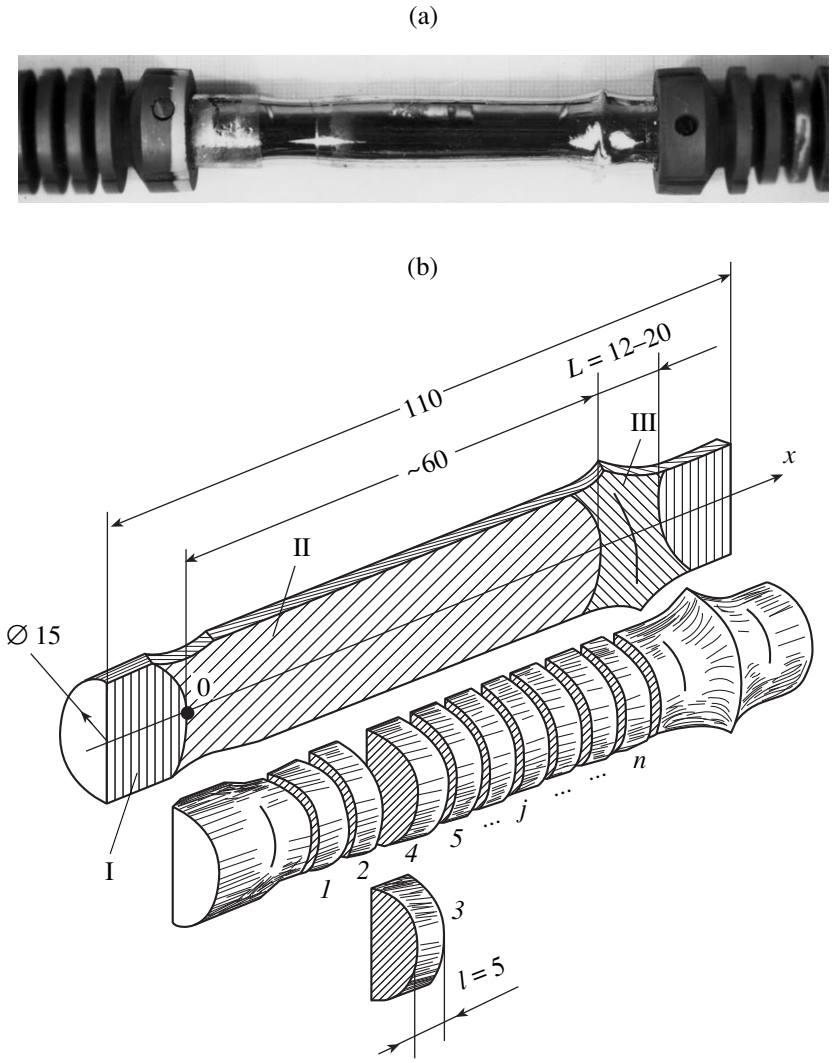

Fig. 1. (a) A typical space single crystal and (b) the scheme of its "tailoring" for further studies: (I) the seeding part, (II) the part crystallized in space during molten-zone motion, and (III) the region of the last stationary crystallized zone.

crystal Ge-rods with a diameter of 15 mm and a Ga concentration ranging within $C_0 = 1 \times 10^{18}$–1.5×10^{19} at/cm^3.

Floating zone melting in space was performed in a sealed vacuum quartz ampule with an inner diameter of 30 mm. A specimen in such an ampule "is hanged" on a special graphite holder so that it has no contact with the ampule walls (Fig. 1a). The control terrestrial experiments were performed in the horizontal version of the floating-zone technique. The initial specimen in an ampule was placed into a quartz tube playing the part of a container with an inner diameter of 20 mm. The container was filled only partly to provide the formation of a free upper surface in the melt, which is a necessary prerequisite for the development of capillary convection in the liquid zone [1].

In order to minimize *thermocapillary* convection, crystallization by the floating zone technique should be performed under low temperature gradients in the molten zone (i.e., under the minimum overheating of the melt with respect to T_m). Overheating within one series of growth experiments ranged from 8 to 13°C. The heater temperature was checked using the orbital telemetry data in the real-time mode and was maintained within ±0.5°C.

The *Zona* setups were supplied with an immobile circular resistive carbon-based composite heater providing the formation of the Ge molten zone 12–20 mm in length. The molten zone is formed while the ampule travels with the specimen through the heater. The total path of the ampule was 60 mm. In the preliminary terrestrial experiments, the zone moved at a velocity of 7 mm/h. However, the first space experiments already showed that stable complete melting of a specimen moving with such a velocity occurs only at doping levels $C_0 > 1 \times 10^{19}$ at/cm^3. At lower initial doping levels,

Basic crystallization parameters and properties of terrestrial and space Ge⟨Ga⟩ single crystals grown by floating zone technique on Zona setups

Sequential number of crystal i	Gallium concentration in the initial ingot (C_0), at/cm^3	Growth rate u, mm/h	Length of the molten zone L, mm	Effective coefficient of Ga distribution averaged along the crystal length (over all the j)	Effective averaged parameter of the boundary diffusion layer, δ, mm	Note
1	1.1×10^{18}		30	0.104	1.1	Terrestrial horizontal floating zone technique
2	3.0×10^{18}	7 ± 0.2	20	0.094	0.69	
3	9.0×10^{18}		17	0.094	0.69	
4	1.2×10^{19}		20	0.096	0.78	
5	1.1×10^{19}	7 ± 0.2	14	0.117	1.6	Foton-1
6	1.2×10^{19}		16	0.124	1.9	
7	1.3×10^{18}		12	0.150	3.8	Foton-3
8	3.0×10^{18}		20	0.128	2.8	Foton-3
9*	4.1×10^{18}		15	0.122*	2.5*	Foton-4
10	1.0×10^{19}	5 ± 0.2	12	0.094	0.95	Foton-6
11	1.0×10^{19}		18	0.092	0.82	Foton-5
12*	1.2×10^{19}		12	0.103*	1.5*	Foton-6
13	1.5×10^{19}		16	0.089	0.63	Foton-5

* The microinhomogeneity data $C(x)$ indicate the effect of an elevated level of microgravitations (vibrations).

only the surface (circular) melting of single crystal rods was observed. Thus, we had to lower the crystallization rate aboard the satellite to 5 mm/h (see table).

We grew nine "space" Ge⟨Ga⟩ single crystals in different *Zona* apparatus of the same design aboard five different spacecrafts of the same type and also four control terrestrial crystals. The total time of the orbital crystallization exceeded 100 h, which corresponded to about 70 near-earth orbits with close parameters. According to the theory of probability, the effect of various known spurious factors deteriorating the reproducibility of the impurity distribution in single crystals for such a scheme of experiments should be of a random nature. Thus, we have managed to create objective prerequisites for performing appropriate and reliable statistical analysis of a considerable data sampling.

METHODS FOR STUDYING SINGLE CRYSTALS AND RESULTS OBTAINED

All the thirteen Ge⟨Ga⟩ crystals were grown according to the same scheme. Each crystal was cut along the longitudinal axis into equal halves (Fig. 1b), one of which was then subjected to selective chemical etching. The morphology of the etched cut was used to determine the shape of the crystallization, the melt fronts, and the dimensions of the two main parts of the ingot—the seed (I) and the recrystallization (II) regions. The length L of the solidification region of the last zone (III) was measured directly and used as the parameter L in the following calculations. The etching data were also used to check the structure perfection (single crystallinity) of the ingots grown. The second "mirror" half of the grown crystal was used for studying the impurity distribution along the crystal length. With this aim, region II was cut into 5 mm-thick (parameter l) specimens in the transverse direction (Fig. 1b). Upon the corresponding processing and formation of the contacts, each specimen (j = 1, 2, …, n) was used for measuring the Hall effect by the standard van der Pauw method [6] at room temperature. The Ga concentration in the specimen was assumed to be equal to the Hall hole concentration, which is quite justified for heavily doped materials ($p \geq 10^{17}$ cm^{-3}). The volume of one Hall specimen was about 0.4 cm^3, each Hall measurement corresponded to the averaged concentration of the dopant incorporated into the crystal for about one hour of the growth process. Thus, we managed to obtain the data necessary for the construction of the axial dopant distribution $C(x)$ for all the single crystals (i = 1, 2, …, 13).

The curves thus obtained were analyzed within the classical theory of zone melting [7] with the use of the Pfann equation

$$C(x)/C_0 = 1 - (1 - k)\exp(-kx/L), \quad (1)$$

where $C(x)$ is the Ga concentration in the transverse cross section of the ingot with the coordinate x measured from the seeding front, k is the effective coefficient of Ga distribution, and L is the molten-zone length. Using equation (1), one can readily construct the theoretical curves of the dopant distribution along the crystal length in the dimensionless coordinates $C(x)/C_0 = f(x/L)$ for any given value of k. Figure 2

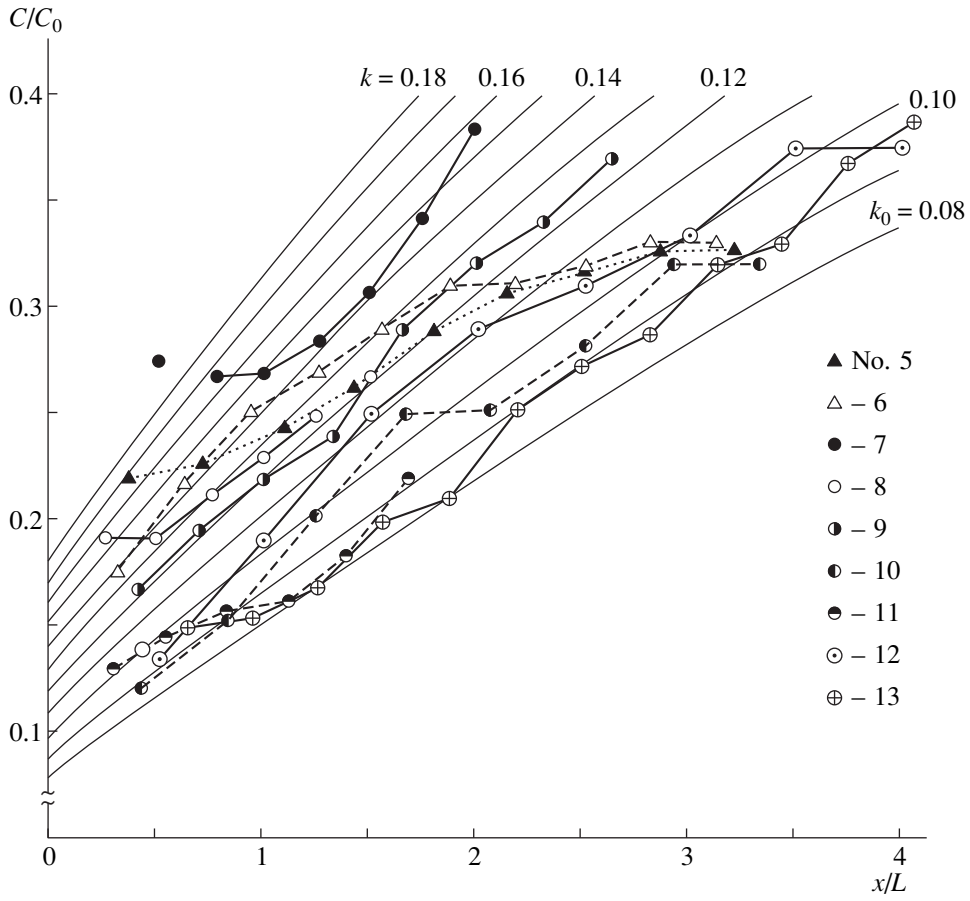

Fig. 2. Relative concentration of gallium C/C_0 as a function of x/L for Ge single crystals grown on *Foton* satellites (the sequential numbers of the crystals correspond to their sequential numbers in the table).

shows several families of such curves calculated for various values of the distribution coefficient beginning with the equilibrium value $k_0 = 0.08$ [8] at a step of 0.01. In fact, the curves of this family form a nomograph convenient for the elementary analysis of the experimental dopant distributions $C(x)$.

Then, for each jth Hall specimen ($j = 1, \ldots, n$) prepared from the ith crystal (see table), the following procedure was performed:

(i) The C_{ij}/C_{0i} value was determined from the data of Hall measurements and the known Ga concentration in the initial ingot.

(ii) The x_{ij}/L_i value was determined from the distance of the Hall specimen from the seeding front and the length of the last zone.

(iii) The corresponding point was plotted in the corresponding system of dimensionless coordinates.

(iv) The value of the effective distribution coefficient k_j was determined from the nomograph.

The results of this procedure for space single crystals are illustrated by Fig. 2.

Column 5 in table lists the averaged values of the effective coefficient of dopant distribution for each Ge⟨Ga⟩ crystal. The comparison of the k and C_0 values (columns 2, 5) shows that the effective distribution coefficient in space crystals depends on Ga concentration in the initial specimen (and, therefore, also in the melt). The further analysis requires the establishment of the concrete form of the k dependence on Ga concentration in the *liquid phase* (C_l). Since crystallization proceeds from the melt of a varying composition (at a continuous increase of C_l), the experimental form of the function $k = f(C_l)$ within one single crystal was determined by the successive solution of the equation of the material balance of the dopant in the crystallization zone of each Hall specimen. We indicate here only the final form of the solution

$$C_{lj} = C_{l(j-1)}\left[1 + (1 - k_j)\frac{l}{2L}\right], \quad j = 1, 2, \ldots, n, \quad (2)$$

where C_{lj} is the time- and volume-averaged Ga concentration in the molten zone where the jth Hall specimen was crystallized. Similar processing of a set of single measurements for all thirteen ingots yielded the dependences $k = f(C_l)$ shown in Fig. 3.

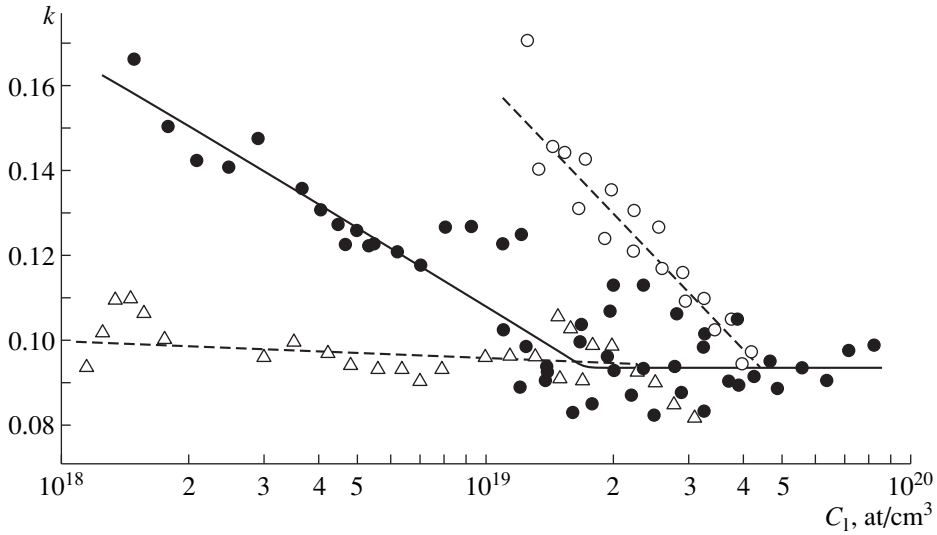

Fig. 3. Experimental dependence of the effective distribution coefficient on Ga concentration in the melt: △ terrestrial crystals (nos. 1–4 in table); ○ space crystals (nos. 5, 6), u = 7 mm/h; ● space crystals (nos. 7–13), u = 5 mm/h.

RESULTS AND DISCUSSION

The main result of this study is the experimental observation of a strong anomalous dependence of the effective coefficient of Ga distribution in Ge on the dopant content in the melt observed *only* in space crystals (Fig. 3). The absence of this effect in terrestrial crystals grown under the same thermal conditions does not allow the interpretation of this effect in terms conventional for the terrestrial technologies. For example, one cannot explain the phenomenon observed in space crystals by invoking the polytropy characteristic of some impurities in heavily doped semiconductors [9]. Thus, we believe that the only cause of the observed experimental dependence $k = f(C_l)$ is the regular intensification of stirring in the molten zone with an increase of the content of the surface-active dopant in the molten zone.

An additional fact supporting such a conclusion is the regular change of the crystallization-front shape with the change of the doping level in the melt (Fig. 4), with the thermal conditions being the same. With an increase of the Ga content, the curvature of the crystallization front decreases, which indicates a more intense stirring process in the melt. It seems that in this case, the convective processes start developing in the subsurface regions and then propagate into the bulk, because at relatively low Ga-concentrations (~10^{17}–10^{18} at/cm^3), the convective instability is often formed resulting, in turn, in the spatial-temporal instability (oscillations) in the position of the melting isotherm. Under the melting conditions, this can lead to the formation of local residual in completely molten fragments of the initial material (Fig. 4b). At high doping levels, no such effects are observed (Fig. 4c).

In order to process the initial data for the subsequent construction of hydrodynamic models necessary for the interpretation of the anomalies in doping of the solid phase, we calculated the effective thickness of the diffusion level (δ) at the interface in the melt as a function of C_l. Each point in Fig. 3 obeys the Burton equation [10]:

$$\delta = -(D/u)\ln\left[\frac{k_0(1-k)}{k(1-k_0)}\right], \qquad (3)$$

where $D = 7.5 \times 10^{-5}$ cm^2/s is the diffusion coefficient of Ga in the Ge melt [11] and u is the crystallization rate taken to be equal to the velocity of the zone motion. The obtained dependences $\delta = f(C_l)$ are shown in Fig. 5.

As is well known, the thickness of the diffusion layer at u = const is uniquely related to the intensity of stirring in the vicinity of the crystallization front. Therefore, the dependence $\delta = f(C_l)$ provides a number of important conclusions (still at the qualitative level) about the specific features of convection in the molten zone under the conditions existing aboard the *Foton* spacecraft still at this stage of the study.

1. Large values of δ (of the order of several millimeters) in relatively lightly doped melts indicate a very weak stirring intensity. The above estimates of δ are in good accord with the earlier data obtained in similar experiments with Ge⟨Sb⟩ which show that at the doping levels of the melt ~10^{18} at/cm^3, the process of heat and mass transfer proceeds by the mixed convective-diffusion mechanism [12].

2. At low growth rates (u = 5 mm/h), an increase of the doping level of the melt results in a logarithmic decrease of δ which, at $C_l \geq 2 \times 10^{19}$ at/cm^3, becomes comparable with the thicknesses of the diffusion layer characteristic of the terrestrial growth processes. We

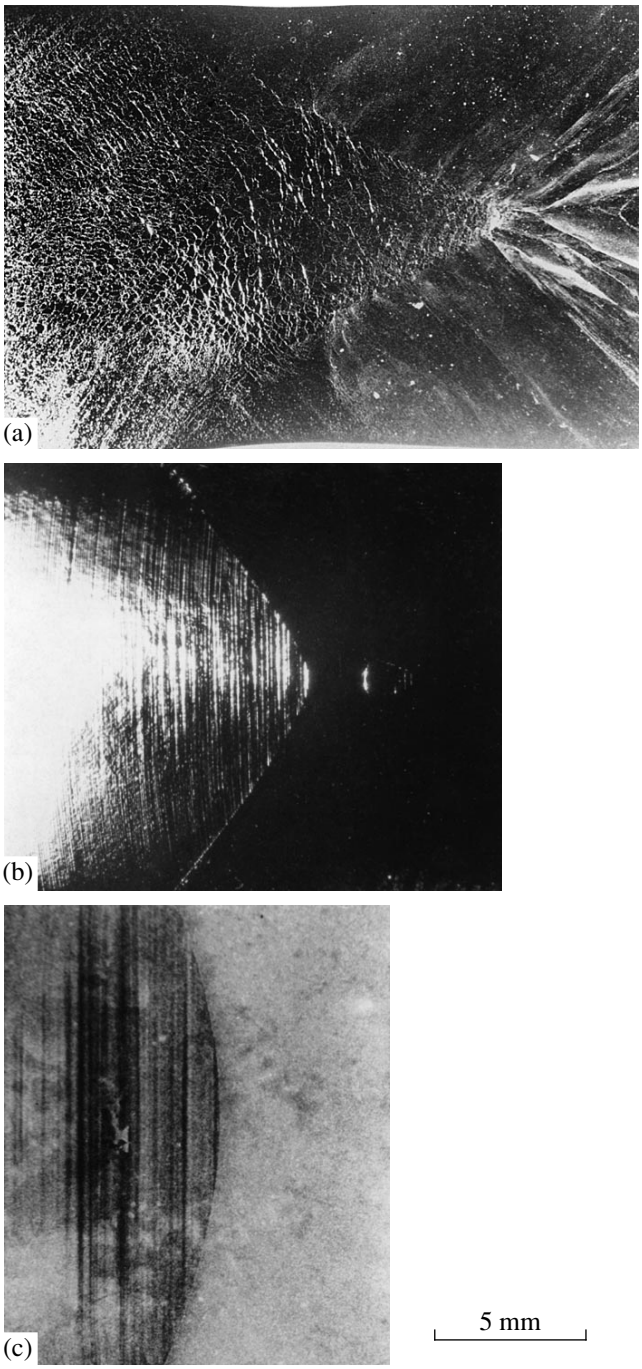

Fig. 4. Dependence of the seeding-front shape in the longitudinal sections of space Ge crystals on the level of melt doping with gallium (the seed is shown on the left): (a) undoped Ge ($n = 10^{12}$ cm^{-3}), (b) $C_0 = 1 \times 10^{18}$ at/cm^3, and (c) $C_0 = 1 \times 10^{19}$ at/cm^3.

believe that this signifies that, in heavily doped Ge⟨Ga⟩ melts in space, the stirring process is fully determined by the concentration-dependent mechanisms, and convection occurs in the whole volume of the molten zone, whereas its intensity becomes comparable with the intensity of the natural terrestrial gravitational convection.

3. With an increase of the crystallization rate (u = 7 mm/h), the point at which the intensities of the convective flows on earth and in space are equal is shifted toward higher dopant concentrations ($C_l \geq 4 \times 10^{19}$ at/cm^3), but the slope of the $\delta \sim \ln(C_l)$ dependence is changed only insignificantly. This indicates that the convection mechanism in space remains the same, but there occur some quantitative changes in the mode of dynamic equilibrium of the heat and mass flows in the melt. Thus, crystallization in space, even at low growth rates (5–7 mm/h), proceeds in the "kinetic" mode.

4. The experimental dependence $k = f(C_l)$ allows one to predict the axial distribution of the Ga-dopant during the melting of ingots of any length. Obviously, the dopant distribution in a crystal grown in space would differ from the distribution in the terrestrial crystals more pronouncedly, the lower the dopant concentration in the initial ingot. The axial profile of the space doping $C(x)$ can be calculated by (1) if one substitutes into (1) the concentration-dependent k values.

5. Obviously, the external dynamic factors acting on the molten zone in space would distort the concentration dependences of δ and k. This is especially well illustrated by experiment no. 9 (see table). The first half of the crystal in this experiment was grown under the conditions of "conventional" microgravitation (μg) aboard the spacecraft. According to [13], the vibration accelerations characteristic of *Photon* satellites at 10^{-3}–75 Hz frequencies against the background of a very low quasistationary residual microgravitation $(10^{-6}–10^{-5})g_0$ range within $(1 \times 10^{-4}–1 \times 10^{-3})g_0$. During crystallization of the second half of the ingot, the μg level had elevated values (according to our estimates, $1 \times 10^{-3} g_0 < \mu g < 1 \times 10^{-2} g_0$). A source of vibrations was a mechanical drive of an operating technological setup *Splav* located on the same mounting base as the *Zona* furnace in the working volume of the spacecraft. The effect of vibrations was revealed from the data on the microinhomogeneity of the Ga distribution in the second half of the crystal (the results are published elsewhere [14]). The points relating to crystal no. 9 in Fig. 5 are indicated by arrows. It is seen that during the growth of the second half of the crystal, the δ value remained constant, which signifies that the hydrodynamics of the melt and the crystallization parameters were determined first and foremost by the gravitational conditions aboard the spacecraft: k, $\delta = f(\mu g)$.

A pronounced inhomogeneity of the $C(x)$ distribution was also observed for single crystal no. 12 (also indicated by arrows in Fig. 5), but in this case, the source of vibrations has not been established.

Most probably, the concentration-dependent convection is considerably "suppressed" in the experiments aboard the piloted spacecrafts because of a high level of noncontrollable microaccelerations usually

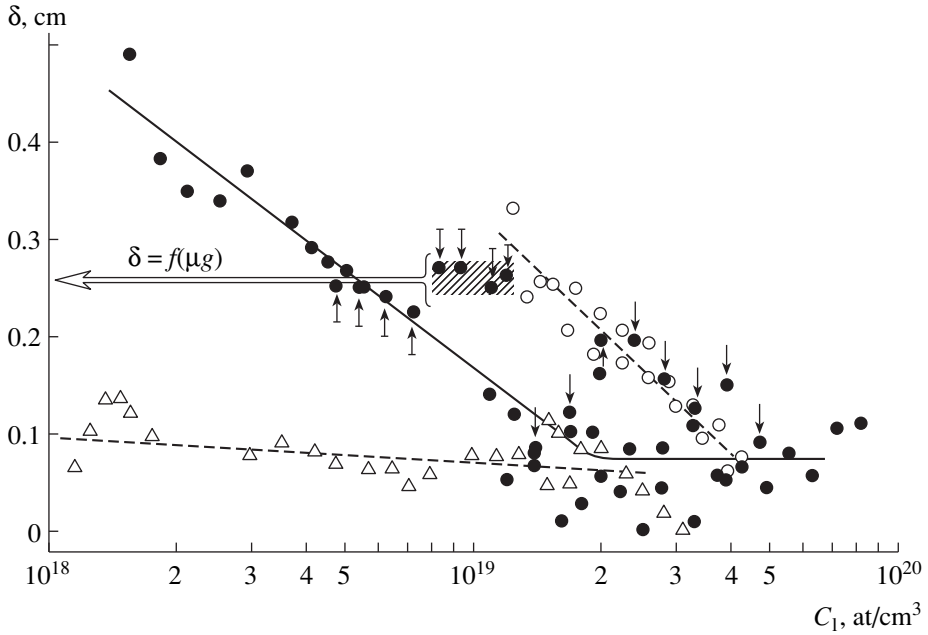

Fig. 5. Dependence of the effective thickness of the boundary front diffusion layer on Ga concentration in the melt calculated from the data given in Fig. 3. The selected points relating to crystal no. 9 are shown by ↥ and those relating to crystal no. 12, by ↑.

characteristic of these spacecrafts. With a decrease of μg, because of the use of special vibration-protective platforms, one can reveal, exactly or partly (in a narrower concentration range), the same effects also aboard piloted spacecrafts. One should take into account that the lightly doped melts (with a high value of δ during crystallization) are more gravitation-sensitive.

6. The experimental data obtained in this study provide a more reasonable attitude to the further development of the methods for control of the impurity distribution in space crystals, e.g., by applying controllable magnetic fields providing melt stirring. Varying the characteristics of external magnetic fields acting onto the melt, one can purposefully decrease δ and k to the their terrestrials values in the whole range of dopant concentrations studied and thus create the prerequisites for growth of crystals with more uniform distributions of charge carriers along the crystal length.

CONCLUSION

The effect of the concentration-dependent doping of semiconductor crystals with a free surface grown from the melt, which was first observed in this study, is, no doubt, one of the fundamental characteristics of crystallization under microgravity. However, one should bear in mind that the empirical dependences shown in Figs. 3 and 5 are only particular consequences of the fundamental hydrodynamic processes occurring in the selected model Ge⟨Ga⟩ system. The development of the general theory of this phenomenon requires further studies with the use of mathematical modeling of the processes determining the state of the melt in the vicinity of the interfaces under the action of the gradients of the surface-tension forces (σ).

The attempts to describe capillary processes by the methods of the hydrodynamic similarity theory will inevitably encounter some methodological problems. First of all, it is necessary to take into account the role played by the concentration-capillary convection. In order to determine the Marangoni concentration criterion, Mn_c, one has to know the gradient of dopant concentration in the diffusion layer close to the front, δ, and in the subsurface melt layer (in the vicinity of the free surface). For a quantitative estimate of the $\mathrm{grad}(C_l)/\mathrm{grad}(\sigma)$ ratio within the one melt zone, one has to know the exact form of the dependence $\sigma = f(C_l)$.

We believe that if the dependence $\sigma = f(C_l)$ is strongly pronounced (i.e., if the dopant is highly surface-active), the thermally-induced capillary convection can give different contributions to the hydrodynamic patterns of differently doped zones. In this case, the quantity σ (a temperature factor in the Marangoni criterion Mn_t) would have different values in the melt zones with different C_l. Moreover, the flows caused by the concentration- and thermally induced capillary convections in the crystallization processes in space can interact with one another [15].

REFERENCES

1. A. V. Kartavykh, É. S. Kopeliovich, M. G. Milvidskiĭ, *et al.*, Kristallografiya **42** (4), 755 (1997) [Crystallogr. Rep. **42** (4), 694 (1997)].

2. É. S. Kopeliovich, V. V. Rakov, and N. A. Verezub, Tsvet. Met. **8**, 52 (1991).
3. Yu. S. Osipov, Kosmonavtika Raketostroenie **6**, 3 (1996).
4. V. I. Nizhenko and L. I. Floka, *Surface Tension of Liquid Metals and Alloys. Reference Book* [in Russian] (Metallurgiya, Moscow, 1981).
5. I. V. Barmin, A. V. Egorov, V. N. Kurokhtin, *et al.*, in *Proc. Joint 10th European and 6th Russian Symp. on Physical Sciences in Microgravity* (St. Petersburg, 1997), Vol. II, p. 325.
6. *ASTM F76 Standard Test Methods for Measuring Resistivity and Hall Coefficient and Determining Hall Mobility in Single-Crystal Semiconductors* (1991).
7. W. Pfann, *Zone Melting*, 2nd edition (New York, 1966; Mir, Moscow, 1970).
8. V. N. Romanenko, *Synthesis of Homogeneous Semiconductor Crystals* [in Russian] (Metallurgiya, Moscow, 1966).
9. V. I. Fistul', *Heavily Doped Semiconductors* [in Russian] (Nauka, Moscow, 1967).
10. J. A. Burton, R. S. Prim, and W. P. Slichter, J. Chem. Phys. **21** (11), 1987 (1953).
11. A. Ya. Nashel'skiĭ, *Technology of Semiconductor Materials* [in Russian] (Metallurgiya, Moscow, 1972).
12. A. V. Kartavykh, É. S. Kopeliovich, M. G. Milvidskiĭ, *et al.*, Kristallografiya **43** (6), 1136 (1998) [Crystallogr. Rep. **43** (6), 1075 (1998)].
13. H. Hamacher, H. E. Richter, R. Jilg, *et al.*, *QSAM Ergebnisse von FOTON-11* (Münich, Deutsches Zentrum für Luft- und Raumfahrt, V, 1998).
14. M. G. Milvidskiĭ, A. V. Kartavykh, E. S. Kopeliovich, *et al.*, Journal of Journals (UNESCO) **2** (1), 6 (1998).
15. V. I. Polezhaev, A. V. Buné, N. A. Verezub, *et al.*, *Mathematical Modeling of Convective Heat and Mass Transfer Based on Navier–Stokes Equations* [in Russian] (Nauka, Moscow, 1987).

Translated by L. Man

Crystallography Reports, Vol. 45, No. 1, 2000, pp. 21–25. Translated from Kristallografiya, Vol. 45, No. 1, 2000, pp. 27–31.

STRUCTURES OF INORGANIC COMPOUNDS

Structure of Selenium and Tellurium Clusters in Cavities of Na*X* Zeolite

Yu. I. Smolin, Yu. F. Shepelev, A. E. Lapshin, and E. A. Vasil'eva

Institute of Chemistry of Silicates, Russian Academy of Sciences, ul. Odoevskogo 24-2, St. Petersburg, 199155 Russia

Received June 20, 1997; in final form, February 10, 1998

Abstract—The structure of Na*X* zeolite crystals with the Se and Te atoms incorporated into the structure from their vapors has been studied. It is shown that selenium atoms form clusters in the shape of six- and four-membered rings located in the cuboctahedral cavities of the structure framework. Single Se_2 molecules are located in large cavities, whereas Te atoms form four-membered rings located in cuboctahedra. Large cavities are occupied by two alternating configurations of Te atoms forming either a chain consisting of 16 links or an eight-membered ring. © *2000 MAIK "Nauka/Interperiodica".*

One of the methods for obtaining systems of nanometer particles widely used in electronics and optics is the synthesis of semiconductor clusters in zeolite cavities. The regular arrangement of such clusters set by the structure of the zeolite matrix allows one to study these clusters by well-developed diffraction methods.

We had the aim to determine the structure and positions of semiconductor selenium and tellurium clusters formed in the cavities of Na*X* zeolite during adsorption of Se and Te vapors. Earlier [1], we obtained and studied single crystals of the zeolite catalyst Te/Na*X* containing tellurium ions coordinated with sodium ones. Two positions of tellurium ions were established. One is located at the center of a cuboctahedron (1.3 tellurium ions per unit cell), whereas the other, in a large cavity (3.7 tellurium ions per unit cell).

The synthesis of semiconductor clusters in Na*X* was performed by the modified multistage method suggested elsewhere [1]; in this method, the last stage was changed—the Na*X*(Te) crystals were treated in a hydrogen flow. In the synthesis of clusters from vapors, the initial matrices were single crystals of Na*X* zeolite of the octahedral shape with a 0.17 mm-long edge and the dehydrated unit-cell composition $Na_{92}Al_{92}Si_{100}O_{384}$ [2]. Because of a small number of available single crystals, the crystals for the X-ray diffraction study were treated together with the fine-crystalline (0.005–0.010) fraction of Na*X* zeolite in the vapors of a semiconductor element. In each cycle of the synthesis, we used 100 mg of fine-crystalline zeolite and several single crystals dehydrated by heating to 400°C mixed with the dried Se or Te powder in the weight ratios 7 : 1 and 6 : 1, respectively. The obtained Na*X* + Se mixture in a sealed ampoule was heated for 24 h at 400°C and then for 24 h at 225°C. The Na*X* + Te mixture was heated for 48 h at 540°C. As a result of the procedure, the synthesized crystals acquired the orange [Na*X*(Se)] or the brown [Na*X*(Te)] color. To prevent possible dehydration, the synthesized crystals were coated with lacquer films. As the X-ray powder diffraction and other X-ray diffraction experiments showed, the treatment of zeolite crystals in the Se and Te vapors leads to a certain degradation of the zeolite lattice—more pronounced for Na*X*(Te) than for Na*X*(Se).

The unit-cell parameters determined on a diffractometer are 25.06(1) Å for a crystal treated in selenium vapors and 25.14(1) Å for a crystal treated in tellurium vapors. The space group for both crystals was determined to be *Fd*3 and coincided with the space group of the initial Na*X* crystals.

The intensity measurements were performed on an automated triple-crystal diffractometer operating in the mode of a normal beam (MoK_α-radiation, graphite monochromator). However, the integrated intensities were estimated by the well-known algorithm used in the profile analysis [3]. The intensities obtained were corrected for polarization and kinematic factors; no absorption correction was introduced. Altogether, the intensities of 330 nonzero nonequivalent reflections were measured for Na*X*(Se) and 256 for Na*X*(Te) crystals. In the following calculations, we used 307 and 236 reflections with $I \geq 3\sigma(I)$, respectively. The initial model structure consisted solely of the framework atoms [2]. The positions of the non-framework atoms were determined from the difference electron-density maps and the intermediate LSM refinements by the AREN-90 complex of programs [4] and the modified version of the ORFLS program [5]. The atomic factors of neutral atoms [6] and the Cruickshank weighting scheme were used [7]. The positions of all the atoms were refined in the isotropic approximation. The final values of the reliability factors were $R = 0.051$, $wR = 0.055$ and $R = 0.097$, $wR = 0.104$ for the Na*X*(Se) and

1063-7745/00/4501-0021$20.00

Atomic coordinates, isotropic thermal parameters, occupancies *p*, and multiplicities *N* of the atomic positions

Atom	*p*/*N*	*x*/*a*	*y*/*a*	*z*/*a*	*B*, A^2
			Na*X*(Se)		
Si	1	0.9470(2)	0.0350(2)	0.1248(2)	1.00(7)
Al	1	0.9460(2)	0.1237(2)	0.0367(2)	.81(7)
O(1)	1	0.8940(4)	0.9991(5)	0.1103(4)	2.0(4)
O(2)	1	0.9974(4)	0.9994(4)	0.1441(4)	1.2(2)
O(3)	1	0.1806(5)	0.0747(5)	0.2811(5)	2.1(3)
O(4)	1	0.9268(4)	0.0725(5)	0.1752(5)	1.8(3)
SeI'*a*	5.9(4)/32	0.0574(6)	0.0574(6)	0.0574(6)	4.8(5)
SeI'*b*	4.0(5)/32	0.072(1)	0.072(1)	0.072(1)	6.7(9)
SeII'	4.0(5)/32	0.166(2)	0.166(2)	0.166(2)	9(2)
SeII	8.2(7)/32	0.2363(4)	0.2363(4)	0.2363(4)	3.2(4)
Se(1)	3.8(6)/48	0.125	0.125	0.037(2)	9(1)
Se(2)	6.9(6)/96	0.274(2)	0.303(2)	0.279(2)	8(1)
Se(3)	7.1(8)/96	0.092(2)	0.155(2)	0.448(2)	7(1)
Se(4)	3.3(6)/96	0.509(4)	0.238(3)	0.356(3)	5(2)
Se(5)	2.9(7)/96	0.418(41)	0.285(4)	0.306(4)	6(2)
Na(1)	4.4(6)/16	0	0	0	1.1(7)
Na(2)	3(2)/32	0.231(3)	0.231(3)	0.231(3)	2(2)
			Na*X*(Te)		
Si	1	0.9476(4)	0.0349(3)	0.1234(6)	.7(2)
Al	1	0.9456(4)	0.1223(6)	0.0368(4)	1.2(3)
O(1)	1	0.895(1)	0.999(1)	0.107(1)	2.0(6)
O(2)	1	0.995(1)	0.996(1)	0.144(1)	1.2(5)
O(3)	1	0.181(1)	0.072(2)	0.284(1)	3.0(7)
O(4)	1	0.929(2)	0.074(2)	0.174(2)	4.6(8)
TeI'	4.1(5)/32	0.079(2)	0.079(2)	0.079(2)	5(1)
TeII'	4.4(6)/32	0.186(2)	0.186(2)	0.186(2)	5(2)
Te(1)	10.2(7)/96	0.490(2)	0.491(2)	0.386(2)	4.5(7)
Te(2)	3.4(5)/32	0.403(2)	0.403(2)	0.403(2)	6(2)
Te(3)	4(1)/96	0.046(6)	0.067(6)	0.438(7)	9(4)
Te(4)	3.9(5)/48	0.125	0.125	0.817(3)	4(1)
Te(5)	5.0(8)/96	0.279(4)	0.026(4)	0.852(4)	6(2)
Te(6)	3.1(6)/32	0.436(2)	0.436(2)	0.436(2)	7.(3)
NaII	33(3)/32	0.232(1)	0.232(1)	0.232(1)	5.3(8)
NaI	3(1)/16	0	0	0	1(3)

Na*X*(Te) crystals, respectively. The atomic coordinates and the isotropic thermal factors are listed in table.

A three-dimensional framework of *X* zeolite consists of cuboctahedra arranged according to the tetrahedral law and connected by hexagonal prisms. In *X* zeolite there are three types of the cavities—those having the shapes of hexagonal prisms and cuboctahedra and the so-called large cavity in the shape of a truncated cuboctahedron. The notation used for the main sites of non-framework atoms corresponds to the generally used nomenclature.

One of the difficulties usually encountered in the determination of the zeolite structures with large voids is the nonunique interpretation of the electron-density maxima. If the corresponding positions are occupied only partly, they can be filled statistically with atoms of different kinds (the mixed positions). One can often observe the splitting of a position into several new ones located close to one another around the initial position

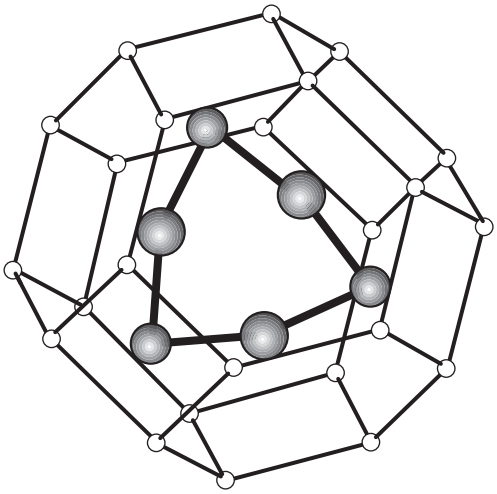

Fig. 1. Six-membered ring formed by Se atoms inside a cuboctahedron.

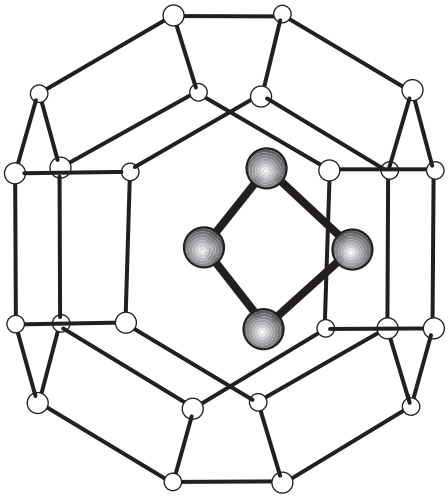

Fig. 2. Four-membered ring formed by Se or Te atoms inside a cuboctahedron.

with the atoms located only in one of these new positions.

The comparison of interatomic distances and valence angles in the aluminosilicate frameworks of the zeolites studied here and the *d*-Na*X* zeolite [2] shows that the zeolite framework is rather stable. Upon crystal treatment in selenium or tellurium vapors, the Si–O–Al angles changed by values not exceeding 5.6°, whereas the (Si, Al)–O bond lengths changed within 0.03 Å. The maximum changes in the structure are associated with the redistribution of the nonframework atoms.

Crystal structure of Na*X*(Se). In the Na*X*(Se) zeolite, the highest occupancy is observed for position I' in the cuboctahedral cavity split into positions I'*a* and I'*b*. The refinement shows that the total occupancy of both positions corresponds to 9.9 Se atoms. Position II' in dehydrated Na*X* is empty. Upon crystal treatment in selenium vapors, this position had the maximum electron density corresponding to the presence of four Se atoms.

In addition to the electron-density maxima in positions I' and II', a new electron-density maximum due to Se(1) is observed opposite the four-membered ring on the twofold axis which was not observed for the initial Na*X* zeolite [2]. The SeI'*a*–Se(1), 2.45(1) Å and the SeI'*b*–SeII' 2.38(4) Å distances are close to the Se–Se 2.37 Å distance in the eight-membered Se_8 rings [8].

The electron microscopy studies showed [9] that the distribution of the Se atoms incorporated into mordenite corresponds to the formation of Se clusters in some unit cells, whereas some other unit cells remain empty. The set of consistent interatomic distances for the crystal studied also leads to a conclusion that selenium atoms have a tendency to be combined inside the cavities and are not statistically distributed over the whole crystal volume. The analysis of the electron-density maxima allows us to state that inside cuboctahedra, alternating differently oriented six- and four-membered rings are formed by the SeI'*a*–Se(1) and SeI'*b*–SeII' atoms (Figs. 1, 2). It should also be emphasized that the occupancies of the corresponding positions agree quite well with this model.

The analysis of the additional electron-density maxima inside the large cavity in Na*X*(Se) zeolite allows us to identify them as the superposition of three crystallographically nonequivalent positions of Se_2 molecules, with each of them being multiplied by the symmetry elements. The Se–Se distances are 2.12(10) and 2.21(6) Å, which is in good agreement with the Se–Se 2.18 Å length in a Se_2 molecule determined by the electron diffraction method in vapors [10].

Crystal structure of Na*X*(Te). The maximum in position I' inside a cuboctahedron in the Na*X*(Te) structure is noticeably displaced to the cuboctahedron center in comparison with its position in Na*X* zeolite, whereas maximum II' is displaced toward the six-membered "window" between the cuboctahedron and the large cavity. These displacements result in a distance between the maxima equal to 2.72(4) Å. The almost equal weights of the maxima in the positions I' and II' and the distance Te–Te 2.72(4) Å (intermediate between the Te–Te 2.56 Å [11] in a Te_2 molecule and the Te–Te 2.86 Å in the Te crystal) lead to the assumption that both positions are occupied with Te atoms which may form a corrugated Te_6-ring similar to that shown in Fig. 2. The large cavity has two alternative configurations of Te atoms forming a ring and a chain, respectively (for a clearer representation, see Figs. 3 and 4). The eight-membered ring (Fig. 3) is formed by three crystallographically independent Te(1), Te(2), and Te(3) atoms multiplied by the symmetry operations. The bond length ranges within 2.72–3.07 Å, the

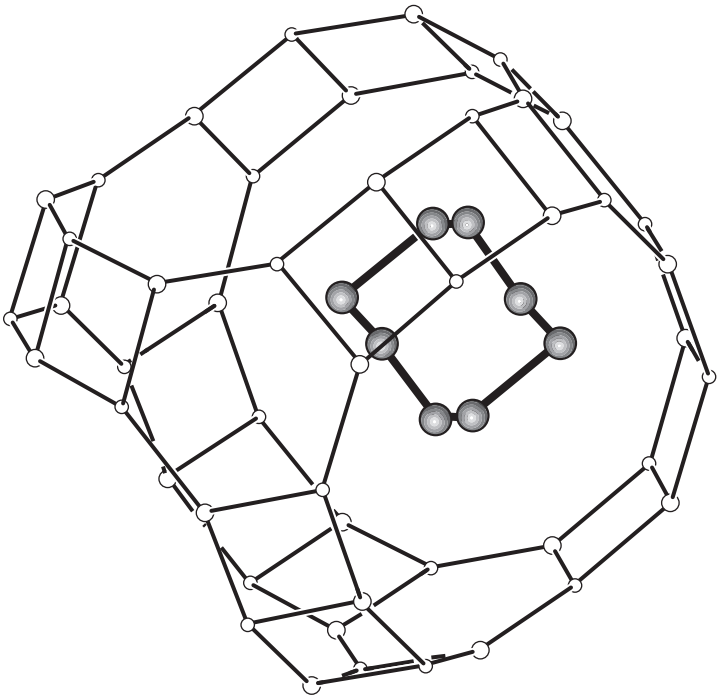

Fig. 3. Eight-membered ring formed by Te atoms in a large cavity.

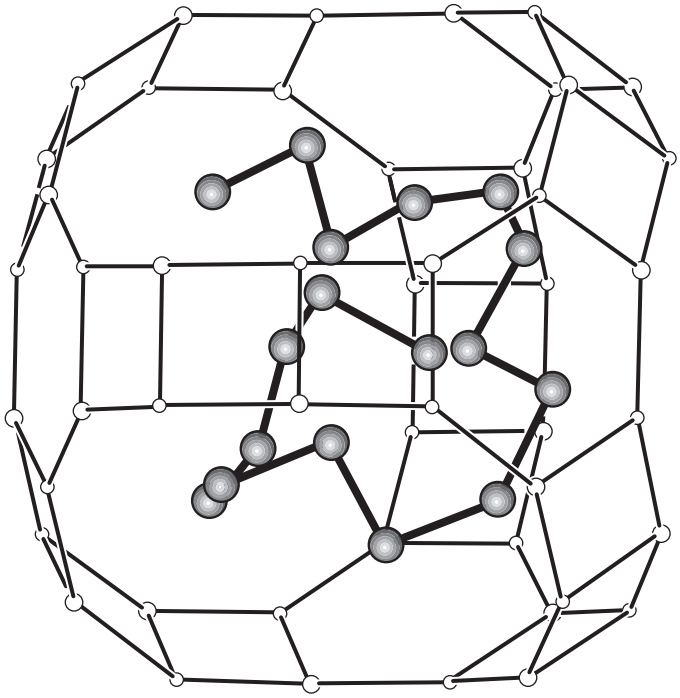

Fig. 4. Fragment of Te-chain in a large cavity.

valence angle ranges within 89.5°–140.3°. It is seen from Fig. 4 that the chain consists of 16 links formed by three other crystallographically nonequivalent atoms, Te(4), Te(5), and Te(6), multiplied by the symmetry operations. The chains in the neighboring cavities can be connected. The Te–Te bond lengths in the chain range within 2.63–2.72 Å, the valence angles, within 95.2°–135.7°. All the atoms in the chain and in the ring are spaced by the distances exceeding 3.11 Å from the framework atoms.

Similar to *d*-Na*X*, the main cationic position II in a large cavity is completely filled with Na atoms. The

coordinates of this position agree with the analogous coordinates in *d*-Na*X*, which indicates that position II is filled solely with Na atoms. Comparing the data obtained in [1] with the results obtained in the present study, we draw the following conclusions. Unlike the data in [1], where the total number of Te atoms per unit cell was determined to be five, the total number of Te atoms per unit cell determined in the present study equals 38. Contrary to [1], in our case, Te atoms are combined to form charged clusters in the form of six-membered rings located in cuboctahedra and eight-membered rings or chains located in the large cavity.

We believe that the 16.5 h treatment of Na*X*(Te) crystals in the [1] reducing atmosphere of the hydrogen flow at 475°C leads to the formation of Te^{2-} ions separated from the negatively charged aluminosilicate–oxygen framework by the tetrahedral groupings of Na^+ ions. Such groupings are located in cuboctahedra and large cavities. The aluminosilicate frameworks described in [1] and determined in the present study have similar structures.

ACKNOWLEDGMENTS

The present study was supported by the Russian Foundation for Basic Research, project no. 95-03-8111.

REFERENCES

1. D. H. Olson, R. J. Mikovsky, G. F. Shipman, *et al.*, J. Catalysis **24**, 161 (1972).
2. Yu. I. Smolin, Yu. F. Shepelev, I. K. Butikova, *et al.*, Kristallografiya **28** (1), 72 (1983).
3. S. Oatley and S. French, Acta Crystallogr., Sect. A: Cryst. Phys., Diffr., Theor. Gen. Crystallogr. **38** (4), 537 (1982).
4. V. I. Andrianov, Kristallografiya **32** (1), 228 (1987).
5. W. R. Busing, K. O. Martin, and H. A. Levy, *ORFLS, Report ORNL-TM-305* (Oak Ridge Nat. Lab, 1962).
6. H. P. Hanson, F. Herman, J. D. Lea, *et al.*, Acta Crystallogr. **17**, 1041 (1964).
7. D. W. J. Cruickshank, *Computing Methods in Crystallography*, Ed. by L. Rollet (Pergamon, London, 1965), p. 112.
8. K. Bégnall, *Chemistry of Selenium, Tellurium, and Polonium* [in Russian] (Mir, Moscow, 1971).
9. O. Terasaki, K. Yamazaki, J. M. Thomas, *et al.*, J. Solid State Chem. **77**, 72 (1988).
10. A. Barrow, O. Chandler, and I. Meyer, Phil. Trans. Roy. Soc. (London) **260**, 395 (1966).
11. J. Stone and A. Barrow, Can. J. Phys. **53**, 1976 (1975).
12. R. Keller, W. B. Holzapfel, and H. Schulz, Phys. Rev. B **16**, 4404 (1977).

Translated by L. Man

Crystallography Reports, Vol. 45, No. 1, 2000, pp. 26–29. Translated from Kristallografiya, Vol. 45, No. 1, 2000, pp. 32–35.

STRUCTURES OF INORGANIC COMPOUNDS

Refinement of the Crystal Structures of Low-Rare-Earth and "Typical" Burbankites by the Rietveld Method

Yu. V. Belovitskaya, I. V. Pekov, and Yu. K. Kabalov

Department of Geology, Moscow State University, Vorob'evy gory, Moscow, 119899 Russia

Received May 20, 1998

Abstract—The crystal structures of two samples of burbankite from the Khibiny massif, namely, low-rare-earth burbankite $(Na_{1.82}Ca_{1.02}Y_{0.02})_{2.86}(Sr_{2.32}Ba_{0.43}Ca_{0.17}La_{0.06}Ce_{0.02})_{3.00}(CO_3)_5$ from pectolite metasomatites and burbankite of the characteristic composition $(Na_{2.22}Ca_{0.65}Y_{0.03})_{2.97} \times$ $\times (Sr_{2.10}Ba_{0.33}Ce_{0.23}Ca_{0.15}La_{0.12}Nd_{0.05}Pr_{0.02})_{3.00}(CO_3)_5$ from alkaline hydrothermolites, were refined by the Rietveld method. The experimental data were collected on an ADP-2 diffractometer (λCuK_α radiation, Ni-filter; $15.00° < 2\theta < 155.00°$; 2θ scan with steps 0.02°; the exposure time per step, 15–20 s; the number of $(\alpha_1 + \alpha_2)$ reflections 556–570). All the calculations were performed using the WYRIET program (version 3.3) in the sp. gr. $P6_3mc$. For low-rare-earth burbankite: $a = 10.5263(1)$ Å, $c = 6.5392(1)$ Å, $R_P = 3.52$, $R_{wp} = 4.49$, $R_B = 4.10$, and $R_F = 4.11$. For burbankite from alkaline hydrothermolites: $a = 10.5313(1)$ Å, $c = 6.4829(1)$ Å, $R_P = 2.54$, $R_{wp} = 3.23$, $R_B = 3.06$, and $R_F = 3.44$. The structures were refined using the anisotropic thermal parameters of cations. © *2000 MAIK "Nauka/Interperiodica".*

INTRODUCTION

Burbankite (Na, Ca, □)$_3$(Sr, *TR*, Ba, Ca)$_3$(CO$_3$)$_5$, a typomorphic mineral of some types of carbonatites and alkaline metasomatites, is often encountered in alkaline massifs. In the so-called rare-earth carbonatites (found in the Khibiny, the Kola Peninsula; Vuoriyarvi, North Kareliya; the Gornoozerskii massif, and in Yakutiya), burbankite occurring as large ore bodies is the most important mineral, for industrial purposes, which can readily be enriched with the complex (*TR*, Sr, Ba) ore.

The burbankite family (burbankite, khanneshite [1], calcioburbankite [2], remondite-(Ce) [3], and petersenite-(Ce) [4]) comprises minerals of the general formula $A_3B_3(CO_3)_5$, where *A* = Na, Ca, or □ and *B* = Sr, Ba, *TR*, or Ca.

Burbankite is characterized by the complicated and varying chemical composition. This mineral contains both light (Na, Ca) and heavy (Sr, *TR*, Ba) elements in substantial amounts, with the cationic composition varying over wide ranges. Generally, burbankites of the different genesis are characterized by different compositions.

The crystal structure of burbankite was solved for the first time on a sample found in carbonatites from Vuoriyarvi in 1967 [5, 6]. Later on, the structure was refined with the use of samples from the Rocky Boy massif (Montana, USA) [7]. According to the data of the cited studies of samples containing 11–16 wt % of TR_2O_3, burbankite crystallizes in the sp. gr. $P6_3mc$. In [3], the structure of remondite-(Ce) was solved, and it was suggested that the majority of the minerals of the burbankite family, apparently, belong to the monoclinic (pseudohexagonal) system.

We studied burbankite found in pectolite metasomatites from the N'orkpakhh mountain of the Khibiny alkaline massif (sample B-104), which is characterized by a very low content of *TR* (1.76 wt % of Ln_2O_3). In other moreds, the sample composition to rare-earth-free was similar to the composition of the end member of the family, $(Na_2Ca)R^{2+}_3(CO_3)_5$, where R^{2+} = Sr, Ca, or Ba. The composition of the mineral under study is $(Na_{1.82}Ca_{1.02}Y_{0.02})_{2.86}(Sr_{2.32}Ba_{0.43}Ca_{0.17}La_{0.06}Ce_{0.02})_{3.00}(CO_3)_5$. The X-ray spectrum of burbankite of this composition had numerous split reflections (doublets or triplets, Fig. 1a) in comparison with the X-ray diffraction patterns of burbankite of a more characteristic composition (10–15% of TR_2O_3), whose typical representative was the sample B-108 also studied in this work. This sample of the composition $(Na_{2.22}Ca_{0.65}Y_{0.03})_{2.97}(Sr_{2.10}Ba_{0.33}Ce_{0.23}Ca_{0.15}La_{0.12} \times Nd_{0.05}Pr_{0.02})_{3.00}(CO_3)_5$ was found in alkaline hydrothermolites from the Kukisvumchorr mountain of the Khibiny massif. The X-ray spectrum of this sample is shown in Fig. 1b.

The comparison of the X-ray spectra of samples B-104 and B-108 (Figs. 1a, 1b) and of the sample studied in [3] lead us to an assumption that the symmetry of burbankite with the low content of rare-earth elements can undergo some changes. The fact that the Na : Ca ratio approximately equal to 2 : 1 is also retained for the *A* position of this mineral indicated that these cations may be ordered. All these facts dictated the refinement of the crystal structures of burbankites of different compositions under the same conditions.

1063-7745/00/4501-0026$20.00

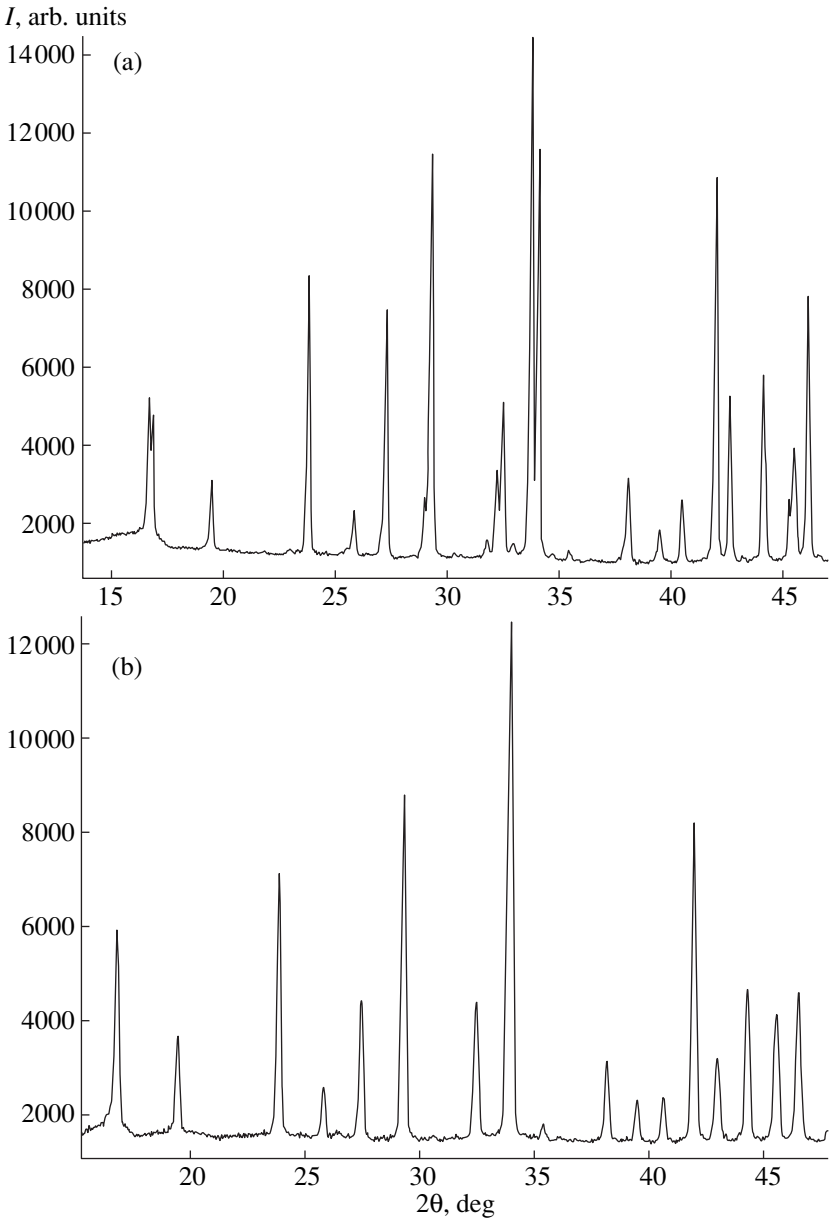

Fig. 1. Fragments of X-ray spectra of the burbankite samples (a) B-104 and (b) B-108.

EXPERIMENTAL

Low-rare-earth burbankite (B-104) occurs as greenish-yellow segregations up to 1.5 cm in size intergrowing with coarse grained prismatic pectolite. No secondary minerals were detected.

Burbankite of the typical composition (sample B-108) consists of bright-yellow grains 3–4 mm in size among thermonatrite from the "sodium carbonate core" of the ultraagpaitic pegmatitic body.

The chemical compositions of various burbankites (Table 1) were determined by analyst I.M. Kulikova, by X-ray spectral analysis (Camebax microbeam; Institute of Mineralogy, Geochemistry, and Crystal Chemistry of Rare Elements). The powdered samples were prepared from pure homogeneous grains of burbankite.

The corresponding X-ray spectra were obtained on an ADP-2 diffractometer (λCu$K\alpha$, Ni filter) by the 2θ scan at a step of 0.02°; the exposure time was 15–20 s. The data reported in [7] were used as the starting structural model. The curves of ionic scattering were used. The peak profiles were approximated by the Pearson VII function with 6FWHM. The asymmetry was refined for $2\theta < 40°$. All the computations were performed using the WYRIET program (version 3.3) [8]. The refinement was carried with an ever increasing number of parameters to be refined and with automatic modeling of the background until the attainment of sta-

Table 1. Chemical composition (wt %) and the formulas of various burbankites

Components	Sample B-104	Sample B-108	Components	Sample B-104	Sample B-108
Na_2O	8.51	10.61	Ce_2O_3	0.44	5.74
CaO	10.04	6.96	Pr_2O_3	–	0.45
SrO	36.28	33.73	Nd_2O_3	–	1.36
BaO	9.91	7.92	CO_2	(32.39)	(33.47)
Y_2O_3	0.48	0.57	Total	99.37	103.75
La_2O_3	1.32	2.94			

Note: The CO_2 content was calculated from the stoichiometric composition.

Table 2. Unit-cell parameters and characteristics of the refinement of crystal structures of various burbankites by the Rietveld method

Characteristic	Sample B-104	Sample B-108
a, Å	10.5263(1)	10.5313(1)
c, Å	6.5392(1)	6.4829(1)
c/*a*	0.6212	0.6156
V, Å^3	627.49(1)	622.68(1)
Sp. gr.	$P6_3mc$	$P6_3mc$
2θ-range, deg	15.00–155.00	15.00–153.00
Number of reflections ($\alpha_1 + \alpha_2$)	570	556
Number of parameters to be refined	54	54
R_p	3.52	2.54
R_{wp}	4.49	3.23
R_{exp}	2.97	2.57
R_B	4.10	3.06
R_F	4.11	3.44
*s**	1.51	1.26
DWD **	1.08	1.43
σ_x^{***}	1.896	1.616

* $s = R_{wp}/R_{exp}$, where R_{exp} is the expected value of R_{wp}.
**DWD is the Durbin–Watson statistics [10].
***σ_x is the factor used in calculations of standard deviations [11].

ble *R* values. The isotropic refinement yielded to the R_{wp} factors of 3.30 and 4.51% for samples B-108 and B-104, respectively.

The most important characteristics of data collection and the results of refinement of the structures of burbankites with the anisotropic (the cations in the *A* and *B* positions) and the isotropic (the oxygen and carbon atoms) thermal parameters are given in Table 2. The positional and the isotropic and the anisotropic thermal parameters of the atoms as well as the position occupancies are given in Table 3.

RESULTS AND DISCUSSION

The data obtained for burbankite of the typical composition (sample B-108) agree with the known data [5, 7]. The structure of low-rare-earth burbankite (B-104) was refined in the sp. gr. $P6_3mc$. The *R* factors (Table 2) confirm the correctness of the refined data.

We made an attempt to refine the structure of the low-rare-earth burbankite (B-104) in the sp. gr. $P2_1$. However, still at the initial stage of this refinement, it became evident that this model is inadequate (the presence of "extra" reflections, absent in the theoretically calculated X-ray diffraction pattern; dubious occupancies for the three Sr positions; and the negative values of the isotropic temperature factors for *A* cations).

The *A* cations in the structure (Na and Ca) occupy eight-vertex polyhedra. The average *A*–O distances are 2.49 and 2.50 Å in samples B-104 and B-108, respectively. The *A* positions are statistically occupied by Na and Ca atoms. Therefore, the Na : Ca ratio in low-rare-earth burbankite that is approximately equal to 2 : 1 is explained only by the necessity of the valence balance and cannot be explained by the ordering of these cations. The *B* cations (Sr, Ba, and *TR*) are located in ten-vertex polyhedra with the average *B*–O distances of 2.69 and 2.70 Å for samples B-108 and B-104, respectively. Three types of the CO_3 groups have different orientations. The C(2) and C(3) triangles are parallel to the (001) plane, whereas the C(1) triangles are inclined to it. On the whole, the C–O distances correspond to the data known for carbonates with a simpler structure (C–O = 1.284 Å [9]).

The splitting of the peaks in the X-ray spectrum of low-rare-earth burbankite (B-104) depends only on the ratio of the unit cell parameters (*c*/*a* = 0.6212). The differences in the values of the interplanar distances in some pairs of reflections become lower with a decrease in the *c*/*a* ratio. Thus, these values become equal for pairs of intense reflections (112)–(301) and (202)–(220) at *c*/*a* = 0.61237. In burbankite of the typical composition (sample B-108), we have *c*/*a* = 0.6156. The burbankites, whose X-ray diffraction patterns have nonsplit peaks, are characterized by close parameter ratios (*c*/*a* = 0.6188 [5] and *c*/*a* = 0.6176 [7]).

Therefore, in spite of substantial variations in the composition, burbankite retains the symmetry $P6_3mc$. It was demonstrated that [4] an excess amount of Na (up to 4 formula units) incorporated into the structure's burbankite-like phases gives rise to the lowering of the symmetry to the monoclinic. In turn, this leads to the transformation of one of the ten-vertex *B* polyhedra into an eight-vertex polyhedron. In the low-rare-earth burbankite under study, the ratio between the numbers of the eight- and ten-vertex polyhedra is typical of this

Table 3. Structural and thermal parameters ($Å^2$) of burbankites

Position	Characteristic	Sample B-104	Sample B-108	Position	Characteristic	Sample B-104	Sample B-108
A	*x*	0.5230(4)	0.5237(6)	C(1)	*x*	0.796(2)	0.799(2)
	y	0.4770(4)	0.4763(6)		*y*	0.204(2)	0.201(2)
	z	0.316(1)	0.319(2)		*z*	0.549(4)	0.53(1)
	B_j	1.5(1)	1.7(2)		B_j	2.4(5)	2.7(6)
	β_{11}	0.0042(8)	0.006(1)	C(2)	*x*	0	0
	β_{22}	0.0042(8)	0.006(1)		*y*	0	0
	β_{33}	0.007(2)	0.011(5)		*z*	0.852(7)	0.85(1)
	β_{12}	0.0017(2)	0		B_j	1.6(9)	2.0(9)
	β_{13}	0.0006(2)	0.003(1)	C(3)	*x*	0.3333	0.3333
	β_{23}	−0.0006(2)	−0.003(1)		*y*	0.6667	0.6667
	q(Na)	1.87(2)	2.20(4)		*z*	0.49(2)	0.49(2)
	q(Ca)	1.03(2)	0.71(2)		B_j	2.2(7)	2.0(8)
B	*x*	0.8430(0)	0.8410(1)	O(1)	*x*	0.382(1)	0.376(2)
	y	0.1570(0)	0.1590(1)		*y*	0.087(1)	0.088(2)
	z	0	0		*z*	0.631(2)	0.628(3)
	B_j	0.89(3)	0.88(3)		B_j	1.7(2)	1.6(3)
	β_{11}	0.0025(2)	0.0021(2)	O(2)	*x*	0.9292(8)	0.931(1)
	β_{22}	0.0025(2)	0.0021(2)		*y*	0.0708(8)	0.070(1)
	β_{33}	0.0067(4)	0.0091(5)		*z*	0.362(2)	0.352(4)
	β_{12}	0.0011(2)	0.0010(2)		B_j	2.3(4)	2.9(5)
	β_{13}	−0.0001(5)	0.001(1)	O(3)	*x*	0.4048(6)	0.406(1)
	β_{23}	0.0001(5)	−0.001(1)		*y*	0.5952(6)	0.594(1)
	q(Sr)	2.15(1)	1.90(1)		*z*	0.482(6)	0.49(1)
					B_j	1.9(3)	1.7(3)
	q(TR + Ba)*	0.45(1)	0.72(1)	O(4)	*x*	0.774(1)	0.770(2)
					y	0.226(1)	0.230(2)
	q(Ca)	0.11(2)	0.14(2)		*z*	0.355(3)	0.358(5)
					B_j	2.1(4)	3.1(5)

* The *f* curves for Ba (B-104) and Ce (B-108) were used for *TR* and Ba atoms.

mineral ($A_3^{VIII} B_3^{X}$). Thus, the mineral retains its initial symmetry if these polyhedra are statistically occupied by the corresponding cations.

REFERENCES

1. G. K. Eremenko and V. A. Vel'ko, Zapiski Vseross. Mineral. Obshchestva **111**, 321 (1982).
2. J. Velthuizen, R. Gault, and J. Grice, Can. Mineral. **33**, 1231 (1995).
3. P. Ginderow, Acta Crystallogr., Sect. C: Crystal. Struct. Commun. **45**, 187 (1989).
4. J. Grice, J. Velthuizen, and R. Gault, Can. Mineral. **32**, 405 (1994).
5. A. A. Voronkov and N. G. Shumyatskaya, Kristallografiya **13** (2), 246 (1968).
6. A. A. Voronkov, N. G. Shumyatskaya, and Yu. A. Pyatenko, Kristallografiya **12** (1), 135 (1967).
7. H. Effenberger, F. Kluger, H. Paulus, *et al.*, Neyes. Jahrb. Miner. Monatsh. **4**, 161 (1985).
8. J. Schneider, in *Proceedings of IV Crystallographic International Workshop on the Rietveld Method* (Petten, 1989), p. 71.
9. J. Zemann, Fortschr. Miner. **59**, 95 (1981).
10. R. Hill and H. Flack, J. Appl. Crystallogr. **20**, 356 (1987).
11. J.-F. Berar and P. Lelann, J. Appl. Crystallogr. **24**, 1 (1991).

Translated by T. Safonova

Crystallography Reports, Vol. 45, No. 1, 2000, pp. 30–34. Translated from Kristallografiya, Vol. 45, No. 1, 2000, pp. 36–40.

STRUCTURES OF INORGANIC COMPOUNDS

Synthesis and Structure of Zirconium and 3*d*-Transition Metal Phosphates $M_{0.5}Zr_2(PO_4)_3$ (M = Mn, Co, Ni, Cu, Zn)

V. I. Pet'kov*, A. I. Orlova*, G. I. Dorokhova, and Ya. V. Fedotova***

** Nizniĭ Novgorod State University, pr. Gagarina, 23, Nizniĭ Novgorod, 603600 Russia*

*** Moscow State University, Vorob'evy gory, Moscow, 117349 Russia*

Received March 26, 1999; in final form, June 21, 1999

Abstract—Double zirconium and 3*d*-transition metal phosphates of the compositions $M_{0.5}Zr_2(PO_4)_3$ [M = Mn (**I**), Co (**II**), Ni (**III**), Cu (**IV**), Zn (**V**)] have been synthesized and the types of their structures have been refined. Compounds **I**, **II**, **III**, **IV**, and **V** are all monoclinic (sp. gr. $P2_1/n$, $Z = 4$) and have the unit cell parameters a = 12.390(3), 12.389(3), 12.385(3), 12.389(3), 12.389(2) Å; b = 8.931(4), 8.928(3), 8.924(4), 8.925(4), 8.929(3) Å; c = 8.843(3), 8.840(2), 8.840(3), 8.841(3), 8.842(2) Å, β = 90.55(1), 90.54(1), 90.53(1), 90.53(1), 90.54(1)°; V = 978.5, 977.7, 977.0, 977.4, 978.1 Å^3, respectively. All the structures have the $\{[Zr_2(PO_4)_3]^-\}_{3\infty}$-type frameworks. The crystallographic data for 3*d*-transition and alkali earth metal phosphates described by the general formula $M_{0.5}Zr_2(PO_4)_3$ are compared. © *2000 MAIK "Nauka/Interperiodica".*

INTRODUCTION

Synthesis and structural studies of some representatives of zirconium and 3*d*-transition metal phosphates with the oxidation degree +2 were considered in several publications [1–7]. Scarce data on the crystal structures of the compounds with the general formula $M_{0.5}Zr_2(PO_4)_3$ (M = Mn, Co, Ni, Cu, and Zn) obtained earlier are often inconsistent with the data of later publications. Thus, the structural studies of polycrystal $Ni_{0.5}Zr_2(PO_4)_3$ and $Zn_{0.5}Zr_2(PO_4)_3$ samples (sp. gr. $R\bar{3}c$) obtained in [1] contradict the earlier studies (sp. gr. $P2_1/n$) [6, 7]. However, one can state that mainly two structure types are characteristic of these phosphates, namely, $NaZr_2(PO_4)_3$ [8] and $Li_3In_2(PO_4)_3$ [9]. The structures of the compounds related to each of these two structure types (Fig. 1) are rather close—they are characterized by polyhedral frameworks of the mixed types in which zirconium or indium cations occupy the octahedral positions, whereas the pentavalent oxygen-containing phosphorus anions are located in tetrahedral voids. Both types of polyhedra are linked only by vertices. The frameworks formed by the strongest chemical bonds of the structure have a large number of voids of various dimensions appropriate for the location of a large number of various cations. These voids can be considered as a buffer for various framework distortions caused by the interactions of the framework with the cations filling the voids. Since the void dimensions do not exactly correspond to the dimensions of the ions filling these voids, the void dimensions should be accommodated to the ion size without changing the framework architecture as a whole or lowering its symmetry.

The present work continues the systematic investigations [10–13] of specific features of the formation and structure of anhydrous orthophosphates in the Me_xO_y–ZrO_2–P_2O_5 systems, where Me are cations with

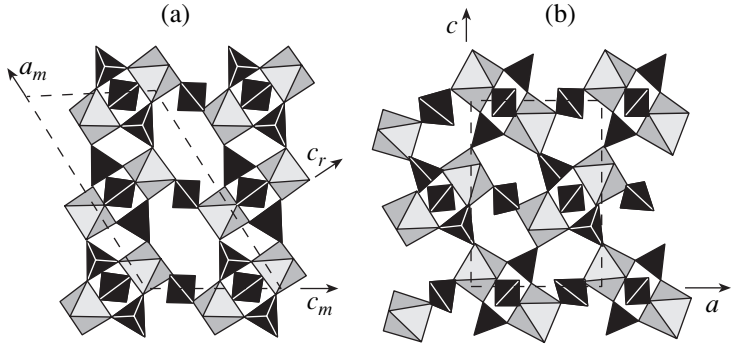

Fig. 1. Fragments of the frameworks of the (a) rhombohedral $NaZr_2(PO_4)_3$ and (b) monoclinic $Li_3In_2(PO_4)_3$ structures projected onto the *xz* plane. The *a*- and *c*-axis in the rhombohedral unit cell are given in the monoclinic setting. Half of the monoclinic unit cell is shown by a dashed line.

1063-7745/00/4501-0030$20.00 © 2000 MAIK "Nauka/Interperiodica"

oxidation degrees varying from +1 to +5. The refinement of the structures of the $M_{0.5}Zr_2(PO_4)_3$ compounds is very important for creating zirconium-phosphate-based ceramics with valuable physical properties [14].

The present study was aimed at the synthesis of zirconium and 3*d*-transition metal phosphates of the general composition $M_{0.5}Zr_2(PO_4)_3$ and the generalization of the characteristic features of the phase formation and the structures of these compounds.

EXPERIMENTAL

Phosphates of the general formula $M_{0.5}Zr_2(PO_4)_3$, where M = Mn, Co, Ni, Cu, and Zn were synthesized by the sole–gel method. The starting materials were chemically pure $MnCl_2 \cdot 4H_2O$, $CoCl_2 \cdot 6H_2O$, $NiCl_2 \cdot 6H_2O$, $CuCl_2 \cdot 2H_2O$, $ZnCl_2$, $ZrOCl_2 \cdot 8H_2O$, and H_3PO_4 reagents. The stoichiometric amounts of aqueous solutions of the 3*d*-transition metal salts and zirconium oxychlorides (preliminarily dissolved in distilled water slightly oxidized by chloric acid to prevent possible hydrolysis) were mixed together under constant stirring at room temperature. Then a solution of the phosphoric acid (also prepared in accordance with the phosphate stoichiometry) was slowly added to the initial solution under constant stirring. The gel formed was dried at 80°C and then thermally treated for 24 h at 600 and for 24 h at 800°C. The heating stages were alternated with dispersion.

The thus synthesized samples were polycrystalline powders with the colors characteristic of the corresponding transition metal ions with the oxidation degree +2. The manganese-containing samples were of the pale beige color, the cobalt-containing ones, of the lilac color, the nickel-containing ones, of the dark-pink color, and the copper-containing ones, of the light blue color; the zinc-containing samples were colorless. The chemical composition and homogeneity of the synthesized powders were checked with the aid of a Camebax microprobe. The results of the electron-probe analysis confirmed the homogeneity of the samples and indicated that their compositions were close to the theoretical values calculated for the general formula $M_{0.5}Zr_2(PO_4)_3$.

The sequences of the processes occurring during the phosphate synthesis and identification and characterization of the synthesized compounds were controlled by the X-ray diffraction method (DRON-3M diffractometer, CuK_α- and CoK_α-radiation, scan rate 1°/min) and also by the combined method of the differential thermal analysis (DTA) and the thermogravimetric analysis (TGA) (derivatograph *Q*-1500D, heating rate 10°/min). The lattice parameters of the compounds were determined from the corresponding diffraction patterns indexed within the angular range $2\theta = 8°–50°$ and then were refined by the least squares method.

RESULTS AND DISCUSSION

It has been established that the phosphate synthesis is completed at temperatures not lower than 600–700°C. The TGA curves obtained at lower temperatures indicated the mass loss, whereas the corresponding diffraction patterns contained reflections due to zirconium dioxide, ZrO_2. The diffraction patterns obtained from the samples annealed at 800°C were similar. Still at this stage, a conclusion about the isostructurality of all the compounds of the probable composition $M_{0.5}Zr_2(PO_4)_3$ with M = Mn, Co, Ni, Cu, and Zn could be drawn. However, their structures can be reliably established only by methods of X-ray structure analysis applied to at least one of these phosphates.

The DTA curves showed the absence of any thermal effects during specimen heating at 800–1000°C; the corresponding TGA curves showed no mass losses; the corresponding diffraction patterns indicated only an insignificant increase of the intensities of the diffraction reflections. All these facts prove the thermal, compositional, and structural stability of the phosphates synthesized within the temperature range studied.

It should also be emphasized that the X-ray diffraction analysis of single crystals was performed only for a limited number of phosphates, and therefore their structures are often unknown. However, the establishment of the phosphate isostructurality for polycrystalline samples (powders) allows one to increase the number of phosphates with the known structures. In order to establish the structure type of double zirconium and 3*d*-transition metal phosphates, we used the results of the complete structural determination of $Ni_{0.5}Zr_2(PO_4)_3$ [6] as the initial data.

The X-ray diffraction data obtained for the synthesized phosphates are listed in Tables 1 and 2. The corresponding data obtained for the $Ni_{0.5}Zr_2(PO_4)_3$ structure [6] are consistent with the data obtained in the present study. We observed a slight monotonic change in the unit-cell parameters of the $M_{0.5}Zr_2(PO_4)_3$ phosphates depending on the radii of the M^{2+} cations (Fig. 2).

Similar chemical formulas, close unit-cell parameters, and the symmetry of all the compounds described indicate that their crystal structures are formed according to the same scheme and that they are isostructural. The the good agreement of the data obtained in the present study and the data of the complete structural determination of the $Ni_{0.5}Zr_2(PO_4)_3$ orthophosphate allows us to state that the structures of the $M_{0.5}Zr_2(PO_4)_3$ phases with M = Mn, Co, Ni, Cu, and Zn are also established.

The crystal structures of these phases consist of the monoclinic frameworks built by zirconium octahedra and phosphorus tetrahedra (Fig. 3). Some voids of the Zr,P-framework are filled with the 3*d*-transition metal cations. The Ni-position determined in [6] is close to the Li(3) position in the $Li_3In_2(PO_4)_3$ structure [9]. All

Table 1. Indexing of diffraction patterns of the $M_{0.5}Zr_2(PO_4)_3$ compounds, where M = Mn, Co, Ni, Cu, Zn (d, Å; I/I_0, %)

h	k	l	Mn			Co			Ni			Cu			Zn		
			d_{calc}	d_{obs}	I/I_0	d_{calc}	d_{obs}	I/I_0	d_{calc}	d_{obs}	I/I_0	d_{calc}	d_{obs}	I/I_0	d_{calc}	d_{obs}	I/I_0
1	0	–1	7.231	7.226	5	7.228	7.226	5	7.227	7.220	4	7.228	7.226	5	7.229	7.226	5
2	0	0	6.195	6.207	8	6.194	6.189	8	6.192	6.189	9	6.194	6.181	8	6.194	6.198	7
1	1	–1	5.620	5.623	7	5.617	5.623	10	5.616	5.616	11	5.617	5.619	8	5.614	5.623	12
0	2	0	4.465	4.467	20	4.464	4.461	34	4.462	4.459	23	4.462	4.459	39	4.465	4.461	29
0	0	2	4.421	4.423	100	4.420	4.417	100	4.420	4.417	100	4.420	4.419	100	4.421	4.419	100
0	1	2	3.962	3.961	6	3.961	3.959	11	3.961	3.958	11	3.961	3.959	12	3.962	3.963	11
1	1	–2	3.784	3.785	34	3.782	3.783	26	3.782	3.783	26	3.782	3.783	35	3.780	3.783	30
3	0	–1	3.756	3.758	41	3.755	3.755	35	3.754	3.753	35	3.755	3.756	39	3.761	3.755	33
3	1	–1	3.462	3.463	3	3.461	3.461	7	3.460	3.459	5	3.461	3.461	3	3.461	3.463	4
2	2	1	3.345	3.346	4	3.345	3.344	13	3.344	3.343	12	3.344	3.344	11	3.345	3.345	13
0	2	2	3.142	3.141	42	3.141	3.141	39	3.140	3.142	42	3.140	3.141	45	3.141	3.143	38
4	0	0	3.097	3.098	24	3.097	3.098	29	3.096	3.097	30	3.097	3.099	32	3.097	3.097	26
1	2	2	3.040	3.041	4	3.040	3.040	11	3.039	3.039	12	3.039	3.039	11	3.040	3.041	12
1	0	–3	2.874	2.874	14	2.873	2.873	15	2.873	2.873	11	2.873	2.873	12	2.873	2.873	13
3	2	–1	2.874			2.873			2.872			2.873			2.873		
2	2	2	2.794	2.795	25	2.794	2.793	10	2.793	2.792	13	2.793	2.793	12	2.796	2.794	9
1	3	–1	2.753	2.752	8	2.752	2.749	24	2.751	2.747	21	2.751	2.748	15	2.752	2.752	23
1	3	1	2.749			2.748			2.747			2.747			2.748		
4	2	0	2.545	2.545	48	2.545	2.545	43	2.544	2.544	52	2.544	2.545	54	2.545	2.545	41
1	2	3	2.409	2.409	5	2.408	2.408	6	2.408	2.408	5	2.408	2.408	5	2.409	2.409	3
5	1	–1	2.311	2.310	2	2.310	2.310	8	2.309	2.309	6	2.310	2.310	4	2.309	2.310	4
0	0	4	2.211	2.211	8	2.210	2.210	8	2.210	2.210	8	2.210	2.210	9	2.210	2.210	7
3	3	2	2.114	2.114	7	2.114	2.114	8	2.113	2.114	6	2.114	2.114	7	2.114	2.114	6
2	3	3	1.980	1.980	27	1.980	1.979	23	1.979	1.979	29	1.979	1.979	28	1.980	1.980	21
6	1	1	1.958	1.958	10	1.958	1.958	22	1.957	1.957	30	1.958	1.958	22	1.959	1.958	26
2	2	4	1.882	1.883	12	1.882	–	–	1.882	–	–	1.882	–	–	1.882	–	–
6	2	0	1.874	–	–	1.874	1.874	6	1.873	1.873	7	1.874	1.874	6	1.874	1.874	6
5	3	–1	1.865			1.864			1.864			1.864			1.864		
6	0	2	1.864	1.864	3	1.864	1.863	9	1.864	1.863	8	1.864	1.863	5	1.864	1.863	5
5	1	–3	1.864			1.863			1.863			1.863			1.863		

Table 2. Crystallographic characteristics of the monoclinic compounds studied (sp. gr. $P2_1/n$, $Z = 4$)

Chemical formula	Unit-cell parameters					ρ_{calc}, g/cm^3
	a, Å	b, Å	c, Å	β, deg	V, Å^3	
$Mn_{0.5}Zr_2(PO_4)_3$	12.390(3)	8.931(4)	8.843(3)	90.55(1)	978.5	3.36
$Co_{0.5}Zr_2(PO_4)_3$	12.389(3)	8.928(3)	8.840(2)	90.54(1)	977.7	3.37
$Ni_{0.5}Zr_2(PO_4)_3$	12.385(3)	8.924(4)	8.840(3)	90.53(1)	977.0	3.38
$Cu_{0.5}Zr_2(PO_4)_3$	12.389(3)	8.925(4)	8.841(3)	90.53(1)	977.4	3.39
$Zn_{0.5}Zr_2(PO_4)_3$	12.389(2)	8.929(3)	8.842(2)	90.54(1)	978.1	3.39

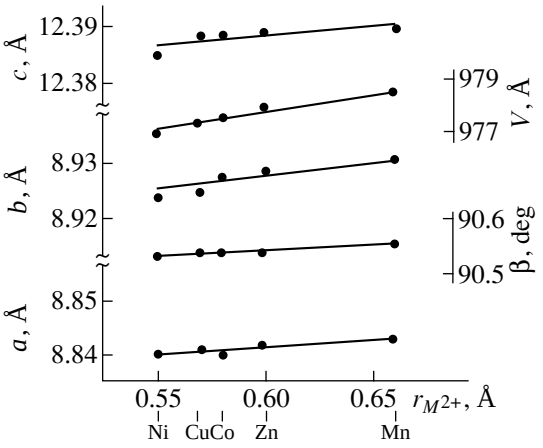

Fig. 2. Parameters *a*, *b*, *c*, β, and volume *V* of the monoclinic unit cell as functions of the radii of the 3*d*-transition metal cations M^{2+} [15] in $M_{0.5}Zr_2(PO_4)_3$ crystals.

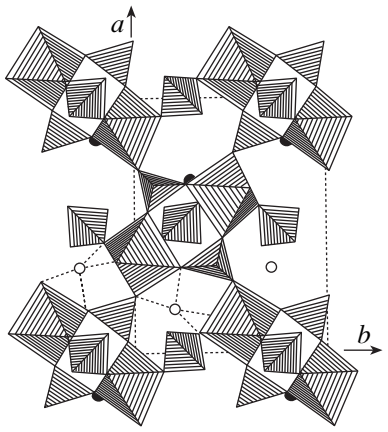

Fig. 3. Characteristic fragment of the $M_{0.5}Zr_2(PO_4)_3$ structure projected onto the *xy* plane [6]. Dark and light circles indicate the positions of *M* cations located at $z \cong 1/4$ and $z \cong 3/4$, respectively.

the Ni and other 3*d*-transition metal ions occupy their positions only statistically (for 50%) and, because of their small dimensions, are characterized by the tetrahedral coordination.

An additional argument in favor of the isostructurality of all the phosphates studied was obtained by the special calculation with due regard for the interatomic distances. The cation–oxygen distances in the tetrahedra formed around Ni^{2+}-ions range from 1.89 to 2.26 Å [6], with the average distance, 2.11 Å, considerably exceeding the sum of the corresponding ionic radii $r_{IV}(Ni) + r_{IV}(O) = 0.55 + 1.36 = 1.91$ Å [15]. A considerable increase of this distance is explained by the fact that Ni-cations cannot appropriately change the polyhedra of the rigid framework in which the nickel position is not a structure-forming one. As a result, this position can be either completely free (as is in $Zr_2(PO_4)_2SO_4$ [16]) or partly (as in $Ni_{0.5}Zr_2(PO_4)_3$) or fully occupied (as in the $Li_3In_2(PO_4)_3$ structure). This indicates that the Ni position can be filled only with cations of a slightly larger size and with the oxidation degree +2, such as the Cu-, Co-, Zn-, and even Mn-cations.

The presence of 3*d*-transition metal cations in the voids of the $\{[Zr_2(PO_4)_3]^-\}_{3\infty}$ framework can give rise only to insignificant deformation of the anionic part of the structure. Thus, four Zr–O distances in each independent Zr-octahedron in the $Ni_{0.5}Zr_2(PO_4)_3$ phosphate are rather close and range within 2.03–2.08 Å and 1.99–2.09 in the Zr(1) in the Zr(2) octahedra, respectively [6]. Two oxygen atoms are spaced from the Zr(1) atom by 2.11 and 2.13 Å and from the Zr(2) atom, by 2.16 and 2.17 Å. As is seen, the $Zr(2)O_6$-polyhedron is more distorted, which is explained by the fact that it shares the edge with a nickel tetrahedron. However, the average Zr(1)–O and Zr(2)–O distances remain the same, 2.08 Å, which corresponds to the standard distance known for such coordination. The P–O distances of the orthophosphate tetrahedra vary within the conventional ranges: from 1.48 to 1.55 Å (the average 1.51 Å) in the P(1)-tetrahedron, from 1.49 to 1.52 Å (the average 1.50 Å) in the P(2)-tetrahedron, and from 1.49 to 1.57 Å (the average 1.53 Å) in the P(3)-tetrahedron.

Because of the existence of large voids forming a system of channels having complicated shapes and the distortion of the $\{[Zr_2(PO_4)_3]^-\}_{3\infty}$ frameworks in the phosphate structures, the ions compensating the framework charge are characterized by different numbers of the nearest neighbors. Thus, in analogous phosphates described by the formula $M_{0.5}Zr_2(PO_4)_3$, where *M* = Mn, Co, Ni. Cu, Zn, Mg, Ca, Sr, and Ba, the *d*-transition metal and magnesium cations fill free tetrahedral voids, whereas the alkali metal cations are characterized by the octahedral coordination [13]. In this case, the unit-cell symmetry is changed from monoclinic to trigonal, whereas the general features of the structure are not changed at all.

The range of existence of the rhombohedral $\{[L_2(PO_4)_3]^{p-}\}_{3\infty}$ framework (where *L* is an octahedral cation), whose voids can be filled with cations having different dimensions almost without changing the void geometry, in the compounds described by the general formula $M_{0.5}Zr_2(PO_4)_3$, noticeably decreases in the transition from alkali earth to 3*d*-transition metals. We believe that this is provided by easy deformation of the oxygen environment of cations with the oxidation degree +2, considerable flexibility of the frameworks built by the sharing-vertices Zr and P coordination polyhedra, and the coordination instability of cations with the oxidation degree +2.

ACKNOWLEDGMENTS

This study was supported by the Russian Foundation for Basic Research, project no. 98-03-32571a.

REFERENCES

1. N. G. Chernorukov, I. A. Korshunov, and T. V. Prokof'eva, Kristallografiya **23** (4), 844 (1978).
2. M. Kinoshita, S. Baba, A. Kishioka, *et al.*, Bull. Chem. Soc. Jpn. **51**, 1233 (1978).
3. A. E. Jazouli, M. Alami, R. Brochu, *et al.*, J. Solid State Chem. **71**, 444 (1987).
4. I. Bussereau, R. Olazcuaga, G. Le Flem, *et al.*, Eur. J. Solid State Inorg. Chem. **26**, 383 (1989).
5. S. Ikeda, Y. Kanbayashi, K. Nomura, *et al.*, Solid State Ionics **40/41**, 79 (1990).
6. A. Jouanneaux, A. Verbaere, Y. Piffard, *et al.*, Eur. J. Solid State Inorg. Chem. **28**, 683 (1991).
7. K. Nomura, S. Ikeda, K. Ito, *et al.*, J. Electroanal. Chem. **326**, 351 (1992).
8. H. Y.-P. Hong, Mater. Res. Bull. **11**, 173 (1976).
9. D. Tran Qui and S. Hamdoune, Acta Crystallogr., Sect. C: Cryst. Struct. Commun. **43**, 397 (1987).
10. V. I. Pet'kov, A. I. Orlova, and O. V. Egor'kova, Zh. Strukt. Khim. **37**, 1104 (1996).
11. O. V. Egor'kova, A. I. Orlova, V. I. Pet'kov, *et al.*, Radiokhim. **39**, 491 (1997).
12. O. V. Egor'kova, A. I. Orlova, V. I. Pet'kov, *et al.*, Neorg. Mater. **34**, 373 (1998).
13. V. I. Pet'kov, A. I. Orlova, and D. A. Kapranov, Zh. Neorg. Khim. **43**, 1540 (1998).
14. A. I. Orlova, V. I. Pet'kov, G. N. Kazantsev, *et al.*, in *Proceedings of Scientific-Technical Conf. Glass and Ceramics: Production and Applications* (1997), p. 26.
15. R. D. Shannon, Acta Crystallogr., Sect. A: Cryst. Phys., Diffr., Theor. Gen. Crystallogr. **32**, 751 (1976).
16. J. Alamo and R. Roy, J. Solid State Chem. **51**, 270 (1984).

Translated by L. Man

Crystallography Reports, Vol. 45, No. 1, 2000, pp. 35–38. Translated from Kristallografiya, Vol. 45, No. 1, 2000, pp. 41–44.

STRUCTURES OF COORDINATION COMPOUNDS

Crystal Structure of Dibarium (Ethylenediaminetetraacetato)cuprate(II) Diperchlorate Hexahydrate, $Ba_2[Cu(Edta)](ClO_4)_2 \cdot 6H_2O$

I. N. Polyakova*, A. L. Poznyak, and V. S. Sergienko***

** Kurnakov Institute of General and Inorganic Chemistry, Russian Academy of Sciences, Leninskiĭ pr. 31, Moscow, 117907 Russia*

*** Institute of Molecular and Atomic Physics, Belarussian Academy of Sciences, pr. F. Skoriny 70, Minsk, 220072 Belarus*

Received November 25, 1997

Abstract—Compound $Ba_2[Cu(Edta)](ClO_4)_2 \cdot 6H_2O$ is synthesized and its crystal structure is determined [R = 0.0500 for 4439 reflections with $I > 2\sigma(I)$]. The structure consists of the $[Cu(Edta)]^{2-}$ anionic complexes, hydrated barium cations, ClO_4^- anions, and molecules of crystallization water, which are interlinked into a framework. The hexadentate $Edta^{4-}$ ligand coordinates the Cu atom forming the polyhedron in a shape of a tetragonal bipyramid, which is asymmetrically stretched along the O_R–Cu–O_R axis (Cu–O, 2.262 and 2.532 Å). The mean lengths of the equatorial Cu–N and Cu–O bonds are 2.011 and 1.952 Å, respectively. The anionic complex is bound to six Ba atoms. Two independent Ba atoms have different environments; their coordination numbers are nine and ten. The Ba–O distances lie in the range 2.669–3.136 Å. Layers of Ba atoms parallel to the *x*0*z* plane are distinguished in the structure. © *2000 MAIK "Nauka/Interperiodica".*

INTRODUCTION

Ethylenediaminetetraacetic acid H_4Edta and its analogues, for example, 1,2-cyclohexanediaminetetraacetic acid H_4Cdta (in the general case, H_4L), form the $[M^{II}L]^{2-}$ anionic complexes with bivalent metal ions. A large number of compounds between these anions and different metal cations M' have been characterized structurally [1–3]. The majority of compounds with doubly charged cations of alkaline-earth and transition metals have the composition $M'[ML]$. Compounds with the ratio $M' : M = 3 : 2$ are also known. Recently [4], the structure of a compound with the ratio $M' : M = 2 : 1$ was studied—$Ba_2[Cu(Edtp)](ClO_4)_2 \cdot 5H_2O$, where H_4Edtp is ethylenediaminetetrapropionic acid. The present paper reports the results of the X-ray diffraction study of a similar compound with the $Edta^{4-}$ ion.

EXPERIMENTAL

A portion of dihydrogen complex $[Cu(H_2Edta)(H_2O)]$ (5 mmol) and an excess of barium carbonate were dissolved in water (25 ml) on heating. After filtration, $Ba(ClO_4)_2$ (8 mmol) was added to the hot solution (90°C). A mixture of pale bluish-green and blue crystals was obtained by slow cooling of the solution in a Dewar flask. The composition of the blue crystals—$Ba_2[Cu(Edta)](ClO_4)_2 \cdot 6H_2O$ (**I**)—was determined in this study. The second compound was not identified. Its X-ray powder diffraction pattern differs from that calculated for $Ba[Cu(Edta)] \cdot 4H_2O$, whose structure is known [5].

Crystals **I** ($C_{10}H_{24}N_2O_{22}Cl_2Ba_2Cu$) are triclinic, a = 9.210(2) Å, b = 10.415(3) Å, c = 13.622(2) Å, α = 84.55(2)°, β = 82.02(2)°, γ = 78.25(2)°, V = 1263.9(5) Å^3, ρ_{calcd} = 2.453 g/cm^3, μ_{Mo} = 4.23 mm^{-1}, Z = 2, and space group $P\bar{1}$.

Intensities of 5240 unique reflections were measured on a CAD4 automated diffractometer (λMoK_α, graphite monochromator, ω scan mode, and θ_{max} = 27°).

The structure was solved by the direct method. All the hydrogen atoms were located from difference Fourier syntheses. Absorption correction was introduced with the DIFABS program [6]. The non-hydrogen atoms were refined in the anisotropic approximation by the least-squares procedure. The hydrogen atoms were assigned the U_{iso} values 0.01 Å^2 larger than the U_{eq} values of the atoms, to which they are attached. The hydrogen atoms were refined within the riding-atom model with fixed thermal parameters. The refinement was based on 4439 reflections with $I > 2\sigma(I)$. The final discrepancy factors are R = 0.0500, wR = 0.0540 (w = 1), and $GOOF$ = 2.8455. The residual electron density on the zero Fourier synthesis lies in the range $-4.48 < \Delta\rho < 2.42$ e/Å^3, and all the significant peaks are close to Ba^{2+} ions or ClO_4^- anions.

1063-7745/00/4501-0035$20.00 © 2000 MAIK "Nauka/Interperiodica"

Atomic coordinates and thermal parameters U_{eq} (for H atoms, U_{iso})

Atom	*x*	*y*	*z*	U_{eq}/U_{iso}, Å^2	Atom	*x*	*y*	*z*	U_{eq}/U_{iso}, Å^2
Ba(1)	0.2559(0)	0.9448(0)	0.5355(0)	0.0198(1)	O(16)	0.268(1)	0.341(1)	0.826(1)	0.105(6)
Ba(2)	0.3701(1)	0.9969(1)	0.8655(0)	0.0496(2)	O(1*w*)	−0.0231(7)	1.1275(6)	0.5753(5)	0.036(2)
Cu(1)	0.8995(1)	0.7423(1)	0.6923(1)	0.0198(3)	O(2*w*)	0.3643(9)	0.8958(7)	0.3332(5)	0.045(3)
O(1)	0.7847(6)	0.8215(5)	0.5848(4)	0.022(2)	O(3*w*)	0.3022(9)	1.1254(7)	0.6716(5)	0.046(3)
O(2)	0.5477(6)	0.8622(6)	0.5606(5)	0.033(2)	O(4*w*)	0.420(1)	0.734(1)	0.9303(7)	0.075(4)
O(3)	1.0717(7)	0.5731(6)	0.6301(5)	0.033(2)	O(5*w*)	0.6112(9)	0.6186(8)	0.4253(6)	0.059(3)
O(4)	1.0821(8)	0.3695(6)	0.5919(6)	0.047(3)	O(6*w*)	0.3074(9)	0.6827(6)	0.5243(7)	0.057(3)
O(5)	1.0532(6)	0.8486(5)	0.6853(4)	0.024(2)	H(1*A*)	0.6829	0.6279	0.8518	0.035
O(6)	1.2629(7)	0.8441(6)	0.7479(4)	0.030(2)	H(1*B*)	0.7346	0.4837	0.8201	0.035
O(7)	0.6833(7)	0.8790(5)	0.7957(4)	0.028(2)	H(2*A*)	0.9753	0.4997	0.8357	0.035
O(8)	0.6352(7)	0.9216(7)	0.9538(5)	0.044(2)	H(2*B*)	0.8792	0.5403	0.9322	0.035
N(1)	0.7708(7)	0.6057(6)	0.7066(5)	0.021(2)	H(3*A*)	0.5548	0.7033	0.7301	0.034
N(2)	0.9463(7)	0.6942(6)	0.8330(5)	0.020(2)	H(3*B*)	0.5937	0.6197	0.6390	0.034
C(1)	0.7587(9)	0.5634(8)	0.8156(6)	0.025(2)	H(5*A*)	0.8094	0.4101	0.6736	0.042
C(2)	0.9057(9)	0.5616(7)	0.8550(6)	0.025(2)	H(5*B*)	0.8068	0.5074	0.5969	0.042
C(3)	0.6288(9)	0.6764(7)	0.6708(6)	0.024(2)	H(7*A*)	1.1682	0.6168	0.8009	0.034
C(4)	0.6528(9)	0.7942(7)	0.5992(6)	0.022(2)	H(7*b*)	1.1388	0.7027	0.8899	0.034
C(5)	0.844(1)	0.4946(8)	0.6451(7)	0.032(3)	H(9*A*)	0.9261	0.8456	0.9064	0.036
C(6)	1.013(1)	0.4774(8)	0.6218(7)	0.031(3)	H(9*B*)	0.8509	0.7444	0.9780	0.036
C(7)	1.1088(9)	0.6943(8)	0.8233(6)	0.024(2)	H(1*w*1)	0.0035	1.1998	0.5786	0.046
C(8)	1.1450(9)	0.8052(7)	0.7484(6)	0.022(2)	H(2*w*1)	−0.0538	1.1210	0.6449	0.046
C(9)	0.8647(9)	0.7878(8)	0.9062(6)	0.026(2)	H(1*w*2)	0.3149	0.9449	0.2965	0.056
C(10)	0.7171(9)	0.8674(7)	0.8824(6)	0.024(2)	H(2*w*2)	0.3643	0.8133	0.3116	0.056
Cl(1)	0.9332(3)	0.1580(2)	0.8695(2)	0.0440(8)	H(1*w*3)	0.1953	1.1872	0.6833	0.057
O(9)	1.070(1)	0.080(1)	0.8741(9)	0.098(5)	H(2*w*3)	0.3524	1.1775	0.6618	0.057
O(10)	0.907(2)	0.275(1)	0.910(1)	0.124(7)	H(1*w*4)	0.4495	0.7508	0.9979	0.085
O(11)	0.848(2)	0.100(2)	0.959(2)	0.18(1)	H(2*w*4)	0.3247	0.7144	0.9169	0.085
O(12)	0.855(2)	0.136(2)	0.799(1)	0.150(9)	H(1*w*5)	0.7397	0.6119	0.4098	0.069
Cl(2)	0.4055(3)	0.3657(2)	0.8439(2)	0.0439(8)	H(2*w*5)	0.5998	0.5909	0.3609	0.069
O(13)	0.501(2)	0.247(1)	0.8588(9)	0.107(5)	H(1*w*6)	0.3829	0.6302	0.5057	0.067
O(14)	0.386(2)	0.441(1)	0.9271(9)	0.100(6)	H(2*w*6)	0.2424	0.6463	0.5599	0.067
O(15)	0.463(2)	0.435(2)	0.7615(9)	0.156(9)					

The calculations were performed with the SHELX76 [7] and SHELXS86 [8] programs. The atomic coordinates and thermal parameters are listed in the table.

RESULTS AND DISCUSSION

Structure **I** is built of the $[Cu(Edta)]^{2-}$ anionic complexes, hydrated barium cations, ClO_4^- anions, and crystallization water molecules, which are linked by multiple interactions into a three-dimensional framework. A fragment of the structure is shown in the figure.

In the anionic complex $[Cu(Edta)]^{2-}$, the hexadentate ligand coordinates the Cu(1) atom forming the polyhedron in the shape of a tetragonal bipyramid with the N(1), N(2), O(1), and O(5) atoms in the base and the O(3) and O(7) atoms in the apices. The base of the bipyramid is essentially nonplanar: the mean deviation of four atoms from their plane is 0.244 Å. The Cu(1) atom deviates from the plane of the base by 0.113 Å. The Cu–N and Cu–O bond lengths in the equatorial plane are equalized (av. 2.011 and 1.952 Å, respectively). The axial Cu–O bonds are elongated to different extents. The bond with the O(7) atom involved in the environment of the Ba(2) atom is longer than the bond with the O(3) atom, which has no additional

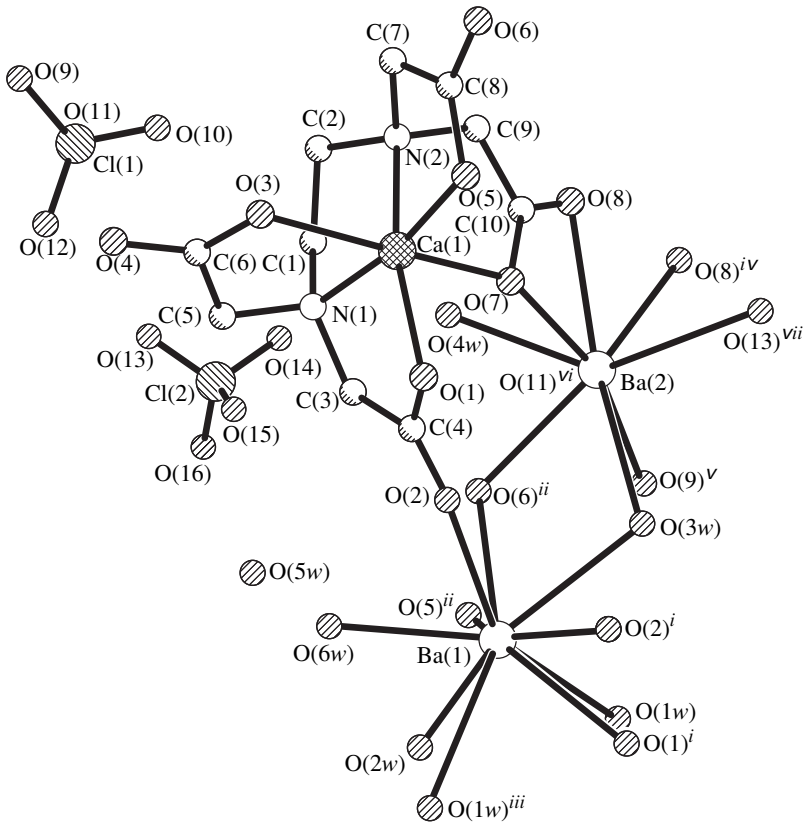

A fragment of the structure (hydrogen atoms are omitted). Raised indices correspond to the following symmetry transformations: $i = 1-x, 2-y, 1-z$; $ii = x-1, y, z$; $iii = -x, 2-y, 1-z$; $iv = 1-x, 2-y, 2-z$; $v = x-1, 1+y, z$; $vi = 1-x, 1-y, 2-z$; $vii = x, 1+y, z$.

bonds with metal atoms [2.532(6) and 2.262(6) Å, respectively]. The conformation (*E*, *G*/*R* [9]) and the geometric characteristics of the $Edta^{4-}$ ligand are normal.

The reviews [1, 2], which were published more than ten years ago, reported two variants of the deformation of the octahedron of a Cu(2+) atom into an elongated bipyramid in chelate complexes of $Edta^{4-}$ and its analogues: along the O_R–Cu–$O_{R'}$ and O_G–Cu–N axes. Since that time, new structural data appeared, which, together with the earlier data, show that the former variant is characteristic of the complexes with the hexadentate ligands and the latter variant is observed in the complexes with pentadentate ligands. Apart from the $Ba_2[Cu(Edta)](ClO_4)_2 \cdot 6H_2O$ reported here, the first group of compounds also includes $K_2[Cu(Edta)] \cdot 3H_2O$ [10], $Cu_2(Edta)(En)_2 \cdot 6H_2O$ [11], $Cu_2(Cdta) \cdot 4H_2O$ [12], $ZnCu(Cdta) \cdot 6H_2O$ [13], $CoCu(Cdta) \cdot 6H_2O$ [14], $Cu_5(Cdta)_2(NO_3)_2 \cdot 15H_2O$ [15], and $M'[Cu(Edta)] \cdot 6H_2O$, where $M'(2+)$ = Mn [16], Zn [17], or Mg [18]. In all of these compounds, the ligand forms six bonds with the central atom and closes five chelate rings. The second group includes the compounds in which one of the acetate arms does not form a chelate ring and the octahedron is elongated in the O_G–Cu–N direction: $Cu(H_2Edta) \cdot H_2O$ [19], $Ag[Cu(Edta)] \cdot 2H_2O$ [20], and $M'[Cu(Edta)] \cdot 4H_2O$, where $M'(2+)$ = Ca [21], Sr, or Ba [5].

Crystals **I** contain two crystallographically inequivalent barium atoms Ba(1) and Ba(2). The Ba(1) atom (coordination number is ten) coordinates five water molecules and five O atoms of three $Edta^{4-}$ ligands. The Ba(2) atom (coordination number is nine) is coordinated by two water molecules, four O atoms of three $Edta^{4-}$ ligands, and three O atoms of different ClO_4^- anions. The Ba(1)–O and Ba(2)–O bond lengths are in ranges 2.689(6)–3.059(6) and 2.669(7)–3.14(2) Å, respectively. Double centrosymmetric bridges formed by alternating O(1*w*) and O(2) atoms link the Ba(1) atoms into chains running along the *x*-axis

$$\text{Ba(1)}\begin{matrix}\text{O(1}w\text{)}\\ \text{O(1}w\text{)}\end{matrix}\text{Ba(1)}\begin{matrix}\text{O(2)}\\ \text{O(2)}\end{matrix}\text{Ba(1)}\begin{matrix}\text{O(1}w\text{)}\\ \text{O(1}w\text{)}\end{matrix}\text{Ba(1)}\ .$$

The Ba(2) atoms are linked by the O(8) atoms into centrosymmetric dimers, and the O(3*w*) and O(6) atoms bridge the dimers with the chains of the Ba(1) atoms into layers parallel to the *x*0*z* plane

$$\text{Ba(1)}\begin{matrix}\text{O(3}w\text{)}\\ \text{O(6)}\end{matrix}\text{Ba(2)}\begin{matrix}\text{O(8)}\\ \text{O(8)}\end{matrix}\text{Ba(2)}\begin{matrix}\text{O(6)}\\ \text{O(3}w\text{)}\end{matrix}\text{Ba(1)}.$$

The layer of barium atoms is represented by the following scheme

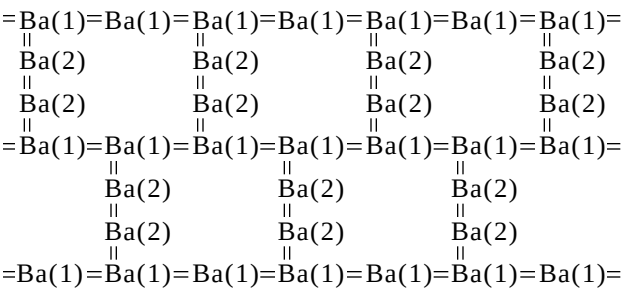

The $[Cu\mathit{Edta}]^{2-}$ anionic complexes and ClO_4^- anions are located between the Ba-layers and bound to them through the oxygen atoms.

The Edta^{4-} ligand forms bonds with six Ba atoms. To our knowledge, in other metal complexes with ligands of the Edta^{4-} type, the number of outer-sphere metal ions bound to the ligand does not exceed five. Five metal ions in the environment of the ligand are observed, for example, in the structures of $Ba[Cu(\mathit{Edta})] \cdot 4H_2O$ [5] and $Ba_2[Cu(\mathit{Edtp})](ClO_4)_2 \cdot 5H_2O$ [4]. In compound **I**, three carboxyl groups link two Ba^{2+} ions each by the same mode: both oxygen atoms are bound to one Ba^{2+} ion, and the carbonyl oxygen atom [uninvolved in the Cu(1) coordination] forms an additional Ba–O bond. The C(3)O(1)O(2) group is bound to two Ba(1) atoms; the C(10)O(7)O(8) group, to two Ba(2) atoms; and the C(8)O(5)O(6) group, to the Ba(1) and Ba(2) atoms. The oxygen atoms of the C(6)O(3)O(4) carboxyl group are not involved in the environment of the barium atom. Since these oxygen atoms can also form bonds with two barium atoms, the number of outer-sphere ions in the environment of the Edta^{4-} ligand can be as many as eight.

The structural functions of two ClO_4^- anions are different: $Cl(1)O_4^-$ is bound through atoms O(9) and O(11) to two Ba(2) atoms, whereas $Cl(2)O_4^-$ forms one Ba(2)–O(13) bond.

In structure **I**, five of the six water molecules are involved in the environment of the barium ions and one [*w*(5)] is a crystallization molecule. Two bound water molecules [*w*(1) and *w*(3)] bridge barium ions. All the water molecules are proton donors in weak hydrogen bonds [O···O distances are 2.79(1)–3.12(1) Å], in which the oxygen atoms of the Edta^{4-} ligand, ClO_4^- anions, and water molecules *w*(5) and *w*(2) serve as acceptors.

REFERENCES

1. T. N. Polynova and M. A. Poraĭ-Koshits, Itogi Nauki Tekh., Ser.: Kristallokhim. **18,** 64 (1984).
2. M. A. Poraĭ-Koshits, Sov. Sci. Rev., Ser. B **10**, 91 (1987).
3. V. N. Serezhkin, T. N. Polynova, and M. A. Poraĭ-Koshits, Koord. Khim. **21** (4), 253 (1995) [Russ. J. Coord. Chem. **21**, 239 (1995)].
4. I. F. Burshteĭn and A. L. Poznyak, Zh. Neorg. Khim. **43** (7), 1148 (1998) [Russ. J. Inorg. Chem. **43** (7), 1053 (1998)].
5. M. Insausti, J. L. Pizarro, L. Lezama, *et al.*, Chem. Mater. **6** (5), 707 (1994).
6. N. Walker and D. Stuart, Acta Crystallogr., Sect. A: Found. Crystallogr. **39** (2), 158 (1983).
7. G. M. Sheldrick, *SHELX76: Program for Crystal Structure Determination* (Univ. of Cambridge, Cambridge, 1976).
8. G. M. Sheldrick, Acta Crystallogr., Sect. A: Found. Crystallogr. **46** (6), 467 (1990).
9. M. A. Poraĭ-Koshits, A. I. Pozhidaev, and T. N. Polynova, Zh. Strukt. Khim. **15** (6), 1117 (1974).
10. M. A. Poraĭ-Koshits, N. V. Novozhilova, T. N. Polynova, *et al.*, Kristallografiya **18** (1), 89 (1973).
11. T. F. Sysoeva, V. M. Agre, V. K. Trunov, *et al.*, Zh. Strukt. Khim. **25** (3), 107 (1984).
12. A. Fuertes, C. Miravitlles, E. Escrivá, *et al.*, J. Chem. Soc., Dalton Trans., No. 9, 1795 (1986).
13. A. Fuertes, C. Miravitlles, E. Molins, *et al.*, Acta Crystallogr., Sect. C: Cryst. Struct. Commun. **12** (4), 421 (1986).
14. A. Fuertes, C. Miravitlles, E. Escrivá, *et al.*, J. Chem. Soc., Dalton Trans., No. 5, 863 (1989).
15. F. Sapiña, E. Escrivá, J. V. Folgado, *et al.*, Inorg. Chem. **31** (18), 3851 (1992).
16. X. Solans, M. Font-Altaba, J. Oliva, *et al.*, Acta Crystallogr., Sect. C: Cryst. Struct. Commun. **39** (4), 435 (1983).
17. M. V. Leont'eva, A. Ya. Fridman, N. M. Dyatlova, *et al.*, Zh. Neorg. Khim. **32** (10), 2494 (1987).
18. I. N. Polyakova, V. S. Sergienko, A. L. Poznyak, *et al.*, Zh. Neorg. Khim. **44** (9), 1454 (1999) [Russ. J. Inorg. Chem. **44**, 1376 (1999)].
19. F. S. Stephens, J. Chem. Soc. A, No. 11, 1723 (1969).
20. Ch. Brouca-Cabarrecq, B. Marrot, and A. Mosset, Acta Crystallogr., Sect. C: Cryst. Struct. Commun. **52** (8), 1903 (1996).
21. Ya. M. Nesterova and M. A. Poraĭ-Koshits, Koord. Khim. **10** (1), 129 (1984).

Translated by I. Polyakova

Crystallography Reports, Vol. 45, No. 1, 2000, pp. 39–43. Translated from Kristallografiya, Vol. 45, No. 1, 2000, pp. 45–49.

STRUCTURES OF COORDINATION COMPOUNDS

Eightfold-Coordinated Diethylenetriaminepentaacetates: Crystal Structures of K[*M*(*Dtpa*)]·3H_2O (*M* = Zr or Hf) and NH_4[Sn(*Dtpa*)] · H_2O

A. B. Ilyukhin*, R. L. Davidovich, I. N. Samsonova**, and L. V. Teplukhina****

**Kurnakov Institute of General and Inorganic Chemistry, Russian Academy of Sciences, Leninskiĭ pr. 31, Moscow, 117907 Russia*

***Institute of Chemistry, Far East Division, Russian Academy of Sciences, pr. Stoletiya Vladivostoka 159, Vladivostok, 690022 Russia*

Received December 15, 1997

Abstract—The crystal structures of K[*M*(*Dtpa*)] · 3H_2O (*M* = Zr or Hf) and NH_4[Sn(*Dtpa*)] · H_2O are studied by X-ray diffraction. The coordination number of the metal atom in all the compounds is eight. The NH_4[Sn(*Dtpa*)] · H_2O complex is isostructural to the (H_5O_2)[*M*(*Dtpa*)] · H_2O (*M* = Sn or Hf) compounds studied earlier. © *2000 MAIK "Nauka/Interperiodica".*

Diethylenetriaminepentaacetic acid (H_2*Dtpa*) forms the stable complexes with tetravalent metals. The data on their structures are few in number. The synthesis and X-ray diffraction data for pairs of the isostructural compounds K[*M*(*Dtpa*)] · 3H_2O (*M* = Zr or Hf) and {C(NH_2)$_3$}[*M*(*Dtpa*)] · 3H_2O (*M* = Zr or Hf) are presented in [1]. The crystal structure of {C(NH_2)$_3$}[Hf(*Dtpa*)] · 3H_2O was determined in [2]. The structures of the isostructural compounds (H_5O_2)[*M*(*Dtpa*)] · H_2O (*M* = Sn or Hf) are described in [3, 4]. The coordination number of the central atom is eight in the (H_5O_2)[*M*(*Dtpa*)] · H_2O complexes and nine in the [C(NH_2)$_3$][*M*(*Dtpa*)] · 3H_2O compounds.

To reveal the factors affecting the structures of the octadentate diethylenetriaminepentaacetates, we determined the crystal structures of K[Zr(*Dtpa*)] · 3H_2O (**I**), K[Hf(*Dtpa*)] · 3H_2O (**II**), and NH_4[Sn(*Dtpa*)] · H_2O (**III**) by X-ray diffraction analysis.

EXPERIMENTAL

Compounds **I** and **II** were synthesized according to the procedure described in [1]. To prepare compound **III**, the (H_5O_2)[Sn(*Dtpa*)] · H_2O complex was dissolved in water upon heating and stirring. Small portions of $NH_4(HCO_3)$ were added to the resultant solution until pH = 5. Then, the solution was filtered in order to remove suspension and evaporated. The crystals suitable for X-ray diffraction analysis were obtained by isothermal evaporation at room temperature. Compound **III** was also obtained by the direct interaction of $SnCl_4$, H_5*Dtpa*, and $NH_4(HCO_3)$ in an aqueous solution followed by evaporation and crystallization.

The main crystal data, data-collection and structure-refinement parameters for **I**–**III** are listed in Table 1. In structure **I**, the positions of K and Zr atoms were found from the Patterson synthesis (SHELXS86 [5]), and the remaining non-hydrogen atoms were located in a series of Fourier syntheses. The coordinates of the non-hydrogen atoms of structure **I** were taken as the starting set for the isostructural compound **II**. Complex **III** is isostructural to (H_5O_2)[*M*(*Dtpa*)] · H_2O (*M* = Sn or Hf), and the refinement of **III** started from the model of the tin compound (excluding the dioxonium ion). The position of the ammonium ion in **III** was found from the Fourier synthesis.

The coordinates of the aliphatic hydrogen atoms in all the structures were calculated from geometric considerations. The ammonium hydrogen atoms in **III** and a part of water hydrogens in **I**–**III** were located from the difference Fourier syntheses. The structures were refined anisotropically by the full-matrix least-squares procedures with the SHELX76 program [6]. The positional and thermal parameters of the hydrogen atoms were fixed.

The atomic coordinates and the thermal parameters are listed in Table 2. Selected bond lengths are presented in Table 3.

RESULTS AND DISCUSSION

Structures **I**–**III** consist of the anionic complexes [*M*(*Dtpa*)]$^-$ (*M* = Zr, Hf, and Sn, respectively), cations (K^+, K^+, and NH_4^+, respectively), and molecules of crystallization water. In all the cases, the coordination number of complex-forming metals is eight.

1063-7745/00/4501-0039$20.00

Table 1. Main crystal data, data-collection and structure-refinement parameters for structures **I**–**III**

Compound	$K[Zr(Dtpa)] \cdot 3H_2O$	$K[Hf(Dtpa)] \cdot 3H_2O$	$NH_4[Sn(Dtpa)] \cdot H_2O$
	I	**II**	**III**
Crystal system	Triclinic	Triclinic	Orthorhombic
a, Å	8.522(1)	8.516(2)	13.645(3)
b, Å	8.717(1)	8.714(2)	12.106(2)
c, Å	15.626(2)	15.596(3)	23.411(4)
α, deg	96.05(1)	96.04(1)	
β, deg	104.91(1)	104.92(1)	
γ, deg	108.28(1)	108.17(1)	
Space group	$P\bar{1}$	$P\bar{1}$	*Pbca*
Z	2	2	8
V, Å^3	1043.0(3)	1040.6(4)	3867(1)
ρ_{calcd}, g/cm^3	1.824	2.106	1.865
μ, mm^{-1}	0.80	5.29	1.39
$2\theta_{max}$, deg	56	56	60
N_a^*	5047	4796	4932
N_o^*	4805	3814	3941
N_p^*	289	290	271
*R***	0.028	0.038	0.032
*wR***	0.034	0.041	0.037
*Gof***	0.92	2.59	2.81
w	1	$1/\sigma^2(F)$	1

Note: The experimental data for compounds **I**–**III** were obtained on a Syntex $P2_1$ diffractometer (for all the crystals, λMoK_α, graphite monochromator, and ω/2θ scan mode); the ψ correction of the data set was performed.

* N_a is the number of the measured unique reflections with $F > 0$, N_o is the number of reflections with $F > 4\sigma(F)$, and N_p is the number of parameters in the refinement.

** $R = \Sigma||F_0| - |F_c||/\Sigma|F_0|$; $wR = [\Sigma w\{|F_0| - |F_c|\}^2/\Sigma\{w\{F_0\}^2\}]^{1/2}$; $Gof = [\Sigma\{w||F_0| - |F_c||^2\}/(N_o - N_p)]^{1/2}$.

The position of a diethylenetriamine chain in the H_5Dtpa complexes can be described in terms of meridional (*mer*) and facial (*fac*) isomers, even though these complexes have nonoctahedral structures [7]. Applying these terms to the compounds with coordination numbers larger than six, we say that the complexes are *mer*(N) isomers if the metal atom and three nitrogen atoms of the diethylenetriamine fragment are approximately coplanar; otherwise, the complexes are *fac*(N) isomers—atoms *M* and 3N essentially deviate from their mean plane. The apparent ambiguity of this definition (the absence of an exact quantitative criterion for coplanarity) is easily avoided when the conformations of both ethylenediamine rings are considered. The *gauche* conformation of the rings, together with the tetrahedral environment of nitrogen atoms, unambiguously determines the identical chirality of both rings in *fac*(N) isomers and their different chirality in *mer*(N) isomers (in the scheme given below, the diethylenetriamine fragment is projected along the *M*–N(central) bond):

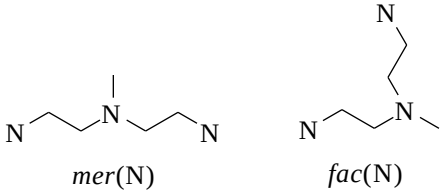

mer(N) *fac*(N)

The dihedral angles between the N*M*N planes in the octadentate diethylenetriaminepentaacetates studied

Table 2. Atomic coordinates and $U_{eq} = 1/3\Sigma_i\Sigma_j U_{ij} a_i a_j \mathbf{a_i^*}\mathbf{a_j^*}$ (for H atoms, U_{iso}) in structures **I–III**

Atom	*x*	*y*	*z*	U_{eq}/U_{iso}, Å^2
		I		
Zr(1)	0.04046(3)	0.08558(2)	0.26752(1)	0.0127(1)
K(1)	0.26927(7)	0.47487(7)	0.48744(4)	0.0278(2)
O(1)	0.0268(2)	0.2149(2)	0.1576(1)	0.0274(7)
O(2)	–0.0782(3)	0.3795(3)	0.0808(1)	0.0344(8)
O(3)	0.0113(2)	0.3013(2)	0.3304(1)	0.0256(6)
O(4)	–0.1428(3)	0.4260(3)	0.3842(2)	0.047(1)
O(5)	0.2166(2)	0.0439(2)	0.1984(1)	0.0230(6)
O(6)	0.2495(3)	–0.0294(3)	0.0656(1)	0.0405(9)
O(7)	0.2774(2)	0.1947(2)	0.3724(1)	0.0230(6)
O(8)	0.5398(2)	0.1989(3)	0.4485(1)	0.0342(7)
O(9)	–0.1108(2)	–0.0303(2)	0.3463(1)	0.0257(7)
O(10)	–0.1831(3)	–0.1886(3)	0.4421(1)	0.0351(8)
O(11)	0.5393(3)	0.4158(3)	0.6301(2)	0.056(1)
O(12)	0.5501(4)	0.5955(4)	0.8051(2)	0.069(1)
O(13)	0.7404(3)	0.4328(4)	0.9111(2)	0.066(1)
N(1)	–0.2590(3)	0.0816(3)	0.2053(1)	0.0207(7)
N(2)	–0.1176(3)	–0.1617(2)	0.1547(1)	0.0207(7)
N(3)	0.1416(3)	–0.1293(2)	0.3287(1)	0.0194(7)
C(1)	–0.0958(3)	0.2664(3)	0.1220(2)	0.0235(9)
C(2)	–0.2718(3)	0.1752(3)	0.1306(2)	0.0267(9)
C(3)	–0.1337(3)	0.3110(3)	0.3364(2)	0.0250(9)
C(4)	–0.2957(3)	0.1670(3)	0.2812(2)	0.0249(9)
C(5)	–0.3756(3)	–0.0944(3)	0.1730(2)	0.0254(8)
C(6)	–0.3045(3)	–0.1822(3)	0.1109(2)	0.0275(9)
C(7)	0.1604(3)	–0.0410(3)	0.1163(2)	0.0241(9)
C(8)	–0.0267(3)	–0.1569(3)	0.0841(2)	0.0272(9)
C(9)	–0.1121(3)	–0.3062(3)	0.1992(2)	0.0256(9)
C(10)	0.0722(3)	–0.2802(3)	0.2558(2)	0.0248(9)
C(11)	0.3923(3)	0.1250(3)	0.3985(2)	0.0221(8)
C(12)	0.3336(3)	–0.0584(3)	0.3606(2)	0.0229(8)
C(13)	–0.0861(3)	–0.1297(3)	0.3992(2)	0.0232(8)
C(14)	0.0784(3)	–0.1655(3)	0.4071(2)	0.0249(9)
H(1)	0.447	0.306	0.616	0.08
H(2)	0.541	0.462	0.676	0.08
H(3)	0.510	0.511	0.833	0.08
H(4)	0.637	0.722	0.815	0.08
H(5)	0.774	0.375	0.966	0.08
H(6)	0.882	0.497	0.918	0.08
		II		
Hf(1)	0.03848(3)	0.08364(3)	0.26728(1)	0.0164(1)
K(1)	0.2691(2)	0.4746(2)	0.48726(9)	0.0284(4)
O(1)	0.0270(7)	0.2164(6)	0.1590(3)	0.029(2)
O(2)	–0.0774(8)	0.3798(6)	0.0808(3)	0.034(2)
O(3)	0.0112(7)	0.2991(5)	0.3309(3)	0.026(2)
O(4)	–0.1404(9)	0.4271(7)	0.3848(5)	0.045(2)
O(5)	0.2160(6)	0.0441(5)	0.1989(3)	0.024(1)
O(6)	0.2477(8)	–0.0308(8)	0.0659(3)	0.038(2)
O(7)	0.2752(6)	0.1948(5)	0.3713(3)	0.022(1)
O(8)	0.5377(7)	0.2005(6)	0.4476(4)	0.035(2)
O(9)	–0.1116(6)	–0.0306(5)	0.3459(3)	0.024(1)
O(10)	–0.1843(8)	–0.1891(6)	0.4425(4)	0.035(2)
O(11)	0.539(1)	0.4164(9)	0.6302(5)	0.057(3)
O(12)	0.551(1)	0.596(1)	0.8055(6)	0.066(3)
O(13)	0.740(1)	0.432(1)	0.9108(6)	0.066(3)
N(1)	–0.2577(7)	0.0813(6)	0.2056(3)	0.021(2)
N(2)	–0.1176(7)	–0.1608(5)	0.1552(3)	0.020(1)
N(3)	0.1415(7)	–0.1299(5)	0.3291(3)	0.020(2)
C(1)	–0.096(1)	0.2670(7)	0.1233(4)	0.025(2)
C(2)	–0.273(1)	0.1744(8)	0.1306(4)	0.027(2)
C(3)	–0.1349(9)	0.3095(7)	0.3364(4)	0.024(2)
C(4)	–0.2953(9)	0.1669(7)	0.2810(4)	0.025(2)
C(5)	–0.3772(9)	–0.0944(7)	0.1726(4)	0.025(2)
C(6)	–0.3055(9)	–0.1830(8)	0.1111(4)	0.029(2)
C(7)	0.160(1)	–0.0402(7)	0.1169(4)	0.025(2)
C(8)	–0.028(1)	–0.1570(8)	0.0838(4)	0.027(2)
C(9)	–0.114(1)	–0.3049(7)	0.1996(4)	0.028(2)
C(10)	0.0718(9)	–0.2800(7)	0.2558(4)	0.027(2)
C(11)	0.3917(9)	0.1267(7)	0.3978(4)	0.023(2)
C(12)	0.3327(8)	–0.0584(7)	0.3610(4)	0.022(2)
C(13)	–0.0861(9)	–0.1295(6)	0.3991(4)	0.022(2)
C(14)	0.078(1)	–0.1663(7)	0.4077(4)	0.027(2)
H(1)	0.452	0.307	0.604	0.08
H(2)	0.539	0.458	0.680	0.08
H(3)	0.604	0.726	0.806	0.08
H(4)	0.592	0.546	0.776	0.08
H(5)	0.764	0.397	0.970	0.08
H(6)	0.869	0.493	0.922	0.08
		III		
Sn(1)	0.91146(2)	0.20740(2)	0.36874(1)	0.0197(1)
O(1)	1.0474(2)	0.1395(3)	0.3358(2)	0.036(1)
O(2)	1.1856(3)	0.1904(5)	0.2937(3)	0.094(2)
O(3)	0.8527(3)	0.0865(3)	0.3126(1)	0.036(1)
O(4)	0.8389(3)	0.0128(3)	0.2263(2)	0.046(1)
O(5)	0.7594(2)	0.1753(2)	0.3933(1)	0.0301(8)
O(6)	0.6023(2)	0.2198(3)	0.3783(2)	0.039(1)
O(7)	1.0287(2)	0.3260(3)	0.3895(1)	0.0295(9)
O(8)	1.1303(3)	0.3995(4)	0.4532(2)	0.054(1)
O(9)	0.9338(2)	0.0648(3)	0.4182(1)	0.0316(9)
O(10)	0.8828(3)	–0.0348(3)	0.4927(2)	0.042(1)
O(11)	0.4598(2)	0.3821(3)	0.3690(2)	0.036(1)
N(1)	0.9367(2)	0.2772(3)	0.2742(1)	0.0237(9)
N(2)	0.8298(2)	0.3765(3)	0.3661(2)	0.0220(8)
N(3)	0.8997(3)	0.2577(3)	0.4676(1)	0.0236(9)
N(4)	0.7256(4)	–0.0095(5)	0.1232(2)	0.070(2)
C(1)	1.0977(4)	0.2020(5)	0.3020(3)	0.047(2)
C(2)	1.0447(3)	0.2933(4)	0.2714(2)	0.033(1)
C(3)	0.8634(3)	0.0844(4)	0.2582(2)	0.028(1)
C(4)	0.9086(4)	0.1902(4)	0.2321(2)	0.033(1)
C(5)	0.8819(3)	0.3819(4)	0.2650(2)	0.030(1)
C(6)	0.8721(3)	0.4465(3)	0.3200(2)	0.026(1)
C(7)	0.6910(3)	0.2426(4)	0.3770(2)	0.026(1)
C(8)	0.7236(3)	0.3544(4)	0.3556(2)	0.028(1)
C(9)	0.8428(3)	0.4326(3)	0.4227(2)	0.027(1)
C(10)	0.8313(3)	0.3531(4)	0.4724(2)	0.028(1)
C(11)	1.0585(3)	0.3427(4)	0.4407(2)	0.031(1)
C(12)	1.0001(3)	0.2860(4)	0.4872(2)	0.032(1)
C(13)	0.8955(3)	0.0543(4)	0.4989(2)	0.028(1)
C(14)	0.8636(3)	0.1590(4)	0.4983(2)	0.030(1)
H(1)	0.495	0.325	0.369	0.05
H(2)	0.496	0.439	0.373	0.05
H(3)	0.769	–0.050	0.094	0.08
H(4)	0.685	–0.073	0.129	0.08
H(5)	0.760	0.026	0.157	0.08
H(6)	0.704	0.050	0.098	0.08

Table 3. The *M*–*L* bond lengths (Å) in structures **I**–**III**

Bond	Structures		
	I	**II**	**III**
M	Zr	Hf	Sn
M(1)–O(1)	2.150(2)	2.144(5)	2.170(3)
M(1)–O(3)	2.143(2)	2.136(5)	2.124(3)
M(1)–O(5)	2.155(2)	2.149(5)	2.188(3)
M(1)–O(7)	2.105(2)	2.098(5)	2.204(3)
M(1)–O(9)	2.111(2)	2.098(5)	2.100(3)
M(1)–N(1)	2.474(2)	2.450(6)	2.394(3)
M(1)–N(2)	2.393(2)	2.369(5)	2.332(3)
M(1)–N(3)	2.476(2)	2.474(5)	2.398(3)

are 17.2°–21.5° and 38.7°–44.7° (Table 4) for the *mer*(N) and *fac*(N) isomers, respectively.

Complexes **I** and **II** have a *fac* structure (Fig. 1a), and complex **III** exhibits a *mer* structure (Fig. 1b).

Structural comparison of complex anions in K[Hf(*Dtpa*)] · $3H_2O$ and {$C(NH_2)_3$}[Hf(*Dtpa*)(H_2O)] · $2H_2O$ [2] reveals a similarity in their configurations (Fig. 2). An imaginary conversion of the anion in K[Hf(*Dtpa*)] · $3H_2O$ to that in {$C(NH_2)_3$}[Hf(*Dtpa*)(H_2O)] · $2H_2O$ proceeds by drawing off the diethylenetriamine chain from the metal atom. The solid angle between the *M*–O bonds increases, and a coordination water molecule occupies the vacancy formed.

Zirconium and hafnium diethylenetriaminepentaacetates can form eight-vertex complexes of both *mer*(N) and *fac*(N) structures; that is, the thermodynamic characteristics of the two isomers are apparently close. The existence of both eight- and nine-vertex complexes of zirconium and hafnium diethylenetriaminepentaacetates is a more remarkable fact. In solution, the zirconium (hafnium) complexonates with coordination numbers equal to eight and nine most probably exist in equilibrium, and, under the effect of the counterion, only one form with one or another configuration of the diethylenetriamine chain is isolated in the course of crystallization (eightfold- and ninefold-coordinated

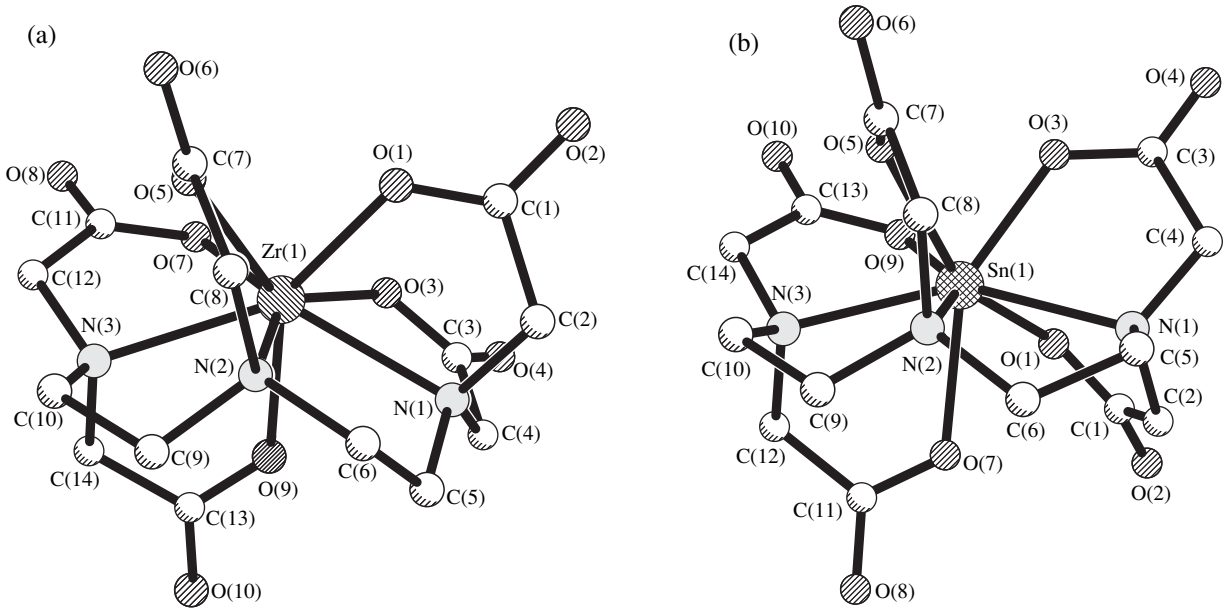

Fig. 1. Structures of the complex anions (a) $[Zr(Dtpa)]^-$ in **I** and (b) $[Sn(Dtpa)]^-$ in **III**.

Table 4. Eightfold-coordinated diethylenetriaminepentaacetates characterized structurally

Compound	Isomer (dihedral angle between the N*M*N planes, deg)	Torsion angle NCCN, deg	Reference
$Na_2[In(Dtpa)] \cdot 7H_2O$	*mer*		[8]
$\{C(NH_2)_3\}_2[In(Dtpa)] \cdot 2H_2O$	*mer* (18.8)	55.3; –60.6	[9]
$(H_5O_2)[Sn^{IV}(Dtpa)] \cdot H_2O$	*mer* (17.7)	52.5; –57.6	[3, 4]
$NH_4[Sn^{IV}(Dtpa)] \cdot H_2O$	*mer* (21.5)	52.9; –55.9	**III**
$(H_5O_2)[Hf(Dtpa)] \cdot H_2O$	*mer* (17.2)	51.4; –56.9	[3]
$K[Zr(Dtpa)] \cdot 3H_2O$	*fac* (38.9)	53.7; 60.4	**I**
$K[Hf(Dtpa)] \cdot 3H_2O$	*fac* (38.7)	52.0; 61.1	**II**
$\{C(NH_2)_3\}[Hf(Dtpa)(H_2O)] \cdot 2H_2O$*	*fac* (44.7)	54.9; 57.9	[2]

* In $\{C(NH_2)_3\}[Hf(Dtpa)(H_2O)] \cdot 2H_2O$, the coordination number of hafnium is nine.

diethylenetriaminepentaacetates with both *mer* and *fac* structures are known [7]).

As noted above, complex **III** is isostructural to $(H_5O_2)[M(Dtpa)] \cdot H_2O$ (M^{IV} = Sn or Hf), and the ammonium ion in **III** replaces the disordered $H_5O_2^+$ ($H_3O^+ \cdot\cdot H_2O$) group.

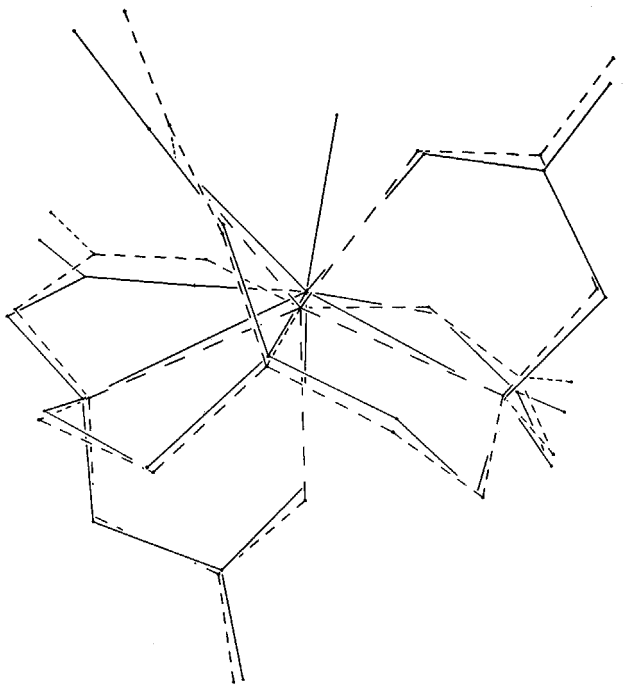

Fig. 2. Structural comparison between the complexes in $K[Hf(Dtpa)] \cdot 3H_2O$ (broken lines) and $\{C(NH_2)_3\}[Hf(Dtpa)(H_2O) \cdot 2H_2O$ (solid lines).

ACKNOWLEDGMENTS

The work was supported by the Russian Foundation for Basic Research, project no. 96-03-32255.

REFERENCES

1. R. L. Davidovich, V. B. Logvinova, and L. V. Teplukhina, Koord. Khim. **18** (6), 580 (1992).
2. M. A. Poraĭ-Koshits, L. M. Shkol'nikova, G. G. Sadikov, *et al*., Zh. Neorg. Khim. **39** (11), 1801 (1994).
3. A. B. Ilyukhin, V. S. Sergienko, R. L. Davidovich, *et al*., Zh. Neorg. Khim. **42** (9), 1474 (1997).
4. R. K. Iyer, S. G. Deshpande, and V. Amirthalingam, Polyhedron **3**, 1099 (1984).
5. G. M. Sheldrick, Acta Crystallogr., Sect. A: Found. Crystallogr. **46** (6), 467 (1990).
6. G. M. Sheldrick, *SHELX76: Program for Crystal Structure Determination* (Univ. of Cambridge, Cambridge, 1976).
7. A. B. Ilyukhin and V. S. Sergienko, Ross. Khim. Zh. **40** (4–5), 118 (1996).
8. H. R. Maecke, A. Riesen, and W. Ritter, J. Nucl. Med. **30** (7), 1235 (1989).
9. A. B. Ilyukhin, M. A. Malyarik, S. P. Petrosyants, *et al*., Zh. Neorg. Khim. **40** (7), 1125 (1995).

Translated by I. Polyakova

Crystallography Reports, Vol. 45, No. 1, 2000, pp. 44–45. Translated from Kristallografiya, Vol. 45, No. 1, 2000, pp. 50–51.

STRUCTURES OF COORDINATION COMPOUNDS

Crystal Structure of $[Co(Ox)(NH_3)_4][Bi(Edta)] \cdot 3H_2O$

A. L. Poznyak* and A. B. Ilyukhin**

** Institute of Molecular and Atomic Physics, Belarussian Academy of Sciences, pr. F. Skoriny 70, Minsk, 220072 Belarus*

*** Kurnakov Institute of General and Inorganic Chemistry, Russian Academy of Sciences, Leninskiĭ pr. 31, Moscow, 117907 Russia*

Received December 15, 1997

Abstract—The crystal structure of $[Co(Ox)(NH_3)_4][Bi(Edta)] \cdot 3H_2O$ is determined. The crystals are monoclinic, $a = 9.291$ Å, $b = 22.275$ Å, $c = 11.402$ Å, $\beta = 105.79°$, $V = 2270.7$ Å^3, $Z = 4$, and space group $P2_1/c$. The $[Bi(Edta)]^-$ anionic complexes are linked into polymeric chains through two Bi–O bonds with the neighboring complexes. © *2000 MAIK "Nauka/Interperiodica".*

The crystal structure of $[Co(Ox)(NH_3)_4][Bi(Edta)] \cdot 3H_2O$ (*Ox* is oxalate, and *Edta* is ethylenediaminetetraacetate) was determined by X-ray diffraction.

The crystals are monoclinic, $a = 9.291(2)$ Å, $b = 22.275(4)$ Å, $c = 11.402(3)$ Å, $\beta = 105.79(2)°$, $V = 2270.7(8)$ Å^3, $Z = 4$, space group $P2_1/c$, $\rho_{calcd} = 2.242$ g/cm^3, and $\mu = 8.56$ mm^{-1}. A set of observed intensities was obtained on an Enraf–Nonius CAD4 diffractometer (λMoK_α, graphite monochromator, ψ correction of data set, $\omega/2\theta$ scan mode, $2\theta_{max} = 56°$). A total of 5118 unique nonzero reflections was measured.

The structure was solved by the direct method (SHELXS86 [1]). The hydrogen atoms of crystallization water and coordinated ammonia molecules were located from difference Fourier syntheses, and the coordinates of the aliphatic hydrogen atoms were cal-

Atomic coordinates and $U_{eq} = 1/3\Sigma_i\Sigma_j U_{ij} a_i a_j a_i^* a_j^*$ (U_{iso} for H atoms) in the structure of $[Co(Ox)(NH_3)_4][Bi(Edta)] \cdot 3H_2O$

Atom	*x*	*y*	*z*	U_{eq}/U_{iso}, Å^2	Atom	*x*	*y*	*z*	U_{eq}/U_{iso}, Å^2
Bi(1)	0.06651(2)	0.27541(1)	0.80593(1)	0.0143(1)	N(1)	0.1869(4)	0.3660(2)	0.7574(3)	0.018(1)
Co(1)	−0.41438(6)	0.37037(3)	0.35396(5)	0.0167(2)	N(2)	−0.0721(4)	0.3622(2)	0.8557(3)	0.018(1)
O(1)	−0.0198(4)	0.3017(2)	0.5972(3)	0.023(1)	N(3)	−0.3253(5)	0.2976(2)	0.4333(4)	0.023(1)
O(2)	0.0631(5)	0.3279(2)	0.4390(3)	0.034(1)	N(4)	−0.5455(5)	0.3267(2)	0.2186(4)	0.027(1)
O(3)	0.3408(4)	0.2680(2)	0.8595(4)	0.029(1)	N(5)	−0.5638(5)	0.3669(2)	0.4451(4)	0.024(1)
O(4)	0.5366(5)	0.3201(2)	0.9683(4)	0.045(2)	N(6)	−0.2631(5)	0.3742(2)	0.2642(4)	0.030(1)
O(5)	−0.2022(4)	0.2602(2)	0.7522(4)	0.027(1)	C(1)	0.0754(5)	0.3266(2)	0.5490(4)	0.021(1)
O(6)	−0.4261(4)	0.3019(2)	0.6814(4)	0.035(1)	C(2)	0.2114(5)	0.3552(2)	0.6369(4)	0.022(1)
O(7)	0.1541(4)	0.3035(2)	1.0136(3)	0.024(1)	C(3)	0.4115(5)	0.3167(3)	0.8958(5)	0.027(2)
O(8)	0.0763(5)	0.3264(2)	1.1750(3)	0.033(1)	C(4)	0.3314(5)	0.3750(2)	0.8504(4)	0.024(1)
O(9)	−0.2860(4)	0.4173(2)	0.4813(3)	0.027(1)	C(5)	0.0860(6)	0.4188(2)	0.7500(4)	0.022(1)
O(10)	−0.2475(6)	0.5132(2)	0.5370(4)	0.050(2)	C(6)	0.0156(6)	0.4182(2)	0.8558(4)	0.022(1)
O(11)	−0.4938(4)	0.4454(2)	0.2866(3)	0.027(1)	C(7)	−0.2906(5)	0.3050(2)	0.7307(4)	0.022(1)
O(12)	−0.4799(5)	0.5424(2)	0.3367(5)	0.043(2)	C(8)	−0.2215(5)	0.3662(2)	0.7674(4)	0.023(1)
O(13)	−0.0415(7)	0.5566(2)	0.7434(5)	0.062(2)	C(9)	0.0594(6)	0.3254(2)	1.0643(4)	0.020(1)
O(14)	0.2460(7)	0.0353(3)	0.6076(5)	0.065(2)	C(10)	−0.0839(5)	0.3513(2)	0.9812(4)	0.022(1)
O(15)	0.6398(9)	0.0442(4)	0.5442(7)	0.105(4)	C(11)	−0.3113(6)	0.4736(2)	0.4690(5)	0.028(2)
					C(12)	−0.4397(6)	0.4906(2)	0.3559(5)	0.025(1)

1063-7745/00/4501-0044$20.00 © 2000 MAIK "Nauka/Interperiodica"

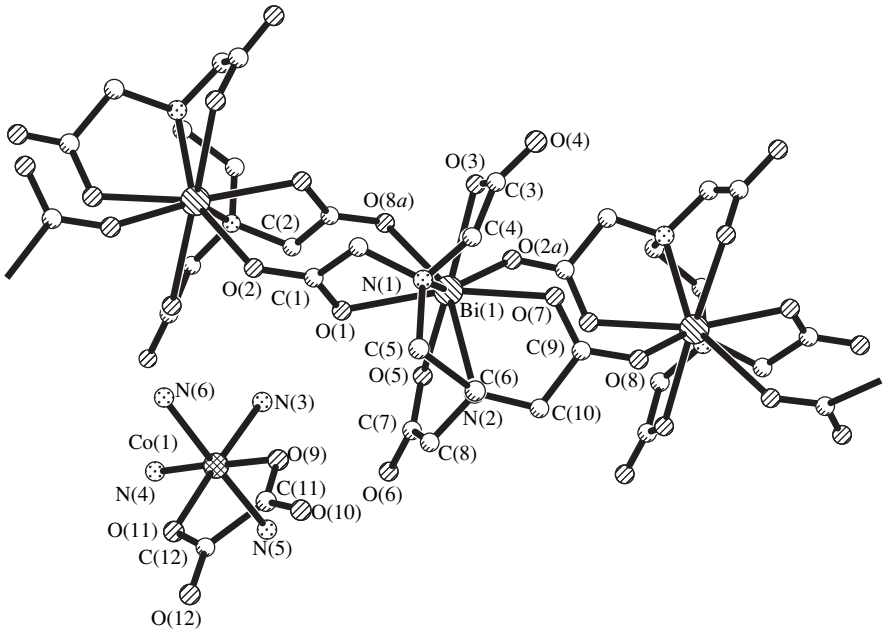

A fragment of the $[Co(Ox)(NH_3)_4][Bi(Edta)] \cdot 3H_2O$ structure.

culated from geometric considerations. The refinement of 316 parameters by the full-matrix least-squares procedure with consideration for fixed positional and thermal parameters of the hydrogen atoms (SHELX76 [2]) led to $R = 0.031$, $wR = 0.042$ ($w = 1/(\sigma^2(F) + 0.0004F^2)$), and $Gof = 1.64$ for 4659 reflections with $F > 4\sigma(F)$.

The atomic coordinates and thermal parameters are listed in the table.

The structure consists of cationic and anionic complexes and molecules of crystallization water.

The cobalt atom in the $[Co(Ox)(NH_3)_4]^+$ cation has an octahedral environment (Co–N, 1.931–1.953 Å; Co–O, 1.918 and 1.903 Å). The $[Bi(Edta)]^-$ anions are linked into polymeric chains (figure) through the two bridging bonds Bi–O(2) and Bi–O(8) (2.762 and 2.729 Å, respectively). The lengths of the main Bi–O bonds are 2.368–2.459 Å, and the Bi–N bond lengths are 2.443 and 2.473 Å.

REFERENCES

1. G. M. Sheldrick, Acta Crystallogr., Sect. A: Found. Crystallogr. **46**, 467 (1990).
2. G. M. Sheldrick, *SHELX76: Program for Crystal Structure Determination* (Univ. of Cambridge, Cambridge, 1976).

Translated by I. Polyakova

Crystallography Reports, Vol. 45, No. 1, 2000, pp. 46–55. Translated from Kristallografiya, Vol. 45, No. 1, 2000, pp. 52–60.

STRUCTURES OF COORDINATION COMPOUNDS

Crystal Structure and Vibrational Spectra of Two Cadmium Halide Complexes with 1,2-Bis[2-(Diphenylphosphinylmethyl)phenoxy]ethane (L^1) and 1,3-Bis[2-(Diphenylphosphinylmethyl)phenoxy]propane (L), $CdBr_2 \cdot L^1$ and $CdI_2 \cdot L$

L. Kh. Minacheva, I. S. Ivanova, I. K. Kireeva, V. G. Sakharova, V. S. Sergienko, and A. Yu. Tsivadze

Kurnakov Institute of General and Inorganic Chemistry, Russian Academy of Sciences, Leninskiĭ pr. 31, Moscow, 117907 Russia

Received January 29, 1998

Abstract—Two cadmium halide complexes with 1,2-bis[2-(diphenylphosphinylmethyl)phenoxy]ethane (L^1) and 1,3-bis[2-(diphenylphosphinylmethyl)phenoxy]propane (L), namely, $CdBr_2 \cdot L^1$ (**I**) and $CdI_2 \cdot L$ (**II**), have been synthesized. An analysis of their vibrational spectra is carried out. The structures of **I** and **II** are determined by X-ray diffraction. Crystals **I** are monoclinic, a = 31.562(6) Å, b = 13.548(3) Å, c = 18.733(4) Å, β = 91.28(3)°, space group $C2/c$, Z = 8, and R = 0.051 for 3776 reflections. Crystals **II** are triclinic, a = 11.803(2) Å, b = 12.554(3) Å, c = 14.686(3) Å, α = 90.30(3)°, β = 90.29(3)°, γ = 106.08(3)°, space group $P\bar{1}$, Z = 2, and R = 0.043 for 4916 reflections. Compounds **I** and **II** exhibit a polymeric chain structure. The potentially tetradentate ligands L^1 and L are coordinated to the metal atoms only through two phosphoryl oxygen atoms and fulfill the bidentate bridging function. The environment of the Cd atom is completed to the tetrahedral coordination by two Br atoms in complex **I** and two **I** atoms in complex **II**. The mean distances are as follows: Cd–Br, 2.526(2) Å; Cd–I, 2.695 Å; and Cd–O, 2.243(8) Å in **I** and 2.210(4) Å in **II**. The L^1 and L ligands in complexes **I** and **II** adopt an *S*-shaped conformation. © *2000 MAIK "Nauka/Interperiodica".*

Our systematic investigations into the structure and complexing properties of the podands with terminal phosphoryl-containing groups of the general formula $Ph_2P(O)CH_2PhO(CH_2CH_2O)_nPhCH_2P(O)Ph_2$ (L^n) have been demonstrated that the L^1 podand is an efficient complexing agent [1–3]. The L^1 podand can form complexes with some alkali, alkaline-earth, and transition metals and rare-earth elements. In these complexes, the studied podand, as a rule, acts as a bidentate bridging ligand, which is coordinated through two phosphoryl oxygen atoms irrespective of the nature of the metal and acido ligand. The exception is the $Ba(NCS)_2 \cdot L^1 \cdot H_2O$ complex, in which the L^1 ligand exhibits the maximum (tetradentate) coordination capacity and can be coordinated via the phosphoryl and anisole oxygen atoms [2].

Despite virtually the same coordination (bridging) mode, the complexes with the L^1 podand can have different (island or polymeric) structures. Moreover, the polymeric chains form layers or networks through the bridging acido ligands or hydrogen bonds [3].

Earlier [4], it was shown that the specificity of complex formation, structure, and stability of complexes with the L^n podands depend, among other factors, on the length of the ethylene glycol chain. It can be expected that an increase in the length of a chain linking the terminal phosphoryl-containing groups through the replacement of the ethylene glycol fragment by the propylene glycol chain unit produces a specific effect on the complex-forming properties of the new podand L and the structure of complexes on its base.

In this work, we synthesized the complexes $CdBr_2 \cdot L^1$ (**I**) and $CdI_2 \cdot L$ (**II**), analyzed their vibrational spectra, and determined the structures of the prepared complexes by X-ray diffraction analysis.

EXPERIMENTAL

Complexes **I** and **II** were synthesized in an alcohol solution according to the procedure described in [2]. Specifically, an anhydrous ethyl alcohol was used to synthesize the bromide complex **I**.

The main crystal data and data collection parameters for structures **I** and **II** are listed in Table 1. In the processing of experimental data, corrections were made for the Lorentz and polarization factors. No absorption corrections were introduced.

Structures **I** and **II** were solved by the direct methods and refined in the full-matrix least-squares approximation. In structure **II**, the carbon atoms of the propy-

1063-7745/00/4501-0046$20.00 © 2000 MAIK "Nauka/Interperiodica"

Table 1. Main crystal data and data collection parameters for structures **I** and **II**

Parameter	**I**	**II**
Empirical formula	$C_{40}H_{36}Br_2CdO_4P_2$	$C_{41}H_{38}CdI_2O_4P_2$
Formula weight	914.85	1022.85
Color, crystal habit	White needles	Green needles
Sample size, mm	$0.2 \times 0.2 \times 0.5$	$0.15 \times 0.15 \times 0.5$
Crystal system	Monoclinic	Triclinic
Space group	$C2/c$	$P\bar{1}$
Unit cell parameters		
a, Å	31.562(6)	11.803(2)
b, Å	13.548(3)	12.554(3)
c, Å	18.733(4)	14.686(3)
α, deg	90	90.30(3)
β, deg	91.28(3)	90.29(3)
γ, deg	90	106.08(3)
V, Å^3	8008(3)	2090.9(7)
Z	8	2
d_{calcd}, g/cm^3	1.518	1.625
μ, mm^{-1}	2.658	2.09
F(000)	3648	1000
Diffractometer	Syntex $P2_1$	Enraf-Nonius CAD-4
Radiation, λ, Å	MoK_α (0.71073), graphite monochromator	
Scan mode	θ–2θ	ω/2θ
Scan range, deg	1.29–26.88	2.10–24.96
No. of measured reflections	3875	5784
No. of unique reflections	3776	4916
R(int)	0.060	0.019
Solution method	Direct methods (SHELXS86)	
Refinement method	Full-matrix least-squares method (SHELXL93)	
No. of parameters refined	191	388
GOOF for F^2	1.067	0.925
R ($I > 2\sigma(I)$)	$R1$ = 0.0513,	0.0425
	$wR2$ = 0.1303	0.1091
R (for all reflections)	$R1$ = 0.1120,	0.0425
	$wR2$ = 0.1556	0.1091

lene glycol chain and the benzene rings at the P(2) atom are statistically disordered and occupy two positions each. The refined occupancies are as follows: 0.65(6) for the C(8), C(9), and C(10) atoms of the propylene glycol chain; 0.35(6) for the C(8*X*), C(9*X*), and C(10*X*) atoms of the propylene glycol chain; 0.50(2) for the C(30)–C(35) and C(30*X*)–C(35*X*) atoms of benzene rings 3 and 3*x*; 0.65(6) for the C(36)–C(41) atoms of benzene ring 4; and 0.35(6) for the C(36*X*)–C(41*X*) atoms of benzene ring 4*x*. All the benzene rings in structure **I** and the statistically disordered rings 3, 3*x*, 4, and 4*x* in structure **II** were refined in the isotropic approximation according to a "rigid body" model. The C atoms of the propylene glycol chain in structure **II** were also refined in the isotropic approximation. The remaining non-hydrogen atoms in structures **I** and **II** were refined in the anisotropic approximation. The positions of hydrogen atoms in **I** and **II** were determined geometrically (C–H, 0.93 Å for the aromatic atoms and 0.97 Å for the remaining H atoms) and refined by a riding-atom model in the isotropic approximation. The hydrogen atoms at the statistically disordered C atoms in structure **II** were not located. All the

Table 2. Atomic coordinates and thermal parameters U_{iso}/U_{eq} in structures **I** and **II**

Atom	*x*	*y*	*z*	U_{iso}/U_{eq}, Å^2
		I		
Cd(1)	0.13003(2)	0.20934(6)	0.36131(4)	0.0449(3)
Br(1)	0.05445(4)	0.23871(1)	0.3214(1)	0.1000(6)
Br(2)	0.18274(4)	0.1508(1)	0.2703(1)	0.0938(6)
P(1)	0.1391(1)	0.4498(2)	0.4317(2)	0.0410(7)
P(2)	0.1412(1)	0.0384(2)	0.5160(2)	0.0525(8)
O(1)	0.1500(2)	0.3428(5)	0.4253(4)	0.047(2)
O(2)	0.1335(3)	0.1033(6)	0.4526(4)	0.078(3)
O(3)	0.0505(2)	0.6038(5)	0.5439(4)	0.066(2)
O(4)	0.0893(3)	0.7926(6)	0.5279(6)	0.088(3)
C(1)	0.0834(3)	0.4702(8)	0.4467(6)	0.048(3)
C(2)	0.0672(2)	0.4387(5)	0.5222(3)	0.046(3)
C(3)	0.0686(2)	0.3400(5)	0.5424(4)	0.062(3)
C(4)	0.0536(3)	0.3117(5)	0.6086(5)	0.088(4)
C(5)	0.0374(3)	0.3820(7)	0.6546(4)	0.100(5)
C(6)	0.0361(2)	0.4807(6)	0.6344(4)	0.086(4)
C(7)	0.0510(2)	0.5091(4)	0.5682(4)	0.053(3)
C(8)	0.0468(5)	0.680(1)	0.598(1)	0.105(6)
C(9)	0.0480(5)	0.7741(9)	0.559(1)	0.118(7)
C(11)	0.0930(3)	−0.1930(7)	0.4562(4)	0.075(4)
C(12)	0.0661(3)	−0.2379(7)	0.4063(6)	0.108(5)
C(13)	0.0719(3)	−0.2227(8)	0.3338(5)	0.132(6)
C(14)	0.1046(4)	−0.1625(9)	0.3112(4)	0.144(7)
C(15)	0.1316(3)	−0.1175(7)	0.3611(6)	0.102(5)
C(16)	0.1258(3)	−0.1328(6)	0.4336(5)	0.065(3)
C(17)	0.1550(3)	−0.0856(8)	0.4904(7)	0.062(3)
C(18)	0.1696(2)	0.5064(5)	0.5053(3)	0.039(2)
C(19)	0.1573(2)	0.5949(5)	0.5361(4)	0.061(3)
C(20)	0.1824(3)	0.6378(5)	0.5897(4)	0.084(4)
C(21)	0.2197(2)	0.5921(6)	0.6123(4)	0.080(4)
C(22)	0.2320(2)	0.5036(6)	0.5815(4)	0.068(4)
C(23)	0.2070(2)	0.4608(4)	0.5280(4)	0.056(3)
C(24)	0.1495(3)	0.5179(6)	0.3474(4)	0.049(3)
C(25)	0.1744(3)	0.6026(6)	0.3491(4)	0.089(4)
C(26)	0.1819(3)	0.6538(5)	0.2863(5)	0.098(5)
C(27)	0.1646(3)	0.6202(7)	0.2219(4)	0.086(4)
C(28)	0.1398(3)	0.5355(7)	0.2203(4)	0.103(5)
C(29)	0.1322(2)	0.4843(5)	0.2830(5)	0.074(4)
C(30)	0.1840(2)	0.0796(5)	0.5742(4)	0.052(3)
C(31)	0.1980(2)	0.1762(5)	0.5670(4)	0.067(4)
C(32)	0.2311(3)	0.2111(4)	0.6103(5)	0.081(4)
C(33)	0.2502(2)	0.1492(6)	0.6607(4)	0.075(4)
C(34)	0.2361(2)	0.0526(6)	0.6679(4)	0.082(4)
C(35)	0.2030(2)	0.0177(4)	0.6247(4)	0.076(4)
C(36)	0.0944(2)	0.0297(6)	0.5719(4)	0.049(3)
C(37)	0.0958(2)	−0.0071(6)	0.6411(4)	0.068(4)
C(38)	0.0589(3)	−0.0133(6)	0.6800(3)	0.086(4)
C(39)	0.0205(2)	0.0173(6)	0.6495(4)	0.084(4)
C(40)	0.0191(2)	0.0542(6)	0.5803(5)	0.081(4)
C(41)	0.0560(3)	0.0604(6)	0.5414(3)	0.083(4)
		II		
Cd(1)	0.10698(4)	−0.17496(4)	0.28102(4)	0.0546(2)
I(1)	0.04137(5)	−0.06344(5)	0.14376(5)	0.0875(2)
I(2)	0.00624(4)	−0.20392(5)	0.44703(4)	0.0840(2)
P(1)	0.3970(1)	−0.0197(1)	0.2692(1)	0.0461(4)
P(2)	1.0974(2)	0.5505(1)	0.2669(1)	0.0489(4)
O(1)	0.3004(4)	−0.1178(4)	0.2998(3)	0.059(1)
O(2)	0.1058(4)	−0.3384(3)	0.2256(3)	0.055(1)
O(3)	0.6399(4)	0.0176(4)	0.0962(4)	0.067(1)

Table 2. (Contd.)

Atom	*x*	*y*	*z*	U_{iso}/U_{eq}, Å^2
		II		
O(4)	0.8457(6)	0.3078(5)	0.2196(5)	0.110(2)
C(1)	0.4111(5)	−0.0180(6)	0.1466(4)	0.051(1)
C(2)	0.4554(5)	−0.1094(5)	0.1079(4)	0.049(1)
C(3)	0.3832(6)	−0.2155(6)	0.0980(5)	0.062(2)
C(4)	0.4246(8)	−0.3008(7)	0.0653(6)	0.077(2)
C(5)	0.5406(8)	−0.2776(7)	0.0383(6)	0.078(2)
C(6)	0.6154(7)	−0.1719(6)	0.0476(5)	0.068(2)
C(7)	0.5731(6)	−0.0879(5)	0.0828(4)	0.053(2)
C(8)	0.765(1)	0.047(1)	0.0783(8)	0.054(3)
C(8*X*)	0.771(2)	0.024(2)	0.110(2)	0.052(5)
C(9)	0.819(1)	0.168(1)	0.1007(9)	0.074(3)
C(9*X*)	0.825(2)	0.138(2)	0.164(2)	0.078(6)
C(10)	0.794(1)	0.191(1)	0.2010(9)	0.077(3)
C(10*X*)	0.780(2)	0.226(2)	0.134(2)	0.066(5)
C(11)	0.7983(8)	0.3937(8)	0.2079(6)	0.083(3)
C(12)	0.7008(9)	0.392(1)	0.1544(7)	0.114(4)
C(13)	0.6587(9)	0.481(1)	0.1513(7)	0.113(4)
C(14)	0.7121(8)	0.5768(9)	0.1977(6)	0.090(3)
C(15)	0.8087(7)	0.5790(7)	0.2505(5)	0.070(2)
C(16)	0.8525(6)	0.4891(6)	0.2580(5)	0.063(2)
C(17)	0.9560(6)	0.4912(6)	0.3197(5)	0.063(2)
C(18)	0.5355(5)	−0.0198(5)	0.3213(4)	0.051(1)
C(19)	0.5825(6)	−0.1079(6)	0.3054(5)	0.065(2)
C(20)	0.6899(8)	−0.1072(8)	0.3434(6)	0.086(3)
C(21)	0.7484(8)	−0.0213(8)	0.3980(6)	0.085(2)
C(22)	0.7012(8)	0.0628(8)	0.4179(7)	0.094(3)
C(23)	0.5946(7)	0.0638(7)	0.3783(6)	0.076(2)
C(24)	0.3703(5)	0.1086(5)	0.3014(5)	0.052(2)
C(25)	0.4302(8)	0.2086(6)	0.2616(7)	0.086(3)
C(26)	0.416(1)	0.3078(7)	0.2940(8)	0.105(3)
C(27)	0.341(1)	0.3093(9)	0.3617(8)	0.096(3)
C(28)	0.281(1)	0.213(1)	0.3986(7)	0.103(3)
C(29)	0.2934(7)	0.1106(7)	0.3697(5)	0.077(2)
C(30)	1.2201(8)	0.565(1)	0.3448(8)	0.061(5)
C(31)	1.335(1)	0.593(1)	0.3129(6)	0.071(4)
C(32)	1.4291(8)	0.614(1)	0.3740(8)	0.086(5)
C(33)	1.408(1)	0.607(1)	0.4671(8)	0.098(6)
C(34)	1.293(1)	0.578(1)	0.4991(6)	0.122(8)
C(35)	1.1990(9)	0.557(1)	0.4379(9)	0.092(5)
C(30*X*)	1.1964(8)	0.5557(8)	0.3622(6)	0.044(4)
C(31*X*)	1.304(1)	0.6368(7)	0.3582(6)	0.072(4)
C(32*X*)	1.3853(8)	0.6477(8)	0.4287(8)	0.093(5)
C(33*X*)	1.3594(9)	0.578(1)	0.5033(7)	0.089(5)
C(34*X*)	1.2521(9)	0.4964(8)	0.5073(6)	0.070(4)
C(35*X*)	1.1705(7)	0.4855(7)	0.4368(6)	0.054(3)
C(36)	1.119(1)	0.4619(7)	0.1737(5)	0.050(4)
C(37)	1.1399(9)	0.3607(7)	0.1921(5)	0.065(3)
C(38)	1.1512(9)	0.2910(6)	0.1208(6)	0.074(3)
C(39)	1.1411(9)	0.3227(7)	0.0313(6)	0.067(3)
C(40)	1.1197(9)	0.4239(8)	0.0129(5)	0.078(4)
C(41)	1.108(1)	0.4935(6)	0.0841(6)	0.067(4)
C(36*X*)	1.117(2)	0.449(1)	0.1905(9)	0.042(6)
C(37*X*)	1.129(2)	0.348(1)	0.2199(8)	0.056(5)
C(38*X*)	1.141(1)	0.269(1)	0.157(1)	0.062(5)
C(39*X*)	1.141(1)	0.291(1)	0.0642(9)	0.052(4)
C(40*X*)	1.129(2)	0.393(1)	0.0348(8)	0.064(5)
C(41*X*)	1.117(2)	0.472(1)	0.0979(9)	0.054(5)

Note: The coordinates of H atoms are available from the authors.

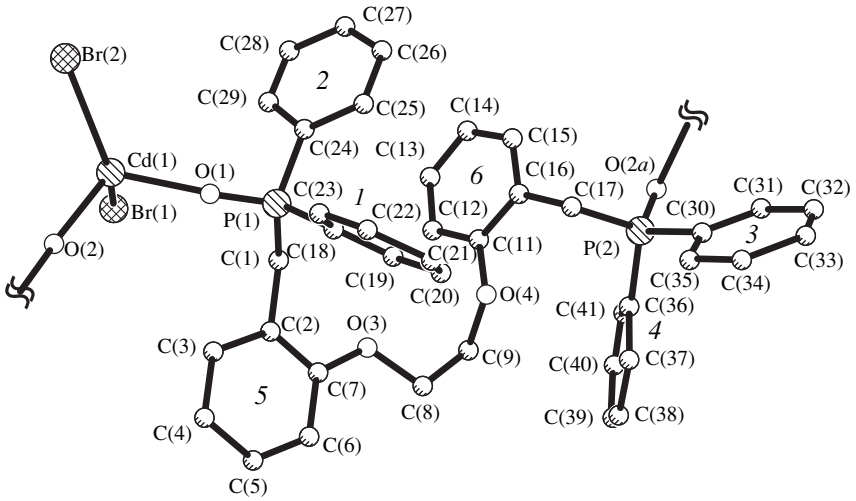

Fig. 1. A chain fragment in the $CdBr_2 \cdot L^1$ (**I**) structure.

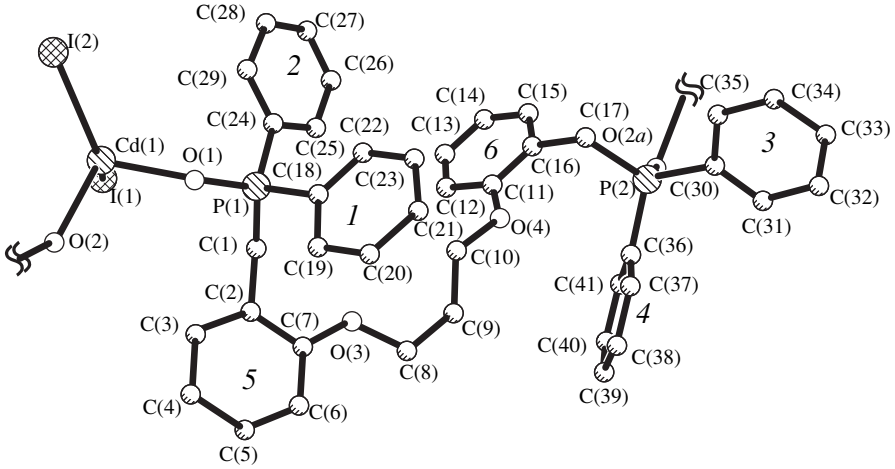

Fig. 2. A chain fragment in the $CdI_2 \cdot L$ (**II**) structure (the second positions of the statistically disordered fragments of propylene glycol chain and the 3*x* and 4*x* benzene rings are omitted).

calculations were carried out on an IBM PCAT 386 by using the SHELXL93 software package [5].

The atomic coordinates are listed in Table 2.

RESULTS AND DISCUSSION

Structural Description of the Complexes

Crystals of compounds **I** and **II** have a polymeric chain structure. Structural fragments of the $CdBr_2 \cdot L^1$ and $CdI_2 \cdot L$ chains are depicted in Figs. 1 and 2, respectively. The potentially tetradentate ligands L^1 in compound **I** and L in compound **II** join the cadmium complexes into the chains and fulfill the bidentate bridging function. Note that only two phosphoryl oxygen atoms participate in the coordination with the metal, and the anisole oxygen atoms are not coordinated to the metal. A similar polymeric structure is observed in the compounds $CdI_2 \cdot L^1$ (**III**) and $ZnI_2 \cdot L^1$ (**IV**) studied earlier in [1].

The coordination polyhedron of the Cd atoms in **I** and **II** is a tetrahedron formed by two phosphoryl oxygen atoms of two podand ligands and also by two Br^- ions in structure **I** or two I^- ions in structure **II**. The polyhedra of the Cd atoms in **I** and **II** are distorted. The angles at the metal atom fall in the range from 95.7° to 118.8° in complex **I** and from 94.9° to 124.8° in complex **II** (from 91.9° to 124.9° in complex **III**). The OCdO angle is smallest, and the *Hal*Cd*Hal* angle is largest. The ICdI angles in structures **II** and **III** are virtually identical. The replacement of the I^- ion in the Cd tetrahedron (structure **III**) by the Br^- ion (structure **I**) brings about a decrease in the *Hal*Cd*Hal* angle by 6° (the angle decreases from 124.8° to 118.8°), which is likely due to a decrease in the size of halogen ion. The OCdO angle insignificantly changes from structure to

Table 3. Torsion angles in structures **I**–**IV**

Angle	**I**	**II**	**III**	**IV**
O(1)P(1)C(1)C(2)	−70.4	−68.0	−64.9	−60.0
C(24)P(1)C(1)C(2)	168.5	169.4	171.2	177.3
C(18)P(1)C(1)C(2)	52.1	54.8	56.4	59.1
P(1)C(1)C(2)C(7)	−117.2	−100.9	−101.5	−91.5
C(1)C(2)C(7)O(3)	0.5	0.2	−2.1	6.1
C(2)C(7)O(3)C(8)	160.9	175.8	156.0	−161.4
C(7)O(3)C(8)C(9)	−178.7	−178.6	175.3	−170.8
O(3)C(8)C(9)C(10)		57.2(−39.2*)		
O(3)C(8)C(9)O(4)	67.5		69.4	−59.1
C(8)C(9)C(10)O(4)		−179.2(171.4)		
C(9)C(10)O(4)C(11)		87.7(−172.2)		
C(10)O(4)C(11)C(16)		160.0(−167.4)		
C(8)C(9)O(4)C(11)	−124.3		−114.8	−173.0
C(9)O(4)C(11)C(16)	−150.2		−147.9	179.8
O(4)C(11)C(16)C(17)	1.0	−0.1	4.0	−1.3
C(11)C(16)C(17)P(2)	95.5	95.7	99.6	−95.3
C(16)C(17)P(2)O(2a)	49.0	51.3	56.1	−72.9
C(16)C(17)P(2)C(36)	−74.0	−66.4(−74.9)	−65.1	47.4
C(16)C(17)P(2)C(30)	173.2	174.4(173.0)	177.0	165.0

* Torsion angles in the second fragment of the propylene glycol chain and in the second positions of benzene rings at the P(2) atom in structure **II**.

structure. The mean bond lengths are as follows: Cd–Br, 2.526(2) Å; Cd–**I**, 2.695(1) Å; and Cd–O, 2.243(8) Å in structure **I** and 2.210(4) Å in structure **II** [Cd–I, 2.685(2) Å and Cd–O, 2.210(2) Å in structure **III**]. The Cd–O bond lengths are close to the sum of covalent radii of the cadmium and oxygen atoms (2.21 Å). The Cd–Br and Cd–I distances are approximately 0.1 Å less than the corresponding sums of covalent radii (Cd and Br, 2.62 Å; Cd and I, 2.81 Å).

In the studied ligands, the P atoms exhibit a tetrahedral coordination. The mean P=O bond lengths in complexes **I** and **II** are equal to 1.496(7) and 1.502(4) Å, respectively. Within the limits of triple standard deviation, the P–C(sp^3) and P–C(sp^2) bond lengths in both compounds are close to each other: 1.806(10) and 1.834(6) Å in complex **I** and 1.810(6) and 1.797(8) Å in complex **II**. The mean OPC angles in structures **I** and **II** are equal to 112.0(4)° and 110.1(3)°, respectively. The mean CPC angles in **I** and **II** are 106.8(4)° and 108.7(4)°, respectively. With allowance for the second orientation of the benzene rings in structure **II**, the mean OPC angle is equal to 113.7(3)°, and the mean CPC angle is 104.8(5)°. In the P tetrahedron, the angles involving the O atoms are larger than the CPC angles, which is characteristic of the RR'R"P=*X*-type compounds [6] and is observed in all the studied compounds with phosphoryl-containing ligands [1, 7, 8].

Within the limits of triple standard deviation, the geometric parameters of the phosphoryl-containing podands L^1 and *L* in structures **I** and **II** are close to each other and to the standard values: C(sp^3)–C(sp^2), 1.48(2) and 1.505(9) Å; C(sp^3)–C(sp^3), 1.55(1) and 1.51(1) Å; O–C(sp^3), 1.46(2) and 1.53(2) Å; and O–C(sp^2), 1.36(1) and 1.36(1) Å; COC, 118(1)° and 115.2(9)°; and OC(sp^3)C(sp^3) angles, 109(1)° and 103(2)° in structures **I** and **II**, respectively.[1]

Table 3 presents the torsion angles in structures **I**–**IV**. The angles were calculated in the same orientation for all the compounds. The L^1 ligands in compounds **I** and **III** and the *L* ligand in **II** take an *S*-shaped conformation, and the L^1 ligand in compound **IV** adopts a *C*-shaped conformation. The L^1 ligand changes its shape upon rotation about the C(8)–C(9) bond, which is accompanied by the change in sign of the torsion angle with respect to this bond (the relevant signs are positive in compounds **I** and **III** and negative in **IV**). The *C*-shaped conformation of the ligand is characterized by identical signs of the torsion angles around the bonds that are symmetric relative to the C(8)–C(9) bond. In the *S*-shaped conformation, these torsion angles differ in sign. This most clearly manifests itself in the sign of the angle around the C(1)–C(2) bond and

[1] For structure **II**, the presented data are averaged over two positions of the propylene glycol chain.

Table 4. Angles between the planes of benzene rings in compounds **I**–**IV**

Plane	**I**	**II**	**III**	**IV**
1–2	104.1	77.3	100.5	92.3
3–4	65.6	78.9	68.0	57.6
3*x*–4*x*		107.7		
5–6	115.6	51.1	56.8	35.6

the C(16)–C(17) bond symmetric relative to the C(1)–C(2) bond. The signs of the torsion angles close to 180° are less informative. Therefore, it can be inferred that a particular type of conformation (*C*-shaped or *S*-shaped) adopted by the L^1 ligand containing one ethylene glycol chain depends on the sign of the O(3)C(8)C(9)C(10) torsion angle and a combination of the signs of the C(11)C(16)C(17)P(2) and P(1)C(1)C(2)C(7) torsion angles. Although the ligand in **II** is lengthened by one methylene group, the signs of the torsion angles around the C(8)–C(9), C(16)–C(17), and C(1)–C(2) bonds are similar to those in structures **I** and **III** and are typical of the *S*-shaped conformation of the ligand.

The O(3)C(8)C(9)O(4) ethylene glycol chain in complex **I** adopts the *gauche* conformation with respect to the C(8)–C(9) bond and the *trans* conformation relative to one of the C–O bonds. The conformation relative to the second C–O bond is intermediate (124°) between the *trans* and *gauche* conformations. Consequently, the ethylene glycol chain can be described by the *TGS* conformation. In the O(3)C(8)C(9)C(10)O(4) propylene glycol chain of complex **II**, the C–C bonds exhibit different conformations, namely, the energetically favorable *gauche* conformation and *trans* conformation. The *trans* and *gauche* conformations are observed in the C–O bonds. As a whole, the propylene glycol chain is characterized by the *TGTG* conformation.

The angles between the benzene rings in structures **I**–**IV** are given in Table 4. It should be mentioned that, in structures **I** and **III** with the *S*-shaped conformation of the L^1 ligand, the angle between the planes of phenyl rings 5 and 6 is substantially larger than that in structure **IV** with the *C*-shaped conformation of this ligand. As can be seen from the table, in structures **I**, **III**, and **IV**, the angles between rings 3 and 4 at the P(2) atom are less than those between rings 1 and 2 at the P(1) atom. In **II**, the angles between two planes of statistically disordered benzene rings are equal to 37.9° for the C(30)–C(35) and C(30*X*)–C(35*X*) rings and 4.6° for the C(36)–C(41) and C(36*X*)–C(41*X*) rings.

In compounds **I**–**IV**, the P=O bonds are directed "outward" with respect to the ligand rather than "inward," as in the Na and Li mononuclear complexes with 1,8-bis[2-(diphenylphosphinylmethyl)phenoxy]-3,6-dioxaoctane [7, 8]. Only with this orientation, the L^n and *L* ligands can act as a bridge between two metal atoms.

The polymeric chains in structure **I** are formed by the translation along the *y*-axis. In structure **II**, the chains are produced by the diagonal translation in the *xy* plane. Only the van der Waals interactions are observed between the chains.

Vibrational Spectra

The vibrational (IR and Raman) spectra of the L^1 podand were discussed and interpreted in detail in the earlier work [2]. The assignment of the main vibrational bands in the spectra of lithium, barium, and mercury complexes with the L^1 podand was also made in [2]. The IR spectra of the L^1 podand and the $CdI_2 \cdot L^1$ and $ZnI_2 \cdot L^1$ complexes were reported in [1]. In these works, we formulated the spectral criteria for determining the coordination mode of the L^1 ligand in metallocomplexes.

The IR spectra of complexes **I** and **III** are virtually identical. According to the coordination mode of the L^1 ligand, the ν(P–O) band in the IR spectrum of complex **I** is shifted by 57 cm^{-1} toward the low-frequency range as compared to the corresponding band in the IR spectrum of the L^1 podand, whereas the band of the ν(*Ph*–O) stretching vibrations retains its location at about 1250 cm^{-1} (Table 5).

Since the conformation of the ethylene glycol chain in the coordinated podand L^1 in complex **I** is identical to that in complex **III** (namely, the *TGS* conformation), the absorption pattern in the conformationally sensitive range 800–1000 cm^{-1} remains unchanged when going from the iodide complex (936, 922, and 828 cm^{-1}) to the bromide complex (932 sh, 921, and 831 cm^{-1}).

The ν_{as}(COC) vibrations are also sensitive to changes in the conformation of the OCH_2CH_2O fragment [9]. Although, as mentioned above, the *TGS* conformation of the ethylene glycol chain is retained in the cadmium bromide complex, the torsion angle around one of the C–O bonds increases up to 124° as compared to 115° in the iodide complex (Table 3). In this case, the ν_{as}(COC) vibration in the IR spectrum of complex **I** is observed at about 1000 cm^{-1}, whereas the ν_{as}(COC) vibration in complex **III** is found at 1110 cm^{-1}. The observed change in the ν_{as}(COC) frequency is in agreement with the data obtained in [10]. As follows from the structural analysis of some podands and complexes on their base [10], a decrease in the torsion angle around one of the C–O bonds is attended by an increase in the ν_{as}(COC) frequency.

The most substantial difference in the geometries of the coordinated podand L^1 in complexes **I** and **III** lies in the angle between benzene rings 5 and 6: its value in the bromide complex is larger than that in the iodide complex (Table 3). Apparently, this discrepancy can be

Table 5. Assignment of vibrational bands (cm^{-1}) in the IR spectra of the L and L^1 podands and the $CdI_2 \cdot L$ and $CdBr_2 \cdot L^1$ complexes

Vibration	$CdBr_2 \cdot L^1$	L^1	L	$CdI_2 \cdot L$
	1598 m	1600 m		1596 m
ν_{Ph}		1592 m	1595 m	1589 m
	1500 s	1500 s	1500 s	1496 s
$\delta(CH_2)$	1457 s	1461 s	1458 s	1455 vs
ν(P–*Ph*)	1442 s	1441 s	1440 s	1438 s
	1408 w	1413 w		
	1385 w	1400 sh	1402 m	1394 m
$\omega(CH_2)$				1333 m
	1321 w	1325 w	1320 w	1318 w
		1304 m		1302 sh
ν(P–*Ph*)	1298 m	1297 m	1294 m	1290 m
	1265 sh	1260 s		
ν(*Ph*–O)	1250 s	1250 s	1250 vs	1250 vs
	1230 s	1231 vs	1230 sh	1240 s
				1220 m
$\tau(CH_2)$	1193 s	1187 sh		1189 m
	1180 w			
ν(P=O)	1140 vs	1197 vs	1190 vs	1140 vs
	1167 m	1165 w	1163 w	1160 vs
δ_{Ph}		1152 s	1151 s	
$\delta_{Ph(P)}$	1130 sh	1123 s	1120 s	1120 vs
		1110 sh	1107 sh	
ν_{as}(COC)	1100 s	1099 s	1095 s	1095 vs
$\delta_{Ph(P)}$	1075 m	1080 w	1069 m	1071 m
		1064 s		
ν_s(COC) + ν(CC)	1055 w	1051 w	1054 m	1050 s
	1040 w	1037 w	1032 w	1030 m
$\delta_{Ph(P)}$	1003 w	1006 w	1000 m	1000 m
			980 m	976 w
		950 s		949 m
	932 sh	937 m	940 w	940 sh
	921 m	914 m	910 sh	908 sh
$\rho(CH_2)$ + ν(CO) + ν(CC)		863 m	868 m	863 sh
			859 sh	850 w
		848 m		843 w
	831 m	834 m	829 m	830 vs
			810 m	804 w
	788 w	782 m	795 vw	790 sh
ν(PC)	775 m	775 m	770 m	776 m
	756 s	753 vs	753 vs	758 vs
	744 s			746 sh
δ_{Ph}	725 s	722 vs	720 vs	722 vs
	700 s	698 vs		
		685 s	689 vs	688 vs
	616 w	614 w	616 vw	615 w
	600 w	605 w	602 w	602 sh
δ(COC), δ(CCO)		594 s	587 m	595 w
	576 w	574 m		574 w
		553 w	545 w	554 w
				541 m
	535 sh	532 s		532 m
	526 s	520 s	522 vs	
	515 s			515 vs
δ(*Ph*PO), δ(CPO)		505 s	510 vs	505 sh
	490 m	490 sh		493 sh
	482 m			
	460 w	468 m	465 m	460 w
	437 w		424 m	

responsible for some differences observed in the IR spectra of complexes **I** and **II** in the spectral range 400–500 cm^{-1}, which, as shown in [7], is very sensitive to changes in the mutual arrangement of benzene rings.

Despite an additional methylene group in the composition of the *L* molecule, the number of bands in the IR spectrum of this podand is substantially less than that in the IR spectrum of the L^1 podand. Nonetheless, the main absorption bands retain their location (Table 5). In the case of the L^1 molecule with only one ethylene glycol unit, we assumed in the earlier work [1] that the multiplet character of bands in the conformationally sensitive spectral ranges stems from the conformational heterogeneity of this podand in the free state [1]. This is supported by the fact that the IR spectra of the zinc and cadmium complexes with a certain conformation of the L^1 molecule exhibit a less complex vibrational structure owing to the disappearance of the splitting of many bands. On this basis, with allowance made for the character of the IR spectrum of the *L* molecule, it can be concluded that, unlike the L^1 podand, the *L* podand in the free state is conformationally homogeneous. However, the conformation of the propylene glycol chain in the *L* podand cannot be judged from the spectral data, because the conformation of the $OCH_2CH_2CH_2O$ fragment is determined by a set of four torsion angles, whereas we have used the correlations between the conformationally sensitive frequency and the conformation of the OCH_2CH_2O fragment, which is described by three torsion angles.

It follows from Table 5 that the location of bands and the ratio of their intensities in the range 1300–1600 cm^{-1} in the IR spectra of the L^1 and *L* podands are virtually identical. The only difference is that the IR spectrum of the *L* podand contains the singlet bands rather than the doublet bands at about 1595, 1402, and 1294 cm^{-1}. In the range 1200–1300 cm^{-1}, the spectra of the L^1 and *L* podands differ essentially. The spectrum of the L^1 podand exhibits two intense bands, namely, the $\nu(Ph\text{–}O)$ doublet at 1260 and 1250 cm^{-1} and the $\tau(CH_2)$ singlet near 1231 cm^{-1}, whereas the spectrum of the *L* podand involves one intense band near 1250 cm^{-1} with a shoulder at 1230 cm^{-1}. In the range 1100–1200 cm^{-1}, the spectra of the L^1 and *L* podands are closely similar to each other with the only exception residing in the splitting of the $\nu(P{=}O)$ vibration band (1197 and 1187 cm^{-1}) in the case of the L^1 podand. It is reasonable that the distinctions are more pronounced in the frequency ranges of the $\nu_s(CO) + \nu(CC)$ stretching vibrations of the OCCO and OCCCO fragments (1000–1100 cm^{-1}) and the $CH_2\rho(CH_2)$ bending vibrations of the CH_2 groups (800–1000 cm^{-1}). These distinctions are caused, on the one hand, by the difference between the OCCO and OCCCO fragments themselves and, on the other hand, by the conformational heterogeneity of the L^1 molecules. By contrast, the $Ph_2P{=}O$ terminal groups in both podands are identical, and the differences can be observed only in the mutual arrangement of the benzene rings. Therefore, the absorption spectra of the L^1 and *L* podands in the range 700–800 cm^{-1} that involves the bands associated with the out-of-plane bending vibrations of benzene rings are close in character. The spectral patterns for the L^1 and *L* podands show individual features in the range 450–550 cm^{-1} corresponding to the $\delta(PhPO)$ and $\delta(PhPC)$ vibrations that are sensitive to the orientation of the *Ph* rings. The same is true for the $\delta(COC)$ and $\delta(CCO)$ vibrations in the range 550–650 cm^{-1}. The number of bands in this range in the spectrum of the L^1 podand is appreciably larger than that in the spectrum of the *L* podand, which is likely accounted for by the conformational heterogeneity of the L^1 podand.

As already mentioned, the above conformational heterogeneity of the noncoordinated L^1 podand is responsible for a more complex structure of its IR spectrum as compared to the spectra of the zinc and cadmium complexes. A different situation is observed for the *L* podand and $CdI_2 \cdot L$ complex: the IR spectrum of the iodide complex contains a larger number of bands (Table 5). This fact can be explained in the following way. According to the X-ray diffraction analysis, the carbon atoms in the propylene glycol chain and the benzene rings at the P(2) atom are statistically disordered. This implies that molecules of two types should contribute to the spectrum of the $CdI_2 \cdot L$ complex. However, the main bands or groups of bands are observed in the frequency ranges typical of the coordinated podands of this type. The coordination leads to a decrease in the $\nu(P{=}O)$ frequency from 1190 cm^{-1} for the *L* podand to 1140 cm^{-1} for the $CdI_2 \cdot L$ complex. The bands of the $\nu(Ph\text{–}O)$ and $\nu_{as}(COC)$ vibrations retain their locations at about 1250 and 1095 cm^{-1}, respectively. The assignment of the remaining bands is evident from Table 5. Consideration of the conformational rearrangement of the *L* molecule as a result of the complex formation is beyond the scope of the present work, first, for the lack of the corresponding spectral–structural correlations and, second, in view of a peculiar "conformational heterogeneity" of the $CdI_2 \cdot L$ complex, due to statistical disordering of some atoms in the *L* molecule.

The results obtained in this work indicate that the *L* podand in the $CdI_2 \cdot L$ complex exhibits an *S*-shaped conformation. The "shorter" podand L^1 in the $CdI_2 \cdot L^1$ complex adopts the same conformation [1]. Consequently, the replacement of the *L* podand by the L^1 podand in the cadmium iodide complex does not change the shape of the bidentate bridging ligand L^1. Moreover, the *S*-shaped conformation of the L^1 ligand is retained upon replacement of the acido ligand, i.e., when going from the $CdI_2 \cdot L^1$ complex to the $CdBr_2 \cdot L^1$ complex. Only the replacement of the central cad-

mium atom with the zinc atom brings about the change in shape of the bidentate bridging ligand L^1: the *C*-shaped conformation rather than the *S*-shaped conformation is realized in the $ZnI_2 \cdot L^1$ complex.

ACKNOWLEDGMENTS

We would like to thank G.G. Sadikov for helpful discussions of the results.

REFERENCES

1. L. Kh. Minacheva, I. S. Ivanova, I. K. Kireeva, *et al.*, Zh. Neorg. Khim. **39** (7), 1143 (1994).
2. I. S. Ivanova, I. K. Kireeva, V. E. Baulin, *et al.*, Zh. Neorg. Khim. **40** (5), 792 (1995).
3. I. S. Ivanova, I. K. Kireeva, V. E. Baulin, *et al.*, Zh. Neorg. Khim. **42** (3), 454 (1997).
4. V. P. Solov'ev, L. V. Govorkova, O. A. Raevskiĭ, *et al.*, Izv. Akad. Nauk SSSR, Ser. Khim., No. 3, 575 (1991).
5. G. M. Sheldrick, *SHELXL93: Program for the Refinement of Crystal Structures* (Univ. of Göttingen, Göttingen, 1993).
6. N. G. Bokiĭ, Yu. V. Struchkov, A. E. Kalinin, *et al.*, Itogi Nauki Tekh., Ser.: Kristallokhim. 88 (1977).
7. L. Kh. Minacheva, I. S. Ivanova, I. K. Kireeva, *et al.*, Koord. Khim. **19** (3), 185 (1993).
8. L. Kh. Minacheva, I. S. Ivanova, I. K. Kireeva, *et al.*, Zh. Neorg. Khim. **37** (10), 2185 (1992).
9. O. A. Raevskiĭ, V. V. Tkachev, A. O. Atovmyan, *et al.*, Koord. Khim. **14** (2), 1697 (1988).
10. I. K. Kireeva, Yu. E. Gorbunova, I. S. Ivanova, *et al.*, Koord. Khim. **23** (11), 853 (1997).

Translated by O. Borovik-Romanova

Crystallography Reports, Vol. 45, No. 1, 2000, pp. 56–63. Translated from Kristallografiya, Vol. 45, No. 1, 2000, pp. 61–68.

STRUCTURES OF COORDINATION COMPOUNDS

Stereochemical Activity of a Lone Electron Pair in Antimony(III) and Bismuth(III) Chelates: Crystal Structures of $Ca[Sb(Edta)]_2 \cdot 8H_2O$ and $Ba\{[Bi(Edta)]_2H_2O\} \cdot H_2O$

A. B. Ilyukhin* and A. L. Poznyak**

**Kurnakov Institute of General and Inorganic Chemistry, Russian Academy of Sciences, Leninskiĭ pr. 31, Moscow, 117907 Russia*

***Institute of Molecular and Atomic Physics, Belarussian Academy of Sciences, pr. F. Skoriny 70, Minsk, 220072 Belarus*

Received April 1, 1998

Abstract—The crystal structures of $Ca[Sb(Edta)]_2 \cdot 8H_2O$ (**I**) and $Ba\{[Bi(Edta)]_2H_2O\} \cdot H_2O$ (**II**) are determined by X-ray diffraction. Crystals **I** are monoclinic, $a = 7.132$ Å, $b = 21.906$ Å, $c = 10.896$ Å, $\beta = 91.13°$, $Z = 2$, and space group $P2_1/n$. Crystals **II** are triclinic, $a = 8.995$ Å, $b = 12.750$ Å, $c = 13.577$ Å, $\alpha = 77.42°$, $\beta = 73.90°$, $\gamma = 86.53°$, $Z = 2$, and space group $P\bar{1}$. In structure **I**, the coordination number of the antimony atom is 6 + LEP (lone electron pair), and the polyhedron is a ψ-pentagonal bipyramid with the lone electron pair at an equatorial position. In structure **II**, two crystallographically independent complexes $Bi(Edta)^-$ and the coordination water molecule form tetranuclear associates. The environments of two independent bismuth atoms (the coordination number is eight) are similar, and their polyhedra can be described as distorted dodecahedra. The effect of the lone electron pair on the structures of polyhedra of antimony and bismuth is discussed. © *2000 MAIK "Nauka/Interperiodica".*

In studies of the complexes of *p* elements in low oxidation states, we came up against the problem concerning the stereochemical behavior of a lone electron pair (LEP). The main structural characteristics of these compounds are adequately described within the model of the valence shell electron pair repulsion (VSEPR) [1]. However, in the case when the coordination number of metal is 6 + LEP, specifically in the complexes of polydentate chelate ligands, the shape of the metal polyhedron or the stereochemical behavior of the lone electron pair are unpredictable within the VSEPR model [1]. Solution of this problem requires accumulation of experimental data on the structures of the complexes under discussion.

In this paper, we report the X-ray crystal structures of antimony(III) and bismuth(III) ethylenediaminetetraacetates, $Ca[Sb(Edta)]_2 \cdot 8H_2O$ (**I**) and $Ba\{[Bi(Edta)]_2H_2O\} \cdot H_2O$ (**II**).

EXPERIMENTAL

The main crystal data, data collection and structure refinement parameters for **I** and **II** are summarized in Table 1. Structures **I** and **II** are solved by the direct method using the SHELXS86 program [2]. The atomic coordinates and thermal parameters are listed in Table 2. The positions of the aliphatic hydrogen atoms in complexes **I** and **II** and hydrogen atoms of the coordination water molecule in complex **II** were calculated geometrically. The hydrogen atoms in one of the crystallization water molecules in **I** were located from a difference Fourier synthesis. Two other molecules of crystallization water in **I** are statistically disordered over two [O(11)] or three [O(12)] positions. In **II**, the positions of crystallization water molecules O(2) and O(3) are half occupied. The occupancies were refined at the fixed isotropic thermal parameters ($U_{iso} = 0.10$ Å^2). The resulting occupancies were fixed in further calculations. Structures **I** and **II** were refined by the full-matrix least-squares procedures in the anisotropic approximation of thermal vibrations of all the atoms, except O(11) and O(12) in **I**. The positional and thermal parameters of the H atoms in **I** and **II** were fixed. The refinement was performed with the SHELX76 program [3].

RESULTS AND DISCUSSION

Structure **I** consists of the $[Sb(Edta)]^-$ anionic complexes (Fig. 1a), calcium cations, and water molecules. The coordination number of the antimony atom is 6 + LEP, and the polyhedron is a ψ-pentagonal bipyramid with the lone electron pair in the equatorial plane and the O(3) and O(5) atoms in the axial positions. The O(6') atom closely approaches (the distance is 3.17 Å) the antimony atom of the neighboring complex. Therefore, we can consider that the coordination number of the Sb atom is 6 + 1 + LEP. The calcium atom is located

1063-7745/00/4501-0056$20.00 © 2000 MAIK "Nauka/Interperiodica"

at the inversion center and has an octahedral coordination.

Structure **II** contains two crystallographically independent Bi(*Edta*)$^-$ complexes, which, together with the coordination water molecule O(1), form tetranuclear associates (Fig. 1b). The environments of two independent bismuth atoms (the coordination number is eight) are very similar, and the polyhedra can be described as severely distorted dodecahedra. The coordination number of the barium atom is ten, and the polyhedron is a pentagonal antiprism.

By now, eight antimony(III) complexes with diaminocarboxylates are structurally characterized, namely, [Sb(H*Edta*)] · $2H_2O$ [4], Na[Sb(*Edta*)] · $3H_2O$ [5], Ca[Sb(*Edta*)]$_2$ · $8H_2O$ (**I**), {$C(NH_2)_3$}[Sb(*Edta*)] · $2H_2O$ [6], [Sb(H*Pdta*)] [7], Na[Sb(*Pdta*)] · H_2O [8], NH_4[Sb(*Pdta*)] · H_2O [8], and [Sb(*Hedtra*)] (two crystallographically independent complexes) [9], where H_4*Pdta* is propylene-1,2-diaminetetraacetic acid and H_3*Hedtra* is *N*-hydroxyethylethylenediaminetriacetic acid. In all the complexes with diamine ligands, the shape of the antimony polyhedron is a severely distorted ψ-pentagonal bipyramid, in which the lone electron pair can be situated at one of two different positions shown schematically in Fig. 2: in the equatorial plane (*A*) or at the axial position (*B*).

The structures of seven-vertex complexes with diamine ligands were discussed in review [10]. It was assumed that the proper symmetry of the complex is 2 (the axis passes through the midpoint of the ethylenediamine C–C bond, the metal atom, and the monodentate ligand). Such a structure is observed in the *A*-type complexes (with allowance for the replacement of the lone electron pair by a monodentate ligand) and complexes with polyhedron in the shape of a single-capped trigonal prism (with a monodentate ligand as a cap). Later, it was shown that the polyhedron can exist in the form of a single-capped trigonal prism in which the monodentate ligand is situated in one of the bases of the prism; it is not described by the proper symmetry 2 [11]. The *B* type compounds have not been observed among the seven-vertex complexes with the hexadentate ligands. The *B*-type structure was first found in {$C(NH_2)_3$}[Sb(*Edta*)] · $2H_2O$; however, the metal polyhedron was inadequately described in [6]. Similar structures were later observed in each of the three H_4*Pdta* complexes [7, 8]. In [8], the structures of the polyhedra in all antimony(III) complexes with diamine ligands were considered, and the polyhedron in {$C(NH_2)_3$}[Sb(*Edta*)] · $2H_2O$ was described correctly. However, as in the original paper [9], the metal polyhedron in [Sb(*Hedtra*)] was described inadequately, and only one of the two independent complexes was considered [8].

Among the nine complexes with diamine ligands, there are four complexes with the lone electron pair at the axial position and five complexes with the lone electron pair in the equatorial plane.

Table 1. Main crystal data, data collection and structural refinement for **I** and **II**

Compound	Ca[Sb(*Edta*)]$_2$ · $8H_2O$ (**I**)	Ba{[Bi(*Edta*)]$_2H_2O$} · H_2O (**II**)
Formula	$C_{20}H_{40}CaN_4O_{24}Sb_2$	$C_{20}H_{28}BaN_4O_{18}Bi_2$
Crystal system	Monoclinic	Triclinic
a, Å	7.132(2)	8.995(2)
b, Å	21.906(5)	12.750(2)
c, Å	10.896(3)	13.577(3)
α, deg		77.42(2)
β, deg	91.13(2)	73.90(2)
λ, deg		86.53(2)
Space group	$P2_1/n$	$P\bar{1}$
Z	2	2
V, Å^3	1702.0(8)	1460.1(6)
ρ_{calcd}, g/cm^3	1.959	2.656
μ, mm^{-1}	1.84	13.45
$2\theta_{max}$, deg	52	50
N_a^*	2997	4176
N_o^*	2148	3410
N_p^*	235	415
*R***	0.036	0.034
*wR***	0.040	0.040
*Gof***	1.26	1.02
w	$1/\{\sigma^2(F) + 0.0001F^2\}$	$1/\{\sigma^2(F) + 0.0001F^2\}$

Note: For both crystals, the data were collected on an Enraf–Nonius CAD4 diffractometer (λMoK_α, graphite monochromator, ω/2θ scan mode), and the absorption correction was introduced by ψ scans.

* N_a is the number of unique reflections with $F > 0$, N_o is the number of reflections with $F > 4\sigma(F)$, and N_p is the number of parameters in the refinement.

** $R = \Sigma||F_o| - |F_c|/\Sigma|F_o|$; $wR = [\Sigma w\{|F_o| - |F_c|\}^2\Sigma\{w\{F_o\}^2]^{1/2}$; $Gof = [\Sigma\{w||F_o| - |F_c||^2\}/(N_o - N_p)]^{1/2}$.

Structures of three antimony(III) complexes with diethylenetriaminepentaacetic acid (H_5*Dtpa*) were determined for different hydrate compositions [Sb(H_2*Dtpa*)] · nH_2O (n = 0 [12], n = 1 [13], and n = 2 [14]). In the first two compounds (Fig. 3a), the lone electron pair is stereochemically active and occupies one of the axial positions in the pentagonal bipyramid of the metal (the coordination number is 6 + *e*). However, the coordination number of the metal in the dihy-

Table 2. Atomic coordinates and thermal parameters $U_{eq} = 1/3\Sigma_i\Sigma_j U_{ij} a_i a_j a_i^* a_j^*$ in structures **I** and **II**

Atom	*x*/*a*	*y*/*b*	*z*/*c*	U_{eq}, Å^2
		I		
Sb(1)	0.21115(6)	0.76492(2)	0.24632(4)	0.0284(1)
Ca(1)	1/2	0	0	0.0297(6)
O(1)	0.3227(6)	0.8629(2)	0.1838(5)	0.051(2)
O(2)	0.2508(7)	0.9435(2)	0.0677(5)	0.056(2)
O(3)	0.1078(6)	0.7843(2)	0.4259(4)	0.036(1)
O(4)	−0.0309(7)	0.8513(3)	0.5445(5)	0.060(2)
O(5)	0.1321(6)	0.7461(2)	0.0540(4)	0.040(2)
O(6)	0.0176(7)	0.6763(3)	−0.0751(4)	0.052(2)
O(7)	0.2836(7)	0.6622(2)	0.3362(5)	0.047(2)
O(8)	0.1606(7)	0.5845(2)	0.4348(5)	0.050(2)
O(9)	0.6558(8)	0.9978(3)	0.1925(5)	0.060(2)
O(10)	0.487(1)	0.9519(3)	0.3959(6)	0.102(3)
O(11*A*)*	0.008(2)	0.0455(7)	0.220(1)	0.099(5)**
O(11*B*)*	−0.040(3)	0.072(1)	0.237(2)	0.096(6)**
O(12*A*)*	−0.146(5)	0.998(2)	0.541(4)	0.16(1)**
O(12*B*)*	−0.21(1)	0.966(3)	0.562(8)	0.22(3)**
O(12*C*)*	−0.150(8)	0.990(3)	0.595(6)	0.15(2)**
N(1)	−0.0364(7)	0.8314(2)	0.2131(4)	0.028(2)
N(2)	−0.0531(6)	0.7015(2)	0.2494(4)	0.026(2)
C(1)	0.2104(9)	0.8968(3)	0.1232(6)	0.038(2)
C(2)	0.0089(9)	0.8752(3)	0.1146(6)	0.036(2)
C(3)	0.0065(9)	0.8325(3)	0.4441(6)	0.037(2)
C(4)	−0.061(1)	0.8657(3)	0.3307(6)	0.037(2)
C(5)	−0.2076(8)	0.7962(3)	0.1771(5)	0.029(2)
C(6)	−0.2222(9)	0.7400(3)	0.2537(6)	0.033(2)
C(7)	0.0398(8)	0.6976(3)	0.0280(5)	0.035(2)
C(8)	−0.0470(9)	0.6650(3)	0.1356(5)	0.035(2)
C(9)	0.147(1)	0.6327(3)	0.3771(6)	0.038(2)
C(10)	−0.0454(9)	0.6597(3)	0.3566(5)	0.032(2)
H(1)	0.580	0.980	0.260	0.08**
H(2)	0.772	0.999	0.193	0.08**
		II		
Bi(1*A*)	0.20446(5)	0.29882(3)	0.17341(4)	0.0172(2)
Bi(1*B*)	0.35575(6)	0.16782(3)	−0.12337(4)	0.0191(2)
Ba(1)	0.7552(1)	0.25903(6)	0.00844(7)	0.0270(3)
O(1*A*)	0.179(1)	0.1714(5)	0.3286(7)	0.022(3)
O(2*A*)	0.270(1)	0.1037(7)	0.4657(9)	0.051(5)
O(3*A*)	0.471(1)	0.3458(5)	0.1090(7)	0.023(3)
O(4*A*)	0.660(1)	0.4485(6)	0.1115(7)	0.026(4)
O(5*A*)	−0.052(1)	0.2603(7)	0.1476(8)	0.034(4)
O(6*A*)	−0.298(1)	0.2095(6)	0.2316(7)	0.030(4)
O(7*A*)	0.167(1)	0.4782(6)	0.1225(7)	0.028(4)
O(8*A*)	0.005(1)	0.6030(7)	0.0898(8)	0.042(4)

Table 2. (Contd.)

Atom	*x*/*a*	*y*/*b*	*z*/*c*	U_{eq}, Å^2
O(1*B*)	0.595(1)	0.2551(6)	−0.1328(7)	0.027(4)
O(2*B*)	0.836(1)	0.3046(8)	−0.2302(9)	0.049(5)
O(3*B*)	0.420(1)	−0.0254(6)	−0.0933(8)	0.036(4)
O(4*B*)	0.606(1)	−0.1408(7)	−0.0910(8)	0.037(4)
O(5*B*)	0.3600(9)	0.3051(5)	−0.2610(7)	0.019(3)
O(6*B*)	0.284(1)	0.3760(7)	−0.3992(8)	0.041(4)
O(7*B*)	0.076(1)	0.1654(6)	−0.0727(7)	0.027(4)
O(8*B*)	−0.129(1)	0.0796(6)	−0.0703(7)	0.025(3)
O(1)	0.251(1)	0.3364(6)	−0.0387(7)	0.029(4)
O(2)*	0.597(3)	0.422(2)	0.484(2)	0.07(1)
O(3)*	0.987(4)	0.038(3)	0.580(3)	0.12(2)
N(1*A*)	0.297(1)	0.3731(7)	0.2996(8)	0.021(4)
N(2*A*)	−0.024(1)	0.3575(7)	0.2994(9)	0.024(4)
N(1*B*)	0.573(1)	0.1195(8)	−0.2653(9)	0.028(4)
N(2*B*)	0.242(1)	0.1089(7)	−0.2454(8)	0.019(4)
C(1*A*)	0.251(2)	0.179(1)	0.391(1)	0.040(6)
C(2*A*)	0.356(1)	0.2813(8)	0.368(1)	0.021(5)
C(3*A*)	0.525(1)	0.4160(9)	0.149(1)	0.022(5)
C(4*A*)	0.422(1)	0.4533(9)	0.245(1)	0.023(5)
C(5*A*)	0.161(2)	0.4351(9)	0.367(1)	0.034(6)
C(6*A*)	0.014(2)	0.3685(9)	0.393(1)	0.028(5)
C(7*A*)	−0.166(2)	0.247(1)	0.228(1)	0.030(6)
C(8*A*)	−0.154(2)	0.2757(9)	0.325(1)	0.027(5)
C(9*A*)	0.035(2)	0.5168(9)	0.149(1)	0.033(6)
C(10*A*)	−0.081(2)	0.467(1)	0.243(1)	0.041(7)
C(1*B*)	0.707(1)	0.2580(9)	−0.220(1)	0.020(5)
C(2*B*)	0.686(1)	0.2128(8)	−0.306(1)	0.023(5)
C(3*B*)	0.544(1)	−0.0526(9)	−0.127(1)	0.027(6)
C(4*B*)	0.656(2)	0.0279(8)	−0.215(1)	0.027(5)
C(5*B*)	0.524(2)	0.0997(8)	−0.355(1)	0.028(5)
C(6*B*)	0.360(2)	0.0390(9)	−0.313(1)	0.028(5)
C(7*B*)	0.297(2)	0.3021(9)	−0.329(1)	0.027(5)
C(8*B*)	0.190(2)	0.1998(8)	−0.315(1)	0.022(5)
C(9*B*)	0.004(2)	0.0921(9)	−0.102(1)	0.027(5)
C(10*B*)	0.111(1)	0.0407(8)	−0.186(1)	0.022(5)
H(1)	0.316	0.387	−0.066	0.08**
H(2)	0.167	0.358	−0.053	0.08**

* In compound **I**, the site occupancies of the O(11*A*), O(11*B*), O(12*A*), O(12*B*), and O(13*C*) atoms are 0.58(1), 0.42(1), 0.44(2), 0.26(2), and 0.28(2), respectively; in compound **II**, the O(1) and O(2) sites are occupied by 0.50(1).

** The values of U_{iso} are given.

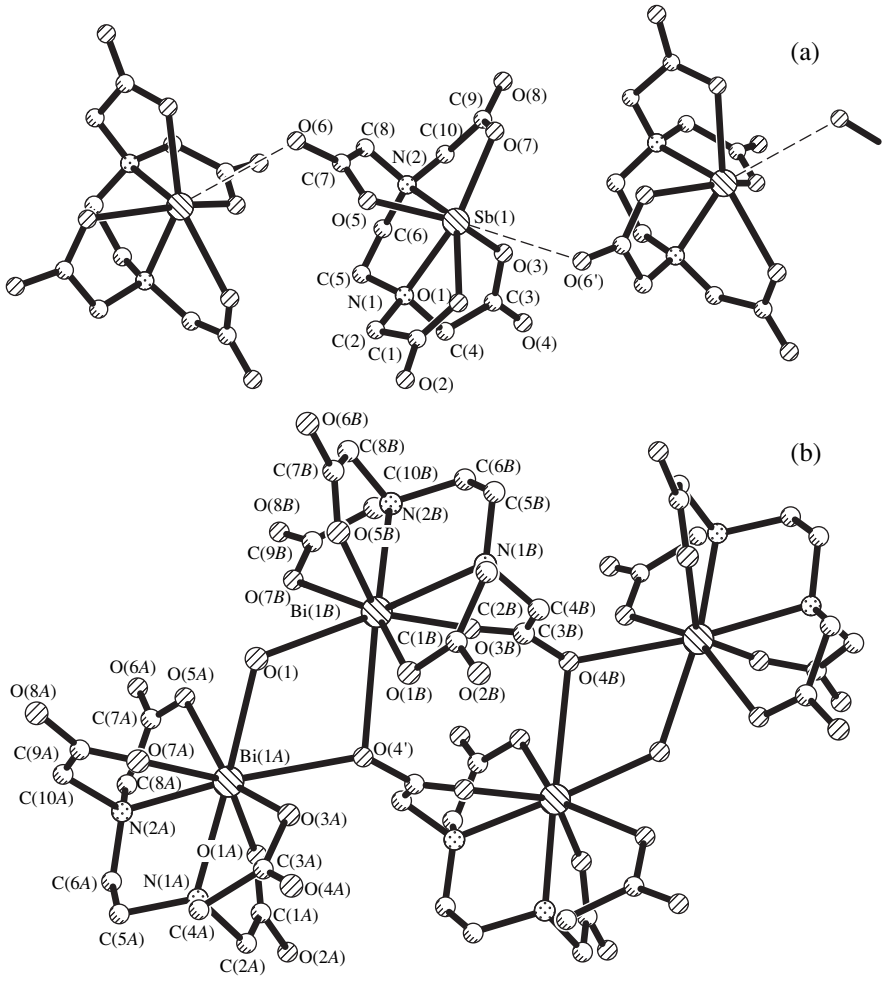

Fig. 1. Structure of (a) the $[Sb(Edta)]^-$ anionic complex in $Ca[Sb(Edta)]_2 \cdot 8H_2O$ and (b) $\{[Ba(Edta)]_2H_2O\}_2^{4-}$ tetranuclear associate in $Ba\{[Bi(Edta)]_2H_2O\} \cdot H_2O$.

drate (Fig. 2b) is 5 + 3; that is, the lone electron pair exhibits a partial stereochemical activity.

In the centrosymmetric binuclear complex $[Sb_2(\mu\text{-}Ttha)(H_2O)_2]$ [15] (where H_6Ttha is triethylenetetraaminehexaacetic acid), the polyhedron is best of all approximated by a ψ-octahedron. According to the description of the antimony polyhedron given in [15], the oxygen atom of the water molecule is included in the first coordination sphere (the Sb–O distance is 2.94 Å), and the polyhedron is considered as a ψ-pentagonal bipyramid; however, the mean atomic deviation from the rms plane of this base is 0.37 Å.

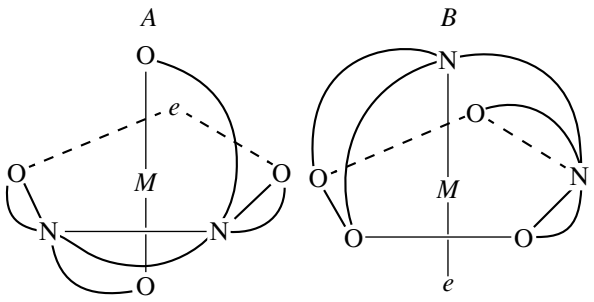

Fig. 2. Schematic drawing of the ψ-pentagonal bipyramid with two different positions of the lone electron pair (*e*): (*A*) in the equatorial plane and (*B*) at the axial position.

Considering the shapes of the polyhedra in the compounds mentioned above, we come across the problem of assigning the ligands to the first and second coordination spheres. The ranges of the Sb–O and Sb–N distances in the compounds discussed are 2.02–3.25 and 2.25–2.78 Å, respectively. It is reasonable to assign both the oxygen atoms of the protonated carboxyl groups in $[Sb(HEdta)] \cdot 2H_2O$ and $[Sb(HPdta)]$ and the oxygen atoms of the alcohol groups in $[Sb(HEdtra)]$ to the first coordination sphere, since their consideration, within good accuracy, results in reasonable polyhedra. The atoms, which are separated from the antimony atom by more than 3 Å, and also (in our opinion) the

oxygen atom of water molecule in the $[Sb_2(\mu\text{-}Ttha)(H_2O)_2]$ complex should be assigned to the second coordination sphere.

Division of the metal–ligand bond lengths into two ranges in the $[Sb(H_2Dtpa)] \cdot 2H_2O$ compound is rather arbitrary, even though it adequately reflects the structure of the complex.

Note a considerable nonequivalence of the Sb–N bond lengths in diamine ligands of the *A* and *B* structural types: the mean differences in lengths of two bonds are 0.05 and 0.23 Å, respectively. This clearly illustrates the different stereochemical behavior of two nitrogen atoms in the *B*-type complexes and the change from the proper symmetry *m* (*B* type, Fig. 4a) to the proper symmetry 2 (*A* type, Fig. 4b). A substantial difference in the structures of the pentagonal–bipyramidal complexes with the lone electron pair at the equatorial and axial positions is also observed in the bulk occupied by the lone electron pair. In the complexes with the *B*-type structure, we can draw a plane in such a way that all the coordinating atoms of the ligand appear on the same side of this plane (Fig. 4a), whereas, in the *A*-type complexes, the sector free of donor atoms is smaller (Fig. 4b). The *m* symmetry is retained in the $[Sb(H_2Dtpa) \cdot nH_2O$ compounds, where $n = 0$ or 1 (it is clear that the replacement of the ligand results in the changes in metal coordination), in which the lone electron pair is in the axial position in the ψ-pentagonal bipyramid; it is the proper symmetry of the complex in the monohydrate and the crystallographic symmetry in the anhydrous compound.

Thus, among the thirteen antimony(III) complexes (twelve compounds), four structural types of polyhedra are observed (without regard for distinctions in the second coordination sphere). In the twelve compounds, the lone electron pair is stereochemically active, and, only in one compound, namely, $([Sb(H_2Dtpa)] \cdot 2H_2O)$, the lone electron pair exhibits a partial stereochemical activity.

It can be expected that the antimony(III) compounds are most similar in the behavior of lone electron pair to the Sn(II) complexes. The structures of two Sn(II) aminocarboxylates are known: $Sn[Sn(Edta)] \cdot 2H_2O$ [16] and $[Sn(H_2Edta)]$ [17]. In the former compound, the polyhedron of the complex-forming lead atom has the shape of a ψ-pentagonal bipyramid with the lone electron pair in the equatorial plane. The lead polyhedron in the latter complex is a severely distorted ψ-single-capped trigonal prism (with the lone electron pair as a cap). Hence, we meet one more type of metal coordination, which has not been found for the antimony chelates.

It is known [18, 19] that the stereochemical activity of the lone electron pair decreases within the group from the top down [in our case, from Sb(III) to Bi(III)]. Bismuth aminocarboxylates confirm this thesis: none of the eighteen complexes characterized structurally

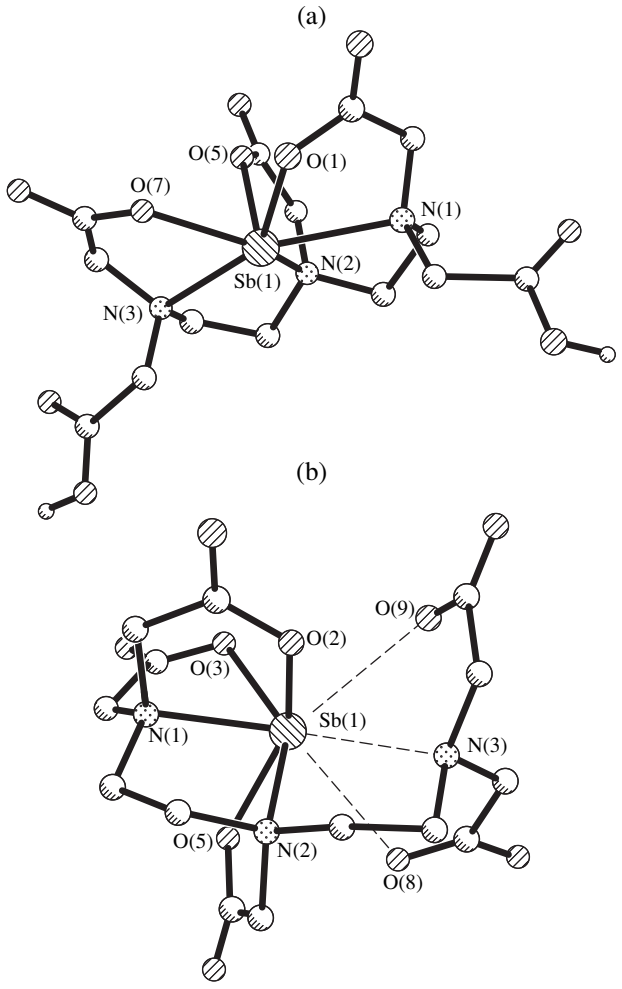

Fig. 3. Structure of the $[Sb(H_2Dtpa)]$ complex in (a) $[Sb(H_2Dtpa)] \cdot H_2O$ and (b) $[Sb(H_2Dtpa) \cdot 2H_2O$.

(seventeen compounds) [20–31] exhibits the stereochemical activity of the lone electron pair.

In some compounds, for example $[(NH_4)_3[Bi(Nta)_2]$ [21] and $[Bi(HEdta)]_n$ [25], the spread of bond lengths in the bismuth polyhedron is minimum (0.20 and 0.22 Å); that is, the lone electron pair is completely delocalized around the complex-forming atom (in the terms accepted in [1, p. 179], the lone electron pair occupies the *s*-type orbital). However, the Bi–O bond lengths are unequal in many complexes. In all the compounds, the longest Bi–O distances correspond to the bonds either with the coordination water molecules or with the bridging oxygen atoms of neighboring ligands. The only exception is provided by $[Bi(HEdta)]_n \cdot 2nH_2O$ [26], in which one of the longest bonds is formed by the carbonyl oxygen atom of the protonated carboxyl group. The distribution of Bi–L bond lengths is commonly characterized by the difference (~0.2 Å) between the "short" and "long" bonds, whereas the spread of the "short" bonds is 0.1–0.3 Å. Hence, the

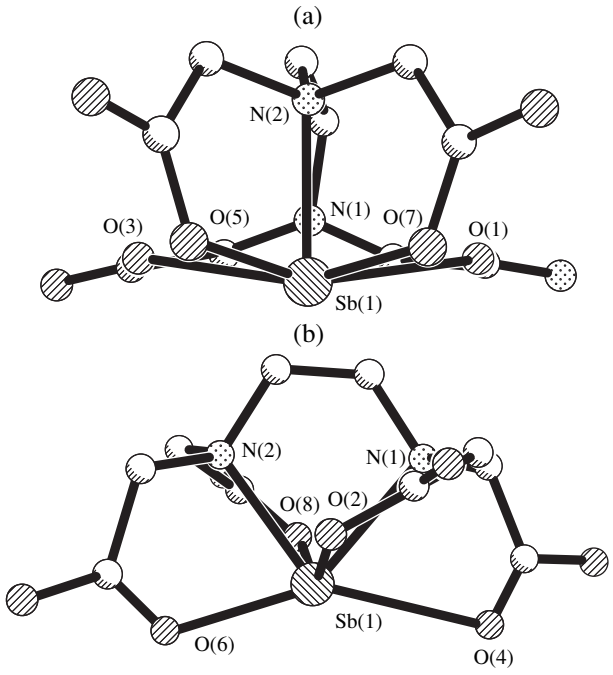

Fig. 4. Structure of the $[Sb(Edta)]^-$ anionic complex in (a) $\{C(NH_2)_3\}[Sb(Edta)] \cdot 2H_2O$ and (b) $Na[Sb(Edta)] \cdot 3H_2O$.

first and second coordination spheres are indistinguishable. We note a wide spread of Bi–O bond lengths in compounds $[C(NH_2)_3\}_2[Bi(Heida)(Heida–H)] \cdot 3H_2O$ [20], $[Ca(H_2O)_7][Bi(Edta)]_2 \cdot H_2O$ [28], and $Ba\{[Bi(Edta)]_2H_2O\} \cdot H_2O$ (complex *B*); it is 0.71, 0.68, and 0.71 Å, respectively.

Now, we dwell on the coordination number of bismuth; it is eight in fifteen compounds and nine in three compounds. The coordination number of a metal normally increases with the potential coordination capacity of ligands, so that the coordination number of nine in bismuth diethylenetriaminepentaacetates is not surprising: the relatively compact ligand pulls together its donor sites, thus allowing the penetration of an additional ligand.

We do not consider the shapes of coordination polyhedra of the bismuth atom, because adequate description of the polyhedra with widely differing metal–ligand bond lengths is ambiguous.

By and large, the structural variety of antimony complexes is greater than that of similar bismuth compounds. Based on the data discussed in this paper and those on other compounds of trivalent antimony and bismuth [32, 33], we expect the existence of antimony complexes with a lower stereochemical activity of the lone electron pair. On the other hand, there is reason to hope that bismuth aminocarboxylates with a greater degree of the lone electron pair localization will be synthesized.

REFERENCES

1. R. J. Gillespie and I. Hargittai, *The VSEPR Model of Molecular Geometry* (Allyn and Bacon, Boston, 1990; Mir, Moscow, 1992), pp. 79, 163, 179.
2. G. M. Sheldrick, Acta Crystallogr., Sect. A: Found. Crystallogr. **46** (6), 467 (1990).
3. G. M. Sheldrick, *SHELX76: Program for Crystal Structure Determination* (Univ. of Cambridge, Cambridge, 1976).
4. M. Shimoi, Y. Orita, T. Uehiro, *et al.*, Bull. Chem. Soc. Jpn. **53**, 3189 (1980).
5. Xie Zhao-Xiong and Hu Sheng-Zhi, Jiegou Huaxue (J. Struct. Chem.) **10** (2), 129 (1991).
6. V. É. Mastryukov, A. V. Sergeev, Yu. N. Mikhaĭlov, *et al.*, Koord. Khim. **13** (8), 1129 (1987).
7. Hu Sheng-Zhi and Lin Wen-Feng, Jiegou Huaxue (J. Struct. Chem.) **8** (4), 249 (1989).
8. Hu Sheng-Zhi, Tu Lian-Dong, Huang You-Qing, *et al.*, Inorg. Chim. Acta **232**, 161 (1995).
9. Gu Da, Zhou Hengnan, and Lu Yun-Jin, Yinyong Huaxue (Chin. J. Appl. Chem.) **10** (2), 63 (1993).
10. T. N. Polynova and M. A. Poraĭ-Koshits, Itogi Nauki Tekh., Ser.: Kristallokhim. **18,** 64 (1984).
11. A. B. Ilyukhin, M. A. Malyarik, S. P. Petrosyants, *et al.*, Zh. Neorg. Khim. **40** (7), 1125 (1995) [Russ. J. Inorg. Chem. **40** (7), 1083 (1995)].
12. Gu Da, Lu Bin, and Lu Yun-Jin, Jiegou Huaxue (J. Struct. Chem.) **8** (4), 311 (1989).
13. L. M. Shkol'nikova, V. S. Fundamenskiĭ, R. L. Davidovich, *et al.*, Zh. Neorg. Khim. **36** (8), 2042 (1991).
14. Zhou Heng-Nan and Lu Yun-Jin, Jiegou Huaxue (J. Struct. Chem.) **12** (3), 233 (1993).
15. Hu Sheng-Zhi and Xie Zhao-Xiong, Jiegou Huaxue (J. Struct. Chem.) **10** (1), 81 (1991).
16. F. P. van Remoortere, J. J. Flynn, F. P. Boer, *et al.*, Inorg. Chem. **10** (7), 1511 (1971).
17. K. G. Shields, R. C. Seccombe, and C. H. L. Kennard, J. Chem. Soc., Dalton Trans., 741 (1973).
18. G. Galy and G. Meunier, J. Solid State Chem. **13** (2), 142 (1975).
19. G. Galy and R. Enjalbert, J. Solid State Chem. **44** (1), 1 (1982).
20. You-Qing Huang, Sheng-Zhi Hu, L. M. Shkol'nikova, *et al.*, Koord. Khim. **21** (12), 891 (1995) [Russ. J. Coord. Chem. **21** (12), 853 (1995)].
21. K. D. Suyarov, L. M. Shkol'nikova, M. A. Poraĭ-Koshits, *et al.*, Dokl. Akad. Nauk SSSR **311** (6), 1397 (1990).
22. K. D. Suyarov, L. M. Shkol'nikova, R. L. Davidovich, *et al.*, Koord. Khim. **17** (4), 455 (1991).
23. Z. A. Starikova, T. F. Sysoeva, S.S. Makarevich, *et al.*, Koord. Khim. **17** (3), 317 (1991).
24. R. N. Shchelokov, Yu. N. Mikhaĭlov, V. É. Mistryukov, *et al.*, Dokl. Akad. Nauk SSSR **293** (3), 642 (1987).
25. L. M. Shkol'nikova, K. D. Suyarov, R. L. Davidovich, *et al.*, Koord. Khim. **17** (2), 253 (1991).
26. L. M. Shkol'nikova, M. A. Poraĭ-Koshits, R. L. Davidovich, *et al.*, Koord. Khim. **20** (8), 593 (1994) [Russ. J. Coord. Chem. **20** (8), 559 (1994)].

27. M. A. Poraĭ-Koshits, A. S. Antsyshkina, L. M. Shkol'nikova, *et al.*, Koord. Khim. **21** (4), 311 (1995) [Russ. J. Coord. Chem. **21** (4), 295 (1995)].
28. L. M. Shkol'nikova, M. A. Poraĭ-Koshits, and A. L. Poznyak, Koord. Khim. **19** (9), 683 (1993) [Russ. J. Coord. Chem. **19** (9), 634 (1993)].
29. L. M. Shkol'nikova, M. A. Poraĭ-Koshits, R. L. Davidovich, *et al.*, Koord. Khim. **19** (8), 633 (1993) [Russ. J. Coord. Chem. **19** (8), 588 (1993)].
30. A. B. Ilyukhin, L. M. Shkol'nikova, R. L. Davidovich, *et al.*, Koord. Khim. **17** (7), 903 (1991).
31. S. P. Summers, K. A. Abboud, S. R. Farrah, *et al.*, Inorg. Chem. **33** (1), 88 (1994).
32. Yu. N. Mikhaĭlov and A. S. Kanishcheva, in *Problems of Crystal Chemistry*, Ed. by M. A. Poraĭ-Koshits (Nauka, Moscow, 1985), pp. 70–121.
33. L. M. Volkova and A. A. Udovenko, in *Problems of Crystal Chemistry*, Ed. by M. A. Poraĭ-Koshits (Nauka, Moscow, 1987), pp. 46–80.

Translated by I. Polyakova

Crystallography Reports, Vol. 45, No. 1, 2000, pp. 6–9. Translated from Kristallografiya, Vol. 45, No. 1, 2000, pp. 12–15.

Termination Effect in X-ray Diffraction Studies of Disordered Systems

V. P. Kazimirov, S. Yu. Smyk, and V. É. Sokol'skiĭ

Kiev State University, ul. Glushkova 6, Kiev, 252127 Ukraine

Received September 8, 1997; in final form, March 18, 1998

Abstract—The effect of termination on the structural parameters of the radial distribution function of atoms has been analyzed with the use of the structure factor calculated for the model of soft spheres. It is shown that in the range of the experimentally attainable magnitudes of the diffraction vector s_{max}, the position R_1 and the area Z_1^{sym} of the first maximum of the radial distribution function of atoms linearly depends on $1/s_{max}$. The method is suggested for taking into account the effect of termination on the structure parameters. © *2000 MAIK "Nauka/Interperiodica".*

The termination effect in diffraction studies of disordered materials is caused by the limitation imposed on the reciprocal space because of a finite wavelength of the radiation used. The radial distribution function (RDF) of atoms with the errors caused by the effect of termination (termination errors) shown in Fig. 1 is an oscillating curve with the maximum amplitude being in the vicinity of the first maximum and affecting both its position and shape. Thus, since the position of the first maximum determines the most probable closest distance between the atoms in the melt, R_1, whereas its area determines the coordination number, Z_1, used in the model interpretation of the structures of disordered materials [1], the termination effect should necessarily be taken into account.

All the known methods allowing for the termination effect can conditionally be divided into two groups: (1) the use of a factor of the type $\exp(-bs^2)$ or the Lanczos's σ-factor [2, 3] in the Fourier transform of the radial distribution function and (2) the representation of the experimental scattering factor as an expansion into a series with respect to the system of orthogonal functions with its subsequent extrapolation to the region $s > s_{max}$ (where s is the diffraction vector) [2, 4, 5].

These methods are successfully used in the method of small-angle scattering. However, they are almost neglected in the diffraction studies of disordered systems over a wide range of scattering angles. The only exception is the introduction of a temperature factor, which, unfortunately, reduces the RDF resolution, especially in the vicinity of the first maximum and, thus, also distorts the extracted information. The second approach seems to be more attractive, but the presence of various errors in the experimental curve does not allow the reliable extrapolation of the scattering curve beyond the range of experimentally measurable scattering angles.

The most reliable and detailed studies of this problem for disordered systems were performed in [6–8], where various methods for taking into account the termination effect for the RDF were suggested. Thus, Hosemann *et al.* [6] derived the following relationship:

$$L_{1/2,\,exp}^2 = L_{1/2}^2 + (\pi/s_{max})^2, \qquad (1)$$

where $L_{1/2,\,exp}$ and $L_{1/2}$ are the halfwidths of the first maximum of the function $Rg(R)$ obtained experimentally and calculated theoretically with due regard for

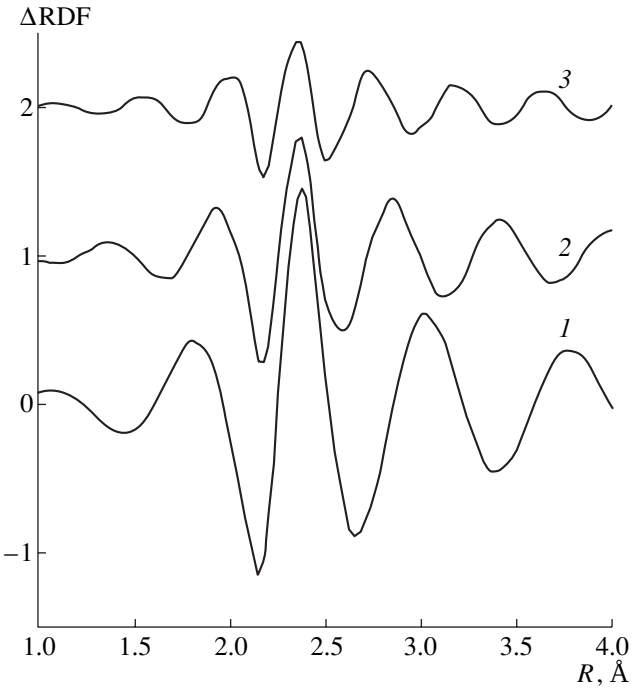

Fig. 1. The error in the RDF caused by the termination effect at three values of s_{max}: (*1*) 9.7, (*2*) 12.5, (*3*) 18.0 Å^{-1}.

1063-7745/00/4501-0006$20.00 © 2000 MAIK "Nauka/Interperiodica"

the termination effect, respectively, and s_{max} is the maximum experimental magnitude of the diffraction vector. Equation (1) allows one to take into account the dependence of the half-width of the first RDF maximum on s_{max} and to correct the coordination number appropriately. A similar equation but with a somewhat different angular coefficient was suggested and successfully tested in an electron diffraction study of amorphous films [7]. An original approach suggested in [8] seems to lead to the somewhat ambiguous restoration of the intensity curve in the region $s > s_{max}$. It should be noted that the recommendations given in [6, 7] are reduced mainly to the allowance for the effect of termination on the coordination number Z_1^{sym} determined by the symmetric resolution of the first RDF maximum.

Unfortunately, the aforementioned results have found no application in X-ray diffraction studies of disordered systems, which, we believe, is associated with an insufficiently developed theory of this problem. Thus, the dependence of R_1 on s_{max} has not been studied at all; there are no recommendations for taking into account the termination effect in disordered materials. Most researchers are interested, first of all, in answering the question at which s_{max}-value the termination error in the Z_1 and R_1 would not exceed the total experimental error. The answer to this question can be obtained from analysis of the structural parameters of the RDF calculated from the structure-factor curve at various values of s_{max} and of the dependences of R_1, Z_1^{sym}, and $L_{1/2}$ on s_{max}. Such a study can be successfully performed with the use of the model structure factor containing no experimental errors and readily calculated for any s_{max}-value.

In the present study, we used the model of soft spheres in the Hoshino modification [9], which is more advantageous than the model of hard spheres because the "softness" of the interparticle potential provides considerable damping of far oscillations, thus making the model structure factor closer to the real one at large scattering angles. To solve the above formulated problem, calculate the RDF in the form

$$4\pi R^2\rho(R) = 4\pi R^2\rho_0 + \frac{2R}{\pi}\int_0^\infty s[a(s)-1]\sin(sR)ds$$

$$= 4\pi R^2\rho_0 + \frac{2R}{\pi}\int_0^{s_{max}} s[a(s)-1]\sin(sR)ds \qquad (2)$$

$$+ \frac{2R}{\pi}\int_{s_{max}}^\infty s[a(s)-1]\sin(sR)ds,$$

where $\rho(R)$ is the atomic-density function, ρ_0 is the macroscopic density of the specimen, $s = 4\pi\sin\theta/\lambda$ is the magnitude of the diffraction vector, λ is the radiation wavelength, and $a(s)$ is the structure factor. Two first terms in (2) determine the RDF at the finite s_{max} value, whereas the third term determines the error caused by the termination effect whose form at different s_{max}-values is shown in Fig. 1. It is well known that the structure factor of melts is characterized by different degrees of oscillation damping with an increase in s, which is associated with a different character of atomic disordering. Thus, the termination effect for liquid germanium and iron differently affects the structural parameters obtained at the same s_{max}. In our model, this fact is taken into account by the introduction of a special coefficient of packing density, η, which determines the height (amplitude), $a(s_1)$, of the first maximum of the structure factor and, thus, also the amplitudes of far oscillations. Therefore, we used three

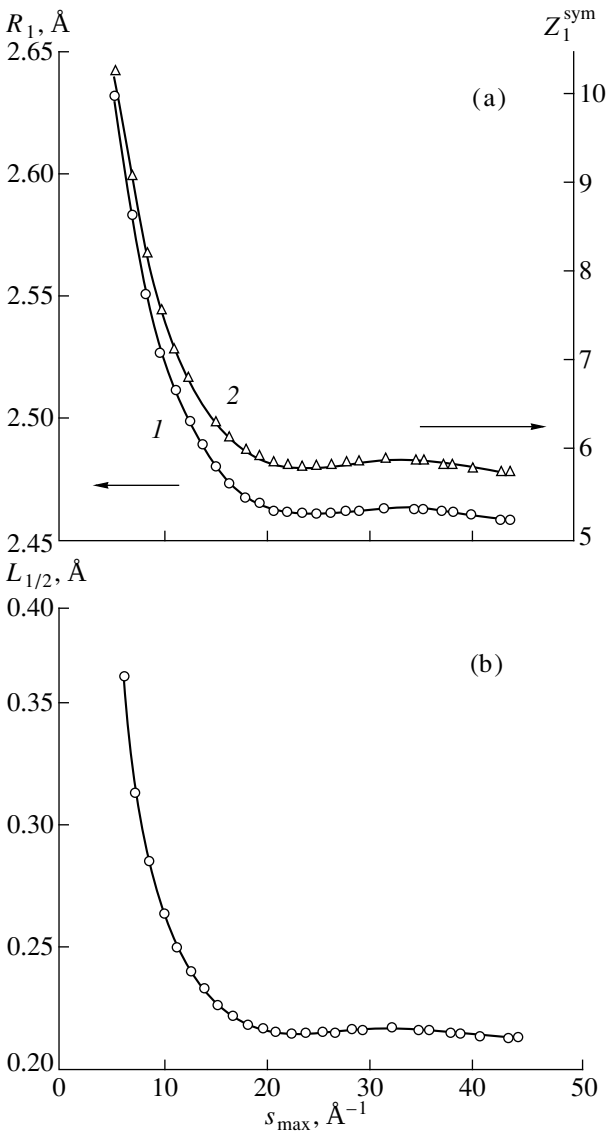

Fig. 2. Dependences of (a) (*1*) R_1 and (*2*) Z_1^{sym} and (b) $L_{1/2}$ on s_{max} for the structure factor with the amplitude $a(s_1)$ = 2.56.

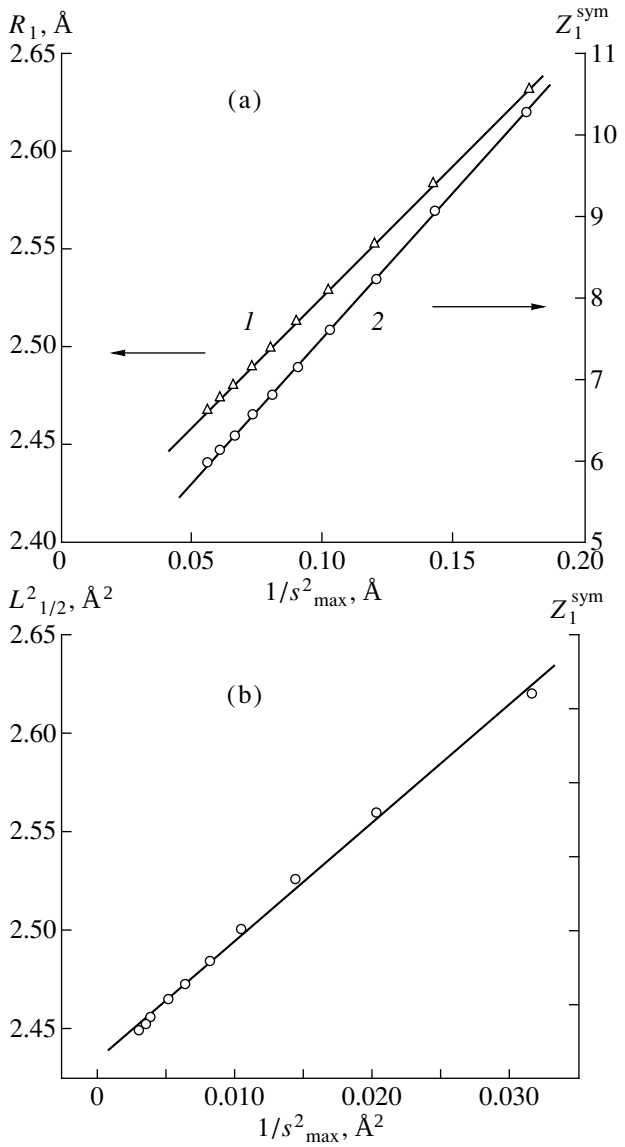

Fig. 3. (a) Dependences of (*1*) R_1 and (*2*) Z_1^{sym} on $1/s_{max}$ and (b) $L^2_{1/2}$ on $1/s^2_{max}$ for the structure factor with the amplitude $a(s_1) = 2.56$.

structure factors with different heights of the first maxima, namely, $a(s_1) = 2.11$, 2.56, and 3.17. The normalization coefficient of the structure factor was checked for each s_{max}-value.

The dependences of the position R_1, the area Z_1^{sym}, and the halfwidth $L_{1/2}$ of the first RDF maximum described by the Gaussian function of s_{max} are shown in Fig. 2 for the structure factor of the height $a(s_1) = 2.56$. It is seen that in all cases, the limiting values of all the parameters with due regard for the determination error [10] are attained at $s_{max} \cong 17$ Å^{-1}. In the region $s_{max} < 17$ Å^{-1}, the values of the structure parameters R_1

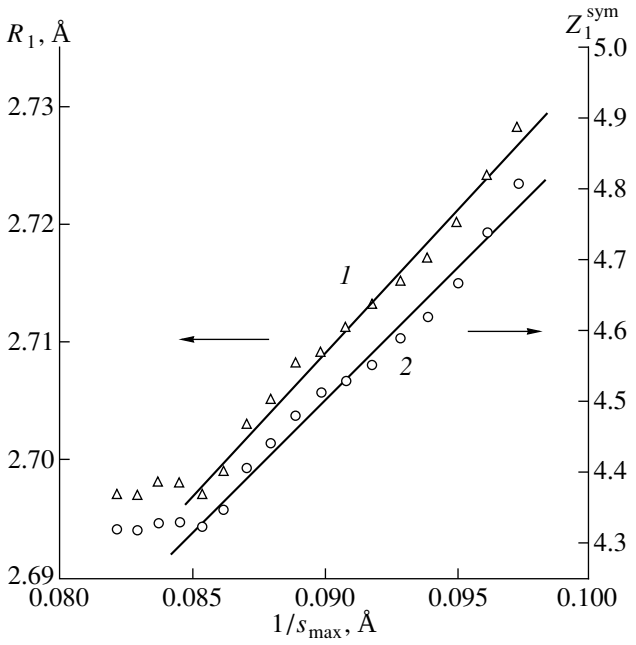

Fig. 4. Dependences of (*1*) R_1 and (*2*) Z_1^{sym} on $1/s_{max}$ for liquid germanium at 1253 K.

and Z_1^{sym} are described by the corresponding linear dependence on $1/s_{max}$ with the correlation coefficient exceeding 0.999 (Fig. 3a). The $L_{1/2}$ values in this region of the diffraction vector are described by an equation of type (1) (Fig. 3b). The limiting values of the structure parameters in the region $s_{max} > 17$ Å^{-1} are explained by small oscillations of the structure factor in this region, so that neglecting these oscillations almost does not affect the structural parameters. For the structure factors with $a(s_1) = 2.11$ and 3.17, the limiting values of the structural parameters are attained in the regions ~14 and ~26 Å^{-1}, respectively. The latter fact was confirmed experimentally. For example, amorphous alloys based on the 3*d*-transition metals (Fe–B, Pd–Si, etc.) are characterized by a considerable height (exceeding 3) of the first maximum of the structure factor [11]. Therefore, the diffraction study of such alloys should necessarily be performed up to high s_{max}-values, which can be attained in a time-of-flight neutron diffraction experiment.

The linear dependence of R_1 and Z_1^{sym} on $1/s_{max}$ can be used for introducing the correction for the termination effect into the experimental values of the structural parameters obtained from the RDF at low s_{max}-values. With this aim, one has to construct the dependences of R_1 and Z_1^{sym} on $1/s_{max}$ in the attainable region of scattering angles and then to extrapolate the obtained lines to the corresponding s_{max}-value in order to determine the refined structural parameters. The $L^2_{1/2}$ value is refined

in the similar way by constructing the $1/s_{max}^2$ dependence. This method was successfully tested on liquid Ge (Fig. 4). Taking into account that in this case, $a(s_1) = 1.60$, the limiting values of the structural parameters independent of s_{max} are attained at $s_{max} \cong 12.5$ Å^{-1}, the value that can be attained in the X-ray diffraction experiment with the use of the MoKα-radiation.

Concluding the article, emphasize once again that the values of the structural parameters corrected for the termination effect are obtained by extrapolating the experimental data to a certain s_{max}-value determined in each concrete case from the degree of damping of structure-factor oscillations. The role of the criterion of the degree of oscillation damping can be played by the height of the first maximum of the structure factor.

ACKNOWLEDGMENTS

This study was supported by the ISSEP, grant no. PSU063101.

REFERENCES

1. A. V. Romanova and A. G. Il'inskiĭ, Ukr. Fiz. Zh. (Russ. Ed.) **19**, 1565 (1974).
2. D. I. Svergun and L. A. Feĭgin, *X-ray and Neutron Small-Angle Scattering* (Nauka, Moscow, 1986).
3. B. H. Toby and T. Egami, Acta Crystallogr., Sect. A: Found. Crystallogr. **48**, 336 (1992).
4. A. S. Krylov and B. M. Shchedrin, Kristallografiya **34** (5), 1088 (1989).
5. M. B. Kozin and D. I. Svergun, Kristallografiya **41** (5), 817 (1996) [Crystallogr. Rep. **41** (5), 775 (1996)].
6. R. Hosemann, K. Lemm, and H. Krebs, Z. Phys. Chem. (Munich) **41**, 121 (1964).
7. O. I. Andrievskiĭ, Ya. D. Nabitovich, Ya. I. Stetsiv *et al.*, Ukr. Fiz. Zh. (Russ. Ed.) **13**, 1596 (1968).
8. R. Kaplow, S. L. Strong, and R. L. Averbach, Phys. Rev. A **138**, 1336 (1965).
9. R. Hoshino, J. Phys. C: Solid State Phys. **13**, 3097 (1980).
10. V. P. Kazimirov, S. Yu. Smyk, V. É. Sokol'skiĭ *et al.*, Kristallografiya **41** (6), 971 (1996) [Crystallography Rep. **41** (6), 921 (1996)].
11. Y. Waseda, Prog. Mater. Sci. **26**, 1 (1981).

Translated by L. Man

Crystallography Reports, Vol. 45, No. 1, 2000, pp. 64–70. Translated from Kristallografiya, Vol. 45, No. 1, 2000, pp. 69–76.

STRUCTURES OF COORDINATION COMPOUNDS

Specific Structural Features of 1-Hydroxyethane-1,1-Diphosphonic Acid (HEDP) and Its Salts with Organic and Alkali-metal Cations

V. S. Sergienko

Kurnakov Institute of General and Inorganic Chemistry, Russian Academy of Sciences, Leninskiĭ pr. 31, Moscow, 117907 Russia

Received April 13, 1998

Abstract—Specific structural features of 1-hydroxyethane-1,1-diphosphonic acid (HEDP, H_4L) and its ten salts with organic and alkali-metal cations are discussed. The following problems are addressed: (1) the dependence of the P–O bond lengths on whether the oxygen atom is protonated or not and on the total charge of the H_nL^{n-4} anion; (2) the variants of the statistical distribution of the shared protons; (3) the modes of connection of the H_nL^{n-4} anions by hydrogen bonds into dimers or polymeric chains; (4) coordination modes of polydentate H_nL^{n-4} ligands in the salts of alkali-metal cations. © *2000 MAIK "Nauka/Interperiodica".*

INTRODUCTION

A number of 1,1-diphosphonic acids $H_2O_3P–CR(R')–PO_3H_2$ differing in the nature of the *R* and *R*' substituents are presently known [1]. Among these acids, 1-hydroxyethane-1,1-diphosphonic acid (HEDP; *R* = OH and *R*' = CH_3) is, perhaps, of the greatest interest. Its central carbon atom bears, in addition to two acid phosphonic groups, a hydroxy group, which exhibits basic properties. The combination of these groups makes it possible to classify the H_4L acid with organophosphorus complexones. The combination of acid and basic functional groups in H_4L determines its specific properties and its pronounced ability to form complexes with different metals, from alkali metals to rare-earth elements.

A great number of different metal complexes and salts with organic cations formed by 1-hydroxyethane-1,1-diphosphonic acid have been characterized structurally. The compounds of this class show a wide variety of structures: they differ in structural type (oligomerization or polymerization degree), the functions and coordination capacity of the H_nL^{n-4} ligand, the type of geometric isomer of the complex, etc.

Earlier [2], we discussed the specific features of the crystal structures of the oxo complexes of Mo(VI) and W(VI) with HEDP. In this review, the structures of the compounds of 1-hydroxyethane-1,1-diphosphonic acid with organic and alkali-metal cations are considered.

STRUCTURE OF 1-HYDROXYETHANE-1,1-DIPHOSPHONIC ACID MONOHYDRATE

In the structure of 1-hydroxyethane-1,1-diphosphonic acid monohydrate $H_4L \cdot H_2O$, where H_4L = $(PO_3H_2)_2COH(CH_3)$ (**I**) [3], separate H_4L molecules (Fig. 1) are linked into columns through hydrogen bonds involving hydroxy COH and phosphonate POH groups. Water molecules, involved in donor and acceptor hydrogen bonds with one another and with H_4L molecules, are also arranged in columns. In structure **I**, we observe a distinct correlation between the P–O(H) bond lengths and the O(H)···O distances in two pairs of hydrogen bonds. Actually, the stronger hydrogen bonds (av. O···O is 2.465 Å) are formed by the shorter P–O(H) bonds (av. 1.539 Å), whereas the relatively weaker hydrogen bonds (av. O···O is 2.615 Å) are formed by the longer P–O(H) bonds (av. 1.555 Å).

The planar O=P–C–P=O fragment has a *cis* configuration (the *W*-like shape). Two phosphonyl atoms O(H) at both P atoms, as well as the OH and CH_3 substituents at the C atom, are situated on either side of the

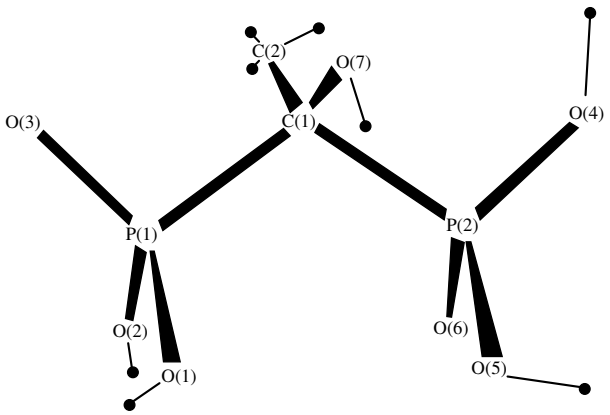

Fig. 1. Molecular structure of H_4L in **I**.

1063-7745/00/4501-0064$20.00

Table 1. Mean P–O distances in the structures of compounds $H_4L \cdot H_2O$ and $A_{4-n}[H_nL] \cdot mH_2O$ (A = H_2Pip, H*Phen*, NH_2Me_2, NH_4, Na, K, Rb, or Cs; n = 2, 2.5, or 3; and m = 0–4)

No.	Compound	$PO_3H_x^{x-2}$ group (x = 1, 1.5, or 2)	Distance, Å			Reference
			P=O	P–OH	P–$OH_{0.5}$	
I	$H_4L \cdot H_2O$	PO_3H_2	1.506(2) ± 0.001	1.547(2) ± 0.012		[3]
II	$(H_2Pip)(H_3L)_2$	PO_3H_2	1.488(1)	1.557(1) ± 0.002		[5]
		PO_3H	1.508(1) ± 0.003	1.572(1)		
III	$(HPhen)(H_3L) \cdot 2H_2O$	PO_3H_2	1.477(2)	1.549(2) ± 0.004		[6]
		PO_3H	1.505(2) ± 0.001	1.566(2)		
IV	$(NH_2Me_2)(H_3L) \cdot H_2O$	PO_3H_2	1.486(2)	1.544(2) ± 0.012		[7]
		PO_3H	1.508(2) ± 0.005	1.583(2)		
V	$(NH_4)(H_3L) \cdot 2H_2O$	$PO_3H_{1.5}$	1.490(2) ± 0.003	1.569(2) ± 0.003	1.525(2) ± 0.005	[8]
VI	$K(H_3L) \cdot 2H_2O$	$PO_3H_{1.5}$	1.490(3) ± 0.003	1.568(3) ± 0.003	1.527(3) ± 0.001	[8]
VIIa*	$Rb(H_3L) \cdot 2H_2O$	$PO_3H_{1.5}$	1.486(6) ± 0.007	1.565(6) ± 0.010	1.526(5) ± 0.003	[9]
VIIb*	$Rb(H_3L) \cdot 2H_2O$	$PO_3H_{1.5}$	1.490(3) ± 0.003	1.563(3) ± 0.009	1.529(3) ± 0.001	[10]
VIIc*	$Rb(H_3L) \cdot 2H_2O$(n)**	$PO_3H_{1.5}$	1.485(3) ± 0.002	1.566(3) ± 0.008	1.524(2) ± 0.003	[11]
VIII	$Cs(H_3L) \cdot 2H_2O$	PO_3H_2	1.497(3)	1.550(3) ± 0.009		[9]
		PO_3H	1.506(3) ± 0.011	1.583(3)		
IXa	$Na(H_3L) \cdot H_2O$	$PO_3H_{1.5}$	1.498(2) ± 0.010	1.561(2) ± 0.008	1.526(2) ± 0.007	[12]
IXb	$Na(H_3L) \cdot H_2O$	$PO_3H_{1.5}$	1.492(4) ± 0.009	1.555(4) ± 0.004	1.520(4) ± 0.007	[13]
X	$(NH_4)_{1.5}(H_{2.5}L) \cdot 2H_2O$	$PO_3H_{1.5}$	1.492(2)	1.555(2)	1.531(2)	[14]
		PO_3H	1.506(2) ± 0.009	1.563(2)		
XI	$Na_2(H_2L) \cdot 4H_2O$	PO_3H	1.505 ± 0.006***	1.580 ± 0.004***		[15]

* Based on the data of three independent studies.

** n denotes a neutron diffraction study.

*** For compound **XI**, the σ(P–O) range is 0.003–0.006 Å, and the individual errors are omitted in [15].

above plane; this minimizes the repulsion between the H(O), H(C), and phosphonic O atoms. Two PO_3 groups in structure **I** have an eclipsed conformation relative to the P–P axis. On the other hand, in the structure of methylene-1,1-diphosphonic acid (H_4MDP, $R = R'$ = H), the PO_3 groups are "skewed," that is, rotated by 35° relative to the P–P axis [4]. In the opinion of the authors in [3], different conformations determine the different acidity of H_4L and H_4MDP in aqueous solutions: the eclipsed conformation of the molecule, which is due to the OH and *Me* substituents attached to the C atom, is responsible for the weaker acidity of H_4L.[1]

STRUCTURES OF THE SALTS OF HEDP WITH ORGANIC AND ALKALI-METAL CATIONS

The following ten compounds of 1-hydroxyethane-1,1-diphosphonic acid with organic and alkali-metal cations have been characterized structurally by now (Table 1, [5–15]): piperazinium, phenanthrolinium, and the dimethylammonium salts $(H_2Pip)(H_3L)_2$ (**II**), $(HPhen)(H_3L) \cdot 2H_2O$ (**III**), and $(NH_2Me_2)(H_3L) \cdot H_2O$ (**IV**); the two ammonium salts $(NH_4)(H_3L) \cdot 2H_2O$ (**V**) and $(NH_4)_{1.5}(H_{2.5}L) \cdot H_2O$ (**X**); three alkali-metal compounds of the general formula $Cat(H_3L) \cdot 2H_2O$, where Cat = K^+ (**VI**), Rb^+ (**VII**), or Cs^+ (**VIII**), which are isostructural to **V**; and the two sodium salts $Na(H_3L) \cdot H_2O$ (**IX**) and $Na_2(H_2L) \cdot 4H_2O$ (**XI**).

The O=P–C–P=O fragments in the H_nL^{n-4} anions of compounds **II**–**XI** are roughly planar and have a typical *W*-like shape, similar to that in the starting acid H_4L (**I**); the O–P–C–P torsion angles range between 170° and 177°. The O(P) atoms at both phosphorus atoms, as well as the OH and CH_3 substituents at the carbon atom, are situated on either side of the plane passing through the above five atoms.

The mean values of the phosphorus–oxygen distances in compounds **I**–**XI** are listed in Table 1.

The P–O distances in the compounds under consideration depend mainly on whether the oxygen atom is protonated or not and on the total charge of the H_nL^{n-4}

[1] It is supposed [3] that in solution, both H_4L and H_4MDP have the same conformations as in the crystal phase.

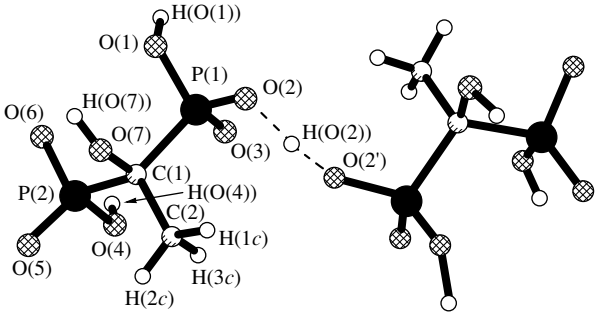

Fig. 2. Dimeric anionic fragment $H_5L_2^{3-}$ of structure **X**.

anion (and, in particular, on the charge of the phosphonic groups $PO_3H_x^{x-2}$).

For compounds **II**–**IX** containing the singly charged H_3L^- anion, two variants of charge distribution are possible. In the first variant, which is observed in compounds **II**–**IV** [5–7], two $PO_3H_x^{x-2}$ groups are inequivalent: one of them (the phosphonate group) is monoprotonated, and the other (the phosphonic group) is biprotonated

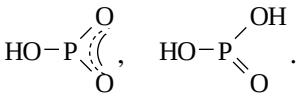

PO_3H^- PO_3H_2

The second variant is observed in structures **V**–**IX** [8–13]: Both $PO_3H_{1.5}^{-0.5}$ groups are equivalent, and each of them contains a protonated oxygen atom and the so-called "half-protonated" oxygen atom $OH_{0.5}$, whose proton is shared by the neighboring anions in a strong O–H···O or O···H···O hydrogen bond.

In compound **X** [14] (Fig. 2), two $PO_3H_x^{x-2}$ groups of the $H_{2.5}L^{1.5-}$ anion are inequivalent and have different formal charges, –0.5 for $PO_3H_{1.5}$ and –1 for PO_3H. Compared to structures **V**–**IX**, in which the anions are linked in pairs through double hydrogen bridges, asymmetric to some degree or another (for details, see below), the anions in **X** are linked into dimers by single nonlinear symmetric hydrogen bridges (the H atom is located at a special position on the twofold axis). In structure **XI** [15], two phosphonic groups PO_3H^- of the H_2L^{2-} anion are equivalent.

It is evident from Table 1 that the P–O distances in the structures considered are divided into three groups: (1) short bonds (1.477–1.508 Å) involving terminal oxygen atoms (P=O or P···O), (2) long bonds (1.543–1.583 Å) involving protonated oxygen atoms (P–OH), and (3) bonds of intermediate length (1.525–1.531 Å) involving bridging half-protonated oxygen atoms (P–$OH_{0.5}$). A more detailed analysis reveals that, within a group, the distances slightly increase with increasing charge of the $PO_3H_x^{x-2}$ group in going from PO_3H_2 through $PO_3H_{1.5}^{-0.5}$ to PO_3H^-. On the whole, the mean phosphorus–oxygen bond lengths in compounds **I**–**XI** decrease in the following sequence:

$$\underset{1.575 \pm 0.012}{\text{P–OH}(PO_3H)} > \underset{1.563 \pm 0.008}{\text{P–OH}(PO_3H_{1.5})} > \underset{1.550 \pm 0.007}{\text{P–OH}(PO_3H_2)}$$

$$> \underset{1.526 \pm 0.006}{\text{P–OH}_{0.5}(PO_3H_{1.5})} > \underset{1.506 \pm 0.002}{\text{P···O}(PO_3H)}$$

$$> \underset{1.490 \pm 0.008}{\text{P=O}(PO_3H_{1.5})} \approx \underset{1.490 \pm 0.016}{\text{P=O}(PO_3H_2)}.$$

We should keep in mind that the understanding of the formal charge of a $PO_3H_x^{x-2}$ group is conventional, since hydrogen atoms are, as a rule, located by X-ray diffraction with poor accuracy. Moreover, the symmetric position of the bridging H atom between two phosphonic groups of neighboring H_nL^{n-4} anions (or of the same anion, as in the complexes of transition metals with HEDP) often results from averaging two equally probable hydrogen positions at two PO_3 groups. The disordering of two protons H[O(2)] and H[O(5)] (two equally probable positions for each proton) in different $PO_3H_x^{x-2}$ groups of the same anion is observed in structures **V** and **VI** (Fig. 3).

A more or less asymmetric position of the bridging H atom relative to the O atoms in structures **VII**–**IX** (the short O–H bonds lie in the range 1.09–1.20 Å, the long bonds are 1.22–1.36 Å, and the $\Delta\{(O\cdots H) - (O–H)\}$ differences are 0.02–0.25 Å; see Table 2) does not exclude the averaging of two hydrogen positions in two switching groups PO_3H^- and PO_3H_2. We suppose that the symmetric position of the proton in structure **X** exactly midway between the oxygen atoms [O···H is 1.28(6), O···O is 2.508(2) Å, and angle OHO is 160(6)°] also results from the superposition of the PO_3H^- and PO_3H_2 groups of neighboring anions; that is, the H_2L^{2-} and H_3L^- anions in the structure occupy two positions randomly, in an equal ratio. This conclusion is supported by the coincidence of the mean P–OH ($PO_3H_{1.5}$) bond length (1.563 Å) with the average of the P–OH (PO_3H_2) and P–OH (PO_3H) bond lengths (1.550 and 1.575 Å, respectively). An additional support is provided by the equality of the mean lengths of the half-protonated P–$OH_{0.5}$ bond (1.526 Å) to the average of the P=O (1.490 Å) and P–OH (1.563 Å) bond lengths in the $PO_3H_{1.5}^{0.5-}$ groups (see Table 1).

Now, we return to the isostructural series of four compounds **V**–**VIII** of general formula $Cat(H_3L) \cdot 2H_2O$. Based on the analysis of the phosphorus–oxygen distances in structure **VIII** [9], the authors concluded that both the phosphonic PO_3H_2 and phosphonate

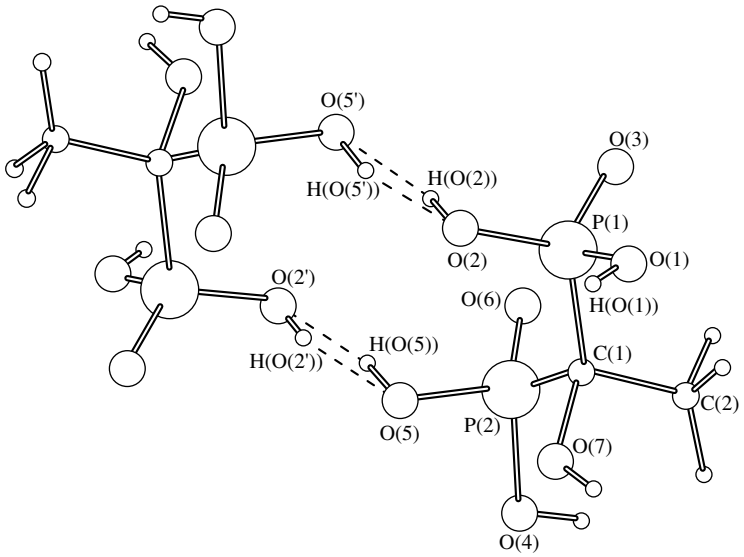

Fig. 3. Dimeric anionic fragment $(H_3L^-)_2$ in structures **V** and **VI**.

PO_3H^- groups occur in the crystal. The ordering of the H atoms in the $PO_3H_x^{x-2}$ groups in this compound, in contrast to their random positioning in the remaining three structures **V**–**VII**, is attributed to the large radius of the alkali metal. However, even in the structure of the cesium salt **VIII**, the P=O bond (1.517(3) Å) adjacent to the bridging H atom is distinctly longer than the two other P=O bonds [1.495(3), 1.497(3) Å], and the corresponding P–OH bond [1.541(3) Å] is shorter than the two other P–OH bonds [1.559(3), 1.583(3) Å]. Hence, the geometry observed can be alternatively interpreted as the averaging of two $PO_3H_{1.5}^{-0.5}$ groups (similar to structures **V**–**VII**), in which the mean P=O, P–OH, and $P–OH_{0.5}$ distances are 1.496 ± 0.001, 1.571 ± 0.012, and 1.529 ± 0.012 Å, respectively.

It was concluded in [9] that the nature (and size) of a metal atom affects the mutual arrangement of two phosphonic groups in the H_nL^{n-4} anions. As was shown in [16], the *W*-like configuration and the eclipsed position of the $PO_3H_x^{x-2}$ groups favor the minimization of steric interactions between the H(*Me*) atoms and terminal oxygens of the planar O–P–C–P–O fragment and

Table 2. Geometric parameters of intermolecular O–H···O hydrogen bonds between the "half-protonated" $PO_3H_{1.5}^{0.5-}$ groups in structures **V**–**X**

No.	Compound	Distance, Å			OHO angle, deg	Reference
		O···O	O–H	H···O		
V	$(NH_4)(H_3L) \cdot 2H_2O$	2.454(3)	0.64(6)	1.82(6)	173(6)	[8]
		2.454(3)	0.76(6)	1.70(6)	175(5)	
VI	$K(H_3L) \cdot 2H_2O$	2.437(3)	0.76(8)	1.82(9)	164(6)	[8]
		2.437(3)	0.88(6)	1.57(6)	162(6)	
VIIa*	$Rb(H_3L) \cdot 2H_2O$	2439(8)	1.16(8)	1.28(8)	166(5)	[9]
VIIb*	$Rb(H_3L) \cdot 2H_2O$	2.415(5)	1.20(6)	1.22(6)	171(4)	[10]
VIIc*	$Rb(H_3L) \cdot 2H_2O$ (n)**	2.433(3)	1.174(3)	1.261(3)	175.8(2)	[11]
VIII	$Cs(H_3L) \cdot 2H_2O$	2.453(4)	1.12(8)	1.36(8)	167(7)	[9]
IXa	$Na(H_3L) \cdot H_2O$	2.415(3)	1.09(5)	1.34(5)	166(4)	[12]
IXb	$Na(H_3L) \cdot H_2O$	2.426(5)	1.17	1.29	164	[13]
X	$(NH_4)_{1.5}(H_{2.5}L) \cdot H_2O$	2.508(2)	1.28(6)	1.28(6)	160(6)	[14]

* Based on the data of three independent studies.

** *n* denotes a neutron diffraction study.

Table 3. Interatomic *M*–O distances (*M* = Na, K, Rb, or Cs) in the HEDP salts of alkali-metal cations

No.	Compound	*M*–O distances, Å	Mean *M*–O distance, Å	CN of the metal	Reference
VI	$K(H_3L) \cdot 2H_2O$	2.701(3)–3.109(4)	2.880	7	[8]
VIIa*	$Rb(H_3L) \cdot 2H_2O$	2.889(4)–3.224(6)	3.028	7	[9]
VIIb*	$Rb(H_3L) \cdot 2H_2O$	2.887(2)–3.230(3)	3.030	7	[10]
VIIc*	$Rb(H_3L) \cdot 2H_2O$	2.888(3)–3.226(4)	3.028	7	[11]
VIII	$Cs(H_3L) \cdot 2H_2O$	3.070(3)–3.678(3)	3.366	11	[9]
IXa	$Na(H_3L) \cdot H_2O$	2.294(2)–2.463(2)	2.393	6	[12]
IXb	$Na(H_3L) \cdot H_2O$	2.300(4)–2.471(4)	2.390	6	[13]
XI	$Na_2(H_2L) \cdot 4H_2O$	2.303(3)–2.453(6)	2.394	6 : Na(1)	[15]
		2.302(3)–2.453(6); 2.857(5)	2.471	4 + 1 : Na(2)	

* Based on the data of three independent studies.

restrict rotation about the P–C bonds. In [16], it was assumed that the metal–oxygen interactions partly lift the restrictions imposed on the rotation about the P–C bonds. This supposition is confirmed by structures **V**–**VIII**: the values of the torsion angles about the P(1)···P(2) vector increase with an increase in the metal-atom size. The values of the O–P–P–O angles in the $Cat(H_3L) \cdot 2H_2O$ structures lie in the ranges ±9.6°–13.4° for $Cat = NH_4^+$ (structure **V**), ±11.8°–15.4° for K^+ (**VI**), ±13.0°–22.0° for Rb^+ (**VII**), and ±16.0°–26.0° for Cs^+ (**VIII**) [9].

Note that in structures **V**–**X**, sharing the proton by neighboring anions results in the formation of different associates. In the series of isostructural compounds **V**–**VIII**, $Cat(H_3L) \cdot 2H_2O$ [8–11], the double hydrogen bridges link the anions into centrosymmetric dimers. In structure **IX**, $Na(H_3L) \cdot H_2O$ [12, 13], pairs of diphosphonic anions are linked by single hydrogen bridges into zigzag polymeric chains. Finally, in structure **X**, $(NH_4)_{1.5}(H_{2.5}L) \cdot H_2O$ [14], the $H_5L_2^{3-}$ dimers are formed through the single hydrogen bridges.

Distinguishing the dimers in structures **V**–**VIII** (or polymeric chains in structure **IX**) seems reasonable, since the O···O distances in the $O–H_{bridging}···O$ bonds in the five structures (2.415–2.454 Å, Table 2) are noticeably shorter than similar contacts in other O–H···O hydrogen bonds (the interval that is next in length of the O···O contacts in structures **V**–**IX** is 2.544–2.556 Å). The only exception is provided by structure **X**: the O···O contact of 2.508(2) Å in the arbitrarily distinguished dimer is even slightly longer than one of the "interdimer" O···O contacts [2.499(2) Å].

On the whole, the structural units in all the structures considered (**II**–**XI**) are interlinked by extensive networks of hydrogen bonds $(H_nL)O–H···O(H_nL)$, $(H_2O)O–H\cdot\cdot O(H_nL)$, $(H_nL)O–H\cdot\cdot O(H_2O)$, $(H_2O)O–H\cdot\cdot O(H_2O)$, $N–H\cdot\cdot O(H_nL)$, and $N–H\cdot\cdot O(H_2O)$ involving almost all active protons of the H_nL^{n-4} anions, water molecules, and organic or ammonium cations.

COORDINATION OF ALKALI-METAL ATOMS IN HEDP SALTS

The *M*–O distances (*M* = Na, K, Rb, Cs) in the salts of HEDP with alkakine-metal cations **VI**–**IX** and **XI** [8–13, 15] are listed in Table 3. All five compounds were isolated as crystal hydrates. In the isostructural compounds **VI**–**VIII**, the metal atoms (K, Rb, Cs) are coordinated only by oxygen atoms of the HEDP anions; water molecules do not take part in metal coordination.

The seven-vertex polyhedra of the alkali metals in the compounds $M(H_3L) \cdot 2H_2O$, where *M* = K (**VI**) or Rb (**VII**), are described in [8, 9] as "an irregular triangle over a square."[2] In structure **VII**, according to the data in [9], the eighth oxygen atom is situated at a distance of 3.571(6) Å from rubidium. The local valence balance for **VII** (calculated according to the procedure in [17]) indicates that the contribution of the eighth O atom is insignificant (S_{ij} = 0.029 val. units vs. the total value ΣS_{ij} = 0.932 val. units). Thus, according to [9], it is reasonable to consider the coordination of the Rb atom as sevenfold. The angle between the square and triangle coordination planes is 4.5° in **VI** and 1.5° in **VII**. The metal atom deviates from these planes by –1.103 and 1.420 Å in structure **VI** and –1.023 and 1.443 Å in structure **VII**. Smaller distortions of the rubidium polyhedron in structure **VII** as compared to the potassium polyhedron in **VI** are, according to [9], due to the larger ionic radius of the metal.

Going from rubidium to cesium in the structure of $Cs(H_3L) \cdot 2H_2O$ (**VIII**) leads to an increase in the coor-

[2] The seven-vertex polyhedron of Rb in compound **VII** is described in [10] as a severely distorted pentagonal bipyramid in which the deviations of five equatorial oxygen atoms from the mean plane lie in the ±0.13–0.51 Å range.

dination number of the metal to eleven, which is related in [9] to the increased ionic radius. The Cs–O distances are distinctly divided into two groups: seven distances lie in the 3.07–3.43 Å range, and the remaining four distances are within 3.56–3.63 Å. With consideration for only the seven oxygen atoms closest to the metal, the polyhedron of Cs in **VIII** is similar to that of Rb in structure **VII**. However, the local valence balance indicates the better coincidence of the total bond valences for the coordination number of Cs equal to eleven (ΣS_{ij} = 1.007 val. units).

The sodium atom in compound $Na(H_3L) \cdot H_2O$ (**IX**) has a typical distorted octahedral coordination. One of the coordination sites is occupied by a water molecule. One of the two independent sodium atoms, Na(1), in the structure of $Na_2(H_2L) \cdot 4H_2O$ (**XI**) has exactly the same octahedral coordination: 5O(HEDP) + O(H_2O). The second atom, Na(2), has an elongated tetragonal-pyramidal coordination (4 + 1) with the O(P) atom of the HEDP ligand at the axial position (at a Na–O distance as long as 2.86 Å) and two O(H_2O) atoms in the equatorial plane [the Na–O_{eq} distances range between 2.30 and 2.45 Å).

Table 3 shows that the spread in Na–O bond lengths in structures **IX** and **XI** (omitting the axial Na(2)–O bond in the latter compound) is significantly smaller than the spread of the K–O distances in **VI**, Rb–O in **VII**, and, especially Cs–O in **VIII**. This fact can be attributed to the increasing contribution of the covalent component to the ionic *M*–O bond in the Cs, Rb, K, and Na sequence. Actually, the difference in the ionic radii[3] of cesium and sodium is 0.70 Å, whereas the mean Cs–O distance in structure **VIII** (3.37 Å) and the Na–O distance in the octahedral complexes of structures **IX** and **XI** (2.39 Å) differ by 0.98 Å; that is, on going from Cs to Na, the shortening of the *M*–O distances is sharper than the decrease in the ionic radii of the alkali metals.

COORDINATION MODES OF POLYDENTATE HEDP LIGANDS IN THE SALTS OF ALKALI METALS

1-Hydroxyethane-1,1-diphosphonic acid (H_4L) contains seven active coordination sites: three O(P) [or (H)O(P)] atoms in each of the two phosphonate groups and the O(C) [or (H)O(C)] atom of the α-hydroxy group.

In compounds of transition metals, the H_nL^{n-4} ligands (n = 0–3)[4] of 1-hydroxyethane-1,1-diphosphonic acid deprotonated to some degree or another act as flexidentate: from two to six oxygen atoms are involved in metal coordination. The oxygen sites that coordinate a metal are, as a rule, deprotonated.[5] This is true for all phosphonic (P)O^- atoms (without exceptions) and for most of the (C)O^- atoms of the α-hydroxy groups [in complexes of Mo(VI) and W(VI)]. Only in two compounds, $K_4Na_2[Cu(L)_2] \cdot 12H_2O$ [19] and $[Cu_3(HL)_2(H_2O)_4] \cdot 2H_2O$ [20], the copper atoms are coordinated by protonated (C)O(H) atoms.

In the salts of HEDP with alkali-metal cations, the metal–oxygen bonds are principally ionic. As mentioned above, the notions of coordination number and polyhedron, as well as the coordination capacity of anions H_nL^{n-4}, are indistinct for heavy alkali metals. On the other hand, the ionic character of the *M*–O bonds in the compounds considered eliminates the advantage of metal coordination by acido atoms O^- over neutral OH groups: in the HEDP salts with alkali-metal cations, the *M*–O^- and *M*–OH contacts are equally possible.

Thus, in salts $M(H_3L) \cdot 2H_2O$, where *M* = K (**VI**) or Rb (**VII**), the H_3L^- anion acts as a pentadentate tetrachelate μ_4-bridging ligand.[6] It coordinates four metal atoms by four phosphonic oxygens—one (of the two) deprotonated (P)O^- atoms, both "half-protonated" $(P)O(H_{0.5})^{0.5-}$ atoms, and one (of the two) protonated (P)O(H) atoms—and the protonated (C)O(H) atom of the α-hydroxy group. One (P)O^- atom and one (P)O(H) atom do not coordinate the *M* atoms. Coordination of a metal by four H_3L anions is accompanied by the formation of one six-membered and three five-membered chelate rings (Fig. 4a).

In the cesium salt **VIII**, the H_3L^- anion acts as a hexadentate heptachelate μ_5-bridging ligand (Fig. 4b); one of the three protonated phosphonic (P)O(H) atoms remains free of coordination ("terminal"). Totally, the H_3L^- anion coordinates five cesium atoms and closes seven chelate rings: two of them are six-membered, four are five-membered, and one is four-membered.[7]

In the structure of sodium salt monohydrate $Na(H_3L) \cdot H_2O$ (**IX**), the H_3L^- ligand performs a pentadentate tetrachelate μ_2-bridging function: tridentate chelate and bidentate chelate relative to two metal atoms. Two (of the three) protonated (P)O(H) and deprotonated (P)O^- phosphonic atoms coordinate the metal, and the remaining (P)O^- and (P)O(H) atoms are not involved in coordination. In **IX** and the four other structures considered in this chapter, the (C)O(H) atom of the α-hydroxy group coordinates the alkali-metal

[3] The following ionic radii (Å) are used: 0.97 for Na^+, 1.33 for K^+, 1.47 for Rb^+, and 1.67 for Cs^+ [18].

[4] For the acid deprotonated at the oxygen atom of the α-hydroxy group, the formula of the ligand is $(H_nL^*)^{n-5}$ (n = 0 or 1) [2].

[5] Since the terminal P–O and P–O^- bonds in the HEDP compounds have equal lengths (are delocalized), we conventionally consider them in this context as deprotonated $P(O)^-$.

[6] By "coordination capacity," a number of atoms bound to a metal (rather than a number of bonds formed by the H_nL^{n-4} anion with a metal is meant).

[7] Recall that if only seven (of eleven) oxygen atoms closest to the metal are considered, the coordination mode of the H_3L^- ligand in structure **VIII** is similar to that in structures **VI** and **VII**.

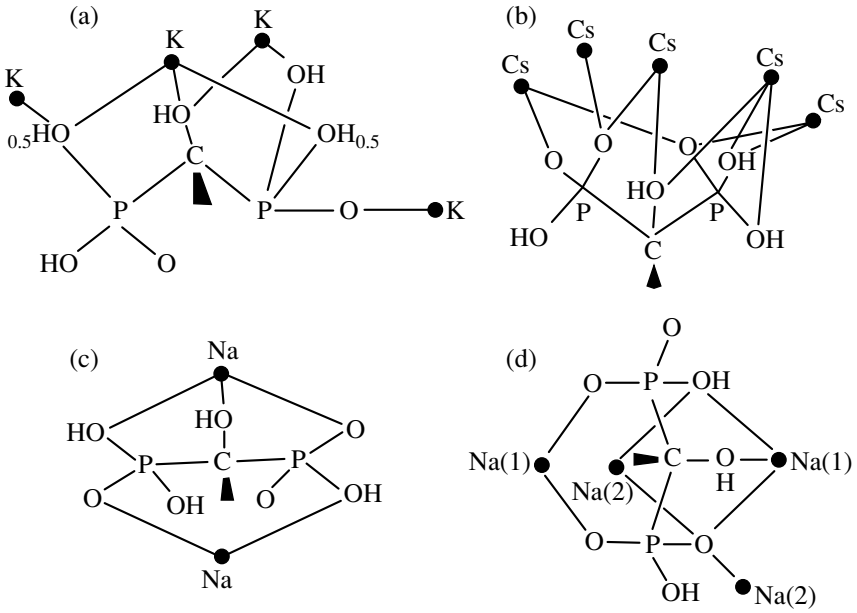

Fig. 4. Coordination modes of polydentate H_nL^{n-4} ligands (n = 2 or 3) in the structures of (a) $K(H_3L) \cdot 2H_2O$, (b) $Cs(H_3L) \cdot 2H_2O$, (c) $Na(H_3L) \cdot H_2O$, and (d) $Na_2(H_2L) \cdot 4H_2O$.

atom. Metal chelation results in the formation of four chelate rings; two of them are six-membered and two are five-membered (Fig. 4c).

In the structure of sodium salt tetrahydrate $Na_2(H_2L) \cdot 4H_2O$ (**XI**), the doubly charged H_2L^{2-} ligand performs a pentadentate pentachelate μ_4-bridging function. One protonated (P)O(H) and one deprotonated $(P)O^-$ oxygen atoms remain terminal, and the second protonated phosphonic atom (P)O(H) bridges two independent atoms Na(1) and Na(2). The coordination results in the formation of five chelate rings; two of them are six-membered, two are five-membered, and one is a four-membered bimetal ring (Fig. 4d).

REFERENCES

1. S. S. Jurisson, J. J. Benedict, R. C. Elder, *et al.*, Inorg. Chem. **22** (9), 1332 (1983).
2. V. S. Sergienko, Kristallografiya **44** (5), 939 (1999).
3. V. A. Uchtman and R. A. Gloss, J. Phys. Chem. **76** (9), 1298 (1972).
4. D. de La Matter, J. J. McCullough, and C. Calvo, J. Phys. Chem. **77** (9), 1146 (1973).
5. G. G. Aleksandrov, V. S. Sergienko, and E. G. Afonin, Kristallografiya **42** (3), 438 (1997).
6. V. S. Sergienko, G. G. Aleksandrov, and E. G. Afonin, Kristallografiya **42** (6), 1049 (1997).
7. L. M. Shkol'nikova, E. G. Afonin, E. V. Kalugina, *et al.*, Kristallografiya **36** (1), 77 (1991).
8. L. M. Shkol'nikova, A. A. Masyuk, G. V. Polyanchuk, *et al.*, Koord. Khim. **15** (4), 486 (1989).
9. L. M. Shkol'nikova, A. A. Masyuk, E. G. Afonin, *et al.*, Koord. Khim. **15** (6), 747 (1989).
10. P. Charpin, M. Lance, M. Neirlich, *et al.*, Acta Crystallogr., Sect. C: Cryst. Struct. Commun. **44** (6), 990 (1988).
11. J.-P. Silvestre, I. Brouche-Waksman, G. Heger, *et al.*, New J. Chem. **14** (1), 29 (1990).
12. L. M. Shkol'nikova, A. A. Masyuk, and E. G. Afonin, Koord. Khim. **16** (7), 902 (1990).
13. R. Rochdaoui, J.-P. Silvestre, and N. Q. Dao, Acta Crystallogr., Sect. C: Cryst. Struct. Commun. **46** (11), 2083 (1990).
14. V. S. Sergienko, E. O. Tolkacheva, and A. B. Ilyukhin, Zh. Neorg. Khim. **38** (7), 1129 (1993) [Russ. J. Inorg. Chem. **38**, 1047 (1993)].
15. B. L. Barnett and L. C. Strickland, Acta Crystallogr., Sect. B: Struct. Crystallogr. Cryst. Chem. **35** (5), 1212 (1979).
16. V. A. Uchtman, J. Phys. Chem. **76** (9), 1304 (1972).
17. I. D. Brown and D. Altermatt, Acta Crystallogr., Sect. B: Struct. Sci. **41** (3), 244 (1985).
18. L. M. Ahrens, Geochim. Cosmochim. Acta, No. 2, 155 (1955).
19. Z. Pan, X. Jin., M. Shao, *et al.*, Chem J. Chin. Univ. **6** (1), 69 (1985).
20. A. Neuman, A. Safsaf, H. Gillier, *et al.*, Phosphorus, Sulfur Silicon Relat. Elem. **70** (2), 273 (1992).

Translated by I. Polyakova

Crystallography Reports, Vol. 45, No. 1, 2000, pp. 71–77. Translated from Kristallografiya, Vol. 45, No. 1, 2000, pp. 77–83.

STRUCTURES OF ORGANIC COMPOUNDS

Crystal and Molecular Structures of Complex between Ammonium Iodide Monohydrate and the *cis–syn–cis* Isomer of Dicyclohexano-18-Crown-6

M. S. Fonar'*, V. Kh. Kravtsov*, Yu. A. Simonov*, É. V. Ganin, and J. Lipkowski*****

** Institute of Applied Physics, Academy of Sciences of Moldova, Chisinau, Moldova*

*** Physicochemical Institute for Human and Environmental Protection, Education Department, National Academy of Sciences of Ukraine, Odessa State University, Odessa, Ukraine*

**** Institute of Physical Chemistry, Polish Academy of Sciences, Warsaw, Poland*

Received April 8, 1998

Abstract—The structure of the $[(DCH\text{-}6A \cdot NH_4)(H_2O)I]_2$ complex obtained by the reaction between the *cis*–syn–*cis* isomer of dicyclohexano-18-crown-6 (DCH-6A) and NH_4I has been determined by X-ray diffraction analysis. The crystals are triclinic, a = 9.314(3) Å, b = 11.951(2) Å, c = 12.040(1) Å, α = 77.36(1)°, β = 81.59(1)°, γ = 80.41(2)°, space group $P\bar{1}$, Z = 2, and the final R factor is 0.044. The structure is built up of the $(DCH\text{-}6A \cdot NH_4)^+$ cationic complexes, iodide anions, and water molecules. The ammonium ion forms three hydrogen bonds of the NH···O type [N···O, 2.881(5)–2.890(5) Å] with the oxygen atoms of the crown ether molecule. The organic cations are joined together into centrosymmetric dimers through the system of hydrogen bonds of the NH···OH···I type. The $I^-\cdots O$ distances (where the O atom belongs to the bridging water molecule) fall in the range 3.558(4)–3.610(4) Å. © *2000 MAIK "Nauka/Interperiodica".*

INTRODUCTION

At present, a considerable amount of experimental information on the complexes of crown ethers with cations of alkali, alkaline-earth, transition, and post-transition metals has been accumulated. Much attention of researchers has been given to the complexes with tripodal "guests" of the $-XH_3$ type, specifically with the salts of ammonium and its substituted derivatives. Compounds of this type are of fundamental interest as model systems formed by cooperative hydrogen bonds between components [1, 2]. Investigations of various interactions in these aggregates open up fresh opportunities for the understanding of more complex macromolecular systems, including proteins and amino acids.

The crown ether complexes with salts of ammonium and its substituted derivatives have been studied by various physicochemical techniques, among them gas-phase methods and mass spectrometry [3, 4]. It was found that the affinity of unsubstituted crown ethers for the ammonium ion increases in the order: 12-crown-4 < 15-crown-5 < 18-crown-6 < 21-crown-7 [3, 4]. According to the molecular mechanics calculations [5] and the experimental data, the affinity of ammonium ions for a crown ether decreases in the order: primary > secondary > ternary. The introduction of substituents into the crown ether molecule and an increase in the length of alkyl chain in a primary amine lead to an increase in the degree of connectivity, which is associated with an additional stabilization because of the van der Waals interactions.

The experimental data on dicyclohexano-18-crown-6 complexes with ammonium salts are virtually absent in the literature. The studies of the specific features of complex formation in this system are usually reduced to the determination of stability constants for the complex between dicyclohexano-18-crown-6 (unknown isomer) and NH_4^+ in aqueous solutions [6].

In the present work, we synthesized the complex between the *cis–syn–cis* isomer of dicyclohexano-18-crown-6 (DCH-6A) and ammonium iodide monohydrate and determined its crystal structure.

EXPERIMENTAL

Synthesis of the $[(DCH\text{-}6A \cdot NH_4)(H_2O)I]_2$ complex. Iodomethane (170 mg, 1.2 mmol) and a 25% ammonia solution (2 ml) were added to a solution of the *cis*–syn–*cis* isomer of dicyclohexano-18-crown-6 (372 mg, 1 mmol) in methanol (3 ml). The mixture obtained was allowed to evaporate at 15°C down to a volume of 0.2–0.3 ml. Crystals were separated by the decantation. The yield of complex was 465 mg (87%), and the melting temperature T_m was 146–148°C. The results of chemical analysis are as follows.

For $C_{20}H_{42}INO_7$ anal. calcd. (%): C, 44.86; H, 7.91; N, 2.62.

Found (%): C, 44.75; H, 8.02; N, 2.79.

According to the data of thermogravimetric analysis (OD-102 derivatograph; weighed portion, 70 mg; platinum crucible; heating rate, 10 K/min), the sample

Table 1. Crystal data, data collection, and refinement parameters for the structure of the $[(DCH\text{-}6A \cdot NH_4)(H_2O)I]_2$ complex

Compound	$[(DCH\text{-}6A \cdot NH_4)(H_2O)I]_2$
Empirical formula	$C_{20}H_{42}INO_7$
Molecular weight	535.45
Crystal system	Triclinic
Temperature, K	293(2)
Radiation	CuK_α(λ = 1.5418 Å)
Space group	$P\bar{1}$
Unit-cell parameters:	
a, Å	9.314(3)
b, Å	11.951(2)
c, Å	12.040(2)
α, deg	77.36(1)
β, deg	79.14(2)
ν, deg	80.41(2)
V, Å^3	1273.3(5)
Z	2
d_{calcd}, g/cm^3	1.397
μ, mm	10.183
F(000)	556
Crystal size, mm	$0.25 \times 0.20 \times 0.20$
τ range, deg	3.81–70.20
Index ranges	$-10 < h < 11$, $-13 < k < 14$, $0 < l < 14$
Diffractometer	KUMA
Scan mode	$\omega/2\theta$
No. of measured reflections	4710
No. of unique reflections, [R_{int}]	4710[0.0]
Goodness-of-fit $S(F^2)$	1.045
Refinement technique	Full-matrix, based on F^2
Final *R* factors for reflections with [$I > 2\sigma(I)$]	$R1 = 0.0437$, $wR2 = 0.1192$
Final *R* factors for all reflections	$R1 = 0.0574$, $wR2 = 0.1283$
$\Delta\rho_{min}$, eÅ^{-3}	–1.185
$\Delta\rho_{max}$, eÅ^{-3}	0.891

undergoes thermal destruction at 95–150°C, which is accompanied by the endothermic effect and the loss of one mole of water passing into the gas phase.

X-ray structure analysis. A prismatic crystal 0.25 × 0.20 × 0.20 mm in size was chosen for the X-ray diffraction analysis. The determination of the unit cell parameters and the collection of reflection intensities were carried out on a KUMA diffractometer (CuK_α radiation, graphite monochromator, room temperature). The main crystal data for the complex are given in Table 1. The structure was solved by the direct methods using the SHELXS86 program package [7]. The refinement was performed in the anisotropic approximation for the non-hydrogen atoms with the use of the SHELXL93 program package [8]. Correction for absorption was introduced with the DIFABS program [9]. The hydrogen atoms of the water molecule and the ammonium ion were independently located from the difference Fourier synthesis and refined in the isotropic approximation. The remaining hydrogen atoms were geometrically calculated and refined in the rigid-group model. The coordinates of the basis atoms in the complex are listed in Table 2.

RESULTS AND DISCUSSION

The crown ether complexes with salts of ammonium and its derivatives are thoroughly investigated by X-ray diffraction analysis. The data on crystal structures of

72 compounds belonging to this class of complexes are available in the Cambridge Structural Database [10]. Among these compounds, we chose the complexes of crown ethers with ammonium salts (Table 3). This table also contains the $N\cdots O_{crown}$ distances differentiated according to the participation of hydrogen atoms in them (the NH···O hydrogen bonds and the $N^+\cdots O$ electrostatic interactions).

The complexes with 15-crown-5 and benzo-15-crown-5 have a sandwich-like crystal structure, in which the ammonium ion is located between two crown ether molecules. All four hydrogen atoms of the ammonium ion are involved in both classic and bifurcated $NH\cdots O_{crown}$ hydrogen bonds.

In the case of eighteen-membered crown ethers, since the tripodal fragment of the NH_4^+ cation is topologically compatible with the cavity of the eighteen-membered cycle, the NH···O interactions occur with each second oxygen atom of the cycle with the formation of three classic hydrogen bonds. The distances to the other three oxygen atoms also appear to be shortened as compared to the sum of the van der Waals radii of the nitrogen and oxygen atoms (Table 3).

In the dibenzo-18-crown-6 molecule, the benzene rings are rigidly attached to the heterocyclic skeleton. Four out of six oxygen atoms of the crown ether molecule are bonded to the sp^2 carbon atoms and lie virtually in the same plane with the aromatic substituents. As a result, the molecule adopts the conformation of a flattened boat. In the complexes with dibenzo-18-crown-6, the ammonium ion can approach the cycle both from the side of the benzene substituents, as in the CILDUW complex, and from the opposite side, as is the case in the FAXLAR, FENZUT, GARMAN, and YUFYUT complexes (Table 3). The FENZUT complex has a rather interesting structure. In this structure, apart from the interactions with the macrocyclic molecule, two ammonium ions, which are sandwiched between two crown ether molecules, form the hydrogen bonds with the picrate anion. Apparently, these sufficiently strong interactions are responsible for the escape of the cation from the cavity and an increase in the $N\cdots O$ distances (all the distances are longer than 3 Å).

The centrosymmetric dimeric complex $[(DCH\text{-}6A \cdot NH_4)(H_2O)I]_2$ is depicted in the figure. The ammonium ion approaches the crown ether molecule from the side of the cyclohexane substituents and forms the $(DCH\text{-}6A \cdot NH_4)^+$ cation. The coordination is accomplished through three NH···O hydrogen bonds (one bond with each second oxygen atom of the cycle). The N···O distances are as follows: N(1)···O(1), 2.889(5) Å; N(1)···O(7), 2.881(5) Å; and N(1)···O(13), 2.890(5) Å. The distances to the other three oxygen atoms of the macrocycle are also shortened and fall in the range 2.952(5)–3.056(5) Å. The geometric parameters of hydrogen bonds in the complex are listed in Table 4 and agree with the corresponding parameters for the 18-crown-6 complexes.

Table 2. Atomic coordinates ($\times 10^4$) and equivalent isotropic thermal parameters ($Å^2 \times 10^3$) for the $[(DCH\text{-}6A \cdot NH_4)(H_2O)I]_2$ complex

Atom	x	y	z	U_{eq}
I(1)	4890(1)	7371(1)	8753(1)	54(1)
O(1)	2449(4)	1575(3)	7989(3)	54(1)
C(2)	1656(7)	1284(5)	9121(6)	77(2)
C(3)	93(7)	1841(5)	9110(6)	76(2)
O(4)	64(4)	3047(3)	8953(3)	56(1)
C(5)	−1371(5)	3655(5)	8899(5)	63(1)
C(6)	−1324(6)	4911(5)	8719(5)	63(1)
O(7)	−470(3)	5284(3)	7628(3)	51(1)
C(8)	−446(5)	6505(4)	7332(4)	50(1)
C(9)	−133(5)	6842(4)	6028(4)	49(1)
O(10)	1271(3)	6223(3)	5635(3)	45(1)
C(11)	1416(6)	6117(4)	4467(4)	48(1)
C(12)	2908(6)	5518(4)	4092(4)	51(1)
O(13)	3074(4)	4370(3)	4745(3)	50(1)
C(14)	4310(6)	3659(5)	4267(4)	54(1)
C(15)	4244(6)	2430(5)	4811(4)	58(1)
O(16)	4372(4)	2241(3)	6001(3)	47(1)
C(17)	4396(6)	1040(4)	6547(4)	51(1)
C(18)	3907(5)	966(4)	7832(4)	50(1)
C(19)	4976(7)	1412(5)	8379(5)	64(1)
C(20)	6494(7)	741(6)	8157(7)	79(2)
C(21)	7010(6)	802(5)	6874(7)	74(2)
C(22)	5939(6)	371(4)	6332(5)	64(1)
C(23)	−119(6)	8145(5)	5669(5)	60(1)
C(24)	945(8)	8573(5)	6228(6)	74(2)
C(25)	642(8)	8217(5)	7533(6)	74(2)
C(26)	634(6)	6916(5)	7904(5)	61(1)
N(1)	2450(4)	4042(3)	7231(3)	43(1)
H(1N1)	245(6)	327(18)	747(5)	130(3)
H(2N1)	152(3)	440(4)	733(4)	76(2)
H(3N1)	284(5)	419(5)	649(2)	80(2)
H(4N1)	300(4)	429(4)	765(3)	56(2)
O(1*w*)	4315(7)	4541(4)	8605(4)	86(1)
H(1*w*)	439(2)	533(3)	862(7)	190(5)
H(2*w*)	439(8)	408(5)	935(3)	100(3)

In [29], on the basis of theoretical calculations, the assumptions were made as to the more preferable location of the ammonium ion on one of the sides of the cavity in the complex with the *cis*–syn–*cis* isomer of dicyclohexano-18-crown-6. The inference that the "cramped" complex is preferably formed is in agree-

Table 3. Some characteristics of complexes between oxygen-containing crown ethers and ammonium salts

Complex	N···O and N^+···O** distances	Code in CSD*, reference
L = 15-crown-5 $[(NH_4)(L)_2]_2[(UO_2Cl_4)] \cdot 2CH_3CN$	2.923–3.019*** 3.040–3.077 2.916–2.973 3.037–3.096	GARLUG [11]
L = benzo-15-crown-5 $[(NH_4)(L)_2]_2[(UCl_6)] \cdot 4CH_3CN$	2.887–2.910*** 3.031–3.080 2.874–3.010 3.010–3.028	GARLOA [11]
$[(NH_4)(L)_2][Cd_2(NCS)_6] \cdot CH_3CN$	2.830–2.947*** 3.101–3.186 2.886–3.037 3.055–3.084	LETLIF [12]
L = 18-crown-6 $[(NH_4)(L)][Br] \cdot 2H_2O$	2.857–2.884 3.001–3.127	HOCDAB [13]
$[(NH_4)(L)][Cl] \cdot 2H_2O$	2.903–2.906 3.002–3.166	VUXNOR [14]
$[(NH_4)(L)]_2[Cl] \cdot [PF_6] \cdot 0.9CH_2Cl_2$	2.868–2.921*** 2.986–3.062 2.882–2.913 2.957–3.075	VUXNIL [14]
$[(NH_4)(L)]_2[UCl_6] \cdot 2CH_3CN$	2.886–2.888 3.058–3.059	GICLIN [15]
$[(NH_4)(L)]_2[UO_2(NCS)_4] \cdot H_2O$	2.877–2.944 3.030–3.085	FIJGIO [16]
$[(NH_4)(L)][(PdCl_2)(SCN)]_2$	2.853–2.924 2.982–3.089	FUZXAZ [17]
$[(NH_4)(L)][MoOBr_4(C_4H_8O)] \cdot C_4H_8O$	2.807–2.947 2.985–3.029	VOZWAI [18]
$[(NH_4)(L)]_2[Ag(NCS)_2]_2$	2.873–2.895*** 3.002–3.071 2.867–2.954 2.939–3.050	KAKNOZ [19]
L = *cis–syn–cis-dicyclohexano*-18-crown-6 $[(NH_4)(L)H_2O)I]_2$	2.881–2.890 2.952–3.056	This work
L = dibenzo-18-crown-6 $[(NH_4)(L)]_2[Co(NCS)_4] \cdot C_3H_6O$	2.867–2.961	CILDUW [20]
$[(NH_4)(L)]_2[Co(NCS)_4] \cdot C_7H_8O$	2.818–2.902*** 2.844–2.892	FAXLAR [21]
$[(NH_4)(L)][C_6H_2N_3O_7]$	3.036–3.090	FENZUT [22]
$[(NH_4)(L)]_2[UO_2Cl_4] \cdot 2CH_3CN$	2.920–2.974	GARMAN [11]
$[(NH_4)(L)]_2[Ag(NCS)_2]_2$	2.806–2.854*** 2.846–3.013	YUFYUT [23]
L = 1,3-xylyl-18-crown-5 $[(NH_4)(L)][(C_{12}H_8B_1O_4)]$	2.827–2.998 3.042–3.060	JULHUT [24]
L = 5nitro-1,3-xylyl-18-crown-5-2-olate $[(NH_4)(L)]$	2.883–2.885 3.073	CUXNUE [25]
L = 9,9'-spirobifluorene-22-crown-5 $[(NH_4)(L)][SCN]$	2.922 3.035–3.154	POPATC10 [26]
L = 2,5,8,11,14,18,21,24,27,30-decaoxatricyclo[13.17.0.0$^{1.15}$]dotriacontane $[(NH_4)_2(L)][SCN]_2$	2.928–2.989*** 3.032–3.114 2.928–2.989 3.030–3.114	BOVPOR [27]
L = 1,5,12,16,23,26,29,32-octaoxa(10^{3,14})–(5.5)orthocyclophane $[(NH_4)(L)][I] \cdot 1.5H_2O$	2.718–2.868	DAGLEC [29]

* CSD is the Cambridge Structural Database System.
** All the distances are taken from the Cambridge Structural Database System.
*** Data for two independent complexes.

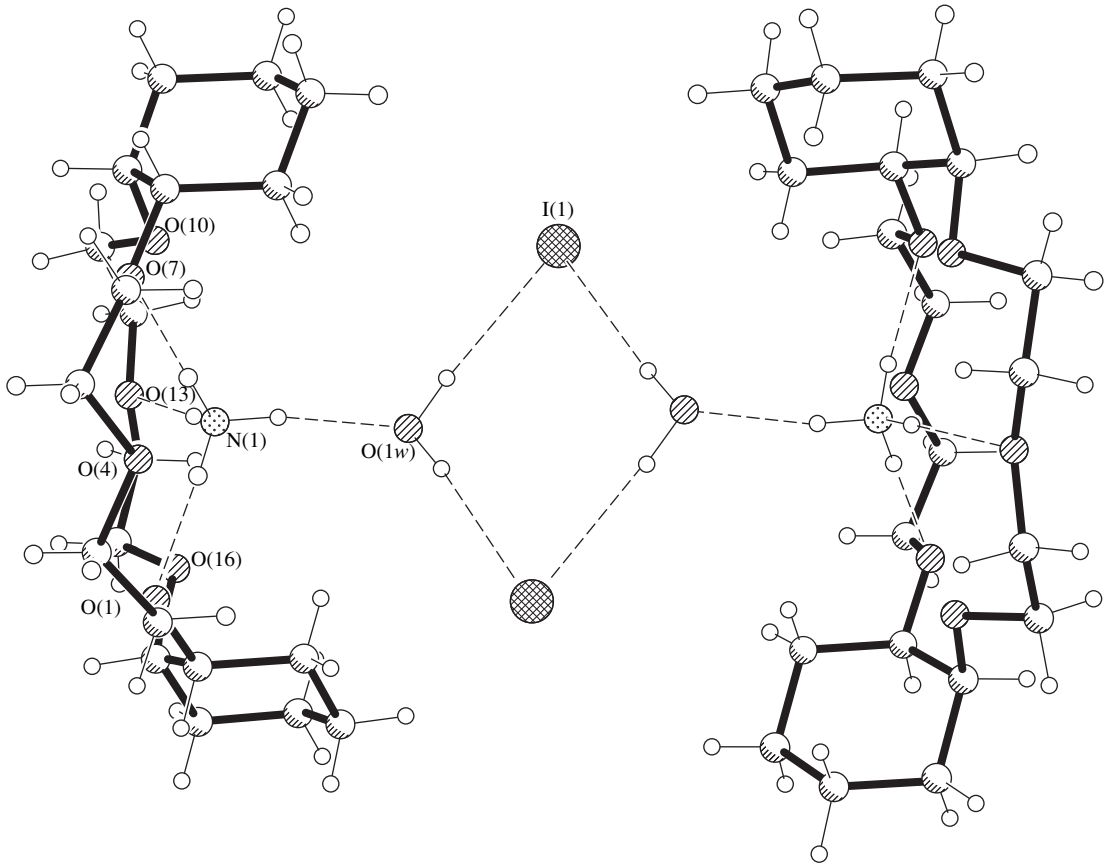

Structure of the $[(DCH\text{-}6A \cdot NH_4)(H_2O)I]_2$ complex.

ment with the data of X-ray diffraction analysis. However, the use of the crystal structure of barium complex with dicyclohexano-18-crown-6 as the initial model for calculations performed in [29] undeniably introduced some errors in the ultimate results and, particularly, in the lengths of intermolecular hydrogen bonds. The N···O distances calculated within the final model (2.794 ± 0.008 Å) turn out to be somewhat underestimated as compared to the data of X-ray diffraction analysis.

The fourth N–H bond of the ammonium cation in the complexes with eighteen-membered crown ethers is virtually perpendicular to the cycle cavity and is oppositely directed from this cycle. As a rule, the hydrogen atom of this bond participates in the intermolecular contacts with the anion to form, in each case, a specific architectural structural motif, for example, a dimer in the VUXNIL complex or a polymeric chain in the GICLIN complex. In the structures with 1,3-xylyl-18-crown-5 and its nitrophenolate derivatives [24, 25], the same hydrogen atom of the ammonium ion is involved in the hydrogen bond with the catecholborate or nitrophenolate anion to give a neutral associate of the 1 : 1 stoichiometry in the former case or a centrosymmetric dimer in the latter case.

In the complex studied in this work, the fourth N–H bond of the ammonium ion is also almost perpendicular to the cycle cavity, and its hydrogen atom forms the hydrogen bond of the NH···O type with a lone electron pair of the oxygen atom in the water molecule: N(1)···O(1*w*), 2.824(6) Å. In turn, the water molecule serves as a bridge between the cationic complex and the two iodide anions and forms two OH···I hydrogen bonds characterized by the following distances: O(1*w*)···I, 3.558(4) Å and O(1*w*)···I($1 - x$, $1 - y$, $2 - z$), 3.610(4) Å. This gives rise to a centrosymmetric parallelogram with two water molecules and two iodide anions in vertices. Similar parallelograms are also observed in the related structures, for example, in the complexes of nitrogen-containing macrocycles and cryptands with sodium bromide hydrates [30] and HBr [31].

As can be seen from Table 3, four complexes contain water as a solvate, and three of them (HOCDAB, VUXNOR, and DAGLEC) involve both water and halide anions. In these cases, the repetitive structural unit is a parallelogram, which is formed by two water molecules and two halide anions (Cl^-, Br^-, or I^-) via the hydrogen bonds. Both hydrogen atoms of each water molecules participate in the formation of the parallelo-

Table 4. Geometric parameters of intermolecular hydrogen bonds in the $[(DCH\text{-}6A \cdot NH_4)(H_2O)I]_2$ complex

D(donor)–H···*A*(acceptor)	*d*(*D*–H), Å	*d*(H··*A*), Å	*d*(*D*··*A*), Å	<(*DHA*), deg
N(1)–H(1N1)···O(1)	0.90(2)	1.99(2)	2.889(5)	179(5)
N(1)–H(2N1)···O(7)	0.90(2)	1.99(2)	2.881(5)	175(4)
N(1)–H(3N1)···O(13)	0.90(2)	2.04(2)	2.890(5)	160(4)
N(1)–H(4N1)···O(1*w*)	0.92(2)	1.93(2)	2.824(6)	170(4)
O(1*w*)–H(1*w*)···I(1)	0.96(2)	2.61(2)	3.558(4)	173(8)
O(1*w*)–H(2*w*)···I(1^i)	0.95(2)	2.67(2)	3.610(4)	169(6)

Note: Symmetry transformation for symmetry-related atoms *i*: $-x + 1, -y + 1, -z + 2$.

gram. In the HOCDAB and VUXNOR complexes, the parallelograms are joined into chains with the side cationic complexes $(18\text{-crown-6} \cdot NH_4)^+$:

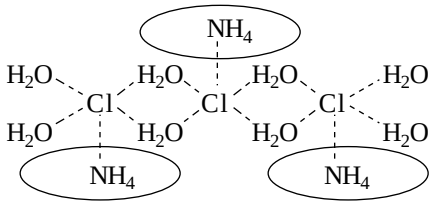

For the DAGLEC complex with a more bulky macrocycle, two macrocyclic molecules and two ammonium ions in between are joined into a centrosymmetric dimer. These associates form columns whose cavities are occupied by chains of joined parallelograms. Therefore, in all the above complexes, the water vacancy as a proton acceptor does not participate in hydrogen bonding.

In the $[(DCH\text{-}6A \times NH_4)(H_2O)I]_2$ complex under consideration, the water molecule serves as a bridge between the oppositely charged particles. A shortening of the polymeric chain down to a dimeric associate is explained by the shielding effect of the cyclohexane substituents: in the two crown ether molecules related by an inversion center, the cyclohexane substituents are oriented toward each other and encapsulate the aforementioned parallelogram.

The crown ether molecule in the studied complex adopts a conformation of the boat elongated toward the cyclohexane substituents. The O···O cross-cyclic distances in the cycle are as follows: O(1)···O(10), 5.687(4) Å; O(4)···O(13), 5.351(5) Å; and O(7)···O(16), 5.633(6) Å. Four oxygen atoms O(1), O(4), O(7), and O(13) are coplanar accurate to within 0.045 Å. The two other oxygen atoms O(10) and O(16) deviate from this plane by 0.510(5) and 0.468(5) Å, respectively. The deviation of the nitrogen atom from the plane defined by four oxygen atoms of the macrocycle is equal to 1.129(4) Å. The torsion angles about the C–C bonds lie in the range 59.5(5)–69.0(5)°, and the torsion angles about the C–O bonds fall in the range 155.1(4)–179.3(5)°. The crown ether molecule in the complex exhibits a normal geometry.

CONCLUSION

The complexes presented in Table 3 can be divided into four groups involving different numbers of compounds: the complexes with fifteen-membered crown ethers (group I), 18-crown-6 ethers (group II), dibenzo-18-crown-6 ethers (group III), and other crown ethers (group IV). Let us generalize some characteristic features of the complexes belonging to the first three groups.

The complexes belonging to group I are the sandwich cations with the stoichiometry NH_4^+ : crown ether = 1 : 2. In structures with the independently located hydrogen atoms of the ammonium ion, the hydrogen atoms are involved in one classic and one bifurcated NH···O hydrogen bonds with three oxygen atoms of each crown ether molecule. The distances to the other two oxygen atoms are larger than 3 Å.

In the complexes assigned to group II, there are two types of the N···O contacts: three NH···O hydrogen bonds [d(N···O) < 3 Å] and three N^+···O electrostatic interactions [$d(N^+\cdots O) > 3$ Å], which alternate in the cycle. The eighteen-membered cycle is described by the D_{3d} pseudosymmetry with alternation of the signs of the *gauche* torsion angles about the C–C bonds and the signs of deviations of the oxygen atoms from their mean plane.

In the complexes of group III, all the N···O distances are close to each other and cannot be classified into two types characteristic of the complexes with 18-crown-6. The fact that all these distances are virtually identical suggests that all six oxygen atoms of the macrocycle participate to the same extent in the interactions with the ammonium ion. This is likely associated with the fact that the benzene substituents conjugated with the heterocyclic skeleton impart the rigidity to the molecule, which manifests itself in the reduced degree of freedom (mobility) of each oxygen atom as compared to the oxygen atoms in the 18-crown-6 ether molecule.

The DCH-6A complex with ammonium iodide is first described in the present work. In this complex, as in the complexes with 18-crown-6 (group II), there are two types of N···O distances alternating in the cycle. Moreover, like the 18-crown-6 molecule with the D_{3d}

pseudosymmetry, the studied complex exhibits alternation of the signs of the *gauche* torsion angles about the C–C bonds along the heterocyclic skeleton. Therefore, compared to the 18-crown-6 molecule, the presence of the cyclohexane substituents in the DCH-6A molecule does not change the character of interaction between the oxygen atoms of the macrocycle and the ammonium ion. Their influence manifests itself only in a distortion of the symmetric arrangement of the oxygen atoms in the DCH-6A molecule as compared to the 18-crown-6 molecule.

REFERENCES

1. J. S. Brodbelt, in *Comprehensive Supramolecular Chemistry*, Ed. by J.-M. Lehn, J. L. Atwood, J. E. D. Davies, D. D. MacNicol, and F. Vogtle (Pergamon, Oxford, 1996), Vol. 1, p. 465.
2. G. W. Gokel and E. Abel, in *Comprehensive Supramolecular Chemistry*, Ed. by J.-M. Lehn, J. L. Atwood, J. E. D. Davies, D. D. MacNicol, and F. Vogtle (Pergamon, Oxford, 1996), Vol. 1, p. 511.
3. M. Meot-Ner, J. Am. Chem. Soc. **105,** 4912 (1983).
4. C. C. Liou and J. S. Brodbelt, J. Am. Chem. Soc. **114,** 6761 (1992).
5. D. Gehin, P. A. Kollman, and G. Wipff, J. Am. Chem. Soc. **111,** 3011 (1989).
6. G. A. Rechnitz and E. Eyal, Anal. Chem. **44,** 370 (1972).
7. G. M. Sheldrick, Acta Crystallogr., Sect. A: Found. Crystallogr. **46,** 467 (1990).
8. G. M. Sheldrick, *SHELXL93: Program for the Refinement of Crystal Structures* (Univ. of Göttingen, Göttingen, 1993).
9. N. Walker and D. Stuart, Acta Crystallogr., Sect. A: Found. Crystallogr. **39,** 158 (1983).
10. F. N. Allen and O. Kennard, Chem. Design Automat. News **8,** 131 (1993).
11. R. D. Rogers, L. K. Kurihara, and M. M. Benning, Inorg. Chem. **26,** 4346 (1987).
12. Chen Dai-Rong, Hu Qing-Ping, Meng Yong-De, *et al.*, Jiegou Huaxue **13,** 235 (1994).
13. O. Nagano, A. Kobayashi, and Y. Sasaki, Bull. Chem. Soc. Jpn. **51,** 790 (1978).
14. D. A. Pears, J. F. Stoddart, M. E. Fakley, *et al.*, Acta Crystallogr., Sect. C: Cryst. Struct. Commun. **44,** 1426 (1988).
15. R. D. Rogers and M. M. Benning, Acta Crystallogr., Sect. C: Cryst. Struct. Commun. **44,** 1397 (1988).
16. Wang Ming, Zheng Pei-Ju, Zhang Jing-Zhi, *et al.*, Acta Crystallogr., Sect. C: Cryst. Struct. Commun. **43,** 873 (1987).
17. Zhou Zhongyuan, Yu Kaibei, Liu Li, *et al.*, Jiegou Huaxue **7,** 61 (1988).
18. P. Hofacker, A. Werth, A. Neuhaus, *et al.*, Chem. Ztg. **115,** 321 (1991).
19. Du Gaoying, Zhang Wenxing, and Fan Yue-Peng, Wuji Huaxue Xuebao **3,** 34 (1987).
20. S. T. Malinovskiĭ, Yu. A. Simonov, T. I. Malinovskiĭ, *et al.*, Kristallografiya **29** (3), 466 (1984).
21. Fan Yue-Peng and Zhou Zhongyuan, Huaxue Xuebao **44,** 699 (1986).
22. J. A. Kanters, F. H. van der Steen, A. Schouten, *et al.*, J. Inclusion Phenom. **4,** 225 (1986).
23. Hu Qing-Ping, Chen Dai-Rong, Meng Yong-De, *et al.*, Jiegou Huaxue **14,** 206 (1995).
24. R. Goddard, C. M. Niemeyer, and M. T. Reetz, Acta Crystallogr., Sect. C: Cryst. Struct. Commun. **49,** 402 (1993).
25. C. M. Browne, G. Ferguson, M. A. McKervey, *et al.*, J. Am. Chem. Soc. **107,** 2703 (1985).
26. K. Neupert-Laves and M. Dobler, Helv. Chim. Acta **64,** 1653 (1981).
27. J. D. Owen, J. Chem. Soc., Perkin Trans. **2**, 407 (1983).
28. J. A. Bandy, C. H. L. Kennard, D. G. Parsons, *et al.*, J. Chem. Soc., Perkin Trans. **2**, 309 (1984).
29. D. V. Dearden and In-Hou Chu, J. Inclusion Phenom. **29,** 269 (1997).
30. K. Suwinska, Acta Crystallogr., Sect. C: Cryst. Struct. Commun. **51,** 2232 (1995).
31. B. Nieslanik, E. N. Duesler, L. Miao, *et al.*, Acta Crystallogr., Sect. C: Cryst. Struct. Commun. **52,** 205 (1996).

Translated by O. Borovik-Romanova

Crystallography Reports, Vol. 45, No. 1, 2000, pp. 78–86. Translated from Kristallografiya, Vol. 45, No. 1, 2000, pp. 84–92.

STRUCTURES OF ORGANIC COMPOUNDS

Molecular and Crystal Structures of 1-Methyl-2-Oxo-3-Acetoxy-4-Hydroxy-4-(Phenyl)piperidine, 1-Ethyl-2-Oxo-3,4-Dihydroxy-4-(Pyridyl)piperidine, and 1-Benzyl-2-Oxo-3,4-Dihydroxy-4-(Pyridyl)piperidine and the Role of Hydrogen Bonds in Molecular Packing in Crystals

L. N. Kuleshova and V. N. Khrustalev

Nesmeyanov Institute of Organoelement Compounds, Russian Academy of Sciences, ul. Vavilova 28, Moscow, GSP-1, 117813 Russia

Received August 7, 1997

Abstract—The molecular and crystal structures of 1-methyl-2-oxo-3-acetoxy-4-hydroxy-4-(phenyl)hydropyridine, 1-ethyl-2-oxo-3,4-dihydroxy-4-(pyridyl)piperidine, and 1-benzyl-2-oxo-3,4-dihydroxy-4-(pyridyl)piperidine are determined by X-ray diffraction analysis. These three hydroxy derivatives of hydropyridine are the convenient model compounds in studies of the influence of intramolecular and intermolecular hydrogen bonds on the conformation and packing of molecules in crystals. The molecules of hydroxy derivatives possess a considerable conformational flexibility and can form an extended network of intramolecular and intermolecular hydrogen bonds. It is shown that these compounds more often than others form noncentrosymmetric and polysystem crystals. The role of the molecular association and the type of hydrogen-bonded associates (syntons) in crystal packing are discussed. © *2000 MAIK "Nauka/Interperiodica".*

INTRODUCTION

In recent years, considerable interest has been expressed by researchers in organic crystalline materials with specific physical properties dictated by the symmetry of the crystal structure. This has given impetus to the investigations concerned with the revelation of the factors responsible for the crystallization of a material in a particular space group [1]. It is evident that the intermolecular interactions are of crucial importance in the formation of the crystal structure, and the intermolecular hydrogen bonds fulfill the major structure-forming function [2]. Despite notable progress toward an understanding of the basic principles of molecular aggregation in crystals [3], this problem requires further in-depth investigation. The Cambridge Crystal Structure Database remains the main tool for structural studies in this field; however, the investigation into specific series of organic molecules can also be very useful.

In particular, the convenient model compounds in studies of the influence of hydrogen bonding on the molecular conformation and packing in crystals are the dihydro derivatives of piperidine, which we have examined in the framework of structural investigations into the products of oxidative coupling of 4-phenyl-1,2,5,6-tetrahydropyridine and 4-pyridyl-1,2,5,6-tetrahydropyridine with acetone (or acetonitrile) in the presence of $KMnO_4$ [4]. The molecules of these compounds possess the conformational flexibility and can form an extended network of intramolecular and intermolecular hydrogen bonds in crystals. It is known that the crystallization of compounds with conformationally flexible molecules is accompanied, with a high probability, by the formation of different polymorphic modifications [5]. Molecules with several potential proton donors and acceptors rather frequently can form several polymorphic modifications due to the formation of different networks of hydrogen bonds in crystals. Furthermore, the compounds with hydroxy groups often crystallize to form very unusual and interesting packings. It will suffice to mention that, for example, in alcohols, the percentage of crystals whose structure involves several systems of equivalent molecular sites is substantially higher (more than 40%) than that, as a whole, for compounds available in the Cambridge Crystal Structure Database (~8.3%) [3]. This is likely due to the fact that the formation of stable molecular associates in crystals occurs through hydrogen bonding. There are grounds to believe that the above regularities manifest themselves in the crystal structures of the compounds under consideration.

Earlier, we determined the structures of 3,4-dihydroxy-2-oxo-1-methyl-4-(phenyl)piperidine (**I**) [6], 3,4-diacetyl-2-oxo-1-methyl-4-(phenyl)piperidine

1063-7745/00/4501-0078$20.00

(**III**) [7], and 3,4-dihydroxy-1-methyl-2-oxo-4-(pyridyl)piperidine (**IV**) [8].

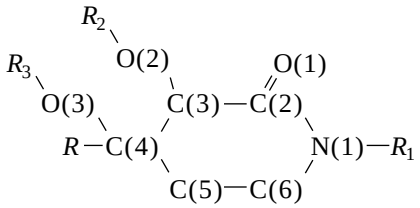

I *R* – *Ph*, R_1 – *Me*, R_2 – H, R_3 – H

II *R* – *Ph*, R_1 – *Me*, R_2 – H, R_3 – *Ac*

III *R* – *Ph*, R_1 – *Me*, R_2 – *Ac*, R_3 – *Ac*

IV *R* – *Py*, R_1 – *Me*, R_2 – H, R_3 – H

V *R* – *Py*, R_1 – *Et*, R_2 – H, R_3 – H

VI *R* – *Py*, R_1 – CH_2Ph, R_2 – H, R_3 – H

In the present work, we carried out the X-ray diffraction analysis of 1-methyl-2-oxo-3-acetoxy-4-hydroxy-4-(phenyl)hydropyridine (**II**) (the molecular structure is shown in Fig. 1, and the atomic coordinates are listed in Table 1), 1-ethyl-2-oxo-3,4-dihydroxy-4-(pyridyl)piperidine (**V**) (the general view of the molecule is depicted in Fig. 2, and the atomic coordinates are given in Table 2), and 1-benzyl-2-oxo-3,4-dihydroxy-4-(pyridyl)piperidine (**VI**) (Fig. 3, Table 3).

EXPERIMENTAL

Crystals **II** ($C_{14}H_{19}NO_5$, M = 281.30) are monoclinic, space group $C2/c$, at 20°C: a = 23.586(5) Å, b = 7.986(2) Å, c = 18.523(4) Å, β = 122.90(3)°, V = 2929(1) Å^3, Z = 8, and d_{calcd} = 1.276 g/cm^3.

Crystals **V** ($C_{12}H_{16}N_2O_3$, M = 236.27) are monoclinic, space group $P2_1$, at 20°C: a = 5.8315(9) Å, b = 10.081(2) Å, c = 9.635(2) Å, β = 90.52(1)°, V = 566.4(2) Å^3, Z = 2, and d_{calcd} = 1.385 g/cm^3.

Crystals **VI** ($C_{17}H_{18}N_2O_3$, M = 298.33) are monoclinic, space group $P2_1/n$, at 20°C: a = 9.8193(11) Å, b = 13.401(2) Å, c = 11.1205(13) Å, β = 92.996(9)°, V = 1461.4(3) Å^3, Z = 4, and d_{calcd} = 1.356 g/cm^3.

The unit cell parameters and the reflection intensities were measured on a Siemens P3 / PC automated four-circle diffractometer (T = 20°C, λMoK_α, graphite monochromator, θ/2θ scan mode, θ_{max} = 25°). The structures were solved by the direct method and refined by the full-matrix least-squares procedure in the anisotropic approximation for the non-hydrogen atoms. The hydrogen atoms were independently located from the difference Fourier synthesis and refined in the isotropic approximation. The hydrogen atoms of the hydroxy groups in structure **VI** are disordered over two positions—H(2O) and H(2'O) at the O(2) oxygen atom and H(3O) and H(3'O) at the O(3) oxygen atom with occupancies of 0.50 and 0.60 in the former case and 0.60 and 0.30 in the latter case, respectively. The final discrepancy factors are as follows: R_1 = 0.037 for 1827 independent reflections with $I > 2\sigma(I)$ and wR_2 = 0.112 for 2557 independent reflections for structure **II**, R_1 = 0.037 for 1053 independent reflections with $I > 2\sigma(I)$ and wR_2 = 0.102 for all 1057 independent reflections for structure **V**, and R_1 = 0.041 for 2141 independent reflections with $I > 2\sigma(I)$ and wR_2 = 0.100 for 2858 independent reflections for structure **VI**. All the calculations were performed on an IBM PC/AT-486 with the SHELXTL PLUS software package.

RESULTS AND DISCUSSION

The bond lengths and angles in all the studied compounds have normal values [9].

The main geometric parameters characterizing the structure and conformation of all the studied compounds are compared in Table 4. It is significant that

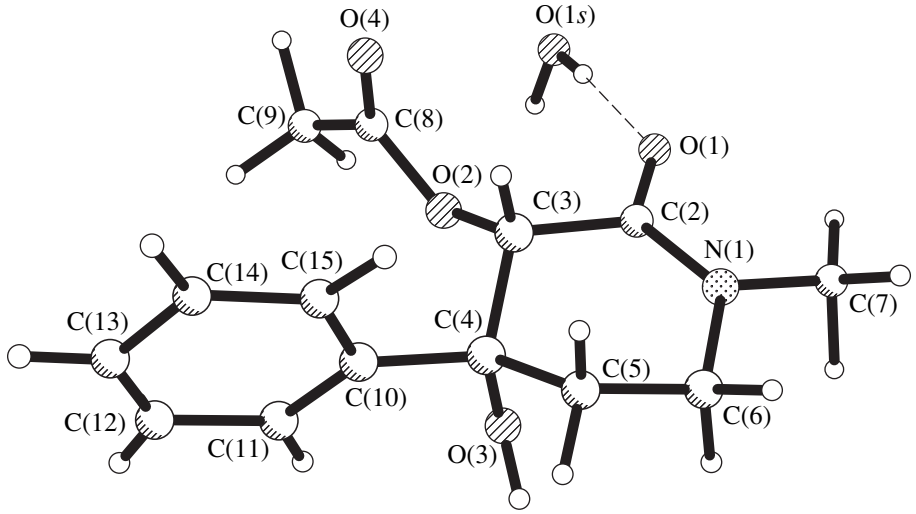

Fig. 1. Structure of molecule **II**.

Table 1. Atomic coordinates ($\times 10^4$) and equivalent (isotropic for H atoms) thermal parameters ($\times 10^3$, Å^2) in structure **II**

Atom	*x*	*y*	*z*	U_{eq}/U_{iso}
O(1)	3792(1)	6057(2)	7619(1)	71(1)
O(2)	3418(1)	5150(1)	8695(1)	42(1)
O(3)	3160(1)	1989(2)	8069(1)	43(1)
O(4)	4161(1)	6563(2)	9882(1)	91(1)
N(1)	4115(1)	3434(2)	7565(1)	53(1)
C(2)	3936(1)	4630(2)	7912(1)	48(1)
C(3)	3944(1)	4196(2)	8718(1)	39(1)
C(4)	3819(1)	2342(2)	8788(1)	38(1)
C(5)	4344(1)	1392(2)	8709(1)	45(1)
C(6)	4234(1)	1679(2)	7835(1)	53(1)
C(7)	4058(2)	3787(4)	6754(2)	79(1)
C(8)	3588(1)	6252(2)	9328(1)	52(1)
C(9)	2974(1)	6976(4)	9250(2)	68(1)
C(10)	3871(1)	2025(2)	9633(1)	43(1)
C(11)	3307(1)	1638(3)	9648(2)	61(1)
C(12)	3368(2)	1437(3)	10441(2)	82(1)
C(13)	3979(2)	1637(3)	11197(2)	78(1)
C(14)	4541(2)	2019(3)	11187(2)	72(1)
C(15)	4489(1)	2213(3)	10415(1)	57(1)
O(1*S*)	3048(1)	8785(2)	7553(1)	75(1)
H(3)	4386(8)	4508(21)	9219(11)	39(4)
H(4O)	3138(11)	904(32)	7938(15)	79(7)
H(5*A*)	4768(10)	1753(24)	9133(12)	52(5)
H(5*B*)	4286(9)	190(25)	8776(11)	53(5)
H(6*A*)	4630(11)	1289(25)	7837(12)	65(6)
H(6*B*)	3840(10)	1007(24)	7389(12)	53(5)
H(7*A*)	4485(15)	3438(37)	6787(16)	95(8)
H(7*B*)	3945(12)	4974(29)	6576(14)	43(5)
H(7*C*)	3549(24)	2964(44)	6208(28)	115(9)
H(9*A*)	3163(19)	8188(40)	9582(15)	99(9)
H(9*B*)	2848(17)	6158(35)	9597(18)	91(8)
H(9*C*)	2553(15)	7028(33)	8591(13)	70(7)
H(11)	2870(10)	1481(24)	9105(13)	57(5)
H(12)	2953(13)	1172(30)	10335(15)	84(8)
H(13)	4007(12)	1532(32)	11741(18)	97(8)
H(14)	4966(13)	2171(33)	11757(18)	99(8)
H(15)	4885(11)	2443(26)	10384(13)	67(6)
H(1*S*)	2629(15)	8354(33)	7285(17)	95(8)
H(2*S*)	3316(12)	7979(33)	7627(14)	77(7)

Table 2. Atomic coordinates ($\times 10^4$, $\times 10^3$ for H atoms) and equivalent (isotropic for H atoms) thermal parameters ($\times 10^3$, Å^2) in structure **V**

Atom	*x*	*y*	*z*	U_{eq}/U_{iso}
O(1)	−4891(4)	1453(3)	−244(2)	38(1)
O(2)	−4262(4)	2094(3)	2449(2)	36(1)
O(3)	564(3)	2220(2)	1924(2)	25(1)
N(1)	−1919(4)	2722(3)	−962(2)	26(1)
N(12)	−355(4)	5701(3)	5641(2)	29(1)
C(2)	−3390(5)	2290(3)	2(3)	26(1)
C(3)	−3302(5)	2953(3)	1438(3)	26(1)
C(4)	−879(5)	3358(3)	1866(3)	24(1)
C(5)	−7(5)	4257(3)	702(3)	26(1)
C(6)	130(6)	3524(3)	−669(3)	29(1)
C(7)	−2210(6)	2275(4)	−2399(3)	33(1)
C(8)	−3954(7)	3099(4)	−3166(4)	41(1)
C(9)	−786(5)	4137(3)	3225(3)	23(1)
C(10)	1175(5)	4092(3)	4064(3)	26(1)
C(11)	1311(5)	4886(3)	5234(3)	30(1)
C(13)	−2229(6)	5751(4)	4828(3)	31(1)
C(14)	−2501(5)	5014(3)	3625(3)	29(1)
H(20)	−549(7)	189(4)	217(4)	38(11)
H(30)	21(6)	178(4)	275(4)	33(9)
H(3)	−423(5)	378(4)	131(3)	26(8)
H(5*A*)	−98(6)	506(4)	62(3)	27(8)
H(5*B*)	145(6)	451(3)	87(3)	21(8)
H(6*A*)	152(6)	289(4)	−76(4)	39(9)
H(6*B*)	42(6)	418(4)	−142(4)	26(8)
H(7*A*)	−268(7)	138(5)	−235(4)	44(10)
H(7*B*)	−82(6)	237(4)	−278(3)	32(9)
H(8*A*)	−393(6)	289(5)	−415(5)	51(11)
H(8*B*)	−543(7)	299(5)	−283(4)	45(11)
H(8*C*)	−360(7)	407(5)	−303(4)	38(9)
H(10)	242(7)	351(4)	388(4)	40(10)
H(11)	271(8)	482(5)	588(4)	55(12)
H(13)	−341(6)	636(4)	505(4)	34(9)
H(14)	−393(6)	512(4)	314(4)	30(9)

despite a considerable conformational flexibility of the hydropyridine cycle, its conformation remains virtually unchanged in molecules with the same substituent *R* at the C(4) atom. In the case when *R* = *Ph* (structures **I**–**III**), the cycle adopts an asymmetric half-chair conformation with a flattened system of the four atoms C(6), N(1), C(2), and C(3). For *R* = *Py* (structures **IV**–**VI**), the conformation of the hydropyridine cycle is more correctly described as a flattened chair [the C(2), C(3), C(5), and C(6) atoms lie in the same plane]. Of course,

it is impossible to answer the question regarding the causes of this difference exactly: with equal probability, these can be both the electronic effects of the *R* substituent and the changes observed in the system of intramolecular and intermolecular hydrogen bonds upon incorporation of an additional heteroatom—a potential proton acceptor.

The remaining substituents have a less pronounced effect on the conformation of the hydropyridine cycle in molecules **I**–**VI**. It should be only mentioned that the C(6)–N(1)–C(2)–C(3) torsion angles responsible for the planarity of the hydropyridine cycle in compounds **I**–**III** decrease with an increase in the size of the substituents at the C(3) and C(4) atoms: 9.5°, 8.4°, and 5.3° in molecules **I**, **II**, and **III**, respectively. The root-mean-square deviations of atoms from the plane decrease in the same order (Table 4). This, at first glance, unexpected result is explained by the absence of hydrogen bonds capable of distorting the conformation of the hydropyridine cycle in the crystal and in the molecule of compound **III** as contrasted to molecules of compounds **I** and **II**, in which the hydrogen bonds exist and this effect likely takes place. The other endocyclic torsion angles characterizing the conformation of the hydropyridine cycle in molecules **I**–**III** are equal to each other within the limits of experimental error. Some discrepancies are accounted for by the differences in positions of the C(4) and C(5) atoms with respect to the mean plane of the cycle: substantially larger deviations from the plane are observed for the C(4) atom in molecule **II** and for the C(5) atom in molecules **I** and **III**. From the foregoing, it can be concluded that variations in the geometric characteristics in the series of compounds **I**–**III** are most likely connected with the influence of crystal environment, i.e., with changes in the system of hydrogen bonds.

Although the N(1) and C(2) atoms in molecules **IV**–**VI**, as in molecules **I**–**III**, exhibit a trigonal-planar configuration, the C(6)–N(1)–C(2)–C(3) angles in molecules **V** and **VI** are increased up to 16.4° and 16.5°, respectively. Therefore, as mentioned above, the conformation of the hydropyridine cycle is described by a flattened half-chair. In compounds **IV**–**VI**, which differ only in the substituent at the N(1) atom, the conformation of the nonrigid hydropyridine cycle is even less flexible: the root-mean-square deviations of atoms from the mean C(2)–C(3)–C(5)–C(6) plane, the deviations of the C(4) and N(1) atoms from this plane, and the endocyclic torsion angles are respectively almost identical (Table 4), even though there are some differences in the systems of intramolecular hydrogen bonds in structures **V** and **VI**.

The orientation of the side substituents in all the compounds under consideration remains unaltered. The phenyl (or pyridyl) group at the C(4) atom occupies the equatorial position, the hydroxy (or acetoxy) group at the C(4) atom is in the axial position, and the O(2)R_2 substituent at the C(3) atom has the equatorial

Table 3. Atomic coordinates ($\times 10^4$) and equivalent (isotropic for H atoms) thermal parameters ($\times 10^3$, Å^2) in structure **VI**

Atom	*x*	*y*	*z*	U_{eq}/U_{iso}
O(1)	4679(1)	8064(1)	10787(1)	57(1)
O(2)	4477(2)	6751(1)	9037(1)	57(1)
O(3)	1576(2)	7093(1)	8876(1)	46(1)
N(1)	2645(1)	7669(1)	11527(1)	38(1)
N(2)	2079(2)	3502(1)	7619(2)	53(1)
C(1)	2722(2)	8523(1)	12359(2)	45(1)
C(2)	3671(2)	7517(1)	10808(2)	39(1)
C(3)	3627(2)	6593(1)	10004(2)	39(1)
C(4)	2178(2)	6309(1)	9566(1)	33(1)
C(5)	1364(2)	6201(1)	10691(2)	39(1)
C(6)	1321(2)	7170(1)	11392(2)	43(1)
C(7)	2189(2)	9488(1)	11812(1)	39(1)
C(8)	3010(2)	10070(1)	11129(2)	48(1)
C(9)	2550(2)	10965(2)	10653(2)	60(1)
C(10)	1257(2)	11291(2)	10851(2)	61(1)
C(11)	422(2)	10715(2)	11522(2)	66(1)
C(12)	884(2)	9815(2)	11998(2)	54(1)
C(13)	2171(2)	5329(1)	8865(1)	33(1)
C(14)	2717(2)	4460(1)	9373(2)	44(1)
C(15)	2648(2)	3583(1)	8732(2)	51(1)
C(16)	1573(2)	4340(2)	7136(2)	55(1)
C(17)	1591(2)	5255(1)	7714(2)	45(1)
H(2O)	4955(35)	7379(27)	9270(30)	41(9)
H(3O)	2211(29)	7370(22)	8330(26)	41(8)
H(2'O)	3808(32)	6915(21)	8443(27)	44(9)
H(3'O)	777(78)	6890(53)	8658(62)	47(22)
H(1*A*)	2180(20)	8332(14)	13052(18)	57(5)
H(1*B*)	3669(21)	8598(13)	12647(16)	51(5)
H(3)	4050(18)	6012(13)	10491(16)	46(5)
H(5*A*)	1790(18)	5670(13)	11168(15)	46(5)
H(5*B*)	411(19)	6006(13)	10430(16)	47(5)
H(6*A*)	654(18)	7644(14)	11014(15)	47(5)
H(6*B*)	1042(19)	7033(13)	12183(17)	52(5)
H(8)	3916(22)	9845(16)	10970(18)	67(6)
H(9)	3118(24)	11396(17)	10227(20)	78(7)
H(10)	934(23)	11948(17)	10537(20)	79(7)
H(11)	–443(25)	10943(18)	11670(20)	82(7)
H(12)	299(23)	9464(16)	12447(20)	74(7)
H(14)	3138(19)	4458(14)	10196(18)	56(5)
H(15)	3067(20)	2995(15)	9037(17)	59(6)
H(16)	1150(23)	4266(16)	6298(21)	74(7)
H(17)	1227(21)	5818(15)	7334(18)	63(6)

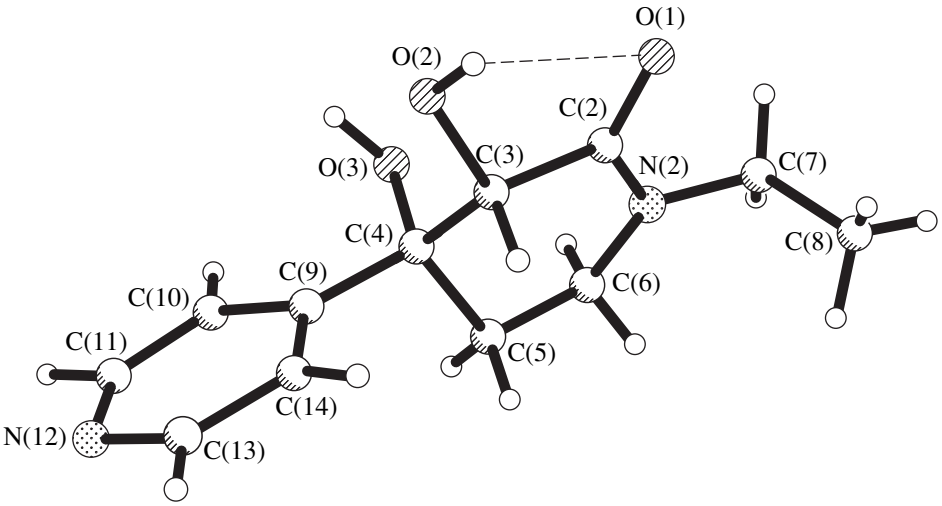

Fig. 2. Structure of molecule **V**.

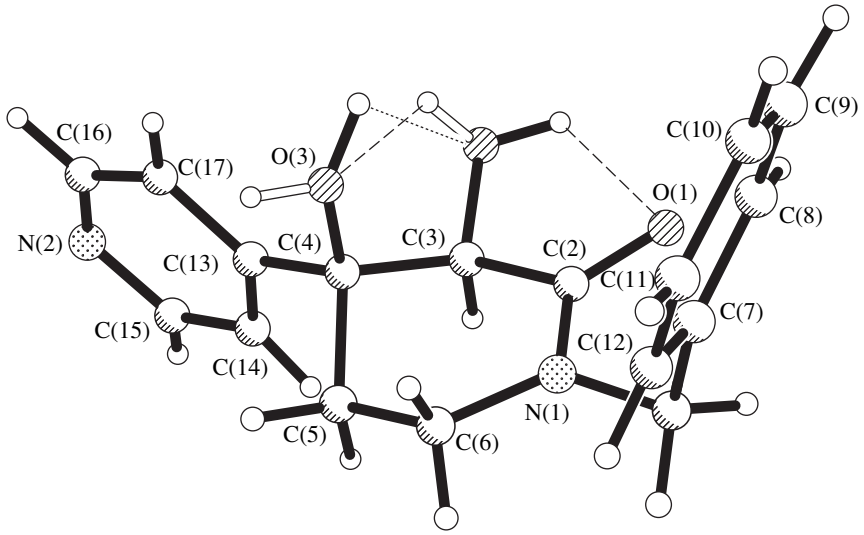

Fig. 3. Structure of molecule **VI**.

orientation. However, the relevant exocyclic torsion angles characterizing the arrangement of substituents are somewhat different. Apparently, the effect of the crystal environment also manifests itself in this case.

Now, we attempt to analyze the influence of hydrogen bonds on the molecular conformation. In diol **I**, the intramolecular hydrogen bond O(3)–H··O(2) [O··O, 2.715(6) Å; H··O, 2.26(5) Å, and O–H··O, 114(3)°] is formed between two hydroxy groups of the molecule. In compounds **II** and **III**, the intramolecular hydrogen bonds are not observed at all. In diols **IV**–**VI**, the hydrogen bond O(2)–H··O(1) is formed between the equatorial hydroxy group at the C(3) atom and the oxygroup of the molecule. This bond is appreciably weaker; it was not described in molecule **IV** by Bekro *et al.* [8], and its parameters in molecule **V** are as follows: O··O, 2.695(4) Å; H··O, 2.40(3) Å; and O–H–O, 104(2)°. In some sense, the system of intramolecular hydrogen bonds in molecule **VI** can be considered as intermediate between the two above variants: there is a disordering (most probably, dynamic) in the positions of protons of both hydroxy groups. Likely, at certain instants of time, all the possible intramolecular hydrogen bonds occur in this molecule (Fig. 3). The O(3)··O(2) and O(2)··O(1) distances are equal to 2.882(2) and 2.624(2) Å, respectively. Possibly, it is these differences in the systems of intramolecular hydrogen bonds which are responsible for the stabilization of a particular conformation of the hydropyridine cycle in the molecules.

Before proceeding to consideration of the role of hydrogen bonds in the formation of molecular packing in crystals, we briefly dwell on the symmetry of the crystal structure itself. All the molecules studied are

Table 4. Main geometric characteristics of studied molecules **I–VI**

Characteristic	**I**	**II**	**III**	**IV**	**V**	**VI**
Space group	$Pna2_1$	$C2/c$	$P2_1/n$	$P2_1$	$P2_1$	$P2_1/n$
Z	8	8	4	2	2	4
Root-mean-square deviation from the plane						
N(1)–C(2)–C(3)–C(6)	0.028	0.026	0.017		0.050	0.119
C(2)–C(3)–C(5)–C(6)				0.30	0.038	0.037
Deviation of the other atoms of cycle from the plane						
C(4)	−0.286	−0.528	−0.368	−0.720	−0.733	−0.717
C(5)	0.452	0.256	0.416			
N(1)				0.240	0.195	0.195
Conformation of hydropyridine cycle	Asymmetric half-chair			Flattened chair		
Endocyclic torsion angle						
C(6)–N(1)–C(2)–C(3)	9.5	8.4	5.3	*	16.4	16.5
N(1)–C(2)–C(3)–C(4)	–19.1	–17.5	–19.6	*	–34.4	–33.8
C(2)–C(3)–C(4)–C(5)	44.3	45.7	46.6	*	56.0	54.6
C(3)–C(4)–C(5)–C(6)	−61.0	−63.4	−63.0	*	−62.6	–56.6
C(4)–C(5)–C(6)–N(1)	52.3	54.5	52.3	*	45.3	44.7
C(5)–C(6)–N(1)–C(2)	–26.0	–28.2	–21.7	*	–21.9	–21.9
Exocyclic torsion angle						
O(1)–C(2)–C(3)–O(2)	42.0	34.6	40.4	*	26.8	23.9
O(2)–C(3)–C(4)–O(3)	52.1	57.0	52.7	*	63.0	62.3
C(2)–C(3)–C(4)–C(9)	164.5	177.2	171.7	*	174.4	174.7
Orientation of side substituents						
R	Equatorial	Equatorial	Equatorial	Equatorial	Equatorial	Equatorial
$-O_2R_2$	Axial	Axial	Axial	Axial	Axial	Axial
$-O_3R_3$	Equatorial	Equatorial	Equatorial	Equatorial	Equatorial	Equatorial
Angle between planes of R and hydropyridine	101.1	87.7	106.0	59.2	59.9	61.1

* Not given in [8].

Table 5. Parameters of intermolecular hydrogen bonds in crystal structures **II**, **V**, and **VI**

Structure	Hydrogen bond	$R(X\cdots Y)$, Å	$d(H\cdots Y)$, Å	XHY angle, deg
II	O(1*s*)–H(2)···O(1)	2.758(2)	1.91(2)	171(1)
	O(3)–H···O(1*s*)	2.693(2)	1.80(2)	174(1)
	O(1*s*)H···O(3)	2.817(2)	1.94(2)	165(1)
V	O(2)–H(20)···O(3)	3.058(4)	2.34(3)	152(2)
	O(3)–H(30)···N(2)	2.805(4)	1.90(3)	164(2)
VI	O(3)–H(30)···N(2)	2.881(2)	1.99(3)	152(3)

chiral and exist in a solution as a racemic mixture of enantiomers. At $R = Ph$, the enantiomeric pairs of molecules **I–III** crystallize in the racemic space groups (the $Pna2_1$ space group, even if noncentrosymmetric, is racemic as well; furthermore, in crystal **I**, there are two symmetrically independent molecules related by the pseudocenter of inversion [6]). In the case when $R = Py$, at $R_1 = CH_2Ph$ (compound **VI**), the crystal with space group $P2_1/n$ is also built up of molecules with different chirality, and, upon crystallization of compounds **IV** and **V** (R = *Me* or *Et*), the enantiomers are spontaneously separated, and both compounds crystallize in the chiral space group $P2_1$.

Let us elucidate the role of intermolecular hydrogen bonds in the formation of the crystal structures of the studied compounds. The system of intermolecular

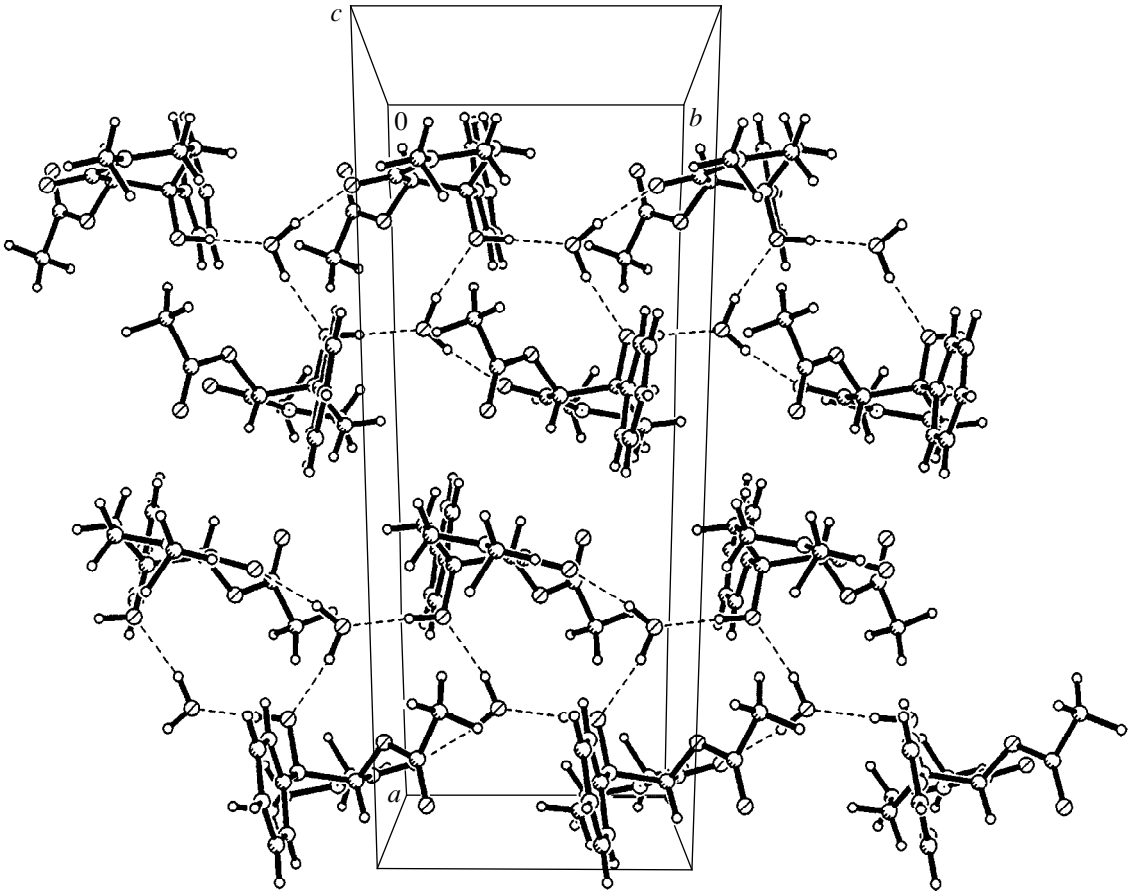

Fig. 4. Packing of the chains with different chirality in crystal **II**.

hydrogen bonds in structure **I** was described in detail in [6]. The crystallographically independent molecules (a pair of enantiomers) are joined into the stable pseudocentrosymmetric dimers through the hydrogen bonds O(3)–H··O'(1). In turn, these dimers are linked by the hydrogen bonds O(2)–H··O(1) (x, 1 + y, z) into ribbons with the $P_c\bar{1}$ pseudosymmetry. Owing to the van der Waals interactions, these ribbons form close-packed layers aligned parallel to the $XY0$ plane. In the crystal, the layers are shifted relative to one another, which leads to the loss of the crystallographic center of inversion, but, apparently, provides a closer packing. Otherwise, in the absence of the shift, the centrosymmetric space group *Pbcn* would be realized in the crystal [6]. It is interesting that this hypothetical situation was observed in the actual crystalline structures of 4-amino-*N*-(4-methyl-2-pyrimidinyl)benzosulfamide [10], which occurs in two polymorphic orthorhombic modifications $Pn2_1a$ and *Pbca*. Both modifications exhibits a repetitive structural motif of centrosymmetric (space group *Pbca*) and pseudocentrosymmetric (space group $Pn2_1a$) dimers. The difference in packings, as in our case, stems from the different arrangement of the layers. Note that, as could be expected, the density of the noncentrosymmetric crystal with the pseudocenter is higher (1.43 g/cm^3, space group $Pn2_1a$) than that of the centrosymmetric crystal (1.35 g/cm^3, space group *Pbca*).

In crystals **II**, the molecules with the same chirality and the solvated water molecules are joined by the intermolecular hydrogen bonds O(1*S*)–H(2)··O(1), O(3)–H··O(1*S*) (x, –1 + y, z), and O(1*S*)–H··O(3) (0.5 – x, –0.5 + y, 1.5 – z) (Table 5) into helixes around the 2_1 axes (Fig. 4). The crystal as a whole can be represented as a packing of helixes with different chirality that are bound to one another only by the van der Waals bonds, and, hence, the space group is centrosymmetric.

In compound **III**, the hydrogen bonds are absent, and the crystal is built up of enantiomeric molecular pairs according to the principles of close packing [7].

Crystals **IV** and **V**, which differ only in the substituent (*Me* or *Et*) at the N(1) atom, crystallize in space group $P2_1$ and possess identical systems of intermolecular hydrogen bonds: the puckered layers of molecules with the same chirality are formed by the hydrogen bonds O(2)–H··O(3) (–1 + x, y, z) and O(3)–H··N(2) (–x, –0.5 + y, 1 – z) (Table 5) and are aligned parallel to the $XY0$ plane (Fig. 5). The layers are arranged congru-

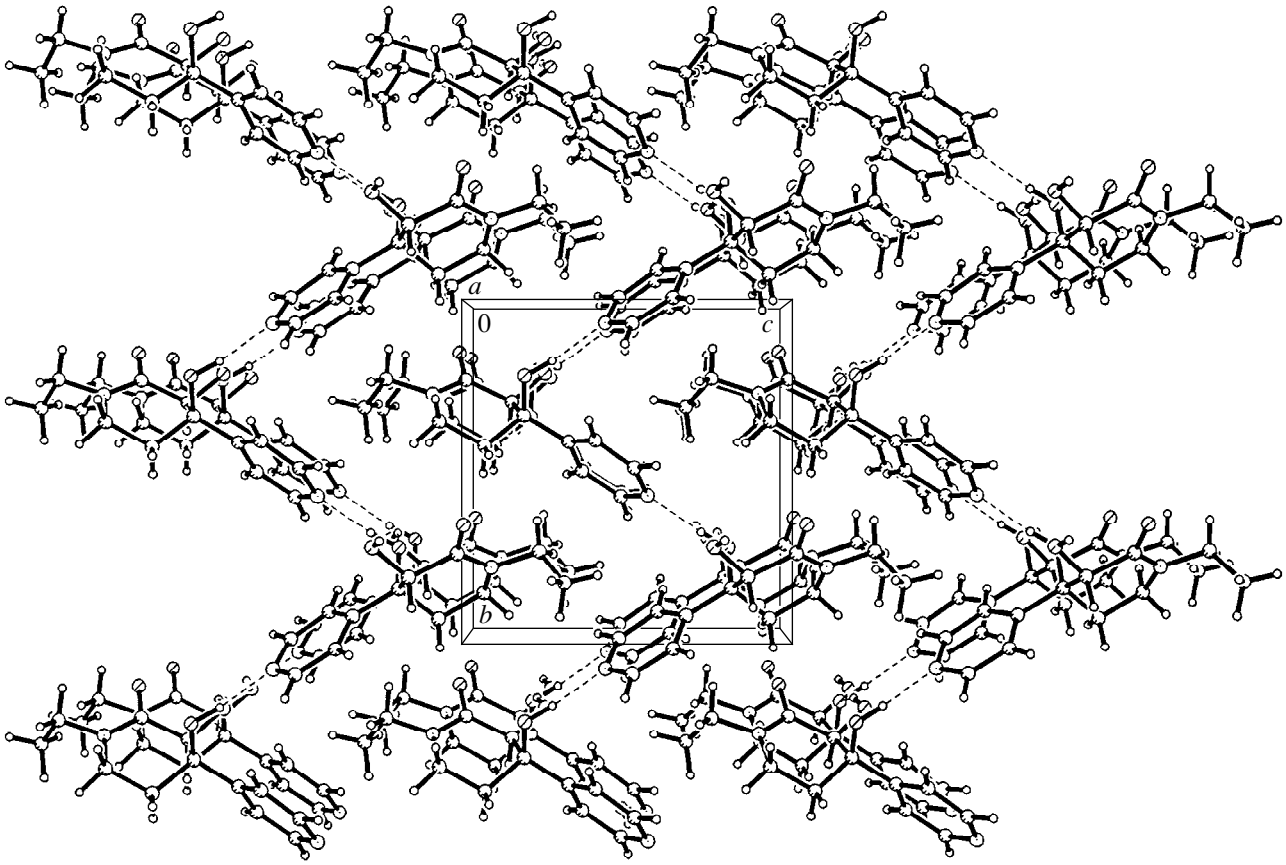

Fig. 5. Packing of the layers with identical chirality in crystal **V**.

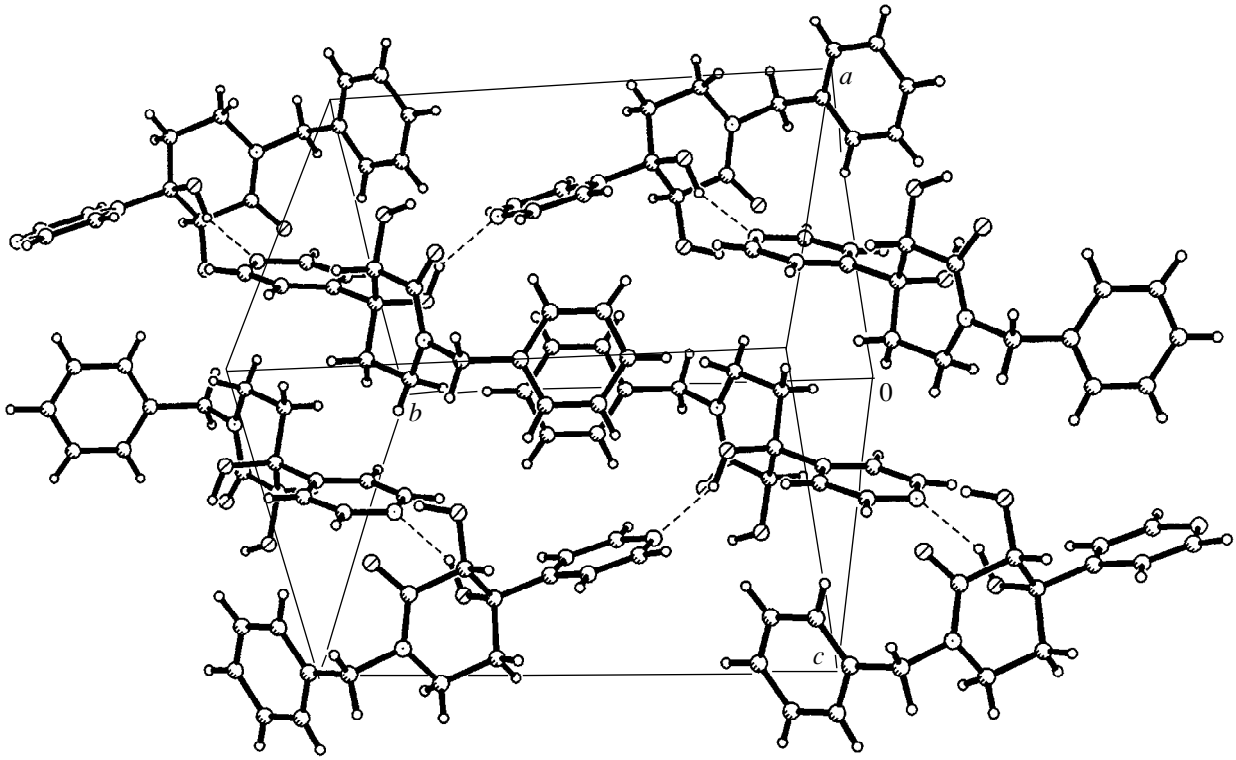

Fig. 6. Packing of the chains with different chirality in crystal **VI**.

ently without inversion, which results in the spontaneous separation of enantiomers.

In crystals **VI**, the molecules with the same chirality are joined by the hydrogen bonds O(3)–H··N(2) (0.5 – *x*, 0.5 + *y*, 1.5 – *z*) (Table 5) into infinite helixes parallel to the *Y*-axis (Fig. 6). These helixes are similar to those in crystals **II**, but free from solvated molecules. However, as in **II**, the crystal as whole is represented not as a congruent superimposition of these chains, but as a packing of helixes with different chirality, which gives rise to the centrosymmetric space group $P2_1/n$.

Therefore, the presence of the stable associate composed of molecules with the same chirality does not ensure the separation of enantiomers upon crystallization, even though it undoubtedly increases the probability of such a separation.

ACKNOWLEDGMENTS

This work was supported the Russian Foundation for Basic Research, project nos. 97-03-33783a and 96-03-33432a.

REFERENCES

1. C. P. Brock and J. D. Dunitz, Chem. Mater. **6,** 1118 (1994).
2. G. R. Desiraju, Angew. Chem. Int. Ed. Engl. **34,** 2311 (1995).
3. A. Gavezzotti, Acc. Chem. Res. **27,** 309 (1994).
4. A. T. Soldatenkov, I. A. Bekro, S. A. Mamyrbekova, *et al.*, Khim. Geterotsikl. Soedin., No. 5, 659 (1997).
5. J. D. Dunitz and J. Bernstein, Acc. Chem. Res. **28,** 193 (1995).
6. L. N. Kuleshova, V. N. Khrustalev, Yu. T. Struchkov, *et al.*, Kristallografiya **41** (4), 673 (1996).
7. L. N. Kuleshova, V. N. Khrustalev, Yu. T. Struchkov, *et al.*, Kristallografiya **41** (4), 755 (1996).
8. I. F. Bekro, A. T. Soldatenkov, A. T. Stash, *et al.*, Khim. Geterotsikl. Soedin., No. 10, 1372 (1996).
9. F. H. Allen, O. Kennard, D. J. Watson, *et al.*, J. Chem. Soc., Perkin Trans. **2,** 1 (1987).
10. M. R. Caira and R. Mohamed, Acta Crystallogr., Sect. B: Struct. Sci. **48,** 492 (1992).

Translated by O. Borovik-Romanova

Crystallography Reports, Vol. 45, No. 1, 2000, pp. 87–90. Translated from Kristallografiya, Vol. 45, No. 1, 2000, pp. 93–96.

STRUCTURES OF ORGANIC COMPOUNDS

Crystal and Molecular Structure of the 1 : 1 Molecular Complex between 1*e*-Benzyl-3*e*-Hydroxy-3*a*-Methyl-4*a*-Tosylhydrazo-6*e*-Phenylpiperidine-4*e*-Carbonitrile and Diethyl Ether

A. S. Lyakhov, A. A. Govorova, T. T. Lakhvich, and L. S. Stanishevskiĭ

Research Institute of Physicochemical Problems, Belarussian State University, ul. Leningradskaya 14, Minsk, 220080 Belarus

Received November 11, 1997; in final form, March 25, 1998

Abstract—The crystal and molecular structure of the 1 : 1 complex between 1*e*-benzyl-3*e*-hydroxy-3*a*-methyl-4*a*-tosylhydrazo-6*e*-phenylpiperidine-4*e*-carbonitrile and diethyl ether is studied by X-ray diffraction (Nicolet *R*3*m* diffractometer, MoK_α radiation, $\vartheta/2\vartheta$ scan mode). The crystals are triclinic, space group $P\bar{1}$, a = 10.547(4) Å, b = 12.382(5) Å, c = 13.487(6) Å, α = 114.79(3)°, β = 97.28(3)°, γ = 98.40(3)°, and Z = 2. The structure is solved by the direct method and refined to R = 0.0605. Molecular structures and hydrogen bonds are discussed. *© 2000 MAIK "Nauka/Interperiodica".*

INTRODUCTION

Derivatives of β-hydroxy- and α-aminopiperidinecarboxylic acids exhibit various biological properties. Their pharmacological effect depends on the relative configuration of stereogenic centers [1]. However, the orientation of the substituents at the quaternary carbon atom is difficult to determine with the use of IR and ^{1}H NMR spectroscopy because of the ambiguity in data interpretation. A comparison of the spin–spin interaction constants for the axial and equatorial carbon-containing substituents and vicinal hydrogen atoms of the ring ($^3J^a$C,H and $^3J^e$C,H, respectively) is very informative [2, 3]. However, application of this method is limited by the specific structure of the substrate.

We found that the interaction between 1*e*-benzyl-3*e*-hydroxy-3*a*-methyl-6*e*-phenylpiperidine-4-one tosylhydrazone [4] with hydrocyanic acid in methanol results in the formation of two epimeric hydrazonitriles

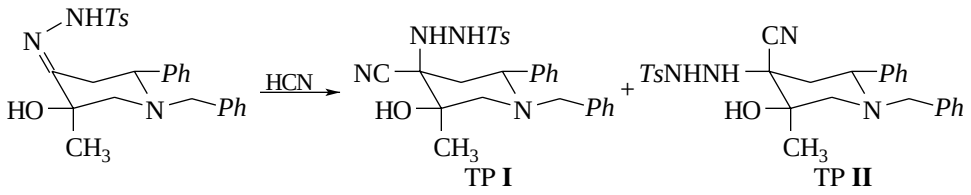

Ph = C_6H_4; *Ts* = SO_2–C_6H_3–CH_3

The purpose of this work is to determine the conformation of one of the stereoisomers obtained.

EXPERIMENTAL

Well-faceted crystals with T_{melt} = 195°C (decomposition) were obtained by crystallization from an ethanol–diethyl ether (10 : 0.5) mixture. A crystal (0.9 × 0.3 × 0.25 mm in size) was chosen for the X-ray diffraction analysis. The three-dimensional set of X-ray diffraction data was collected on a Nicolet *R*3*m* automated four-circle diffractometer (MoK_α radiation, graphite monochromator, $\vartheta/2\vartheta$ scan mode, $2\vartheta_{max}$ = 60°). A total of 8015 reflections was measured, of which 7040 were independent (R_{int} = 0.0206). The compound crystallizes in the triclinic crystal system, space group $P\bar{1}$. The unit-cell parameters are a = 10.547(4) Å, b = 12.382(5) Å, c = 13.487(6) Å, α = 114.79(3)°, β = 97.28(3)°, γ = 98.40(3)°, V = 1547(1) Å^3, Z = 2, d_X = 1.213 g/cm^3, and μ = 1.45 cm^{-1}. The structure was solved by the direct method. The positions of hydrogen atoms were calculated geometrically (except for the hydrogen atoms of the –OH– and –NH–NH– groups, which were located from a difference Fourier synthesis). The non-hydrogen atoms were refined in the anisotropic approximation of thermal vibrations by the full-matrix least-squares procedure. The hydrogen

Table 1. Atomic coordinates ($\times 10^4$) and equivalent isotropic thermal parameters ($Å^2 \times 10^3$) in the structure of the 1 : 1 molecular complex between 1*e*-benzyl-3*e*-hydroxy-3*a*-methyl-4*a*-tosylhydrazo-6*e*-phenylpiperidine-4*e*-carbonitrile and diethyl ether

Atom	*x*/*a*	*y*/*b*	*z*/*c*	U_{eq}
N(1)	−14(2)	4544(2)	7260(2)	50(1)
C(2)	1259(2)	4376(2)	7703(2)	52(1)
C(3)	1800(2)	3512(2)	6745(2)	51(1)
C(4)	832(2)	2294(2)	6007(2)	45(1)
C(5)	−509(2)	2522(2)	5629(2)	47(1)
C(6)	−933(2)	3360(2)	6673(2)	49(1)
C(7)	−456(3)	3062(3)	4803(2)	63(1)
C(8)	−574(3)	5375(2)	8148(2)	60(1)
C(9)	1346(2)	1574(2)	4997(2)	51(1)
N(2)	1707(2)	994(2)	4231(2)	71(1)
N(3)	640(2)	1594(2)	6646(2)	48(1)
N(4)	1740(2)	1123(2)	6839(2)	53(1)
O(1)	−1414(2)	1358(1)	5102(1)	53(1)
S(1)	2182(1)	1370(1)	8147(1)	59(1)
O(2)	2560(2)	2659(2)	8811(2)	71(1)
O(3)	3118(2)	632(2)	8113(2)	78(1)
C(1*a*)	−1853(3)	5562(2)	7675(2)	59(1)
C(2*a*)	−1954(3)	5833(3)	6780(3)	77(1)
C(3*a*)	−3131(4)	5954(4)	6307(4)	103(1)
C(4*a*)	−4220(4)	5788(4)	6700(4)	110(1)
C(5*a*)	−4155(4)	5530(4)	7584(4)	107(1)
C(6*a*)	−2964(3)	5418(3)	8083(3)	83(1)
C(1*b*)	2266(2)	5581(2)	8337(2)	57(1)
C(2*b*)	3124(3)	5771(3)	9294(2)	72(1)
C(3*b*)	4085(3)	6828(4)	9867(3)	91(1)
C(4*b*)	4201(3)	7712(3)	9514(3)	91(1)
C(5*b*)	3370(3)	7544(3)	8576(3)	86(1)
C(6*b*)	2397(3)	6468(3)	7973(3)	70(1)
C(1*c*)	777(2)	815(2)	8504(2)	56(1)
C(2*c*)	455(3)	−405(3)	8280(2)	68(1)
C(3*c*)	−710(4)	−857(3)	8480(2)	78(1)
C(4*c*)	−1564(3)	−127(3)	8903(2)	72(1)
C(5*c*)	−1212(3)	1097(3)	9147(3)	75(1)
C(6*c*)	–58(3)	1571(3)	8955(2)	66(1)
C(7*c*)	−2851(4)	−663(4)	9074(3)	104(1)
O(1*s*)	−3936(2)	1712(2)	5566(2)	97(1)
ë(2*s*)	−4539(4)	1652(5)	6451(5)	131(2)
ë(3*s*)	−4819(4)	1997(5)	4887(5)	132(2)
ë(4*s*)	−3634(6)	1452(5)	7199(5)	148(2)
ë(5*s*)	−4326(5)	1910(5)	3910(5)	146(2)
H(1*o*)	−2220(34)	1459(29)	5256(27)	92(11)
H(3*n*)	− 63(24)	1027(21)	6349(19)	44(6)
H(4*n*)	1705(26)	517(23)	6422(22)	50(8)

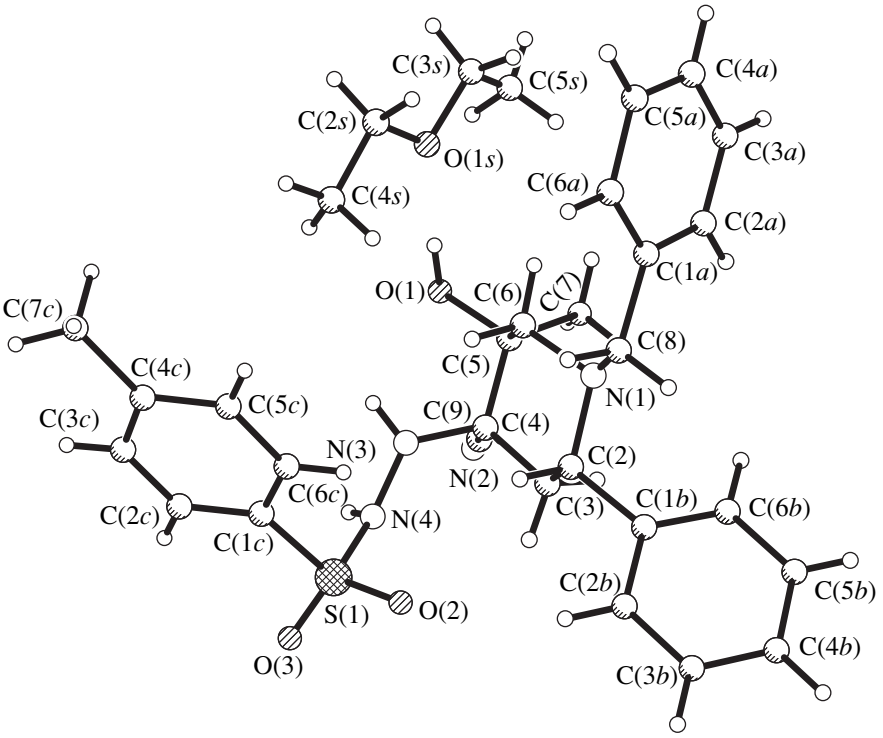

Fig. 1. Molecular structures of TP **I** and diethyl ether and the atomic numbering.

atoms were refined within the riding-atom model (the protons of the –OH– and –NH–NH– groups were refined isotropically). The final discrepancy factors are $R1 = 0.0605$ and $wR2 = 0.1663$ for 3990 reflections with $I > 4\sigma(I)$; $R1 = 0.0985$ and $wR2 = 0.1880$ for all the data. All the calculations were performed with the SHELXS86 [5] and SHELXL93 (*PC* version) [6] programs on an IBM-486 personal computer. The atomic coordinates and equivalent thermal parameters are listed in Table 1.

RESULTS AND DISCUSSION

The X-ray structure analysis revealed that the stereoisomer studied is 1*e*-benzyl-3*e*-hydroxy-3*a*-methyl-4*a*-tosylhydrazo-6*e*-phenylpiperidine-4*e*-carbonitrile (TP **I**) with the axial tosylhydrazo group (in the molecule of the TP **II** epimer, it is equatorial). Note that TP **I** crystallizes as a 1 : 1 molecular complex with a molecule of diethyl ether solvent. Figure 1 shows molecular structures and the atomic numbering. Note some specific structural features of the compound studied. The piperidine ring has the conformation of a distorted chair. The mean deviation of the C(2), C(3), C(5), and C(6) atoms from the rms plane is 0.03 Å, and the C(4)- and N(1)-corners are deflected from the plane by 56.2(2)° and 48.0(2)°, respectively. The benzene rings are planar: the mean atomic deviations from the rms planes of the C(1*a*)··C(6*a*), C(1*b*)··C(6*b*), and C(1*c*)··C(6*c*) rings are 0.005, 0.004, and 0.008 Å, respectively. The rms planes of the above benzene rings are rotated relative to the planar part of the piperidine ring by 60.52(9)°, 89.4(1)°, and 56.5(1)°, respectively. The bond lengths and angles in the piperidine and benzene rings and in the molecule as a whole are normal [7]. The conformation of the TP **I** molecule is additionally stabilized by the intramolecular hydrogen bond (Table 2) between the N(3) atom as a proton donor and the O(1) oxygen atom of the hydroxy group as an acceptor. The geometric characteristics of the diethyl ether molecule only slightly differ from those observed in similar systems studied earlier [8, Tables 2, 3]. Some shortening of the C–C bonds is apparently due to the disordering of the methyl groups of the ether.

Table 2. The parameters of hydrogen bonds in the structure of the 1 : 1 molecular complex between 1*e*-benzyl-3*e*-hydroxy-3*a*-methyl-4*a*-tosylhydrazo-6*e*-phenylpiperidine-4*e*-carbonitrile and diethyl ether

Bond	*D*–H, Å	H··*A*, Å	*D*··*A*, Å	*D*–H··*A*, ω, deg
O(1)–H(1*o*)···O(1*s*)	0.92(3)	1.95(3)	2.862(3)	178(4)
N(3)–H(3*n*)···O(1)	0.86(2)	2.27(2)	2.697(3)	111(2)
N(3)–H(3*n*)···N(2)	0.86(2)	2.58(3)	3.400(4)	161(2)
N(4)–H(4*n*)···O(1)	0.72(3)	2.31(3)	3.021(3)	172(3)

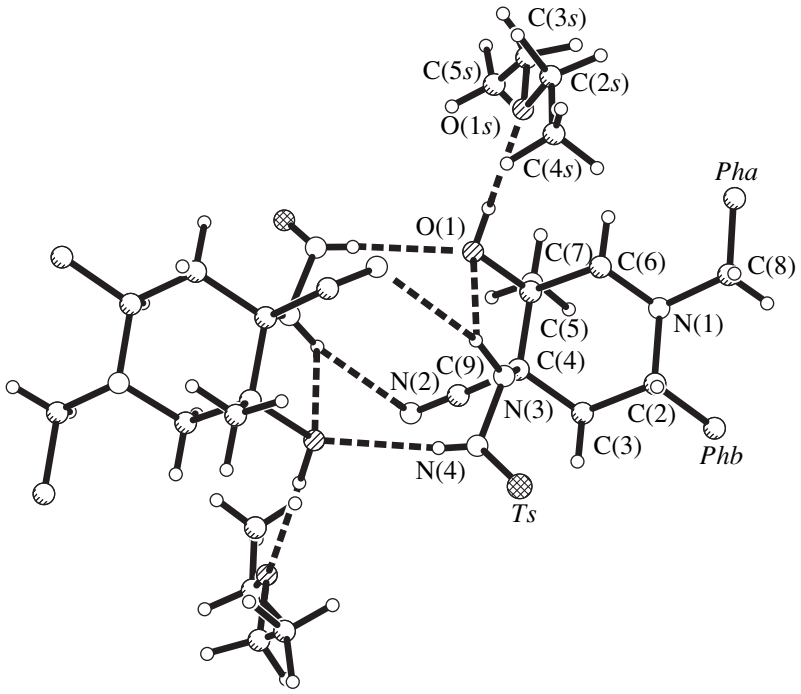

Fig. 2. A structural fragment of the 1 : 1 molecular complex between TP **I** and diethyl ether illustrating the association of four molecules into the hydrogen-bonded aggregate (the hydrogen bonds are shown by dashed lines, *Pha* is the C(1*a*)–C(6*a*) benzene ring, *Phb* is the C(1*b*)–C(6*b*) benzene ring, and *Ts* is the SO_2–C_6H_4–CH_3 tosyl group).

The molecular packing in the crystal is determined by the intermolecular hydrogen bonds (Table 2), which link two TP **I** and two diethyl ether molecules into tetrameric aggregates (Fig. 2). The O(1) oxygen atom of the hydroxy group forms one hydrogen bond as a donor and two bonds as an acceptor of protons (Table 2). In addition to the bridging hydrogen bonds, there is a three-center (bifurcate) hydrogen bond between the N(3) atom as a proton donor and the O(1) and N(2) atoms as acceptors [the O(1)–H(3*n*)–N(2) angle is 78.2(5)°, and the sum of angles at the H(3*n*) atom is 360(3)°]. The tetramers in the structure are connected by the van der Waals forces.

ACKNOWLEDGMENTS

We acknowledge the support of the Russian Foundation for Basic Research (project no. 96-07-89187) in the payment of the licence to use the Cambridge Structural Database, which was employed in the analysis of the results obtained in this work.

REFERENCES

1. P. Jacobsen, I. M. Labouta, K. Schaumburg, *et al.*, J. Med. Chem. **25** (10), 1157 (1982).
2. R. S. Corcoran and J. Ma, J. Am. Chem. Soc. **114** (12), 4536 (1992).
3. T. T. Lakhvich, O. F. Lakhvich, and L. S. Stanishevskiĭ, Khim. Geterotsikl. Soedin., No. 12, 523 (1997).
4. A. M. Zvonok and E. B. Okaev, Khim. Geterotsikl. Soedin., No. 3, 361 (1996).
5. G. M. Sheldrick, *SHELXS86: Program for the Solution of Crystal Structures* (Univ. of Göttingen, Göttingen, 1986).
6. G. M. Sheldrick, *SHELXL93: Program for the Refinement of Crystal Structures* (Univ. of Göttingen, Göttingen, 1993).
7. F. H. Allen, O. Kennard, D. G. Watson, *et al.*, J. Chem. Soc., Perkin Trans. **2**, S1 (1987).
8. F. H. Allen and O. Kennard, Chem. Design Autom. News **8** (1), 31 (1993).

Translated by I. Polyakova

Crystallography Reports, Vol. 45, No. 1, 2000, pp. 91–97. Translated from Kristallografiya, Vol. 45, No. 1, 2000, pp. 97–103.

STRUCTURES OF ORGANIC COMPOUNDS

Crystal Structure of 3-Amino-5-Acetyl-4,7-Dihydro-6-Methyl-4-(2-Nitrophenyl)-2-Cyanothieno[2,3-*b*]-Pyridine and Specific Features of Its Molecular Packing in Crystal

A. E. Lysov*, V. N. Nesterov, K. A. Potekhin*, and Yu. T. Struchkov**†**

** Vladimir State Pedagogical University, Vladimir, Russia*

*** Nesmeyanov Institute of Organoelement Compounds, Russian Academy of Sciences, ul. Vavilova 28, Moscow, GSP-1, 117813 Russia*

Received January 26, 1998; in final form, July 9, 1998

Abstract—The molecular and crystal structures of 3-amino-5-acetyl-4,7-dihydro-6-methyl-4-(2-nitrophenyl)-2-cyanothieno[2,3-*b*]-pyridine is determined by X-ray diffraction. The unit-cell parameters are as follows: a = 14.68(1) Å, b = 8.704(5) Å, c = 25.36(1) Å, V = 3241(6) Å^3, d_{calcd} = 1.453 g/cm^3, Z = 8(1,1), and space group $Pna2_1$. The *o*-nitrophenyl substituent is synperiplanar relative to the hydrogen atom at the C(4) atom of the heterocycle. Two crystallographically independent reference molecules *A* and *B* in the structure can be considered a pair of the enantiomers related by an approximate noncrystallographic center of inversion. The degree of approximation of this pseudocenter is discussed. It is shown that the structure can be described as a combination of two systems of translationally equal layers. The pseudosymmetry of the crystal structure and the possibility of forming a similar molecular packing with a higher crystallographic symmetry are considered. © *2000 MAIK "Nauka/Interperiodica".*

INTRODUCTION

The high biological activity of hydrogenated heterocyclic compounds [1, 2] provokes steady interest in detailed studies of the specific features of their geometric structure. These studies are necessary for estimation of correlations between the structures and properties of the compounds [2]. The possibility of isomerism in the series of compounds under consideration [3–7] results from the presence of a substituent at the sp^3-hybridized carbon atom C(4). A bulky radical at the *ortho* position of this substituent hinders its free rotation about the single C–C bond [8]. Continuing the studies of isomerism in the series of hydrogenated heterocycles [3–7], we determined the X-ray crystal structure of 3-amino-5-acetyl-4,7-dihydro-6-methyl-4-(2-nitrophenyl)-2-cyanothieno[2,3-*b*]-pyridine (**I**).

EXPERIMENTAL

Crystals of compound **I** ($C_{17}H_{14}N_4O_3S$) are orthorhombic; at 20°C, a = 14.68(1) Å, b = 8.704(5) Å, c = 25.36(1) Å, V = 3241(6) Å^3, d_{calcd} = 1.453 g/cm^3, Z = 8(1,1), and space group $Pna2_1$. The unit-cell parameters and intensities of 4523 unique reflections were measured on a Siemens P3/PC four-circle automated diffractometer (λMoK_α, graphite monochromator, $\theta/2\theta$ scan mode, $\theta_{max} = 27°$). The structure was solved by the direct method, which revealed all the non-hydrogen atoms. These atoms were refined by the full-matrix least-squares procedure in the anisotropic approximation using 2210 reflections with $I > 3\sigma(I)$. All the hydrogen atoms were located from difference Fourier syntheses. However, because of large thermal vibrations, only the hydrogen atoms attached to the C(4), N(7), N(18), C(4'), N(7'), and N(18') atoms (there are two independent molecules in structure **I**) were refined with the fixed isotropic thermal parameters U = 0.08 Å^2. The rest of the hydrogen atoms were considered in the refinement at the idealized positions calculated from geometric considerations. The final value of the discrepancy factor R is 0.041 (R_w = 0.041). All the calculations were performed with the SHELXTL PLUS program (PC version) [9].

In crystal **I**, the molecules occupy two systems of equivalent positions. Two crystallographically independent molecules are shown in Fig. 1. The atomic coordinates are listed in the table (the atomic thermal parameters are available from the authors).

A specific feature of this structure is the relation of two crystallographically independent reference molecules *A* and *B* by an approximate noncrystallographic center of inversion into the enantiomeric pair.

Molecules *A* and *B* are close in structure. We calculated the coefficient of noncoincidence [10] after the inversion of one of the molecules. The value of this coefficient is 0.048. The N(20) atom shows the largest

† Deceased.

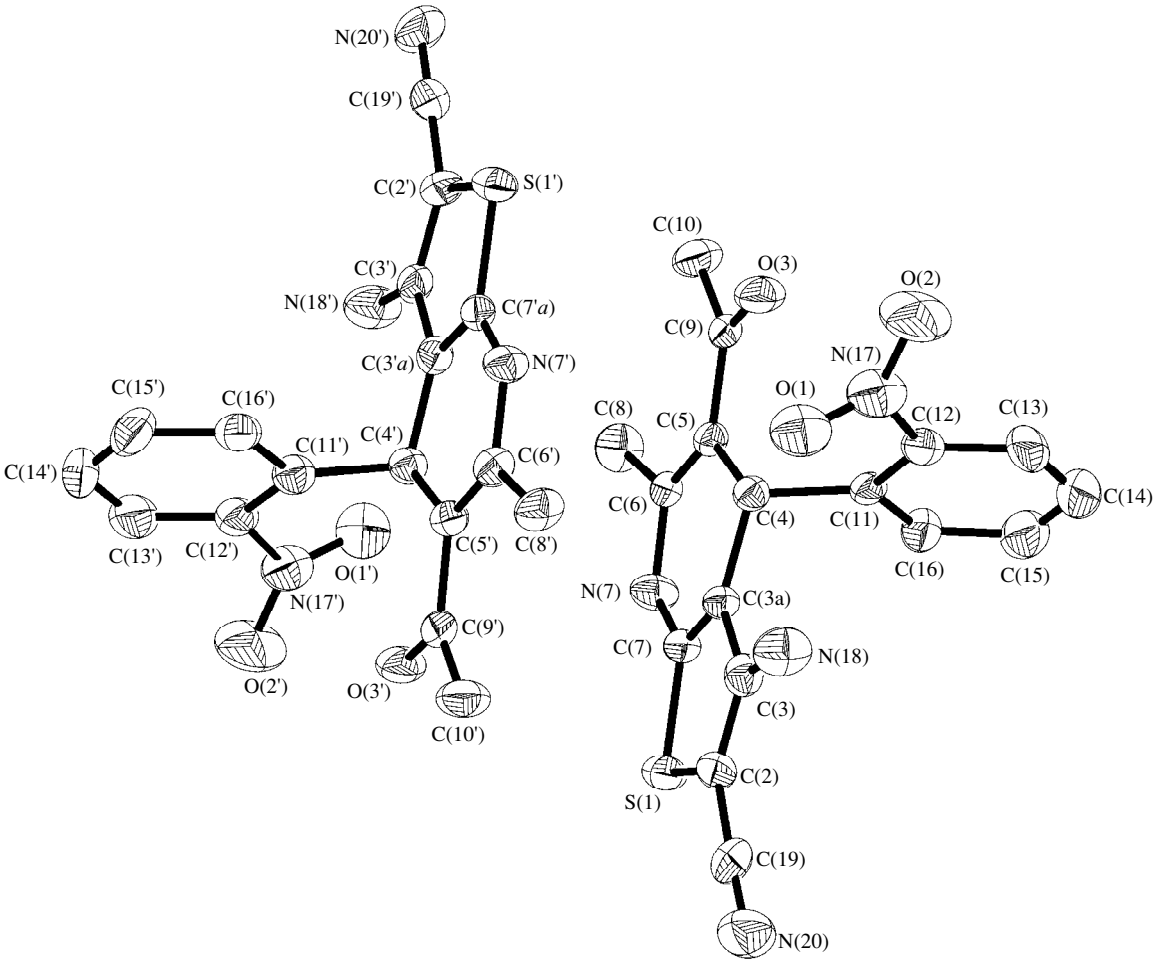

Fig. 1. A general view of crystallographically independent molecules *A* and *B*.

noncoincidence (the discrepancy is 0.124). Omitting the N(20) atom from the calculations results in the coefficient of 0.040 for the remaining molecular fragments.

A comparison of the geometric parameters (bond lengths, bond angles, and torsion angles) that characterize the shape of the symmetrically independent molecules *A* and *B* revealed that the majority of the parameters are identical within the statistically allowed deviations (the differences exceed the errors in estimation of the corresponding parameters no more than six times). In order to compare the torsion angles, one of the molecules was inverted. Hereinafter, describing the molecular structure of **I**, we bracket the values of the discussed parameters for molecule *B* to distinguish them from those for molecule *A*. If a single value is given, it is the average of the corresponding parameters for molecules *A* and *B*, which are considered identical within the experimental error unless otherwise specified.

MOLECULAR STRUCTURE

The *o*-nitrophenyl substituent in molecule **I** is synperiplanar relative to the H(4) atom (the relevant torsion angles have the following values: H(4)–C(4)–C(11)–C(12), 8.3(9)° [–2(1)°]; C(4)–C(11)–C(12)–N(17), –6(1)° [5(1)°]; and C(11)–C(12)–N(17)–O(1), –44(1)° [–41(1)°]. This results in the short nonbonded O(1)···C(4) contact {2.944(8) Å [2.943(7) Å]}, which, according to [11, 12], can be considered the intramolecular C–H···O hydrogen bond: C(4)–H(4), 1.05(5) Å [0.92(5) Å]; H(4)···O(1), 2.19(5) Å [2.34(5) Å]; and C(4)–H(4)···O, 127(3)° [123(3)°].

Molecule **I** contains three cyclic fragments. The six-membered N(7)–C(7*a*)–C(3*a*)–C(4)–C(5)–C(6) heterocycle adopts a flattened envelope conformation. The deviation of the C(4) atom from the mean plane passing through the other atoms of the ring is 0.135 Å [0.118 Å]. This plane forms a dihedral angle of 8.9° [7.8°] with the plane passing through the C(3*a*), C(5), and C(4) atoms. The five-membered S(1)–C(2)–C(3)–C(3*a*)–C(7*a*) ring is virtually planar. The dihedral angle

Atomic coordinates ($\times 10^4$; for H atoms, $\times 10^3$) in structure **I**

Molecule *A*				Molecule *B*			
Atom	*X*	*Y*	*Z*	Atom	*X*	*Y*	*Z*
S(1)	1505(1)	5131(2)	1220	S(1')	5909(1)	4926(2)	3236(1)
O(1)	5661(4)	4328(8)	934(3)	O(1')	1756(4)	5700(7)	3485(3)
O(2)	6769(3)	5893(9)	786(3)	O(2')	637(4)	4154(9)	3623(3)
O(3)	5659(3)	7037(8)	1920(3)	O(3')	1772(3)	2941(8)	2511(3)
N(7)	2461(3)	6819(8)	1926(3)	N(7')	4981(4)	3200(8)	2521(2)
N(17)	5960(4)	5616(10)	810(3)	N(17')	1449(4)	4428(9)	3611(3)
N(18)	3768(5)	3771(9)	525(3)	N(18')	3646(4)	6183(9)	3935(3)
N(20)	1448(7)	2626(10)	–6(5)	N(20')	5923(6)	7535(8)	4432(5)
C(2)	2175(4)	4169(8)	752(3)	C(2')	5235(5)	5850(10)	3702(3)
C(3)	3099(5)	4419(8)	821(3)	C(3')	4313(5)	5599(8)	3629(3)
C(3*a*)	3265(4)	5404(7)	1266(3)	C(3'*a*)	4148(4)	4590(7)	3196(3)
C(4)	4171(4)	6092(8)	1425(3)	C(4')	3252(4)	3913(8)	3021(3)
C(5)	4076(4)	7053(10)	1933(3)	C(5')	3355(4)	2976(10)	2514(3)
C(6)	3251(6)	7380(8)	2154(5)	C(6')	4196(6)	2643(10)	2295(5)
C(7*a*)	2481(4)	5865(8)	1492(3)	C(7'*a*)	4938(4)	4162(9)	2953(3)
C(8)	3044(5)	8233(10)	2655(3)	C(8')	4392(5)	1759(10)	1795(3)
C(9)	4963(5)	7503(7)	2134(5)	C(9')	2475(5)	2488(8)	2276(5)
C(10)	5096(5)	8513(10)	2616(3)	C(10')	2363(5)	1457(10)	1819(3)
C(11)	4518(4)	7094(11)	955(3)	C(11')	2874(5)	2936(11)	3469(3)
C(12)	5313(4)	6803(9)	670(3)	C(12')	2088(4)	3155(11)	3756(3)
C(13)	5561(6)	7711(12)	239(5)	C(13')	1825(6)	2264(13)	4176(5)
C(14)	5006(6)	8928(13)	91(4)	C(14')	2359(6)	1047(11)	4333(3)
C(15)	4221(6)	9227(11)	378(4)	C(15')	3146(6)	718(10)	4050(3)
C(16)	3998(5)	8321(9)	805(3)	C(16')	3400(5)	1664(9)	3629(3)
C(19)	1771(6)	3289(10)	335(3)	C(19')	5624(5)	6768(9)	4102(3)
H(4)	471(6)	533(11)	151(4)	H(4')	289(6)	474(11)	293(4)
H(7)	183(6)	701(11)	210(4)	H(7')	553(7)	254(11)	254(4)
H(18*a*)	448(6)	386(10)	61(3)	H(18*c*)	312(6)	594(12)	389(4)
H(18*b*)	362(6)	332(10)	24(3)	H(18*d*)	373(2)	662(3)	421(1)
H(8*a*)	324	889	269	H(8'*a*)	502	194	175
H(8*b*)	233	847	271	H(8'*b*)	421	51	186
H(8*c*)	319	762	298	H(8'*c*)	406	224	145
H(10*a*)	579	867	266	H(10*d*)	180	119	176
H(10*b*)	474	963	257	H(10*e*)	272	201	145
H(10*c*)	494	816	289	H(10*f*)	269	51	184
H(13)	614	752	7	H(13')	137	241	434
H(14)	514	959	–24	H(14')	221	40	462
H(15)	387	1020	27	H(15')	358	–25	409
H(16)	345	862	100	H(16')	406	156	349

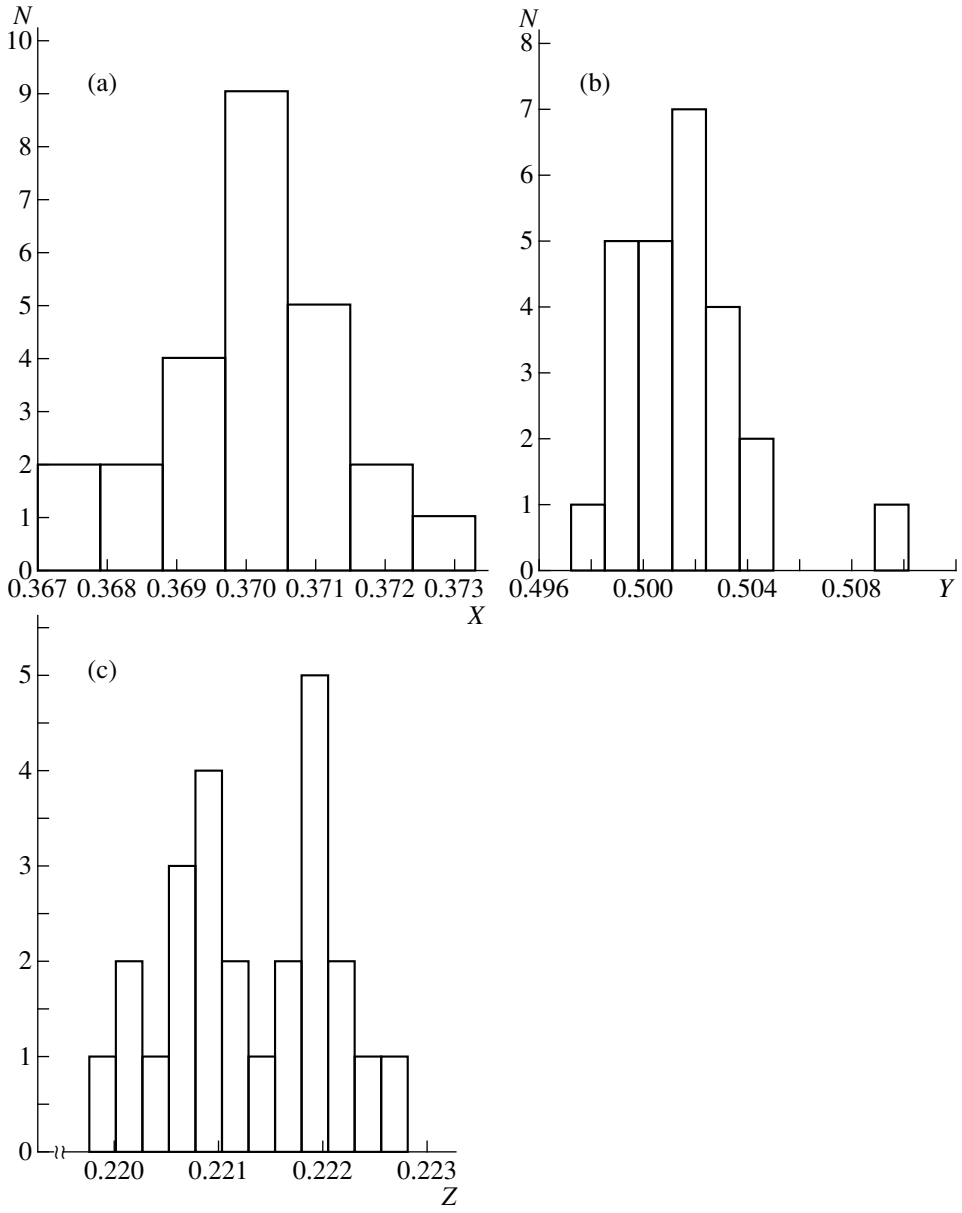

Fig. 2. Distribution of the coordinates (a) *X*, (b) *Y*, and (c) *Z* of geometric centers for pairs of the corresponding atoms in molecules *A* and *B*.

between the above mean planes of five- and six-membered heterocycles is approximately zero (0.6° for molecule *A* and 0.5° for molecule *B*).

The bond lengths in structure **I** coincide with the mean-statistic values within the limits of experimental error [13]. The dihedral angle between the plane of the phenyl ring and the plane of the N(7)–C(7*a*)–C(3*a*)–C(4)–C(5)–C(6) ring is 85° [86°]. The NO_2 group [N(17), O(1), and O(2)] is rotated relative to the mean plane of the phenyl ring by 42° [41°]. The C(6)–C(5)–C(9)–O(3) torsion angle is 5° [3°].

The planar fragments of molecules *A* and *B* (including the atoms of six- and five-membered heterocycles) are parallel within the limits of experimental error. The spacing between the planar fragments of the reference molecules is 3.56(5) Å.

CRYSTAL STRUCTURE

In order to determine the correct position of the approximate center of inversion, we statistically analyzed the coordinates of the inversion centers calculated for each pair of the corresponding atoms in molecules *A* and *B*. The histograms representing the distributions of coordinates *X*, *Y*, and *Z* of the geometric centers for these pairs are shown in Fig. 2.

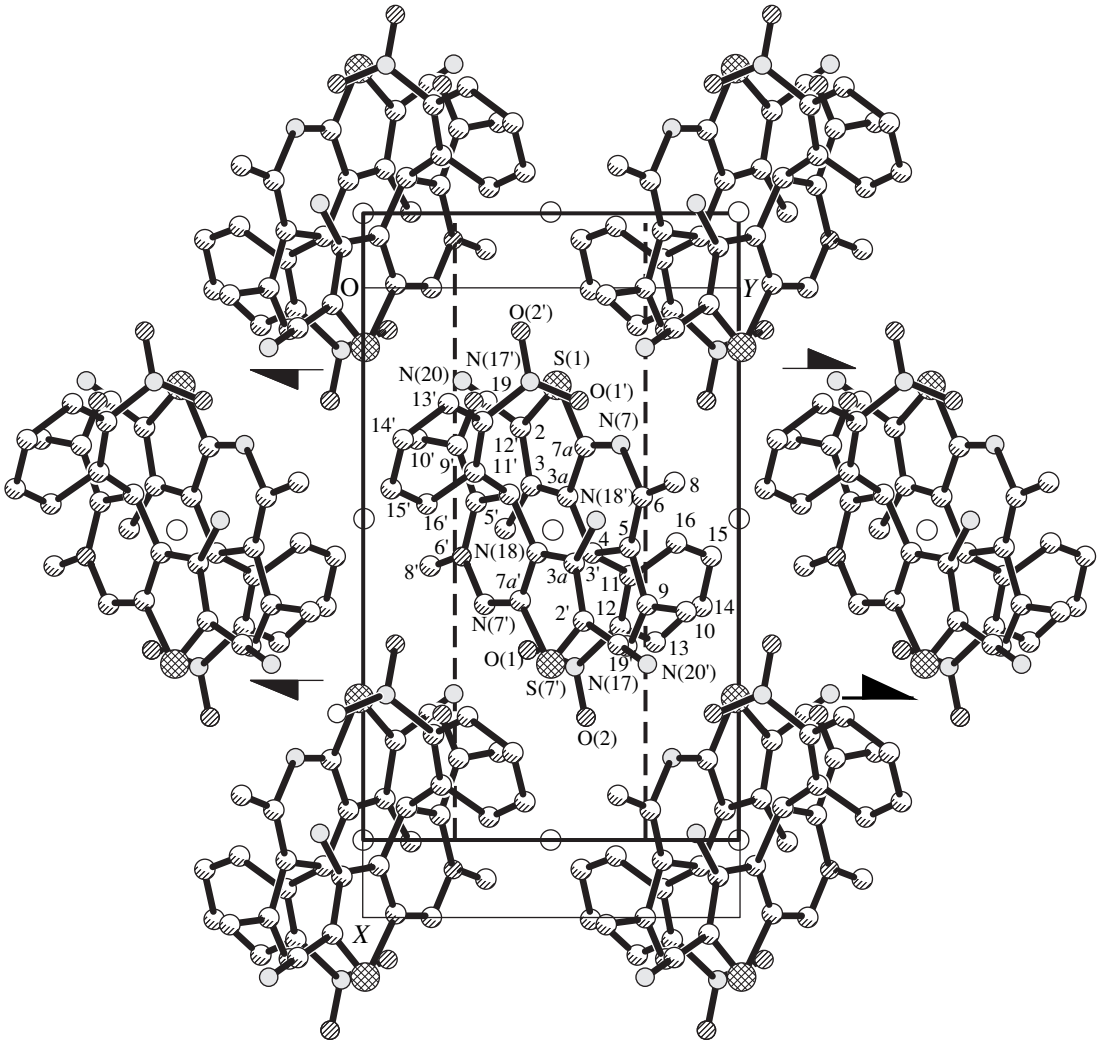

Fig. 3. Projection of a layer onto its specific plane.

It follows from the calculation that all of the 25 pairs of the corresponding atoms can be used to determine the *X* coordinate of the pseudocenter and the error of its estimation (obtained with the formulas of the Student distribution). To calculate the *Y* coordinate of the pseudocenter, it is necessary to reject the pair of the N(20) and N(20') atoms as a blunder, because the deviation of the center calculated for these atoms from the mean position of the center obtained for all the atomic pairs exceeds the rms errors of individual calculations by more than three times. Detailed analysis of the distribution over the *Z* coordinate revealed the superposition of several normal distributions of this coordinate of the pseudocenter. However, the arithmetic mean values of these distributions are situated in the *Z*-axis close to each other (the difference in the *Z* coordinates of the mean values of the adjacent normal distributions is no more than 0.025 Å), and the confidence intervals for estimation of these mean values are close to overlapping one another. The fiducial probability, at which the overlapping of these intervals occurs, is above 99%. Thus, we can state with the certainty degree of 99.9% that the approximate center of inversion relating the molecules is situated at the point with crystallographic coordinates 0.3706(8), 0.500(1), and 0.2216(13).

Most of the discrepancies (the distances between the atoms of molecule *B* (*A*) and the points at which the corresponding atoms of molecule *A* (*B*) are arranged upon its inversion at the pseudocenter) lie in the range of values (0.025–0.078 Å) comparable with the experimental error. The discrepancies that exceed the error in estimation of the bond lengths more than eight times are observed only for three atoms, namely, N(18), N(20), and C(15) (0.082, 0.152, and 0.084 Å, respectively).

The above center of inversion does not serve as an approximate element of symmetry for the structure as a whole. The totality of the inversion centers that is obtained by the composition of the reference approximate transformation and the lattice translations quite

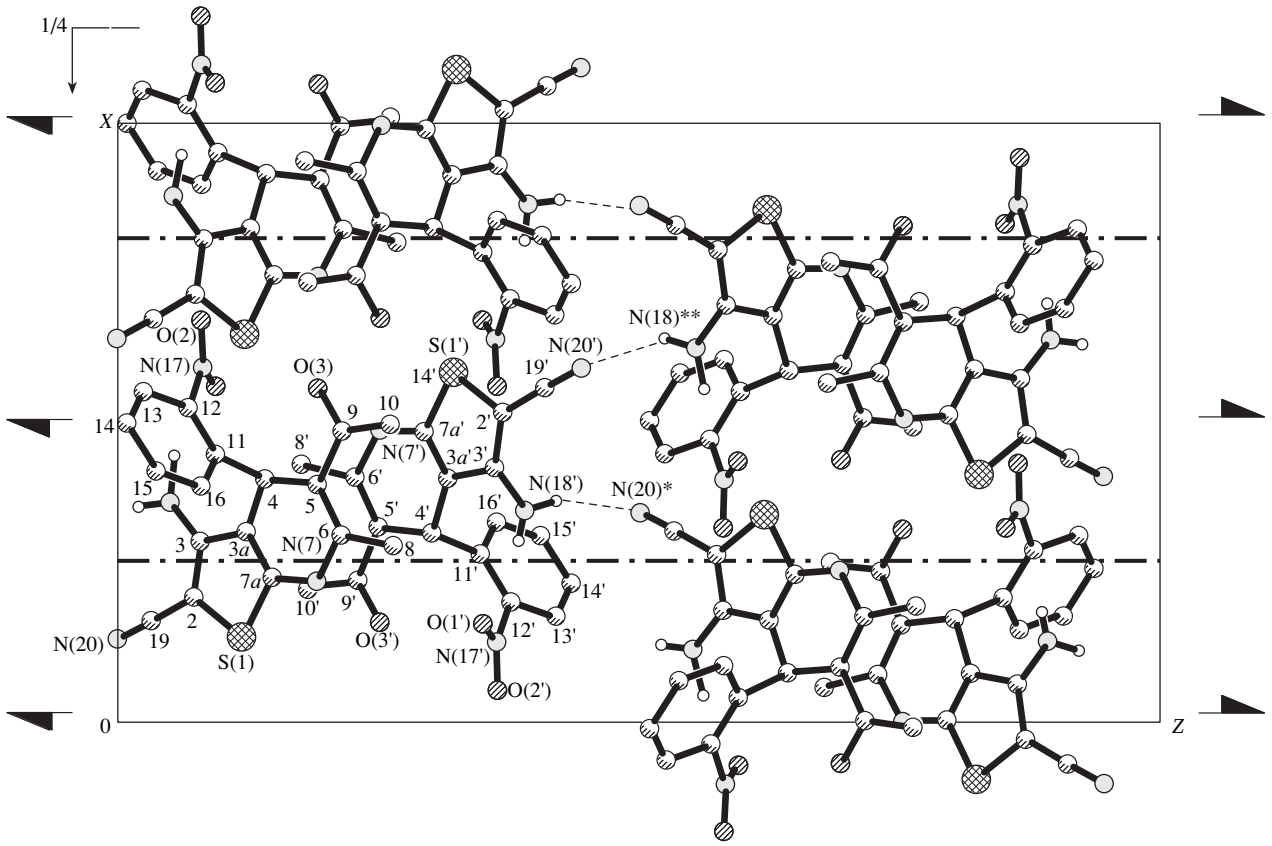

Fig. 4. Projection of crystal structure **I** onto the *XZ* plane. Dashed lines indicate intermolecular hydrogen bonds N–H···N.

accurately brings into coincidence the molecules lying in the *c*/2-thick layer (and the layers translationally equal to it), whose specific plane is parallel to the *X0Y* plane and passes through the point at $Z = 0.2216$.

The approximate symmetry of a separate layer is described by the group of symmetry of layers $P12_1/a1$, $Z = 4(1)$. Plane *a* is a crystallographic element of symmetry, whereas the center of inversion and the 2_1-axis, which lies in the specific plane of the layer, are approximate elements of layer symmetry.

The projection of this layer onto its specific plane and positions of its elements of symmetry are shown in Fig. 3. The unit cell of the layer is highlighted by heavy solid lines, and the projection of the crystallographic unit cell along the *c*-axis is indicated by thin solid lines. The atoms of the reference molecules are numbered (the atomic sort is omitted from the designations of carbon atoms).

The crystallographic twofold screw axis (or plane *n*) transforms the system of layers into the symmetrically equal system with the same characteristics. Therefore, crystal structure **I** can be represented as a combination of two subsystems. Each of the subsystems contains a totality of translationally equal layers (*Z* translation) perpendicular to the crystallographic direction [001]. Figure 4 displays the projection of crystal structure **I** onto the *X*0*Z* plane (perpendicular to the specific plane of the layer discussed). In this projection, we clearly see the layering of the structure.

The hydrogen bonds N(18')–H(18*d*)···N(20)* [the N(20)* atom belongs to the molecule related to the reference *A* molecule by the $*(1/2 - x, 1/2 + y, 1/2 + z)$ transformation] and N(18)**–H(18*b*)**···N(20') [the N(18)** and H(18*b*)** atoms belong to the molecule related to the reference *A* molecule by the $**(1 - x, 1 - y, 1/2 + z)$ transformation] are formed in structure **I**. These bonds link the molecules of different layers and, probably, stabilize the relative position of the subsystems observed in structure **I**.

Now, we consider a theoretical possibility of extending the packing of molecules **I** with the crystallographic center of inversion to a centrosymmetric space group. If we locate the center of inversion in the twofold axis [shifting it by $0.129a$ (1.89 Å) along the *X*-axis], then, after the reduction to the standard setting ($X \longrightarrow X$, $Y \longrightarrow Z$, $Z \longrightarrow -Y$) the symmetry of the crystal structure obtained is described by the centrosymmetric space group *Pnma*, $Z = 8(1)$. Upon the appropriate transformations of the atomic coordinates of the reference molecules (in space group *Pnma*, molecules *A* and *B* become symmetrically equivalent), a single symmetry-independent molecule occupies the general position.

The following main differences in the relative positions of molecules on going to the centrosymmetric group are observed: (1) the elements of approximate symmetry of a layer become crystallographic elements and (2) the relative shift of the subsystems by 3.54 Å is observed in real structure **I** (the shift takes place in the specific plane of the layer; it is directed perpendicular to the 2_1-axis lying in this plane) but is absent in space group *Pnma*.

The shift of the subsystems observed in structure **I** is due to the fact that the structural units in the crystal have tendency to closer packing. Actually, if this shift is absent (space group *Pnma*), the "hill-to-hollow" principle [14] is violated, since the layers in the centrosymmetric group under consideration are related by the *m* plane ("hills" face "hills", and "hollows" face "hollows"). The transition to the centrosymmetric space group would change the relative position of molecules, resulting in unreasonably short intermolecular N(20)···N(20) contacts. The N(20)···N(20) distance in space group *Pnma* would be 1.44 Å {at the mean length of the normal van der Waals contact N···N (3.00 Å [15]), d = 2.85 Å}. Another unreasonably short contact would appear between the phenyl rings of the molecules in different layers (the C(14)···C(14) and H(14)···H(14) distances would be 1.92 and 0.36 Å, respectively, at the mean lengths of the normal van der Waals contacts C···C (3.42 Å), and H···H (2.31 Å) and $d_{C\cdot\cdot C}$ = 3.27 and $d_{H\cdot\cdot H}$ = 2.01 Å [15]). Thus, the centrosymmetric packing of molecules **I** cannot be formed at the given value of the unit-cell parameter *c*. Crystals with space group *Pnma* can be formed only with an increased *c* parameter (so that the contacts between the "hills" of the layers—the N(20), C(14), and H(14) atoms—reach the normal values). However, an increase in the *c* parameter at constant *Z* would result in a unit cell of a larger volume and, consequently, with a smaller coefficient of space filling, which, in most cases, is less profitable than the close packing.

Another possible argument against the occurrence of space group *Pnma* is the impossibility of forming the N···H–N hydrogen bonds, which are observed in the real crystal structure. The molecules within the layers under consideration have only van der Waals contacts, whereas stronger (compared to van der Waals interactions) hydrogen bonds are formed between the molecules of different layers. Apparently, the change in the relative position of the layers would lead to a change in the character (and, hence, the energy) of bonds between the layers: hydrogen bonding would become van der Waals interaction, which is unfavorable for energy reasons.

Thus, based on the above discussion, we conclude that the pseudocenter of inversion in structure **I** is more favorable than the true center at a special position, because it affords, first, a closer molecular packing in crystals and, second, the formation of N···H–N hydrogen bonds.

ACKNOWLEDGMENTS

This work was supported by the Russian Foundation for Basic Research, project nos. 97-03-33783a and 96-15-97367.

REFERENCES

1. D. Lednicer and L. A. Mitscher, *The Organic Chemistry of Drug Synthesis* (New York, Wiley, 1980), Vol. 2, p. 283.
2. S. Goldmann and J. Stoltefuss, Angew. Chem. Int. Ed. Engl. **30** (2), 1559 (1991).
3. V. N. Nesterov, V. E. Shklover, Yu. T. Struchkov, *et al*., Acta Crystallogr., Sect. C: Cryst. Struct. Commun. **41**, 191 (1991).
4. V. N. Nesterov, L. A. Rodinovskaya, A. M. Shestopalov, *et al*., Khim. Geterotsikl. Soedin., No. 5, 643 (1997).
5. A. V. Samet, A. M. Shestopalov, V. N. Nesterov, *et al*., Synthesis, No. 6, 623 (1997).
6. V. N. Nesterov, A. M. Shestopalov, and L. A. Rodinovskaya, in *Proceedings of I National Conf. on Crystal Chemistry* (Chernogolovka, 1988), p. 40.
7. V. N. Nesterov, L. N. Kuleshova, A. A. Samet, *et al*., Kristallografiya **44** (3), 471 (1999).
8. V. M. Potapov, *Stereochemistry* [in Russian] (Moscow, Khimiya, 1988).
9. G. M. Sheldrick, *SHELXTL-Plus/PC* (Madison, Siemens Analytical X-ray Instruments Inc., 1989).
10. A. E. Razumaeva and P. M. Zorkiĭ, Zh. Strukt. Khim. **21** (2), 77 (1980).
11. L. Berkovitch-Yellin and L. Leiserowitz, Acta Crystallogr., Sect. B: Struct. Sci. **40**, 159 (1984).
12. G. R. Desiraju, Acc. Chem. Res. **24** (10), 290 (1991).
13. F. H. Allen, O. Kennard, D. G. Watson, *et al*., J. Chem. Soc., Perkin Trans. **2**, S1 (1987).
14. A. I. Kitaĭgorodskiĭ, *Molecular Crystals* [in Russian] (Moscow, Nauka, 1971).
15. Yu. V. Zefirov and P. M. Zorkiĭ, Usp. Khim. **64** (5), 446 (1995).

Translated by I. Polyakova

Crystallography Reports, Vol. 45, No. 1, 2000, pp. 98–102. From Kristallografiya, Vol. 45, No. 1, 2000, pp. 104–107.

STRUCTURES OF ORGANIC COMPOUNDS

Structure of a Liquid Crystal of 4-Cyano-4'-*n*-Octyloxybiphenyl[1]

Rajnikant*,[2] V. K. Gupta*, R. Gupta*, A. Kumar*, R. K. Bamezaĭ, N. K. Sharma**, and B. Varghese*****

** X-ray Crystallography Laboratory, Department of Physics, University of Jammu, Jammu Tawi, 180006 India*

*** Chemistry Department, University of Jammu, Jammu Tawi, 180006 India*

**** Regional Sophisticated Instrumentation Centre, Indian Institute of Technology, Chennai, 600036 India*

Received June 8, 1998; in final form, October 15, 1998

Abstract—The structure of a liquid crystal of 4-cyano-4'-*n*-octyloxybiphenyl ($C_{21}H_{25}NO$) is determined by X-ray diffraction analysis. The compound crystallizes in the triclinic crystal system with unit cell parameters $a = 7.322(1)$ Å, $b = 12.693(3)$ Å, $c = 20.393(2)$ Å, $\alpha = 92.45(1)°$, $\beta = 99.96(1)°$, $\gamma = 99.35(2)°$, and space group $P\bar{1}$. The structure is solved by the direct method and refined to $R = 0.057$. Two independent molecules are located in the asymmetric unit. No short intermolecular contacts are observed in the crystal packing. © *2000 MAIK "Nauka/Interperiodica".*

The biphenyl and its derivatives have been studied extensively in the past because of the difference found in the inter-ring torsion angles ψ in the solid state [1–3] and in the gas phase [4, 5]. This has entailed extended studies of the molecular geometry, crystal packing, and thermal motion effects [6–9].

Recent papers is have reported the recrystallization and crystal structure analysis of a series of 2,3,4-substituted biphenyl systems [10–13]. The range of crystallization conditions reported so far indicate that the linearly chained biphenyl systems (liquid crystalline materials) would be good objects for a systematic analysis of growth conditions and morphology modifiers for the preparation of organic crystals from organic solvents. In this respect, we have already reported crystallization and structure analysis of two liquid crystalline materials [14, 15]. The present work is a continuation of systematic investigations on the crystallization and preparation of single crystals suitable for X-ray diffraction analysis. Crystals of 4-cyano-4'-*n*-octyloxybiphenyl have been grown from acetic acid. It is known that this material undergoes transformation to the smectic *A* phase at 54.5°C, which finally becomes an isotropic liquid at 80.0°C [16].

EXPERIMENTAL

The growth of X-ray diffraction quality crystals of the title compound was carried out with a variety of known organic solvents. However, success was achieved with acetic acid by employing the solvent loss technique. The X-ray diffraction intensity data for a white needle-shaped crystal were collected from a single crystal of approximate dimensions 0.40 × 0.25 ×

Table 1. Crystal data and other experimental details

Crystal description	White transparent needle
Chemical formula	$C_{21}H_{25}NO$
Molecular weight	307.435
Cell parameters	$a = 7.322(1)$ Å, $b = 12.693(3)$ Å $c = 20.393(2)$ Å, $\alpha = 92.45(1)°$ $\beta = 99.96(1)°$, $\gamma = 99.35(2)°$
Unit cell volume	1837.02Å^3
Crystal system	Triclinic
Space group	$P\bar{1}$
Density (calculated)	1.112 g/cm^3
No. of molecules per unit cell	4
Wavelength	1.5418 Å
Linear absorption coefficient	5.185 cm^{-1}
F(000)	664
Crystal size	0.40 × 0.25 × 0.15 mm
θ range for entire data collection	$0 \le \theta \le 68°$
No. of measured reflections	6757
No. of unique reflections	5409
No. of observed reflections	3693
Software for structure solution	Direct methods (SHELXS86)
Software for Refinement	SHELXL93
No. of parameters refined	416
Final *R*-factor	0.057
$wR(F^2)$	0.1949
Final residual electron density	$0.17 < \Delta\rho < -0.19$ eÅ^{-3}
$(\Delta/\sigma)_{max}$ in the final cycle for non-hydrogen atoms	–0.343 for C18

[1] This article was submitted by the authors in English.

[2] Author for correspondence.

Table 2. Atomic coordinates and equivalent isotropic temperature factors (Å^2) with e.s.d.'s in parentheses, for the non-hydrogen atoms

Atom	Molecule 1				Atom	Molecule 2			
	x	y	z	U^*_{eq}		x	y	z	U^*_{eq}
C(1)	0.0408(3)	0.8028(2)	0.4480(1)	0.0549(9)	C(1')	0.5130(3)	0.5488(2)	0.7435(1)	0.0579(9)
C(2)	0.1835(3)	0.8912(2)	0.4500(1)	0.0623(10)	C(2')	0.4980(4)	0.6284(2)	0.7903(1)	0.0671(10)
C(3)	0.3137(3)	0.8963(2)	0.4077(1)	0.0660(10)	C(3')	0.3612(4)	0.6144(2)	0.8288(1)	0.0690(11)
C(4)	0.3034(3)	0.8100(2)	0.3619(1)	0.0603(9)	C(4')	0.2333(4)	0.5207(2)	0.8226(1)	0.0629(10)
C(5)	0.1620(3)	0.7219(2)	0.3588(1)	0.0600(9)	C(5')	0.2465(4)	0.4391(2)	0.7770(1)	0.0673(10)
C(6)	0.0343(3)	0.7183(2)	0.4013(1)	0.0629(10)	C(6')	0.3837(4)	0.4545(2)	0.7378(1)	0.0647(10)
C(7)	–0.0936(3)	0.7993(2)	0.4943(1)	0.0560(9)	C(7')	0.6583(3)	0.5627(2)	0.7010(1)	0.0553(9)
C(8)	–0.0377(3)	0.8409(2)	0.5597(1)	0.0631(9)	C(8')	0.6182(3)	0.5230(2)	0.6349(1)	0.0589(9)
C(9)	–0.1639(3)	0.8400(2)	0.6026(1)	0.0644(10)	C(9')	0.7544(3)	0.5303(2)	0.5956(1)	0.0598(10)
C(10)	–0.3518(3)	0.7963(2)	0.5802(1)	0.0589(10)	C(10')	0.9366(3)	0.5804(2)	0.6224(1)	0.0554(10)
C(11)	–0.4104(3)	0.7518(2)	0.5158(1)	0.0633(9)	C(11')	0.9790(3)	0.6242(2)	0.6875(1)	0.0680(10)
C(12)	–0.2826(3)	0.7530(2)	0.4734(1)	0.0619(10)	C(12')	0.8424(3)	0.6155(2)	0.7268(1)	0.0665(10)
O(13)	0.4267(3)	0.8035(1)	0.3192(1)	0.0718(7)	O(13')	0.1028(3)	0.5145(2)	0.8628(1)	0.0767(8)
C(14)	0.5787(4)	0.8904(2)	0.3211(1)	0.0661(10)	C(14')	–0.0438(4)	0.4238(2)	0.8538(1)	0.0694(11)
C(15)	0.6937(4)	0.8600(2)	0.2711(1)	0.0706(10)	C(15')	–0.1735(4)	0.4421(2)	0.9010(1)	0.0729(12)
C(16)	0.8627(4)	0.9460(2)	0.2690(1)	0.0706(11)	C(16')	–0.3307(4)	0.3484(2)	0.8996(1)	0.0715(11)
C(17)	0.9750(4)	0.9195(2)	0.2168(2)	0.0763(12)	C(17')	–0.4582(4)	0.3669(2)	0.9491(1)	0.0713(11)
C(18)	1.1394(4)	1.0069(2)	0.2125(1)	0.0729(11)	C(18')	–0.6136(4)	0.2745(3)	0.9505(2)	0.0813(13)
C(19)	1.2520(4)	0.9808(2)	0.1598(2)	0.0804(12)	C(19')	–0.7400(4)	0.2917(3)	1.0000(2)	0.0836(12)
C(20)	1.4141(4)	1.0651(3)	0.1544(2)	0.0938(14)	C(20')	–0.8991(5)	0.2014(3)	0.9999(2)	0.1129(18)
C(21)	1.5245(6)	1.0379(3)	0.1018(2)	0.1288(19)	C(21')	–1.0204(5)	0.2181(4)	1.0510(2)	0.1452(24)
C(22)	–0.4839(4)	0.8024(2)	0.6251(1)	0.0670(11)	C(22')	1.0822(4)	0.5854(2)	0.5827(1)	0.0657(10)
N(23)	–0.5866(3)	0.8117(2)	0.6604(1)	0.0902(12)	N(23')	1.1964(3)	0.5867(2)	0.5510(1)	0.0827(11)

* $U_{eq} = (1/3) \sum_i \sum_j U_{ij} a^*_i a^*_j a_i a_j.$

0.15 mm on an Enraf–Nonius CAD4 diffractometer (CuK_α radiation). The accurate unit-cell dimensions and the orientation matrix were obtained by the least squares fit to the setting angles of 25 reflections. The $\omega/2\theta$ scan was employed. A total number of 6757 reflections were measured in the θ range 0°–68° ($-8 \le h \le 8, -15 \le k \le 14, 0 \le l \le 20$), of which only 3693 were treated as observed with $F_o > 4\sigma(F_o)$). Two strong reflections monitored periodically showed that the crystal was stable to X-rays. The data were corrected for Lorentz and polarization effects. The crystal structure was solved by the direct method using the SHELXS86 software package [17]. Two molecules in the asymmetric unit were found. The isotropic refinement of the structure by the least squares methods using the SHELXL93 software package [18] was followed by the anisotropic refinement of all the non-hydrogen atoms. The hydrogen atoms were placed at geometrically calculated positions and refined in the structure-factor calculations as riding atoms with fixed isotropic temperature factors. The final refinement cycle yielded the residual indices $R = 0.057$ and $wR(F^2) = 0.1949$. The residual electron density in the final difference Fourier map ranges from 0.17 to –0.19 e Å^{-3}. The maximum ratio (shift / e.s.d) is –0.343 for the C(18) atom. Atomic scattering factors were taken from the *International Tables for Crystallography* (1992, Vol. C, Tables 4.2.6.8, 6.1.1.4). Some calculations, for example, the calculation of the least-squares planes, were performed with the PC version of the PARST program [19].

RESULTS AND DISCUSSION

Crystal data is presented in Table 1. The atomic coordinates and equivalent isotropic temperature factors for two independent molecules are given in Table 2. Some selected torsion angles are listed in Table 5. A general view of the molecule with the atomic numbering scheme is shown in Fig. 1 (ZORTEP) [20].

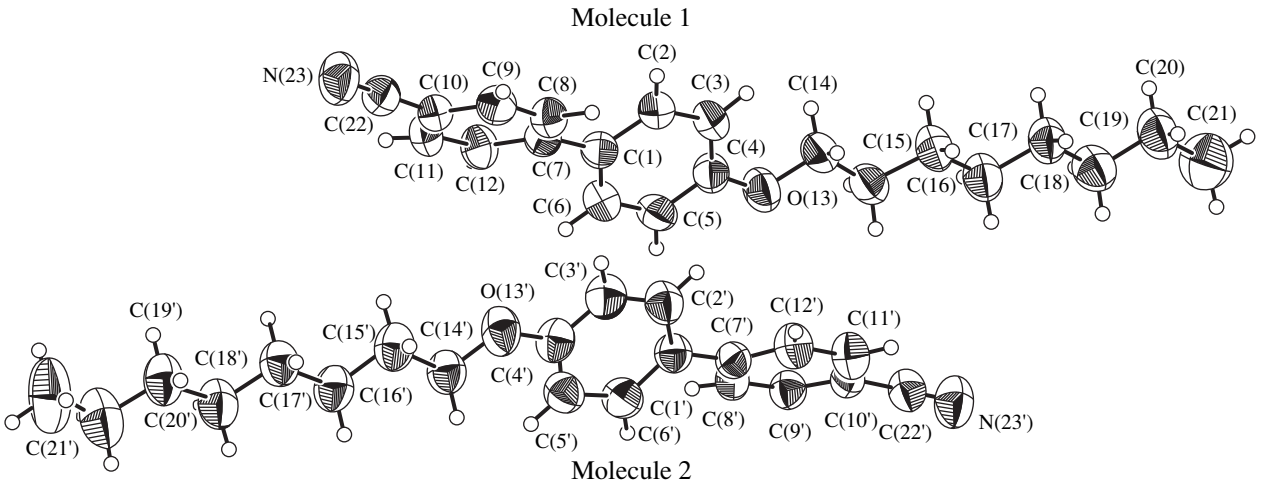

Fig. 1. A general view of the molecules and the atomic numbering scheme.

The crystal structure of 4-cyano-4'-*n*-octyloxybiphenyl contains two crystallographically independent molecules (termed as molecule 1 and 2) in the asymmetric unit. The average bond distances for the phenyl rings in both molecules are in good agreement with those of linear-chained biphenyls such as 4,4'-bis(*n*-propylamino)biphenyl [14], 4-cyano-4'-*n*-dodecylbiphenyl [15], 4-cyano-4'-*n*-undecylbiphenyl [21], and 4-

Table 3. Bond distances (Å) with e.s.d.'s in parentheses

Molecule 1		Molecule 2	
C1–C2	1.397(3)	C1'–C2'	1.391(3)
C1–C6	1.393(3)	C1'–C6'	1.397(3)
C1–C7	1.474(3)	C1'–C7'	1.478(3)
C2–C3	1.388(3)	C2'–C3'	1.370(4)
C3–C4	1.393(3)	C3'–C4'	1.375(3)
C4–C5	1.386(3)	C4'–C5'	1.389(3)
C4–O13	1.367(3)	C4'–O13'	1.358(4)
C5–C6	1.377(3)	C5'–C6'	1.383(4)
C7–C8	1.381(3)	C7'–C8'	1.383(3)
C7–C12	1.397(3)	C7'–C12'	1.405(3)
C8–C9	1.377(3)	C8'–C9'	1.376(3)
C9–C10	1.386(3)	C9'–C10'	1.387(3)
C10–C11	1.375(3)	C10'–C11'	1.381(3)
C10–C22	1.451(5)	C10'–C22'	1.441(4)
C11–C12	1.378(3)	C11'–C12'	1.380(3)
O13–C14	1.428(3)	O13'–C14'	1.422(3)
C14–C15	1.506(4)	C14'–C15'	1.500(4)
C15–C16	1.519(4)	C15'–C16'	1.510(4)
C16–C17	1.511(5)	C16'–C17'	1.526(4)
C17–C18	1.516(4)	C17'–C18'	1.501(4)
C18–C19	1.520(5)	C18'–C19'	1.514(5)
C19–C20	1.486(4)	C19'–C20'	1.494(5)
C20–C21	1.509(6)	C20'–C21'	1.510(6)
C22–N23	1.143(4)	C22'–N23'	1.140(4)

Table 4. Bond angles (°) with e.s.d.'s in parentheses

Molecule 1		Molecule 2	
C6–C1–C7	122.0(2)	C6'–C1'–C7'	120.7(2)
C2–C1–C7	121.0(2)	C2'–C1'–C7'	122.3(2)
C2–C1–C6	116.9(2)	C2'–C1'–C6'	116.9(2)
C1–C2–C3	122.4(2)	C1'–C2'–C3'	121.5(2)
C2–C3–C4	119.0(2)	C2'–C3'–C4'	121.1(2)
C3–C4–O13	124.8(2)	C3'–C4'–O13'	116.8(2)
C3–C4–C5	119.4(2)	C3'–C4'–C5'	118.7(2)
C5–C4–O13	115.8(2)	C5'–C4'–O13'	124.5(2)
C4–C5–C6	120.6(2)	C4'–C5'–C6'	119.7(2)
C1–C6–C5	121.6(2)	C1'–C6'–C5'	122.0(2)
C1–C7–C12	120.9(2)	C1'–C7'–C12'	120.9(2)
C1–C7–C8	121.4(2)	C1'–C7'–C8'	121.1(2)
C8–C7–C12	117.6(2)	C8'–C7'–C12'	117.9(2)
C7–C8–C9	121.5(2)	C7'–C8'–C9'	121.8(2)
C8–C9–C10	119.8(2)	C8'–C9'–C10'	119.5(2)
C9–C10–C22	118.6(2)	C9'–C10'–C22'	120.2(2)
C9–C10–C11	119.9(2)	C9'–C10'–C11'	119.9(2)
C11–C10–C22	121.4(2)	C11'–C10'–C22'	120.0(2)
C10–C11–C12	119.8(2)	C10'–C11'–C12'	120.3(2)
C7–C12–C11	121.3(2)	C7'–C12'–C11'	120.5(2)
C4–O13–C14	118.6(2)	C4'–O13'–C14'	118.9(2)
O13–C14–C15	107.0(2)	O13'–C14'–C15'	107.3(2)
C14–C15–C16	112.2(2)	C14'–C15'–C16'	113.0(2)
C15–C16–C17	113.1(2)	C15'–C16'–C17'	112.4(2)
C16–C17–C18	113.4(2)	C16'–C17'–C18'	114.0(2)
C17–C18–C19	113.6(2)	C17'–C18'–C19'	114.4(3)
C18–C19–C20	114.8(3)	C18'–C19'–C20'	114.8(3)
C19–C20–C21	114.1(3)	C19'–C20'–C21'	114.2(3)

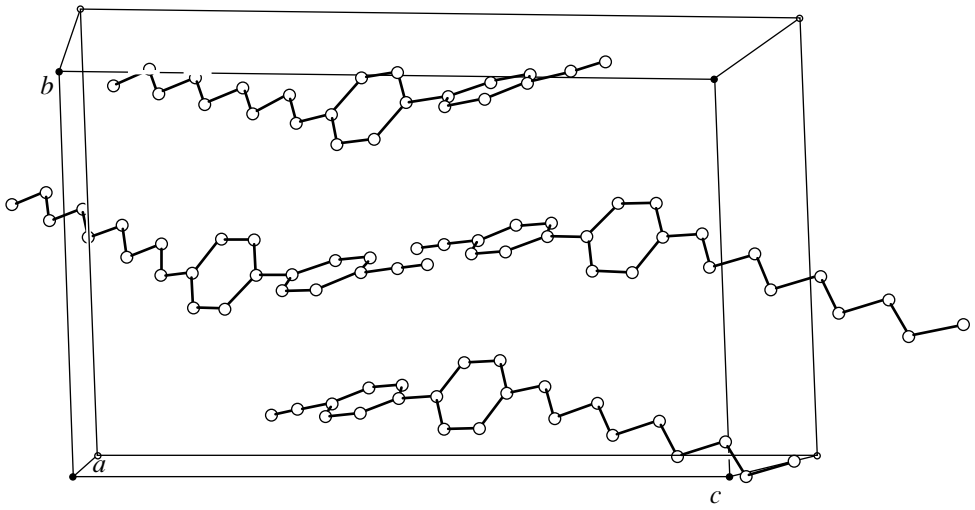

Fig. 2. Molecular packing viewed along the *a*-axis.

cyano-4'-*n*-decylbiphenyl [22]. The four internal ring bond angles in molecule 1 at the atoms C(1) [116.9(2)°], C(4) [119.4(2)°], C(7) [117.6(2)°], and C(10) [118.9(3)°] and in molecule 2 at the atoms C(1') [116.9(2)°], C(4') [118.7(2)°], C(7') [117.9(2)°], and C(10') [119.9(2)°] are slightly smaller than the ideal angles of 120°. However, more or less, these values are in good agreement with those found in some analogous structures [14, 15, 21, 22]. The length of the bond joining two phenyl rings in both molecules [C(1)–C(7), 1.474(3) Å and C(1')–C(7'), 1.478(3) Å] is quite close to the standard length of a single bond between the trigonally linked carbon atoms [23]. A respective comparison of bond distances and angles for both asymmetric molecules reveals a high degree of similarity (Tables 3, 4). The dihedral angles between the phenyl rings in molecules 1 and 2 are 37.79(7)° and 38.67(8)°, respectively. This shows that the two molecules in the asymmetric unit have identical conformations.

Table 5. Torsion angles τ (deg) with the e.s.d.'s in parentheses

Molecule 1		Molecule 2	
atoms	τ	atoms	τ
C(6)–C(1)–C(7)–C(8)	141.5(2)	C(6')–C(1')–C(7')–C(8')	38.0(3)
C(2)–C(1)–C(7)–C(8)	−37.3(3)	C(2')–C(1')–C(7')–C(8')	−141.6(2)
C(6)–C(1)–C(7)–C(12)	−38.2(3)	C(6')–C(1')–C(7')–C(12')	−141.1(2)
C(2)–C(1)–C(7)–C(12)	142.9(2)	C(2')–C(1')–C(7')–C(12')	39.2(3)
C(9)–C(10)–C(22)–N(23)	65.2(6)	C(9')–C(10')–C(22')–N(23')	−54.6(9)

The packing of the molecules in the crystal is shown in Fig. 2 [24]. The molecule is slightly bent at the O(13) atom. This phenomenon generally takes place in the case of liquid crystalline materials having carbon or oxygen at the position joining the biphenyl moiety. The molecular pairs of the asymmetric unit are packed in layers, which is a requirement for the material to be a smectogen. The molecules appear to be extending along the *bc* plane (in the approximate direction [401]). The cohesion of the structure is due to the van der Waals interactions.

ACKNOWLEDGMENTS

One of the authors (Rajnikant) acknowledges the support of the Scientific & Industrial Research Council of the Government of India, project no. 3(796)/96/EMR-II.

REFERENCES

1. A. Hargreaves and S. H. Rizvi, Acta Crystallogr. **15,** 365 (1962).
2. G. P. Charbonneau and Y. Delugeard, Acta Crystallogr., Sect. B: Struct. Crystallogr. Cryst. Chem. **32,** 1420 (1976).

3. G. P. Charbonneau and Y. Delugeard, Acta Crystallogr., Sect. B: Struct. Crystallogr. Cryst. Chem. **33,** 1586 (1977).
4. A. Almenningen and O. Bastianssen, K. Nor. Vidensk. Selsk. Skr. **4,** 1 (1958).
5. O. Bastianssen and M. Traetteberg, Tetrahedron **17,** 147 (1962).
6. C. P. Brock and K. L. Haller, J. Phys. Chem. **88,** 3570 (1984).
7. C. P. Brock and K. L. Haller, Acta Crystallogr., Sect. C: Cryst. Struct. Commun. **40,** 1387 (1984).
8. C. P. Brock and G. L. Morelan, J. Phys. Chem. **90,** 5631 (1986).
9. C. P. Brock and R. P. Minton, J. Am. Chem. Soc. **111,** 4586 (1989).
10. Rajnikant, D. Watkin, and G. Tranter, Acta Crystallogr., Sect. C: Cryst. Struct. Commun. **51,** 2388 (1995).
11. Rajnikant, D. Watkin, and G. Tranter, Acta Crystallogr., Sect. C: Cryst. Struct. Commun. **51,** 1452 (1995).
12. Rajnikant, D. Watkin, and G. Tranter, Acta Crystallogr., Sect. C: Cryst. Struct. Commun. **51,** 2071 (1995).
13. Rajnikant, D. Watkin, and G. Tranter, Acta Crystallogr., Sect. C: Cryst. Struct. Commun. **51,** 2161 (1995).
14. Rajnikant, V. K. Gupta, A. Kumar, *et al.*, Mol. Cryst. Liq. Cryst. (1998) (in press).
15. Rajnikant, V. K. Gupta, R. Gupta, *et al.*, Mol. Mater. (1998) (in press).
16. *British Drug House Liquid Crystal Manual* (Poole, England, 1979).
17. G. M. Sheldrick, *SHELXS86: Program for the Solution of Crystal Structures* (Univ. of Göttingen, Göttingen, 1986).
18. G. M. Sheldrick, *SHELXL93: Program for the Refinement of Crystal Structures* (Univ. of Göttingen, Göttingen, 1993).
19. M. Nardelli, Comput. Chem. **7,** 95 (1983).
20. L. Zsolnai and H. Pritzkow, *ZORTEP: ORTEP Program for Personal Computer* (1994).
21. T. Manisekaran, R. K. Bamezai, N. K. Sharma, *et al.*, Mol. Cryst. Liq. Cryst. **268,** 45 (1995).
22. T. Manisekaran, R. K. Bamezai, N. K. Sharma, *et al.*, Mol. Cryst. Liq. Cryst. **268,** 83 (1995).
23. D. W. J. Cruickshank and R. A. Sparks, Proc. R. Soc. London, Ser. A. **258,** 270 (1960).
24. C. K. Johnson, *ORTEPII: A Fortran Thermal Ellipsoid Plot Program for Crystal Structure Illustrations, ORNL-5138* (Oak Ridge National Laboratory, 1976).